

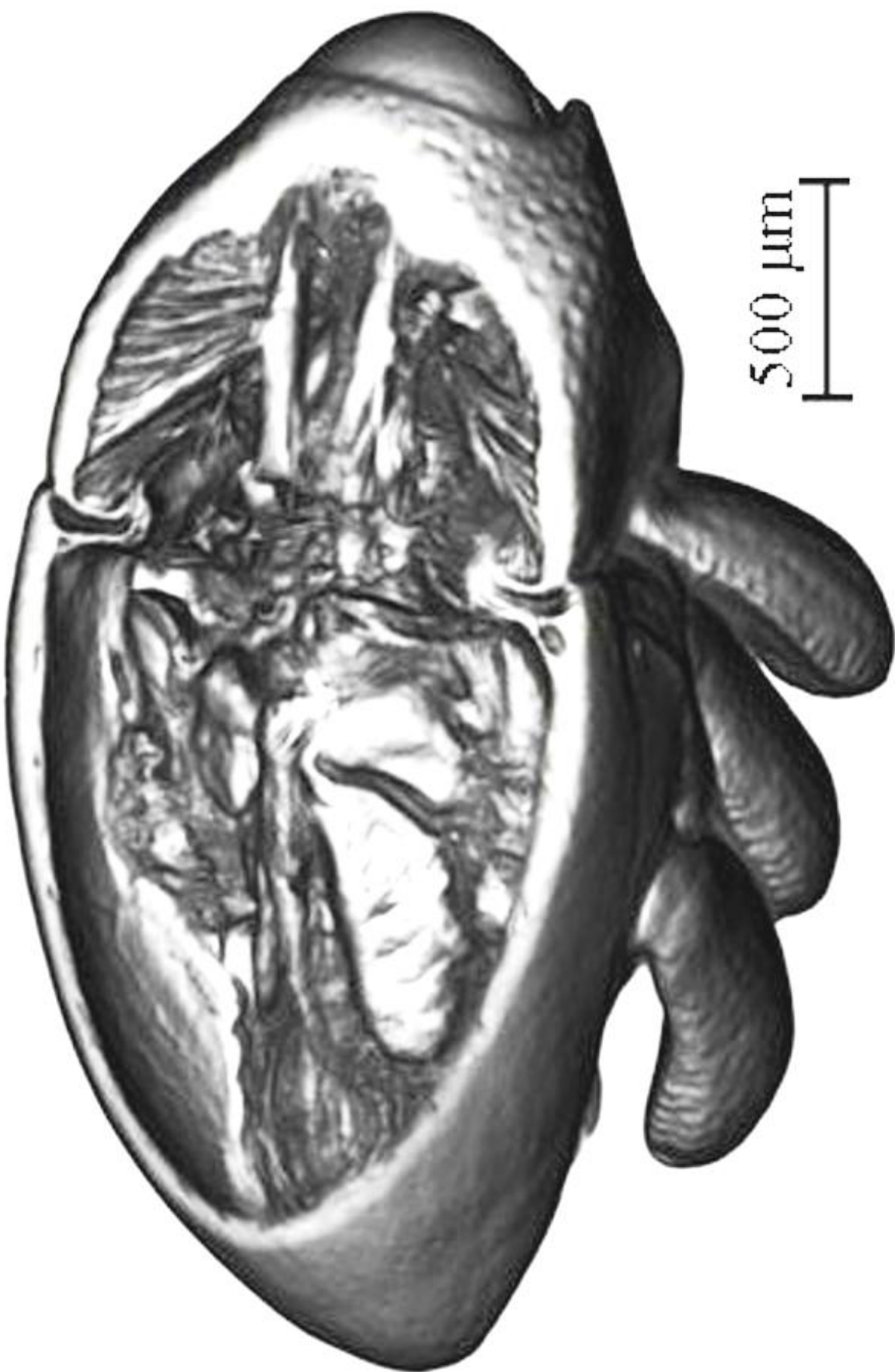
Development of SrI₂:Eu²⁺ - Scintillators For Gamma Ray Spectroscopy and High Resolution X-Ray Imaging



INAUGURALDISSERTATION
zur Erlangung des Doktorgrades
der Fakultät für Chemie und Pharmazie
der Albert-Ludwigs-Universität Freiburg im Breisgau

Vorgelegt von

Leonard Alaribe
aus Logara/Nigeria
2013



The image resolution of a bug „*Trigonopterus vandekampi*“ recorded with the SrI_2 – scintillator detector made in this work.



Dedicated to

Zofia Alaribe
(The desert flower)

and

Uchenna Emmanuel Alaribe
(Thanks for the short time spent together, the
memories will last me a life time)

**Erklärung an Eides Statt
gemäß § 8 (1) 8. und 9. der Promotionsordnung**

- I. Ich erkläre hiermit, dass ich die vorliegende Arbeit ohne unzulässige Hilfe Dritter und ohne Benutzung anderer als der angegebenen Hilfsmittel angefertigt habe. Die aus anderen Quellen direkt oder indirekt übernommenen Daten und Konzepte sind unter Angabe der Quelle gekennzeichnet. Insbesondere habe ich hierfür nicht die entgeltliche Hilfe von Vermittlungs- bzw. Beratungsdiensten (Promotionsberater/Promotionsberaterin oder anderer Personen) in Anspruch genommen. Niemand hat von mir unmittelbar oder mittelbar geldwerte Leistungen für Arbeiten erhalten, die im Zusammenhang mit dem Inhalt der vorgelegten Dissertation stehen. Die Arbeit wurde bisher weder im In- noch im Ausland in gleicher oder ähnlicher Form einer anderen Prüfungsbehörde vorgelegt.
- II. Die Bestimmungen der Promotionsordnung der Fakultät für Chemie, Pharmazie und Geowissenschaften sind mir bekannt. Insbesondere weiss ich, dass ich vor Aushändigung der Promotionsurkunde zur Führung des Doktortitels nicht berechtigt bin.

Ort, Datum

Unterschrift

Vorsitzender des Promotionsausschusses: Prof. Dr. Thorsten Koslowski

Referent: Prof. Dr. Harald Hillebrecht

Korreferent: Prof. Dr. Michael Fiederle

Korreferent: Prof. Dr. Arne Cröll

Tag der mündlichen Prüfung: 01.07.2013

Table of Contents

Acknowledgements.....	xii
Publications.....	xiv
Abbreviations.....	xvii
Abstract.....	xviii
1 Introduction	1
Bibliography.....	3
2 Theory and Scientific Background.....	4
2.1 X-Rays and γ -Rays.....	5
2.1.1 X-Ray and γ -Ray Interaction with Matter	7
2.2 Radiation Detectors	10
2.2.1 Scintillator: Applications and Requirements.....	11
2.3 Scintillation Mechanism of Inorganic Scintillators	19
2.3.1 Scintillator Efficiency η	24
2.4 Gamma Ray Spectroscopy: Experimentation.....	25
2.4.1 Energy Spectrum and Energy Resolution.....	29
2.4.2 Light Yield	31
2.4.3 Decay Time	33
2.5 X-Ray Imaging	34
2.5.1 Image Formation	34
2.5.2 Description of the Image	37
2.5.3 X-Ray Tomography (Absorption Contrast and Phase Contrast)	42
Bibliography.....	44
3 Material Properties of SrI ₂	47
3.1 Physical and Chemical Properties	47
3.1.1 Hydration Levels and the Melting Point of SrI ₂	49
3.2 Structural Properties	51
3.2.1 Doping with Europium (Eu ²⁺)	53
Bibliography.....	58
4 Crystal Growth	60
4.1 Growth Ampoules and Preparations.....	60
4.2 Thermal Dehydration of SrI ₂ (EuI ₂)	65
4.3 Thermodynamics and Kinetics of Nucleation and Crystal Growth.....	65
4.4 Bridgman/Stockbarger Crystal Growth Technique	71
Bibliography.....	76
5 Experiments and Results	78

Table of Contents

5.1	Crystal Growth	79
5.1.1	Simulation of the single-zone furnace	80
5.1.2	Construction of a Two-Zone Bridgman/Stockbarger Furnace	85
5.1.3	Crystal Growth Experiments and Results.....	87
5.2	Crystal Preparations and Packaging	102
5.2.1	Crystal Preparations.....	102
5.2.2	Crystal Packaging.....	102
5.3	Spectroscopic Measurements	107
5.3.1	SrI ₂ : 5% Eu ²⁺ - 1	107
5.3.2	SrI ₂ : 6% Eu ²⁺ - 3	110
5.3.3	SrI ₂ : 6% Eu ²⁺ - 5	117
5.3.4	SrI ₂ : 5% Eu ²⁺ - 6	122
5.3.5	SrI ₂ : 2% Eu ²⁺ - 7	136
5.4	X-ray Imaging Measurements	139
5.4.1	Flat Field Image Recording	143
5.4.2	Mesh Image Recording (Image Spatial Resolution and Contrast)	147
5.4.3	Radiographic Images	151
5.4.4	First X-Ray Tomography Images using SrI ₂	159
	Bibliography.....	169
6	Discussion of Results and Comparison with Literature	171
6.1	Discussion of Results	171
6.2	Comparison of Results with Literature.....	174
	Bibliography.....	177
7	Summary and Outlook.....	178
7.1	Summary	178
7.2	Outlook.....	179
	Attachments	
	Equipments and software	

Acknowledgements

My indebted gratitude goes to all who were part of this work, especially my mentor:

Prof. Dr. Michael Fiederle for the chance to do this research work in your group and under your mentoring. I was able to tap from your expertise through the early morning conversations after the experiments, which helped me to know what was expected next of my work and which step to take. You deserve my special thanks and I guess my biography would always be incomplete without mentioning your name.

Prof. Dr. Arne Cröll for the nice working atmosphere in the laboratories of the crystallography department and also for the korreferent.

I also want to thank the following for making this work, what it is today:

Dr. Alex Fauler: after every conversation with you, I was always close to finding the solution to any problem in the laboratory. I think I owe you so much, because I learnt so much more from you.

Dr. Egbert Keller: one of the best lecturers I ever had. It was always inspirational doing measurements and analysis together; I have always looked for such opportunity to thank you for finding time to witness my wedding.

Dr. Ralf Engels: despite tight schedule, you always found time to measure my samples, thanks for that and for the wonderful reception at the research centre, Jülich. I will never forget that.

Prof. Dr. Arnold Burger: the measurements in your group at the FISK University, Tennessee brought out the best of this work, thanks for the opportunity.

Dr. Angelica Cecilia: this work became interesting with the X-ray images. Thanks a lot for your untiring efforts, support and profitable discussions during the measurements.

Elias Hamann: thank you for finding time on Saturdays for the measurement and also for the profitable discussions.

Dr. Markus Dambacher: you always supported me with profitable advice and tips, especially in the presentation of this work at the IEEE-NSS-2012. Thank you.

Mr. Manfred Kranz-Probst: thanks for your relentless effort in making the ampoules and also for supporting with your knowledge of materials. Guess I did learn so much from you.

Acknowledgments

Mr. Winfried Drayer: thank you for the fine-mechanics and help towards setting up the new furnace.

Claudia Lehmann, Luitgard Rees-Isele & Hans-Peter Winkler: thanks for the assistance in the laboratory and for the thermogravimetric measurements.

Dr. Peter Simon for the simulations.

Dr. Simon Procz: thanks for the colour X-ray images, I think you did portray the art in science with the colour X-ray images in your Ph.D thesis, nice work.

Johannes Feyrer: thank you for the measurements and the nice discussions.

Patrik Vagovic & Tomi dos Santos Rolo: thank you for the measurements together.

Christian Disch: thank you for the measurements and explanations; I really admire your competence.

Andreas Zwerger: thank you for the measurements.

Frank Fischer, Adrian Vogt, Cornelia Haas and Fabian Krahil: thanks for the nice atmosphere in the office and also for helping in one way or the other.

Dr. Bekeny Chegnui: thanks for finding time to go through my manuscript.

Bettina (Mrs) -, Bernd (Mr) -, Jana – and Johannes Bauer: thanks for being such wonderful people.

Michalina Szczotka (Mrs), Krystyna Jandy-Szczotka (Mrs), Andrzej Szczotka (Mr), Mateusz -, Jakub – and Szymon Szczotka: thank you for your hospitality.

The Mother Prioress and all the sisters in Monastery St. Lioba: thanks for everything, too numerous to count and mention.

Anni Hähnel (Mrs): thank you for your assistance.

Sr. Magdalena Löffler: thanks for always being there for us.

Roswitha (Mrs) and Walter (Mr) Faisst: thanks for being such nice people.

Acknowledgments

My family: **Akagwu Alaribe, G. A. Alaribe, C. Alaribe, Stella Nwosu, Vitalis Alaribe, Eunice Chiekezi, Dr. G. N. Alaribe, Vivian Opara, Uchenna (senior) Alaribe, Chinyere Ohaezukosi, Vivian Ugboaku Alaribe, Uchenna (junior) Alaribe, Chidera Alaribe, Chineche Alaribe, Imelda Alaribe, Prisca Alaribe, Nora Alaribe and Theodore Opara** – thanks for bringing me this far.

Last but not least, thanks to my wife **Zofia Alaribe** for her loving support.

Publications and Conference Contributions

Publications

Leonard Alaribe, Christian Disch, Alex Fauler, Ralf Engels, Egbert Keller, Angelica Cecilia, Tomy dos Santos Rolo, Elias Hamann and Michael Fiederle:
 $\text{SrI}_2:\text{Eu}^{2+}$ - Scintillators for Spectroscopy and X-Ray Imaging Applications.
IEEE TRANSACTIONS ON NUCLEAR SCIENCE, VOL. 59, NO. 5, OCTOBER 2012.

Leonard Alaribe, Christian Disch, Alex Fauler, Ralf Engels, Egbert Keller, Angelica Cecilia, Tomy dos Santos Rolo, Elias Hamann, Michael Fiederle:
Development of SrI_2 – Scintillators for Spectroscopy and X-Ray Imaging Applications.
2011 IEEE Nuclear Science Symposium Conference Record.

Leonard Alaribe, Christian Disch, Alex Fauler, Ralf Engels, Egbert Keller, Angelica Cecilia, Tomy dos Santos Rolo, Michael Fiederle:
Bridgman Growth of $\text{SrI}_2:\text{Eu}$ Scintillators.
MRS SYMPOSIUM PROCEEDINGS. Volume 1341 (Nuclear Radiation Detection Materials – 2011). 2011 MRS Spring Meeting.

L. Alaribe, A. Zwerger, C. Disch, A. Fauler, E. Keller, R. Engels, E. Hamann, A. Cecilia, T.D.S. Rolo, J. Feyrer, M. Fiederle:
 $\text{SrI}_2:\text{Eu}^{2+}$ - Scintillator Crystal Growth and Characterization.
FMF – Freiburg Materials Research Center, Report 2011.

Leonard Alaribe, Angelica Cecilia, Elias Hamann, Alex Fauler, Simon Procz, Johannes Feyrer, Arnold Burger, Michael Fiederle:
High Resolution and High Contrast Imaging with Thin SrI_2 -Scintillator Screens.
2012 IEEE Nuclear Science Symposium Conference Record.

Leonard Alaribe, Angelica Cecilia, Elias Hamann, Alex Fauler, Simon Procz, Johannes Feyrer, Arnold Burger, Michael Fiederle:
High Resolution and High Contrast Imaging with Thin SrI_2 -Scintillator Screens.
IEEE TRANSACTIONS ON NUCLEAR SCIENCE, Vol; PP, Issue: 99 (DOI:10.1109/TNS.2013.2255892).

Leonard Alaribe, Alex Fauler, Angelica Cecilia, Tomy Dos Santos Rolo, Michael Fiederle and Arnold Burger:
High Resolution X-Ray Imaging with Thin SrI_2 -Scintillator Screens.
Submitted MRS 2013 SYMPOSIUM PROCEEDINGS.

Conference Contributions

Talks

Leonard Alaribe; Alex Fauler; Angelica Cecilia; Tomy Dos Santos Rolo; Michael Fiederle; Arnold Burger:

High Resolution X-Ray Imaging with Thin SrI₂ – Scintillator Screens.

Materials Research Society (MRS) Spring Meeting, April 1 – 5, 2013. San Francisco.

Alaribe L.; Fauler A.; Zwerger A.; Engels R.; Cecilia A.; Procz S.; Vagovic P.; Hamann E.; Burger A.; Feyrer J.; Fiederle M.:

High Resolution and High Contrast X-Ray Imaging with Thin SrI₂ – Scintillator Screens.

IEEE 2012: NSS MIC RTSD, October 29 – November 3, 2012. Anaheim, California.

Alaribe L.; Disch C.; Fauler A.; Engels R.; Keller E.; Cecilia A.; Dos Santos Rolo T.; Fiederle M.:

Bridgman Growth of SrI₂:Eu – Scintillators.

German Polish Conference on Crystal Growth (GPCCG 2011), 15 – 18 March, 2011. Frankfurt (Oder) /Słubice.

Alaribe L.; Disch C.; Fauler A.; Zwerger A.; Engels R.; Cecilia A.; Dos Santos Rolo T.; Vagovic P.; Hamann E.; Burger A.; Feyrer J.; Fiederle M.:

Crystal Growth and Characterization of SrI₂:Eu²⁺ - Scintillators.

FMF – Colloquium, 16 – 17 October, 2012. Schluchsee.

Alaribe L.; Keller E.; Engels R.; Zwerger A.; Disch C.; Fauler A.; Cecilia A.; Dos Santos Rolo T.; Fiederle M.:

Growth and Characterization of SrI₂:Eu²⁺ Scintillators – Overview.

A. G. MCD Seminar, 11 – 12 May, 2011. Feldberg.

Posters

Alaribe L.; Fiederle M.; Disch C.; Fauler A.; Engels R.; Keller E.; Cecilia A.; Dos Santos Rolo T.:

Bridgman Growth of SrI₂ – Scintillators for Spectroscopy and Imaging Applications.

2011 MRS Spring Meeting and Exhibit, April 25 – 29, 2011. San Francisco, California.

Alaribe L.; Keller E.; Cecilia A.; Dos Santos Rolo T.; Engels R.; Hamann E.; Fiederle M.:

SrI₂:Eu²⁺ - Scintillators for Spectroscopy and X-Ray Imaging Applications.

SCINT 2011, September 12 – 16, 2011. Giessen, Germany.

Alaribe L.; Keller E.; Cecilia A.; Dos Santos Rolo T.; Engels R.; Fauler A.; Disch C.; Hamann E.; Fiederle M.:

Development of SrI₂ – Scintillators for Spectroscopy and X-Ray Imaging Applications.

IEEE 2011: NSS MIC RTSD, 23-29 October, 2011. Valencia, Spain.

Abbreviations

SrI ₂	Strontium Iodide
EuI ₂	Europium Iodide
Z _{eff}	Effective atomic number
γ-rays	Gamma rays
PMT	Photomultiplier tube
at. %	Atomic percent
TG	Thermogravimetry
DSC	Differential scanning calorimetry
HPGe	High-purity Germanium
FWHM	Full width at half maximum
Z	Atomic number
STH	Self trapped hole
STE	Self trapped exciton
CCD	Charge-coupled device
CT	Computed tomography
PET	Positron emission tomography
SPECT	Single photon emission computed tomography
DQE	Detective quantum efficiency
LSF	Line spread function
OD	Optical density
PSF	Point spread function
LSF	Line spread function
MTF	Modulation transfer function
RE	Rare earth

Abstract

Abstract

The motivation for this work is the ever increasing role of scintillators in radiation detection and monitoring. This application requires scintillators with high light yield, high sensitivity to ionizing radiation and chemical stability. The SrI₂ – scintillator has a high conversion efficiency of X-ray radiation and gamma radiation into light photons. Unfortunately it is also hygroscopic and oxygen sensitive, making the crystal growth and field application difficult.

Crystal growth experiments were carried out in silica ampoules to prevent melt hydration and contamination during the crystal growth. In order to reduce induced thermal stress in the crystal through direct contact with the growth ampoule, the Liquid encapsulated Bridgman technique was carried out. At the end it was found that the introduction of excess iodine-gas into the growth ampoules was enough to maintain good heat conductivity between the growing crystal and the ampoule and also to maintain the stoichiometry of the growth material.

Different detector-packaging techniques were tested here, both the use of Teflon tapes, aluminium foils and Spectralon as reflector to achieve an energy resolution as low as 2.7% at 662 keV (FWHM). For the first time, the application of the SrI₂ – scintillator in high resolution X-ray imaging was investigated. The resolution and contrast of the 2D X-ray radiography and 3D X-ray tomography images recorded were high, despite the embedding layers covering the SrI₂ – thin screens.

With the results achieved in this work, it was possible to show that the SrI₂ – scintillator is not only a candidate for high resolution gamma ray spectroscopic detector systems, but also a candidate for high resolution and high contrast X-ray imaging applications.

1 Introduction

The SrI₂ was first discovered in 1968 by Robert Hofstadter as a scintillator [Hofstadter 1968], and rediscovered in 2009 to be the best performing scintillator today considering its versatile application in security and nuclear non-proliferation to identify radioactive sources and their gamma ray signatures. By identifying the isotope giving rise to a particular radiation, information is provided about the radiation type and its energy. Scintillators serve as detectors in industrial measuring systems that use X-rays and in medical diagnostics for high resolution X-ray imaging measurement of radiation intensity distribution in different organs. So there is need for more research work aimed at discovering scintillators with high light yield, good energy resolution, low or no intrinsic background, fast scintillation decay, high chemical stability and an ability to be grown into bulk single crystals needed for most applications.

Until the rediscovery of the SrI₂, LaBr₃ has been the best performing scintillator combining a good energy resolution of 2.6% (FWHM at 662 keV) with a light yield of 60 000 ph/MeV [Cherepy 2009]. The energy resolution of the SrI₂ rivals that of the LaBr₃; with the light yield twice as much. The problem with the LaBr₃ is the difficulty associated with the crystal growth; LaBr₃ tends to fracture along the {0011} - cleavage plane during crystal growth [Zhou 2009]. SrI₂ on the other hand is readily growable into single bulk crystals. The crystal growth is normally done in silica glass ampoules. Unfortunately, the material contact with ampoule wall induces thermal stress. Another problem is the purity of the raw materials and decomposition during crystal growth processes. A comparison of SrI₂ – and LaBr₃ – scintillators is presented in Table 1.1 [Cherepy 2010].

Property	LaBr ₃ (Ce)	SrI ₂ (Eu)	Comparison
Melting Point	783 °C	538 °C	✓ Less thermal stress
Handling	Easily cleaves	Resists cracking	✓ Better processing
Light Yield	60,000 Ph/MeV	90,000 Ph/MeV	✓ Higher
Proportionality contribution	~2.0%	~2.0%	✓ Favorable
Inhomogeneity	0%	>1% (current)	Impurities and surfaces being addressed
Decay time	30 nsec	0.5-1.5 μsec	Fast enough to avoid deleterious signal pile-up
Radioactivity	La ~ intrinsic bckgd	None	✓ Less noise
Hygroscopic / air sensitive?	Very	Very	Similar
γ absorption (2x3", 662 keV)	22%	24%	Similar

Table 1.1: Characteristics of SrI₂ and LaBr₃ scintillators [Cherepy 2010].

To reduce thermal stress in the growing crystals and also subdue material decomposition during the crystal growth, a growth atmosphere based on excess of one of the constituent elements (iodine gas) was used. The decision to introduce excess iodine into the growth ampoule was based on experiments carried out in this work, which showed that excess iodine would not be incorporated into the SrI₂ crystal lattice. This milestone combined with the

Introduction - 1

construction of a two-zoned Bridgman/Stockbarger furnace led to the growth of single crystals as large as 1-inch. The largest SrI₂ crystal diameter commercially available today is 1-inch, with recent reports on the successful growth of 1.5 inch diameter crystals by [Zhang 2012] and up to 2 inches by [Boatner 2013].

This research work was aimed at investigating and optimizing the crystal growth process of producing bulk SrI₂ single crystals up to 1-inch and later up to 2-inches and more. The task is not limited only to the growth of SrI₂ single crystals, but also to the crystal preparation and packaging with the aim of producing high quality scintillator detectors for spectroscopic systems. This work was also later expanded to X-ray imaging using SrI₂-scintillator thin screens, resulting in the recording of high resolution and high contrast X-ray images of light weighted objects like ants and bugs with weak X-ray attenuation.

The remaining part of this thesis is structured as follows:

Chapter 2 presents the physics of scintillation mechanism, radiation interaction with matter and experimental measurable parameters.

Chapter 3 presents the material properties of this relatively new scintillator (SrI₂:Eu²⁺).

In chapter 4, the theory of spontaneous nucleation and crystal growth is presented, followed by the crystal growth method used in this work.

Chapter 5 showcases the results achieved so far and also areas where more improvement is needed.

In chapter 6, the results are discussed and compared to the work of experts in this area.

Chapter 7 summarizes this work in short sentences and also shows the direction where future work on the SrI₂ would be directed.

Bibliography

[Hofstadter 1968]

Robert Hofstadter: Europium activated Strontium Iodide scintillators. United States Patent 3 373 279. Mar 12,1968.

[Cherepy 2009]

Nerine J. Cherepy, Steve A. Payne, Stephen J. Asztalos, Giulia Hull, Joshua D. Kuntz, Thomas Niedermayr, Siddha Pimputkar, Jefferey J. Roberts, Robert D. Sanner, Thomas M. Tillotson, Edgar van Loef, Cody M. Wilson, Kanai S. Shah, Utpal N. Roy, Rastgo Hawrami, Arnold Burger, Lynn A. Boatner, Woon-Seng Choong, and William W. Moses: Scintillators with potential to supersede lanthanum bromide. IEEE Trans. Nucl. Sci, Vol. 56, No.3, June 2009.

[Zhou 2009]

X. W. Zhou, F. P. Doty, Pin Yang: Dislocations in LaBr₃ crystals. Proc. Of SPIE Vol. 7450 745005-1 (2009).

[Zhang 2012]

Ye Zhang, Hongsheng Shi, Kangying Shu, Laishun Qin, Guohao Ren: Crystal growth and luminescent properties of Eu activated strontium iodide crystals. Cryst. Res. Technol. 47, No. 5, 548-552 (2012).

[Boatner 2013]

L.A. Boatner, J. O. Ramey, J. A. Kolopus, R. Hawrami, W. M. Higgins, E. van Loef, J. Glodo, K. S. Shah, Pijush Bhattacharya, Eugene Tupitsyn, Michael Groza, Arnold Burger, N. J. Cherepy, S. A. Payne: Bridgman Growth of Large SrI₂:Eu²⁺ Single Crystals: A high-performance Scintillator for Radiation Detection Applications. Journal of Crystal Growth (2013). <http://dx.doi.org/10.1016/j.jcrysGro.2013.01.035>.

[Cherepy 2010]

Nerine Cherepy, L. Boatner, A. Burger, K. Shah, Steve Payne, Alan Janos, Austin Kuhn: Overview of Strontium Iodide Scintillator Materials. LLNL presentation April 1, 2010. (LLNL-PRES-426327).

2 Theory and Scientific Background

Chapter Overview

Abstract

2.1 X-Rays and γ -Rays	5
2.1.1 X-Ray and γ -Ray Interaction with Matter	7
2.2 Radiation Detectors	10
2.2.1 Scintillator: Applications and Requirements	11
2.3 Scintillation Mechanism of Inorganic Scintillators	19
2.3.1 Scintillator Efficiency η	24
2.4 Gamma Ray Spectroscopy: Experimentation	25
2.4.1 Energy Spectrum and Energy Resolution	29
2.4.2 Light Yield	31
2.4.3 Decay Time	33
2.5 X-Ray Imaging	34
2.5.1 Image Formation	34
2.5.2 Description of the Image	37
2.5.3 X-Ray Tomography (Absorption Contrast and Phase Contrast)	42
Bibliography	44

Abstract

In this chapter the physics of scintillation mechanism, the limiting factors on each step of the relaxation process that determine the scintillation efficiency and the characteristics of good inorganic scintillators are discussed. In the later part of this chapter spectroscopy and X-ray imaging applications of scintillators and their measurable parameters will be discussed, but before then a short insight is provided on the electromagnetic spectrum, especially on the part of it that is of utmost interest to us.

The electromagnetic spectrum ranges from low energy radio waves (long wavelength) through visible light that humans can detect with their eyes to high energy X-rays and gamma rays (low wavelength) as shown in Figure 2.1. A good knowledge of the X-ray and γ -ray components of the electromagnetic spectrum and how to detect them (the study of the interaction between matter and radiated energy) is very important for spectroscopic purposes. Therefore, the main aim of this work is to produce inorganic single scintillator crystals that will be used to detect the high energy X-ray radiations and gamma ray radiations.

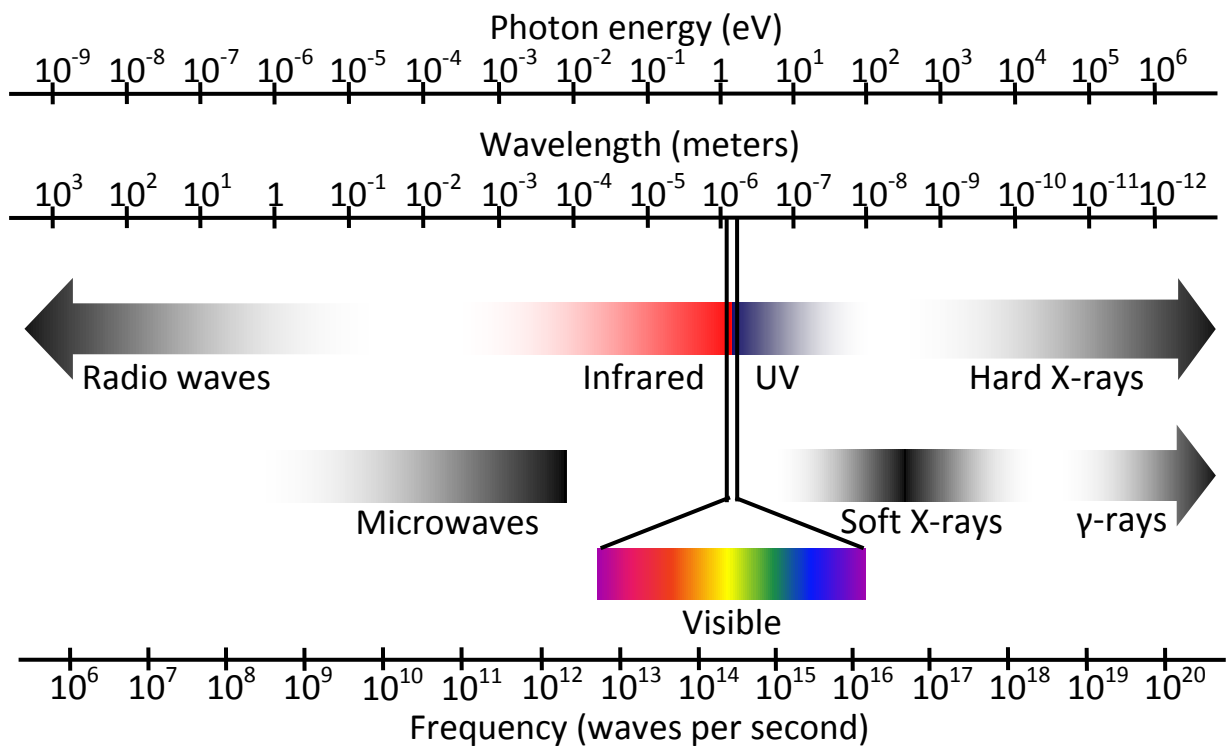


Figure 2.1: The electromagnetic spectrum.

2.1 X-Rays and γ -Rays

X-rays and gamma rays are part of the electromagnetic spectrum; they can be described as identical. The terms X-ray and γ -ray are more or less statements about their origin. X-rays were discovered in 1895 by Wilhelm Conrad Röntgen. During an experiment with a cathode ray tube, he noticed invisible rays with a high penetration capacity and called them X-rays [Kleber 1990]. X-rays (Bremsstrahlung and characteristic X-rays) are generated in X-ray tubes that consist of the cathode and a metal target that serves as the anode. By setting the anode at higher voltage, electrons from the cathode are accelerated and hit the metal target such as tungsten. Figure 2.2 illustrates the mechanism of X-ray generation in an X-ray tube.

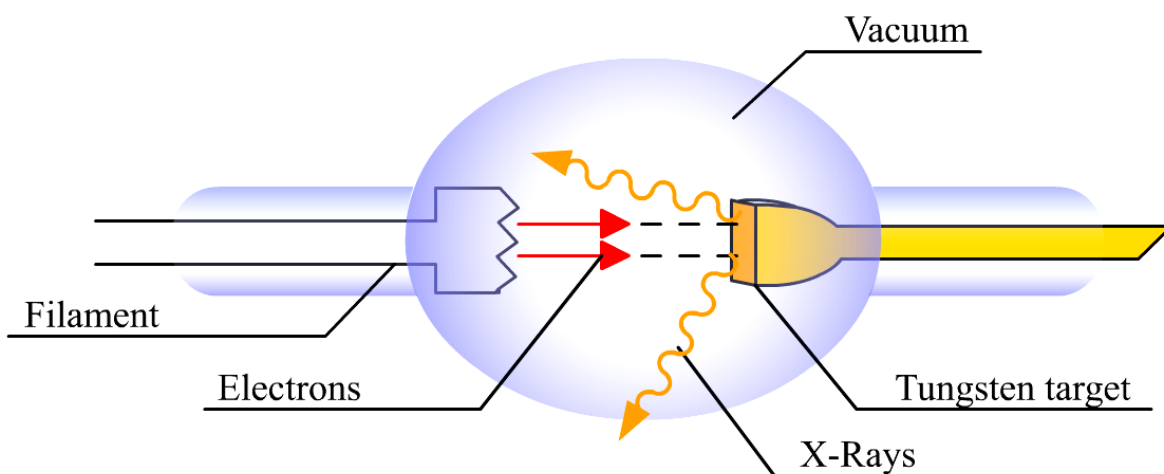


Figure 2.2: X-ray production in an x-ray tube [NDT 2012].

When charged particles decelerate in a medium, Bremsstrahlung is produced; this is caused by the deflection of charged particles through the nucleus of atoms. On the other hand, characteristic X-rays arise as a result of different electron energy transitions as shown in Figure 2.3. If orbital electrons in an atom are knocked from their shells by incident electrons, unstable states are created. Electrons try to rearrange themselves by moving from higher energy levels to lower energy levels, thus the atom can return to its ground state (lowest energy state). The excess energy of the electrons is emitted in the form of characteristic X-rays.

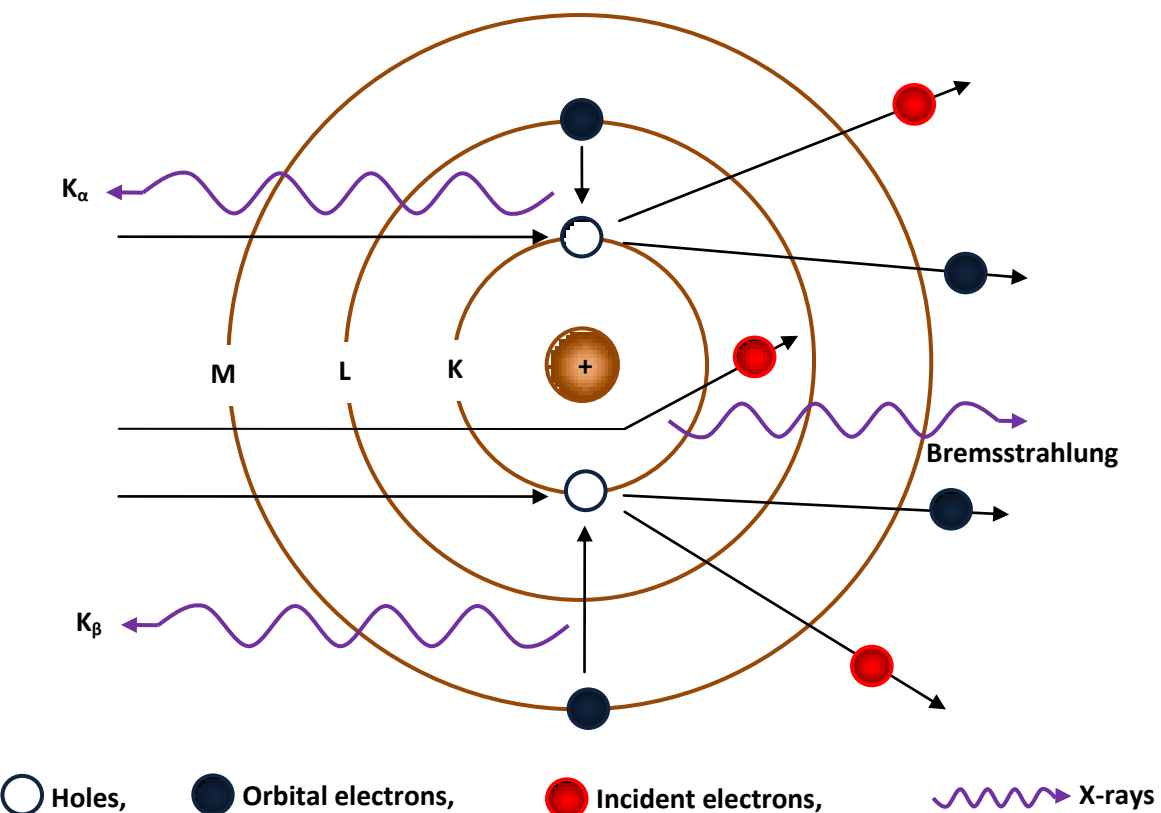


Figure 2.3: Production of Bremsstrahlung and characteristic x-rays.

Suppose the energy of the electrons in the X-ray tube is sufficient to knock one electron out of the K-shell, a hole (an empty state) will be left in the K-shell. This hole will be filled by an electron from a higher energy level like the L-shell or M-shell. Since the energy of these electrons is higher than that required to occupy the new orbitals, the excess energy is emitted as characteristic X-rays. If the electron originates from the L-shell, a K_{α} -photon will be released with energy equal the binding energy between K and L shells. On the other hand, if the electron originates from the M-shell a K_{β} -photon will be released with energy equal the binding energy between K and M shells [Alonso-Finn 1968]. Gamma radiation originates as a result of nuclear de-excitation in the nucleus of atoms [Leo 1994].

2.1.1 X-Ray and γ -Ray Interaction with Matter

Electromagnetic radiation (X-rays and γ -rays) interact with matter mostly in three different ways: 1. photoelectric effect; 2. Compton Effect and 3. pair production. Thus, given that the intensity of the incident beam is I_0 , after passing through a thickness of d (cm) in a substance, its intensity will be reduced to I according to the equation below

$$I = I_0 \cdot \exp^{-\mu d} \quad \text{eq. 2-1}$$

μ is the linear attenuation coefficient in cm^{-1}

The type of interaction depends on the energy of the electromagnetic radiation and also on the nature of the absorber. During these processes, the radiation energy is transferred to the atomic electron completely through total absorption or partially through scattering at a significant angle. Figure 2.4 shows the total attenuation coefficient of SrI_2 and the contribution of each of the three dominant processes. At photon energies equal to the iodine K-shell electron binding energy 33.17 keV and strontium K-shell electron binding energy 16.10 keV, the curves of the photoelectric effect and thus the total attenuation coefficient increases steeply. The graph is plotted using data from a program called XCOM.

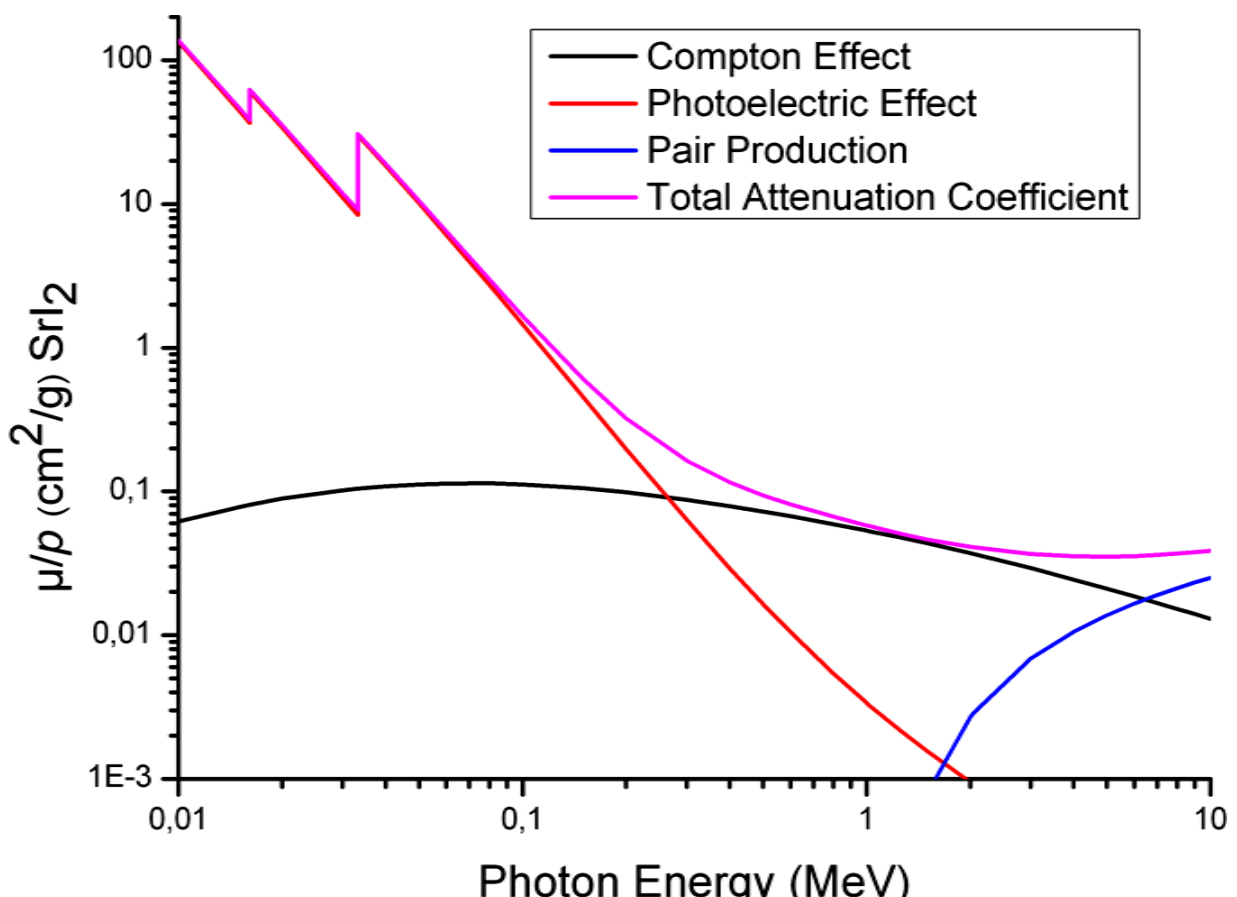


Figure 2.4: The mass attenuation coefficient of SrI_2 as a function of photon energy showing a steep increase at photon energies equal to the K-edges of iodine (33.17 keV) and strontium (16.10 keV) [XCOM].

2.1.1.1 Photoelectric Effect

This is the dominant process whereby an inner shell electron is able to completely absorb the incident photon energy. This means that the electron has enough energy to break from its bound (shell) and is ejected from the atom, leaving behind a vacancy (hole). The energy of the photoelectron produced by the photoelectric process is given as

$$E_e = E_\gamma - E_b \quad \text{eq. 2-2}$$

E_e is the photoelectron energy

E_γ is the incident photon energy

E_b is the electron binding energy

If the energy of the incident photon exceeds the K-shell binding energy, the photoelectron will be ejected from the K-shell; on the other hand, if the incident photon is less than the K-shell binding energy, the photoelectron will be ejected from the L-shell and so on.

The atom becomes ionized and the hole is filled by an electron from a higher energy level radiatively or non-radiatively. During radiative transitions, characteristic X-rays are emitted while auger electrons are produced during non-radiative transitions as shown in Figure 2.5.

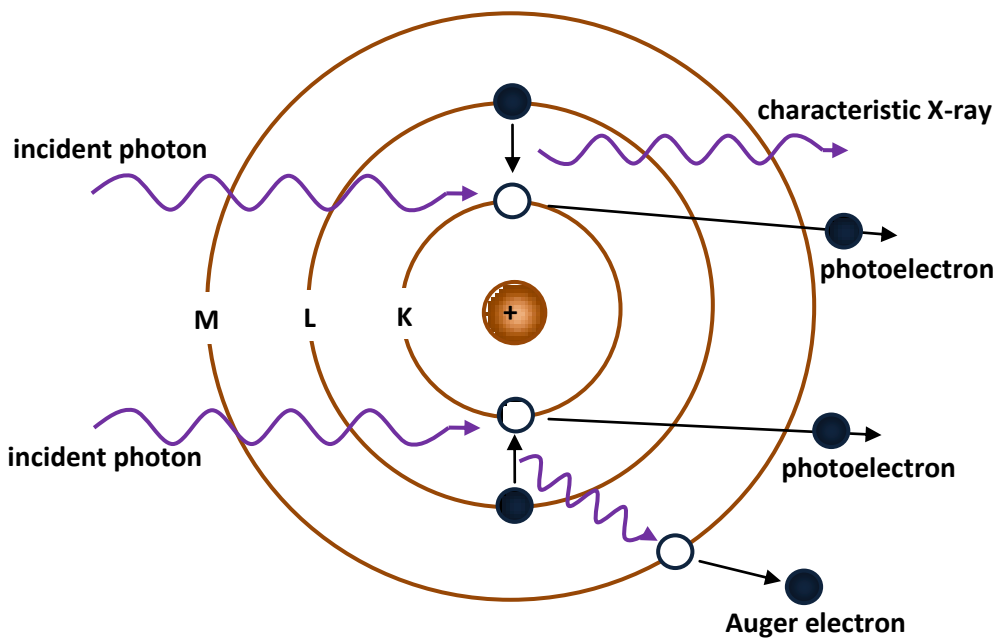


Figure 2.5: Principles of radiative and non-radiative transitions in atoms.

The probability of a photoelectric effect increases with the binding energy and decreases with the photon energy. The cross section for the photoelectric effect σ_{ph} depends strongly on the atomic number Z and the photon energy E_γ as follows

$$\sigma_{ph} \propto \frac{Z^5}{E_\gamma^{3.5}} \quad \text{eq. 2-3}$$

2.1.1.2 Compton Effect

The Compton effect is an elastic collision between a photon and an electron. Only part of the photon energy is transferred to the electron resulting in the creation of a Compton scattered photon and Compton electron. According to [Birks 1964] the electron is initially at rest with the rest mass energy $m_0 c^2 = 511$ keV, after the collision the Compton photon will be scattered at an angle θ to the direction of the incident photon with the reduced energy E'_γ given by the following equation

$$E'_\gamma = \frac{E_\gamma}{1 + \frac{E_\gamma}{m_e c^2} (1 - \cos \theta)} \quad \text{eq. 2-4}$$

m_e is the free electron mass, c is the velocity of light.

The Compton electron will be scattered at an angle φ to the direction of the incident photon with the energy E_{co}

$$E_{co} = E_\gamma - E'_\gamma \quad \text{eq. 2-5}$$

Figure 2.6 illustrates the process of Compton scattering of photons.

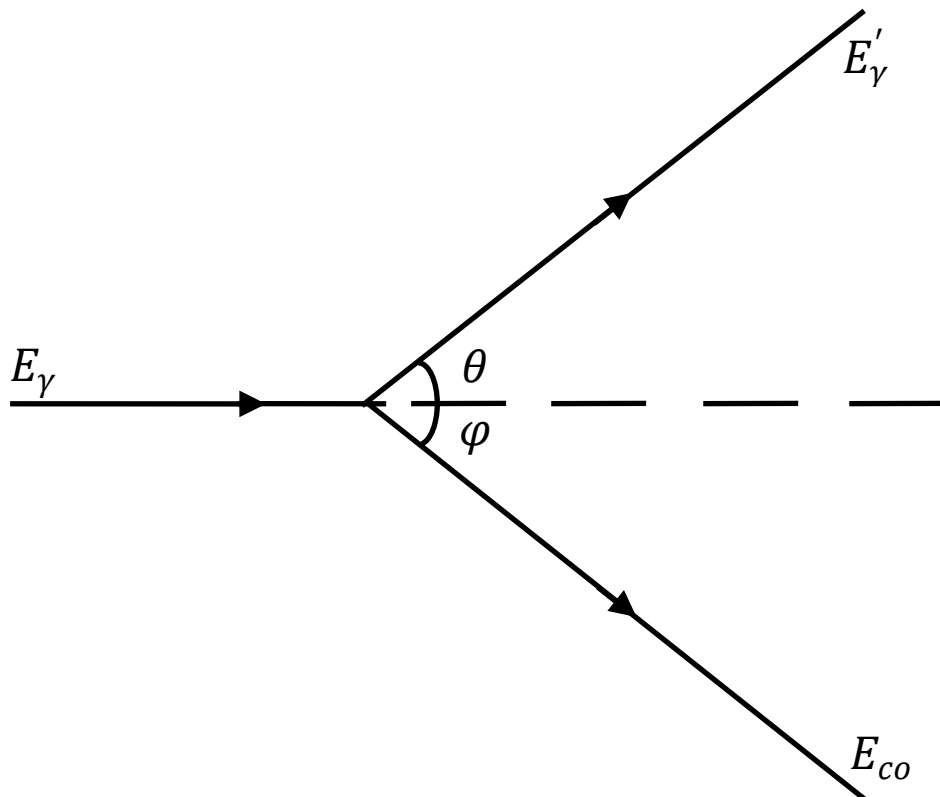


Figure 2.6: Compton scattering of a photon.

The cross section σ_{co} for a Compton event increases with the atomic number Z and decreases with the photon energy E_γ as follows

$$\sigma_{co} = \frac{Z}{E_\gamma} \quad \text{eq. 2-6}$$

During scintillation measurements, the Compton scattering would affect the number of charge carriers produced in the scintillator if after impact, the Compton scattered photon leaves the scintillator. In the case where the Compton scattered photon is reabsorbed in the scintillator through a photoelectric effect, the number of charge carriers produced in the scintillator would be approximately the same as in a single photoelectric interaction.

2.1.1.3 Pair Production

The pair production starts at incident photon energies $E_\gamma = 2m_e c^2$. With $m_e c^2 = 0.511 \text{ MeV}$; meaning that the pair production starts at photon energies of 1.022 MeV as shown in Figure 2.4. According to [Rodnyi 1997], pair production takes place in the coulomb field of a nucleus and not with the atomic electrons. During a pair production interaction, the incident photon energy E_γ is completely absorbed leading to the production of an electron-positron pair with the total energy E_{pp}

$$E_{pp} = E_\gamma - 2m_e c^2 \quad \text{eq. 2-7}$$

The probability of a pair production event in the nuclear field increases with the energy E_γ and the atomic number Z . The cross section σ_{pp} for the pair production is given as

$$\sigma_{pp} = Z^2 \ln 2 E_\gamma \quad \text{eq. 2-8}$$

The positron is annihilated in a collision with an electron producing two photons, each with the energy of 511 keV. One or both photons may escape or may be absorbed by the scintillator in a photoelectric - or Compton interaction [Birks 1964].

2.2 Radiation Detectors

There are two primary classes of radiation detectors as shown in Figure 2.7, semiconductors and scintillators. The main difference is what happens with the charge carriers at the end of the energy cascade.

For the semiconductor, the thermalized electrons and holes are rapidly swept out with the application of an electric field and recorded as an electronic pulse with the number of charge carriers being proportional to the energy of the incident photon [Milbrath 2008].

In a scintillator, the electron-hole pairs recombine to form optical photons that are converted in an external photodetector (PMT or photodiode) into electronic signals with the number of photons being proportional to the energy of the incident photon. Scintillator detectors are preferred over semiconductor detectors in applications where large detector volumes are

needed for better radiation absorption. Another advantage of scintillator detectors over semiconductor detectors like HPGe-detectors is the lack of cryogenic cooling.

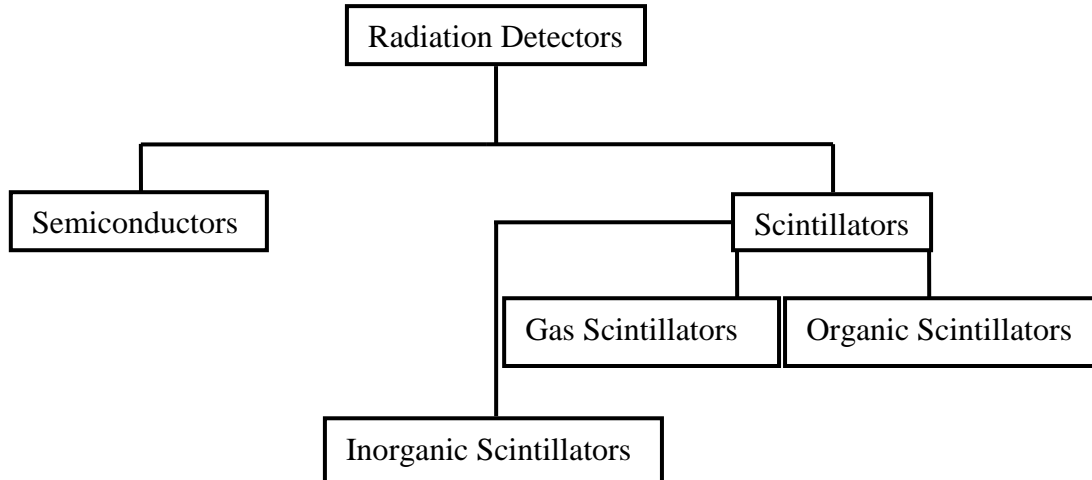


Figure 2.7: Classification of radiation detectors.

2.2.1 Scintillator: Applications and Requirements

There are two possible answers to the question; what is a scintillator and where can it be applied?

A scintillator is a material that exhibits luminescence (light emission). There are two types of luminescence: fluorescence and phosphorescence as shown in Figure 2.8.

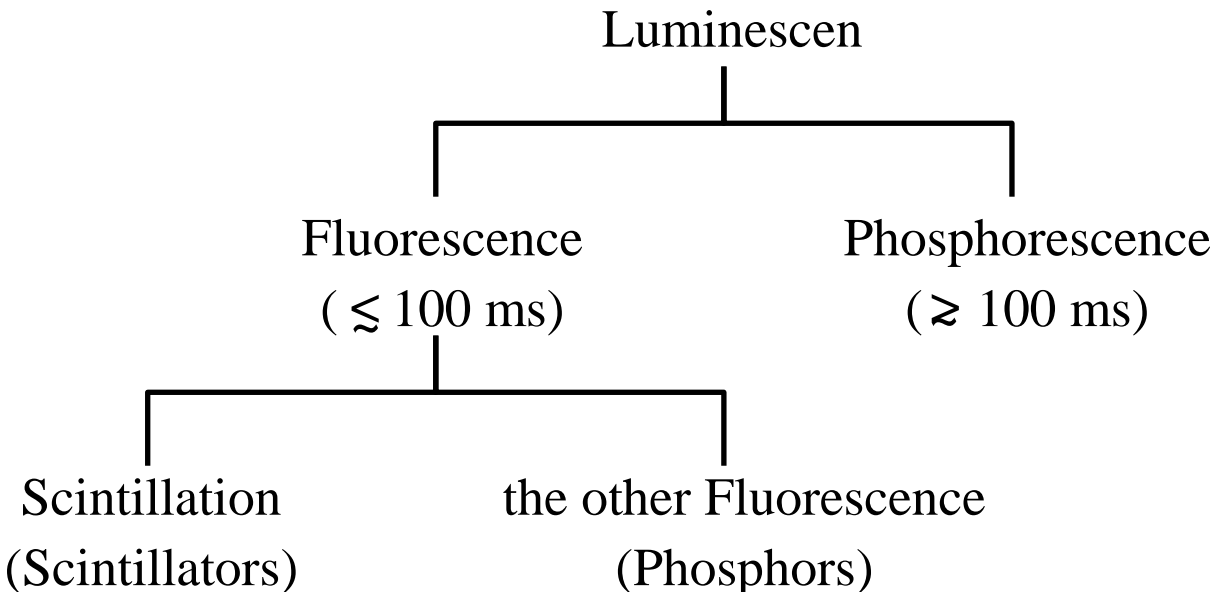


Figure 2.8: Types of luminescence [Kobayashi 2003].

Fluorescence is produced during radiative transitions from the lowest excited singlet states to the ground state in a time scale of $\sim 10^{-8}$ to 10^{-9} s [Birks 1964]. So fluorescence can be said to be luminescence during excitation [Kobayashi 2003].

Phosphorescence on the other hand has a decay time of $\sim 10^4$ s or longer and is caused by metastable triplet state with non-radiative initial conversion from the excited state. The metastable state is located below the lowest excited singlet states. The electron in the metastable state may acquire enough thermal activation energy over time to return to the lowest excited state leading to delayed fluorescence [Birks 1964]. So phosphorescence on the other hand can be said to be luminescence after excitation [Kobayashi 2003], see Figure 2.9. As luminescent material, scintillators are used as screens in computer monitors, and television sets.

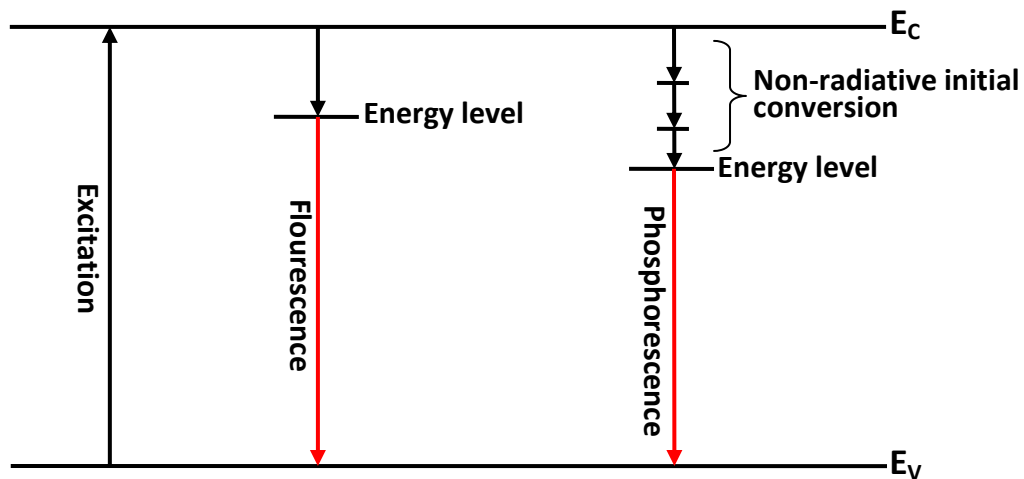


Figure 2.9: Excitation, fluorescence and phosphorescence

As radiation detector, a scintillator is a wavelength shifter, meaning that a scintillator absorbs the high energy low wavelength X-ray- and γ -ray-photons and converts them into low energy photons with wavelength mostly in UV or visible region.

There are numerous and diverse applications of scintillators as radiation detectors, to mention but a few; scintillators are used in high energy physics experiments to measure the energy of particles, in X-ray imaging, X-ray radiography, CT, mammography, PET and medical diagnostics for a high resolution measurement of the spatial distribution of radiation intensity in different organs, as radiation detector in industrial measuring systems that use X-rays, in exploration and mining processes and in nuclear non-proliferation, homeland security and national defence, to identify radioactive sources and their gamma ray signatures. By identifying the isotope giving rise to a particular radiation, information can be provided on the radiation type and its energy.

These areas of application also have certain scintillator requirements. While high energy physics requires a scintillator with a radiation resistance of over 10^6 to 10^7 rad/year, short main luminescence decay times of 3 to 30 ns, good energy resolution and a high stopping power, X-ray imaging on the other hand requires a scintillator with a high density and high effective atomic number, high spatial resolution, short decay time of < 3 to 5 ns and light output of > 5 to 10% of NaI:Tl [Rodnyi 1997].

2.2.1.1 Properties of a good Scintillator

As already mentioned, different applications require different scintillator properties, needed for most applications is a scintillator with:

1. High light output of $\geq 25\,000$ photons/MeV.

This means a high coefficient of conversion of ionizing radiation into light photons. In scintillation counting, the light yield is a more significant quantity than the scintillation efficiency. It is the number of photons emitted per unit energy absorbed (usually 1 MeV) and is given as

$$L = \frac{E_\gamma}{\beta \cdot E_g} \cdot S \cdot Q \quad \text{eq. 2-9}$$

If the efficiency of transfer of charge carriers to the luminescence centre and the quantum efficiency of the luminescence centre are assumed to be hundred percent, meaning that ($S = 1$ and $Q = 1$), and if the energy necessary to create an electron-hole pair is assumed to be equal to $2E_g$ (making $\beta = 2$), the theoretical light yield of inorganic scintillators can be calculated as follows

$$L = \frac{0.5}{E_g} \times 10^6 \left[\frac{\text{photons}}{\text{MeV}} \right] \quad \text{eq. 2-10}$$

This means that the light yield of inorganic scintillators is strongly dependent on the bandgap.

2. Good energy resolution of $< 3\%$ at 662 keV (FWHM).

The energy resolution of a scintillator is its ability to separate two closely lying energy peaks as shown in Figure 2.10 and is given by

$$\text{Resolution } R (\%) = \frac{\Delta E}{E} \times 100 \quad \text{eq. 2-11}$$

ΔE is the full width at half the maximum of the photopeak located at the energy E

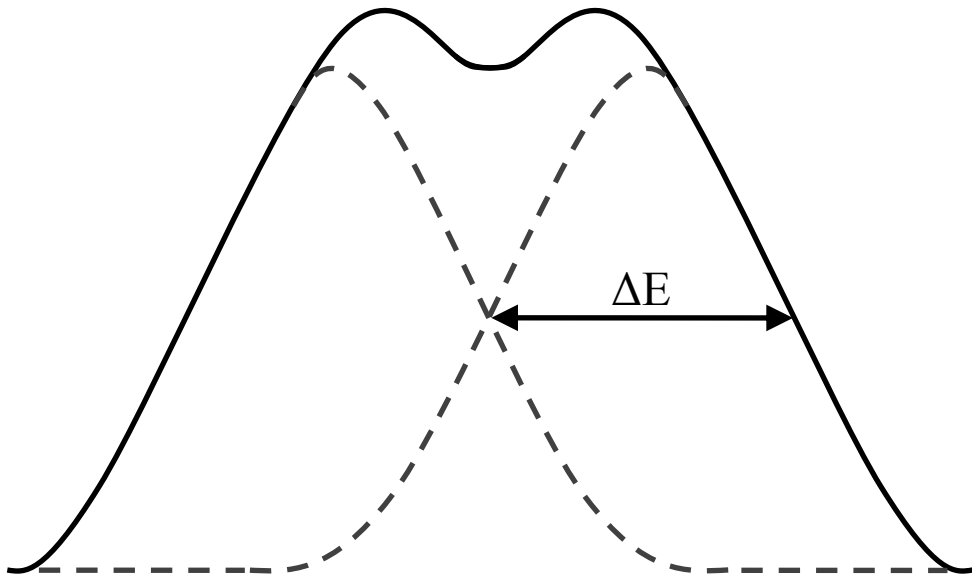


Figure 2.10: The energy resolution.

Two peaks are said to be resolved if they are separated by a distance greater than their full widths at half maximum [Leo 1994]. The energy resolution of a scintillator detector is the quadratic sum of the scintillator (R_S) and the PMT (R_{PMT}) contributions [Rodnyi 1997] as follows

$$R^2 = R_S^2 + R_{PMT}^2 \quad \text{eq. 2-12}$$

3. Fast scintillation decay time to avoid the pile of signals (10 – 100 ns).

The scintillation decay time, is the required time for the emission intensity to decrease to e^{-1} . The rise time of emission intensity in scintillators is usually shorter than the decay time and is assumed to be at $t = 0$. The decay time of most scintillators is described by a simple exponential decay function

$$I(t) = I(0) \exp\left(-\frac{t}{\tau}\right) \quad \text{eq. 2-13}$$

$I(t)$ is the number of emitted photons at time t

$I(0)$ is the total number of emitted photons at $t = 0$

τ is the decay constant

Some scintillators though exhibit more complex decay processes that are best described by a two component exponential decay function

$$I(t) = I_1 \exp\left(-\frac{t}{\tau_f}\right) + I_2 \exp\left(-\frac{t}{\tau_s}\right) \quad \text{eq. 2-14}$$

τ_f and τ_s denote the decay constants of the fast and slow components respectively.

4. Low afterglow.

Afterglow is luminescence (phosphorescence) due to thermal release of charge carriers from traps. Traps are created by impurities in the crystal lattice and dislocations caused by irradiation. Afterglow is the residual light measured after the primary decay time of the main emission, the decay time of the afterglow τ_S is given by

$$I(t) = \frac{kN_S}{\tau_S} \exp\left(-\frac{t}{\tau_S}\right) \quad \text{eq. 2-15}$$

N_S is the number of carriers captured by traps.

k is the probability that a luminescent center captures the carrier.

5. Stable response over a wide temperature range.

The light output of a scintillator is a function of the temperature, even though most scintillators are operated at room temperatures, their response over a certain temperature range caused by changes in ambient conditions and irradiation should be stable. Studies by [Mikhail 2011] show the emission wavelength of $\text{SrI}_2:5\%\text{Eu}^{2+}$ to shift towards the longer wavelength with temperature as shown in Figure 2.11, this is probably due to the decrease of the bandgap with temperature. The light output also decreased with temperature due to thermal quenching as in Figure 2.12 .

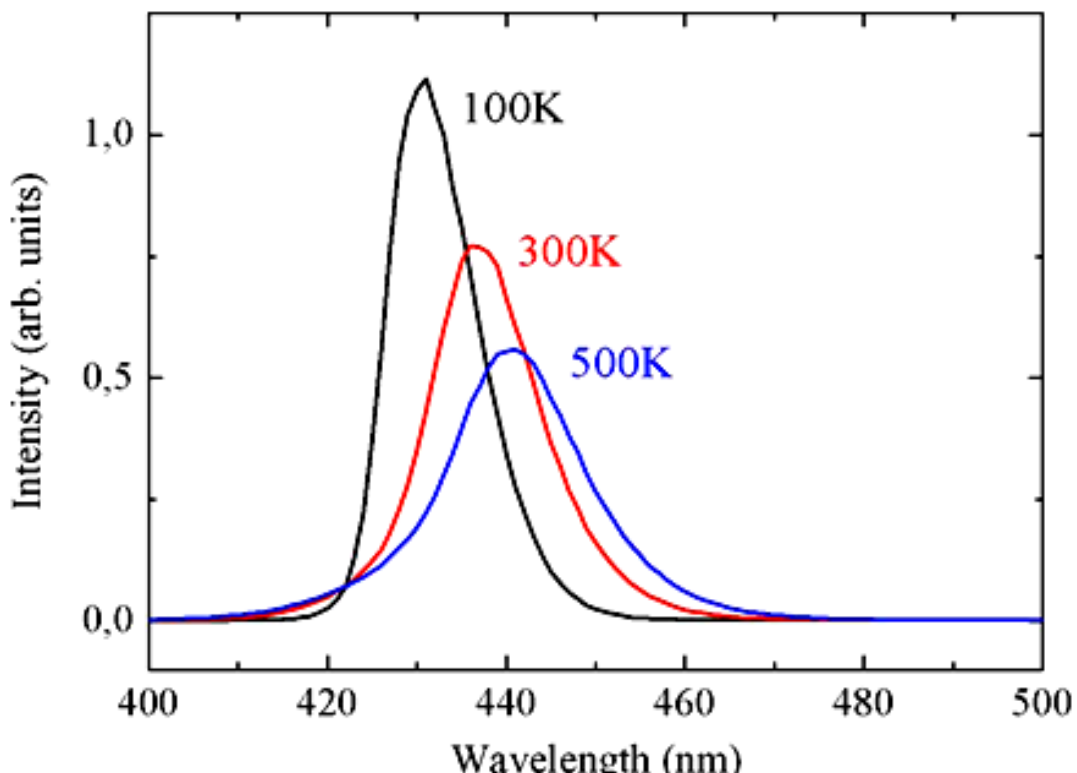


Figure 2.11: Shifting of the emission wavelength as a function of temperature in X-ray excited emission of $\text{SrI}_2:5\%\text{Eu}^{2+}$ [Mikhail 2011].

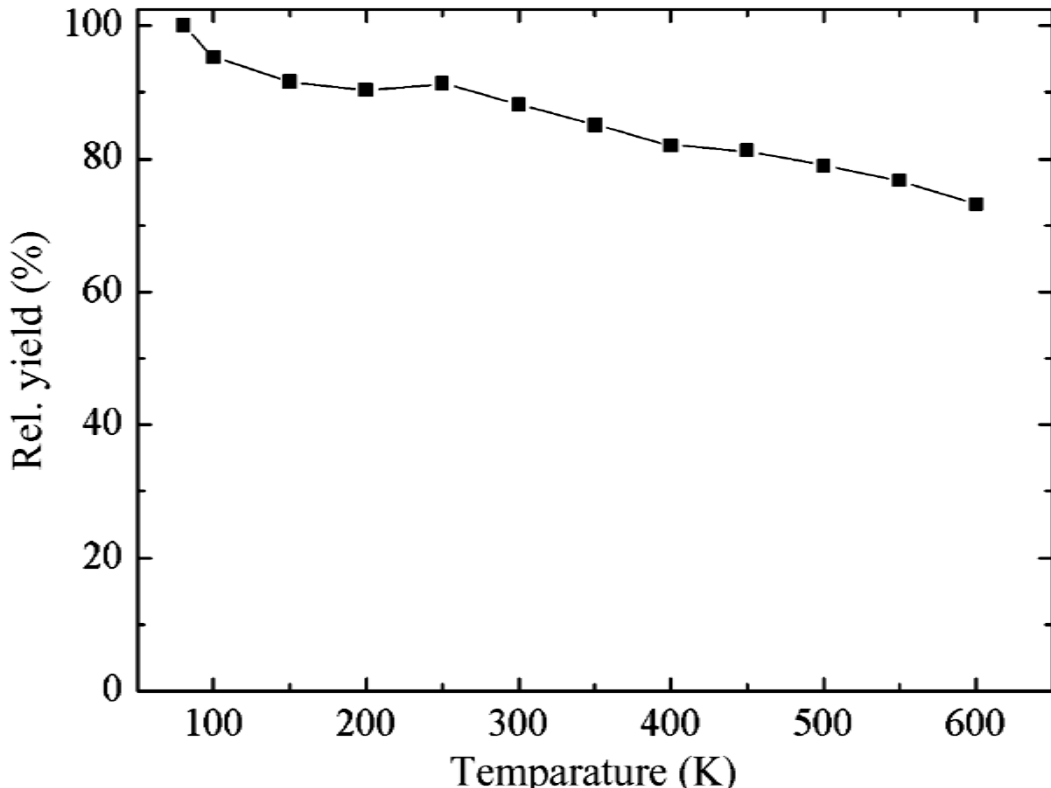


Figure 2.12: Temperature dependence of the $\text{SrI}_2:5\%\text{Eu}^{2+}$ light output [Mikhail 2011].

6. Good optical properties.

A good scintillator should be transparent to its own light. Self-absorption in scintillators is caused by impurities in the crystal lattice and reabsorption due to overlapping in scintillator absorption and emission bands. [Mikhail 2011] has reported on the overlapping of the absorption and emission bands of Eu^{2+} in SrI_2 around 415 nm, this overlapping also showed a strong dependence on temperature.

Another important material property of scintillators that influence the light collection efficiency is the refractive index. According to [Birks 1964], if μ is the refractive index of a scintillator, a fraction of the light intensity incident normally on a scintillator-air interface is internally reflected

$$\text{Internally reflected light (\%)} = \frac{(\mu-1)^2}{(\mu+1)^2} \quad \text{eq. 2-16}$$

Beyond the critical angle θ_{crit} the light is totally internally reflected. Because the refractive index of solid scintillators is $> \sqrt{2}$, their critical angle is less than 45° .

$$\theta_{crit} = \sin^{-1}\left(\frac{1}{\mu}\right) \quad \text{eq. 2-17}$$

7. High sensitivity and good resistance to radiation induced damage (Radiation hard).

Most applications require a scintillator detector with a good sensitivity to a particular type of radiation. Detector sensitivity to a given type of radiation depends above all, on the cross section for ionizing reactions in the detector. This is defined as the probability that the incident radiation will convert part or all its energy in the detector into the form of ionization [Leo 1994].

The scintillator should be able to resist radiation induced damage like the creation of dislocation centres and shallow traps. Dislocation centres lead to the formation of colour centres which can absorb emitted photons leading to a decrease in the optical transmission. Radiation induced shallow traps tend to increase the level of afterglow. The radiation hardness is not a well-defined quantity according to [Rodnyi 1997], it is a measure for the maximum dose tolerated in actual detectors.

8. High density of $> 5 \text{ g/cm}^3$ and high effective atomic number of > 50 .

High density scintillator is needed especially in gamma-ray detection and spectroscopy for a high absorption efficiency of gamma quanta in small scintillator volumes. A high atomic number Z would maximize the gamma quanta absorption through a photoelectric effect. The gamma-ray absorption by photoelectric effect per cm $\propto \rho Z_{eff}^{3-4}$ [Eijk 2001].

9. Emission wavelength in the spectral response of photodetectors.

The emission wavelength of a scintillator should lie near the maximum quantum efficiency of photodetectors. The quantum efficiency against the wavelength is shown in Figure 2.13 for most materials used for PMT photocathodes.

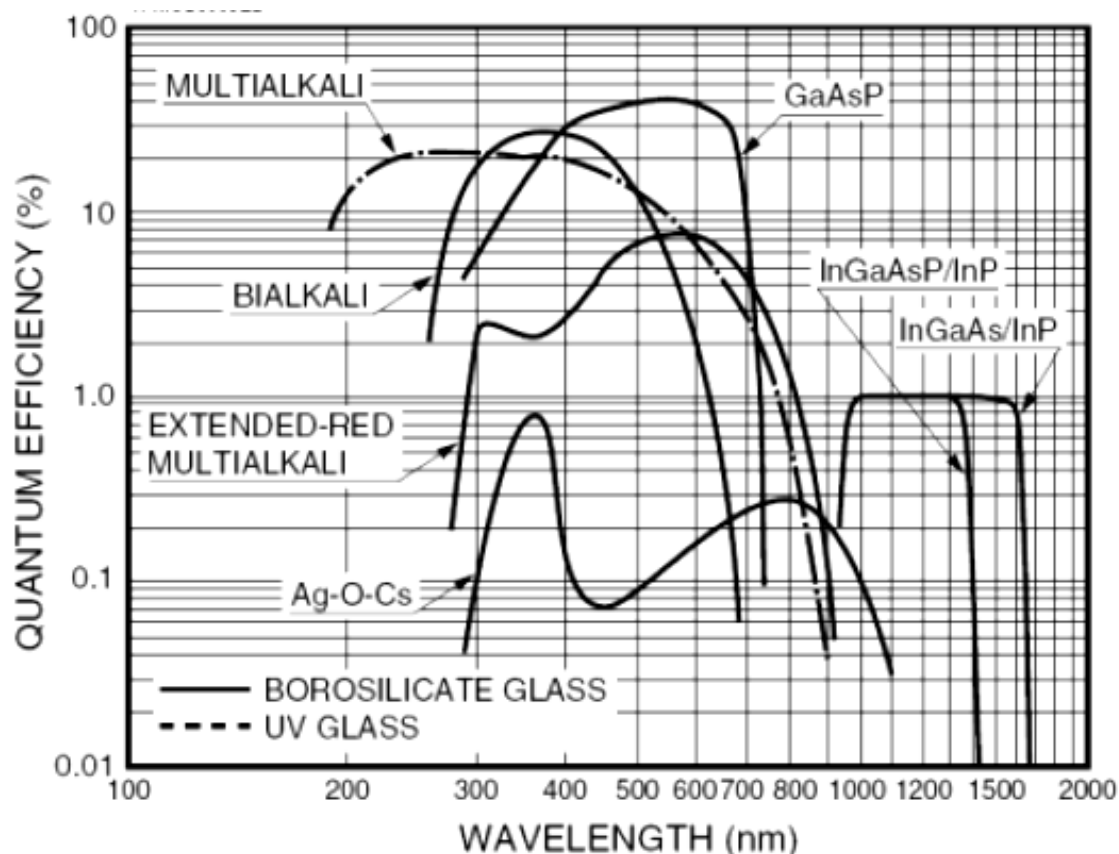


Figure 2.13: Spectral response characteristics of most photocathodes [HAMAMATSU].

10. Good mechanical and stable chemical properties and readiness to be grown into single crystals.

Considering the application of scintillators in exploration activities, a scintillator should be crack resistant, robust and machinable. Chemical stability is also very important, most alkaline halide and alkaline earth halide scintillators are hygroscopic and oxygen sensitive as is the case with the SrI_2 scintillators at high temperatures, decomposing to SrO .

For a scintillator material to be readily grown into single crystals, it is important that it doesn't have strong anisotropy of thermal expansion coefficients along the crystallographic axes that would lead to cleavage in the growing crystal, nonhygroscopicity is also desirable so that simple crystal growth techniques like the Czochralski method could be used without melt hydration. Most alkaline halide and alkaline earth halide scintillators require canning for practical applications.

11. Good proportionality of response.

The response of a good scintillator should be proportional over a wide energy range. [Van Loef 2009] has reported on the excellent light yield proportionality as a function of electron energy of $\text{SrI}_2:\text{Eu}$ rivaling that of LaBr_3 , while [Cherepy 2010] reported on $\text{SrI}_2(\text{Eu})$ been more proportional than $\text{LaBr}_3(\text{Ce})$. Non-proportionality is caused by fluctuations in ionization density or charge carrier density.

2.3 Scintillation Mechanism of Inorganic Scintillators

The scintillation mechanism is divided into three stages here for simplicity and better understanding: 1) the energy cascade; 2) the thermalization and migration of charge carriers to the luminescence centre and 3) the excitation and emission of the luminescence centre.

1) The energy cascade

The energy cascade starts with the absorption of a high energy photon $\hbar\nu$ by an atom A , the creation of a high energy primary electron e and an inner shell hole as shown below



The primary electron and the inner shell hole relax differently. The inner shell hole relaxes radiatively emitting a photon or nonradiatively producing an Auger electron. There is the probability that a photon emitted during a radiative relaxation can leave the crystal or be absorbed by another atom yielding a new deep hole and a free electron. According to [Rodnyi 1997], the probability of nonradiative decay is usually higher than that of radiative decay. The Auger electron loses its energy through electron scattering. The primary electron relaxes by the inelastic scattering of atoms on electrons (electron-electron relaxation) as follows



After the ionization, the primary electron causing the ionization and the produced secondary electron are indistinguishable and may produce more ionization giving rise to an avalanche of electrons and holes [Rodnyi 1997].

This electron multiplication process continues until the energy of the electrons is less than the ionization threshold ($< 2E_g$). Electrons are produced in the conduction band and all the holes will occupy the valence band with no core band lying above the auger process threshold (general case) [Lecoq 2006], as shown in stage-1 of Figure 2.14. The energy cascade process takes place in a time scale of $\sim 10^{-15}$ to 10^{-13} s [Weber 2004]. Plasmons are produced when primary electrons lose their energy through interaction with valence electrons. The number of electron-hole-pairs created when a high energy photon is absorbed is given as

$$N_{eh} = \frac{E_\gamma}{\beta E_g} \quad \text{eq. 2-20}$$

N_{eh} is the number of electron-hole-pairs

E_γ is the photon energy

β is a constant, ~ 1.5 to 2 for ionic crystal scintillators

E_g is the bandgap

Theory and Scientific Background - 2

2) The thermalization and migration of charge carriers to the luminescence center

At the end of the energy cascade, hot electrons and holes interact with the host lattice through electron-phonon relaxation as shown in stage-2 of Figure 2.14. The electrons thermalize to the bottom of the conduction band, while the holes move to the top of the valence band. [Rodnyi 1997] described the thermalization process as carrier migration with a characteristic length $L = 10^2$ to 10^3 nm for ionic crystal scintillators.

During the migration, electrons and holes can be captured by traps (traps are undesired electronic defects in the bandgap), free and bound (self trapped exciton STE) excitons are created. An exciton is an electron-hole-pair held together by the weak electrostatic Coulomb force. A self trapped exciton would be created in the SrI₂-scintillator for example, if a hole localizes to one iodine-ion on reaching the top of the valence band resulting in the creation of an unstable iodine atom as shown below



The iodine atom would polarize its environment resulting in the sharing of the hole with another iodine-ion as follows



This state of the iodine molecule is called cation vacancy (V_k) or self trapped hole (STH). The self trapped hole tends to capture an electron forming a self trapped exciton (STE) as



The STE can emit a photon (excitonic emission) which has been reported in SrI₂-scintillators by [Mikhail 2011]. Excitons have lifetimes in the order of nanoseconds, after which the ground electronic state would be restored with the emission of photons or phonons. The time scale for the thermalization process is in the order of $\sim 10^{-12}$ to 10^{-9} s [Weber 2004].

3) The excitation and emission of the luminescence centre

At the end of the thermalization process as shown in stage-3 of Figure 2.14, charge carriers recombine to produce light photons. The luminescence is either intrinsic or extrinsic. The two types of intrinsic luminescence are excitonic luminescence and cross luminescence.

Excitonic luminescence has been observed in many inorganic scintillators and is known to originate from the radiative annihilation of STEs. The formation of STEs in inorganic scintillators is discussed with the SrI₂ scintillator as example under thermalization and migration of charge carriers to the luminescence center. Excitonic luminescence is efficient only at low temperatures; nonradiative processes dominate at high temperatures.

Theory and Scientific Background - 2

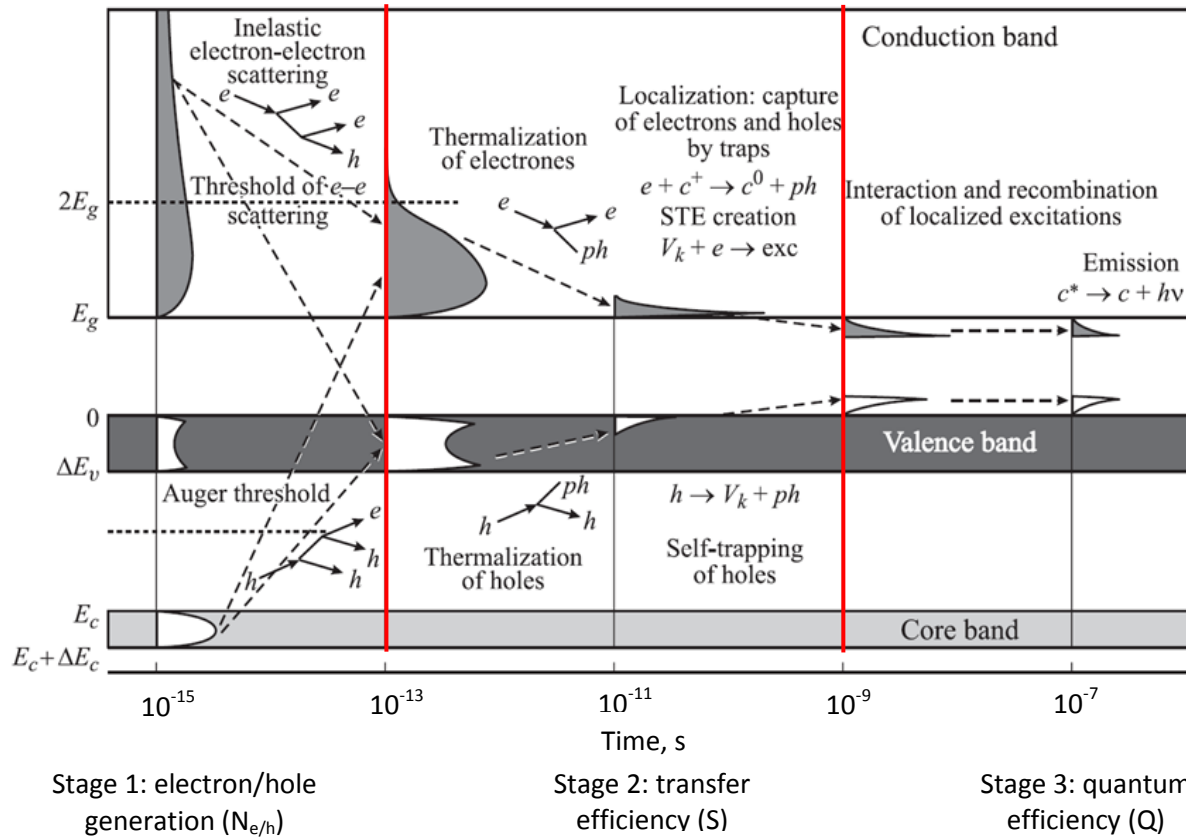


Figure 2.14: The excitonic luminescence model of scintillation in inorganic scintillators, from [Pédrini 2005] and modified for clarity.

Cross luminescence or core-to-valence luminescence is another type of intrinsic luminescence that involves valence band electrons and outermost core band holes as shown in Figure 2.15. [Rodnyi 1997] has reported on the creation of holes both in the valence band (2pF) and in the uppermost core band (5pBa) of BaF₂ scintillators under high energy excitation. The core band holes recombine with valence band electrons to produce light photons and are responsible for a fast subnanosecond luminescence in the relaxation of electronic excitations of cross-luminescent systems [Lecoq 2006].

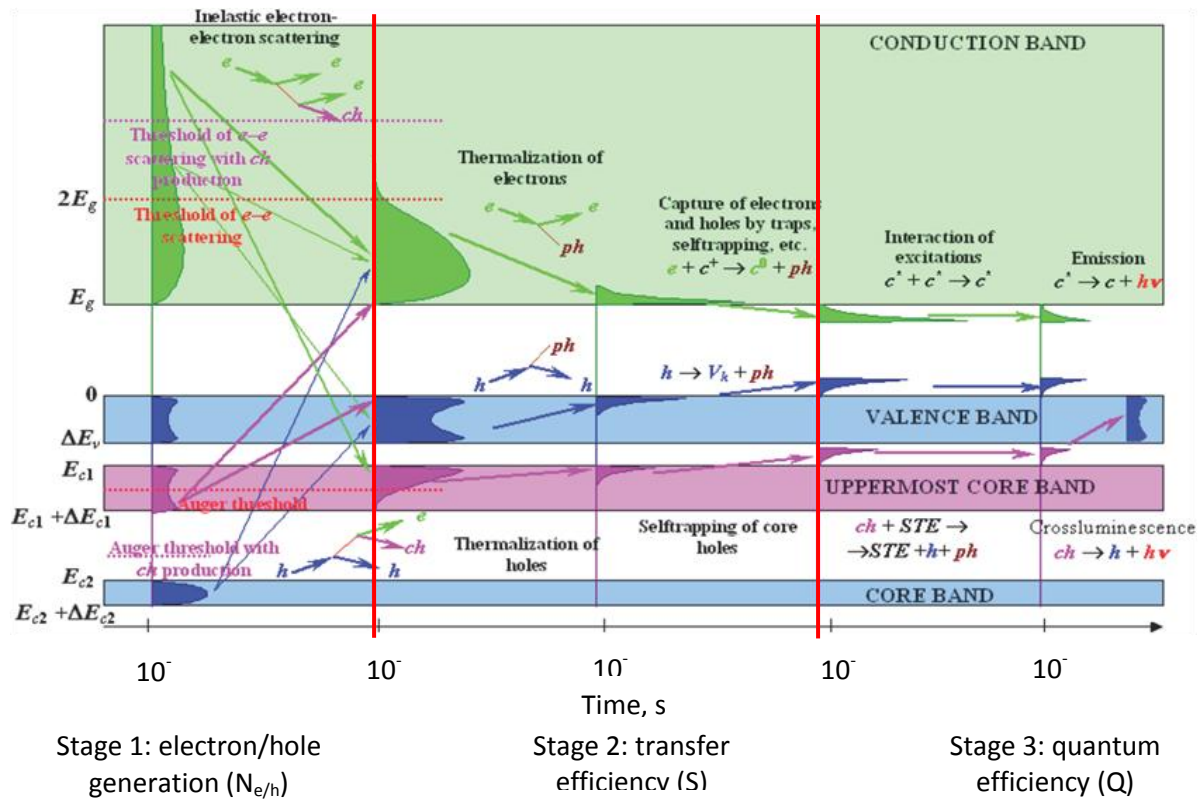


Figure 2.15: The cross luminescence model of scintillations, modified version from [Lecoq 2006].

Extrinsic luminescence usually involves rare earth ions in the band gap of the host matrix, Figure 2.16. The rare earth (RE) ions are excited through impact excitation by subsequent electron-hole capture as shown with equations below



Or hole-electron capture as shown below



This radiative transition (photon emission) or non-radiative transition (phonon emission) to the ground state of the luminescence centre takes approximately $\sim 10^{-9}$ s [Weber 2004].

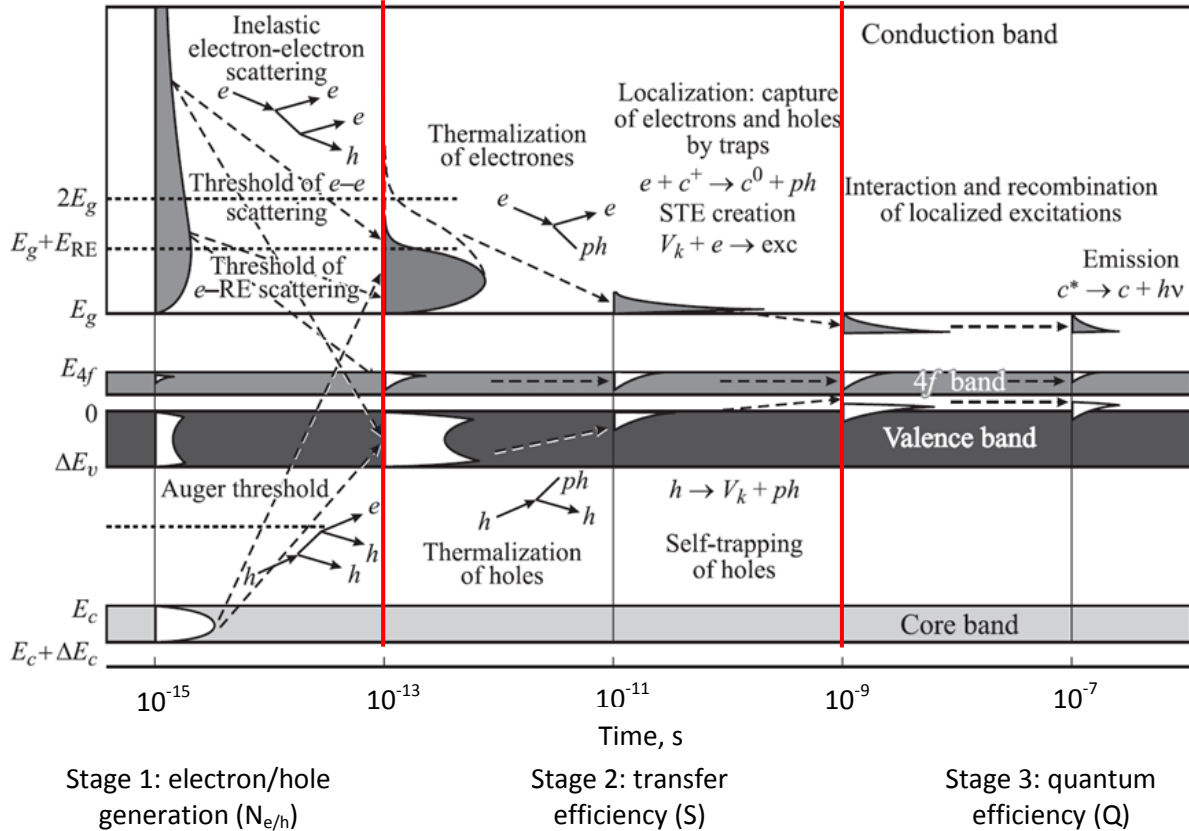


Figure 2.16: The extrinsic luminescence model of scintillation involving rare earth ions [Pédrini 2005].

Figure 2.17 shows the potential energy diagram of a luminescence centre from [Birks 1964]. The energy E is plotted against the configuration co-ordinate x (mean distance between a luminescence centre and the surrounding ions). A and B mark the ground and excited states of the centre respectively.

At excitation, a transition occurs from A to C, a non-equilibrium energy state is created, and so the system will relax from C to B dissipating excess vibrational energy thermally to the host matrix. The emission corresponds to transition from B to D followed by another thermal dissipation of vibrational energy to the host matrix for the transition D to A. Depending on the electron density at B, excited electrons can thermally be activated to reach F, where a transition from the excited state to the ground state would take place through lattice vibrations (quenching). The shift between the absorption band A and emission band B along the x-axis is called stokes shift.

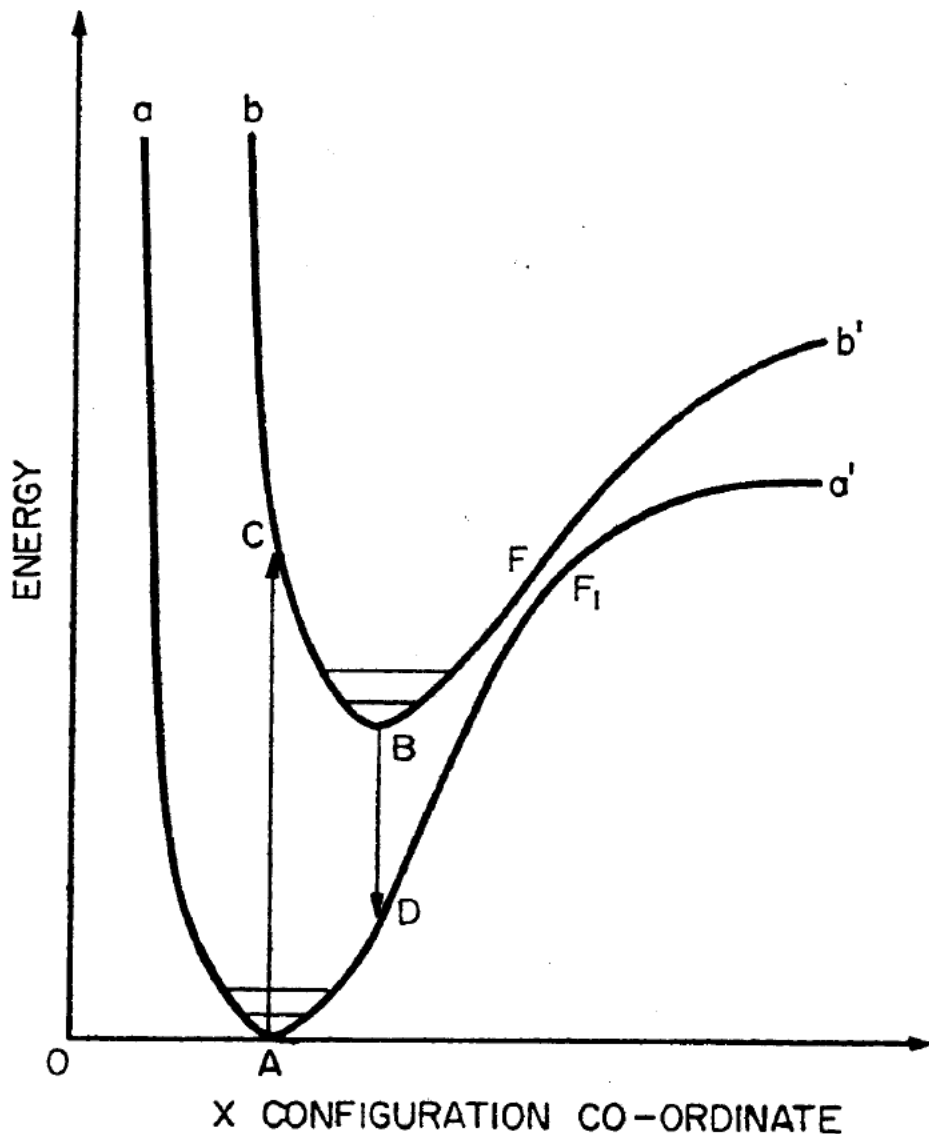


Figure 2.17: Configuration co-ordinate diagram of a luminescence center [Birks 1964].

2.3.1 Scintillator Efficiency η

The efficiency of a scintillator η (energy efficiency) is the effectiveness of converting ionization radiation to light photons and is given as

$$\eta = \frac{N_{ph}\langle h\nu \rangle}{E_\gamma} \quad \text{eq. 2-26}$$

N_{ph} is the number of light photons

$h\nu$ is the mean energy of the emitted photons

E_γ is the energy of a gamma quantum

With

$$N_{ph} = N_{eh}SQ \quad \text{eq. 2-27}$$

N_{eh} is the number (efficiency of creation) of electron holes per unit energy absorbed

S is the transfer efficiency of electrons and hole to the luminescence centre

Q is the quantum efficiency of the luminescence centre

This means that the scintillation efficiency is strongly dependent on the three scintillation stages as discussed below.

The first stage (N_{eh}) is defined as the efficiency of conversion of the radiation energy into electronic excitations. The limiting factor at this stage is the bandgap. The number of electron-hole pairs produced in a scintillator when a gamma quanta is absorbed is given as

$$N_{eh} = \frac{E_\gamma}{E_{eh}} \quad \text{eq. 2-28}$$

A generally accepted estimation of E_{eh} is $(1.5 \text{ to } 2)E_g$ in a scintillator for which thermalized electrons and holes are the only types of electronic excitations. The case is different for scintillators with core-valence transition where the number of uppermost core holes also matters a lot [Pédrini 2005].

The transfer efficiency S is an important parameter governing the scintillation mechanism. Not much is known about S , but it is thought to depend on some factors like impurity ion concentration (traps) and temperature (thermal energy). Impurity ions can trap migrating electrons and holes, thereby quenching or delaying the scintillation process. [Pédrini 2005] reported of charge transfer luminescence quenching in YAG:Yb³⁺ at low temperature and long component in the fluorescence decay profiles due to detrapping at the temperature of the peaks. This means that trapped electrons and holes or STEs can be thermally activated to reach the luminescence centre, thereby contributing to the scintillation process.

The quantum efficiency Q is better understood and related to the position of the luminescence center relative to the energy bands. For high quantum efficiency, the ground state of the luminescence centre should be above the valence band and the emitting 5d excited state below the conduction band. The lowest emitting 5d state should not be too close to the conduction band in order to limit the auto-ionization of the excited electrons back into the conduction band, resulting in emission quenching [Bizarri 2010].

2.4 Gamma Ray Spectroscopy: Experimentation

Gamma ray spectroscopy is the quantitative study of the energy characteristics of gamma ray sources ie the isotope giving rise to a particular radiation, radiation type and energy. Most gamma ray detector systems are scintillator based due to the low energy required to operate such systems in their compact form (Figure 2.18), lack of cooling in operations and also the use of large detector volumes in order to detect more energy events.



Figure 2.18: Compact (handheld) scintillator-based detector systems.

Scintillator-based detector systems are normally made up of the scintillator crystal, the photodetector (PMT or photodiode), the preamplifier, the amplifier and the multichannel analyzer (pulsheight analyzer, A/D converter, memory and display) as shown in Figure 2.19. The preamplifier is attached directly to the anode end of the PMT to minimize signal distortion while the scintillator/PMT unit is separated from the electronics module by a cable.

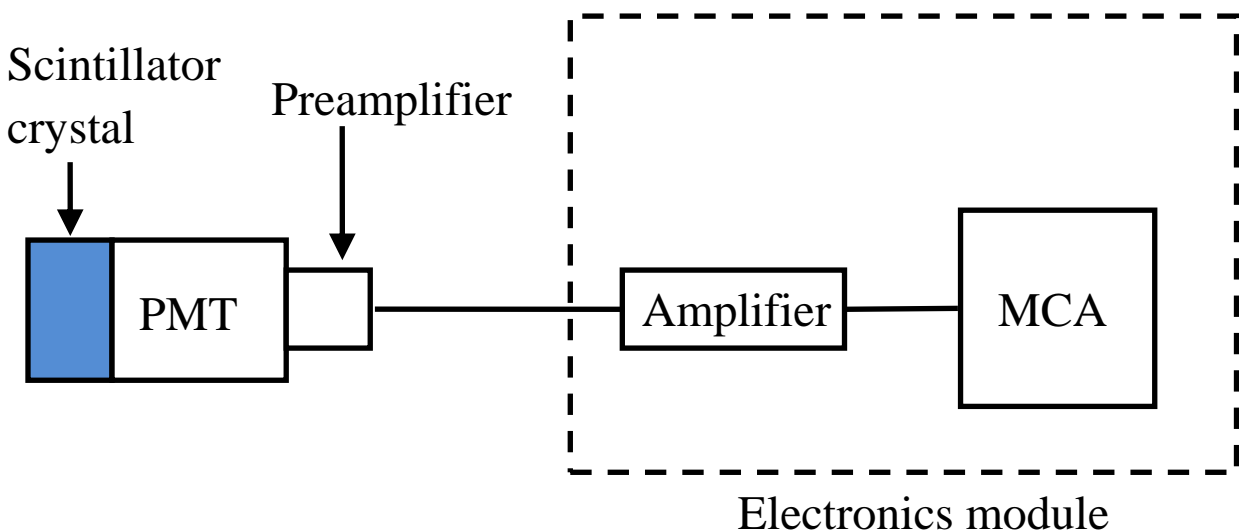


Figure 2.19: Block diagram of a scintillator-based detector system.

[Birks 1964] used a similar image as in Figure 2.20 to show the general arrangement of the PMT scintillation counter and the basic processes involved in the detection and measurement of an ionizing particle.

An incident gamma photon of energy E would dissipate its energy in the excitation of electrons (electron-hole creation). A fraction of the incident energy is converted into light photons N which are radiated in all directions. The scintillator is usually covered by a

Theory and Scientific Background - 2

reflector that reflects the photons towards the photocathode of the PMT. A fraction of the light photons N^* would impinge on the photocathode.

$$N^* = GN \quad \text{eq. 2-29}$$

G is the scintillator light collection efficiency, a parameter that depends, among other factors, on the scintillator surface finish, reflectivity of packaging materials and optical coupling to the PMT. G is equal to 1 at 100 % light collection efficiency.

A fraction of the photons N^* incident on the photocathode would cause the emission of photo-electrons T

$$T = N^* \times (Q.E) \quad \text{eq. 2-30}$$

$Q.E$ is the quantum efficiency of the PMT; defined as the number of light photons needed to produce a single photo-electron at the photocathode.

$$Q.E = \frac{T}{N^*} \quad \text{eq. 2-31}$$

T photo-electrons strike the first dynode ejecting further electrons by secondary emission. The photo-electrons are accelerated by the potential applied between the cathode and the first dynode. If $R \sim (3 - 5)$ is the average number of secondary electrons ejected at the first dynode per incident electron, then RT electrons would impinge on the second dynode.

This electron multiplication process would be repeated at subsequent dynodes, with the dynodes set at higher potentials than the preceding one. With n dynodes, each with a multiplication factor R , the number of electrons at the anode Q_0 would be given as

$$Q_0 = R^n T \quad \text{eq. 2-32}$$

R^n is the PMT gain typically 10^5 to 10^8

Q_0 produces a voltage pulse in the output capacitor that is proportional to the energy impinging on the scintillator.

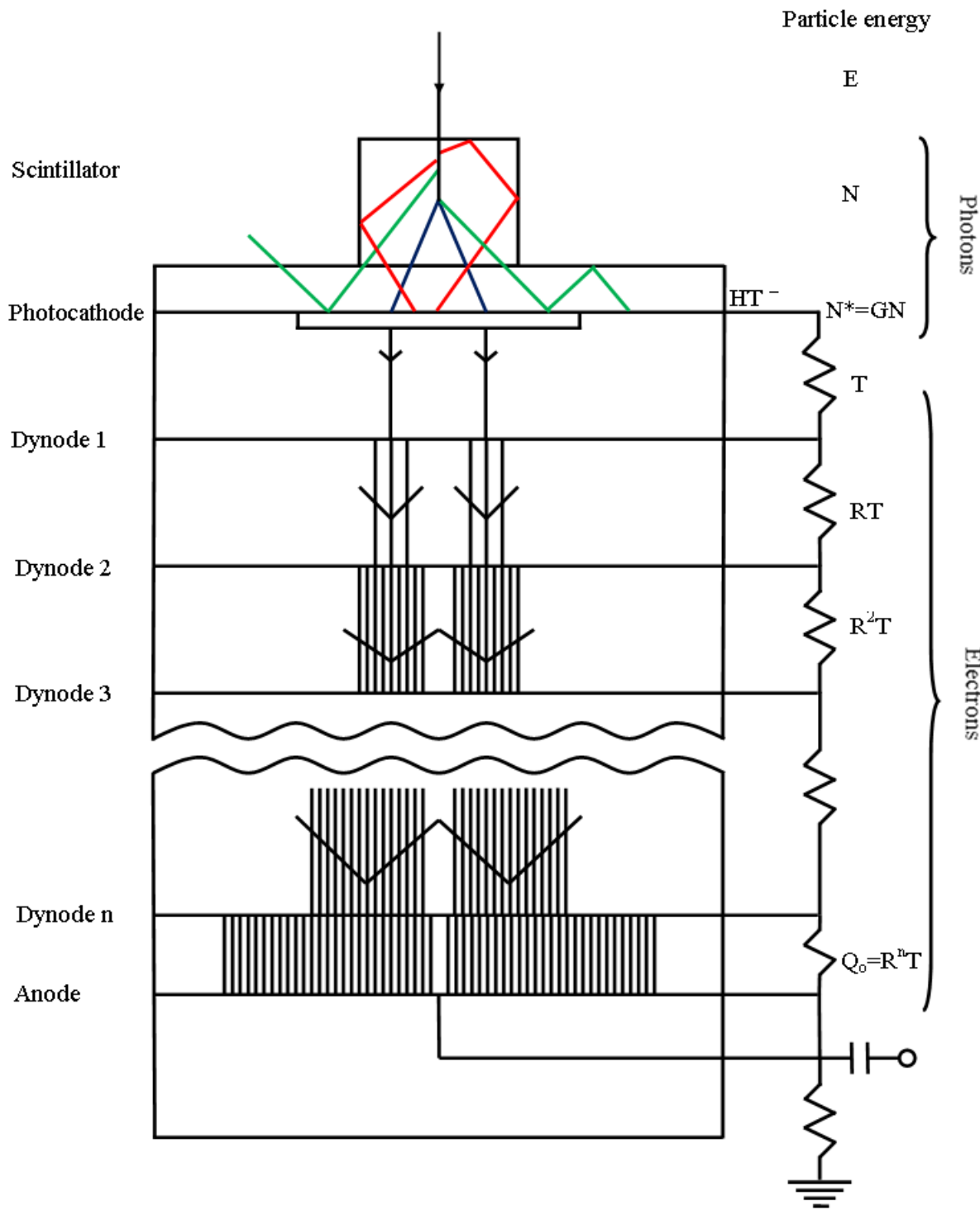


Figure 2.20: PMT scintillation counter. Reproduced after [Birks 1964] and modified for better understanding.

The signal output of the PMT anode is generally very small, this is boosted and integrated through a charge-sensitive preamplifier. The preamplifier output is amplified further and shaped into series of discrete pulses by the amplifier. The pulses are discriminated according to their heights by the pulse height analyzer and then converted from analogue to digital as shown in Figure 2.21. Finally they are accumulated in the memory and plotted as spectrum on the screen.

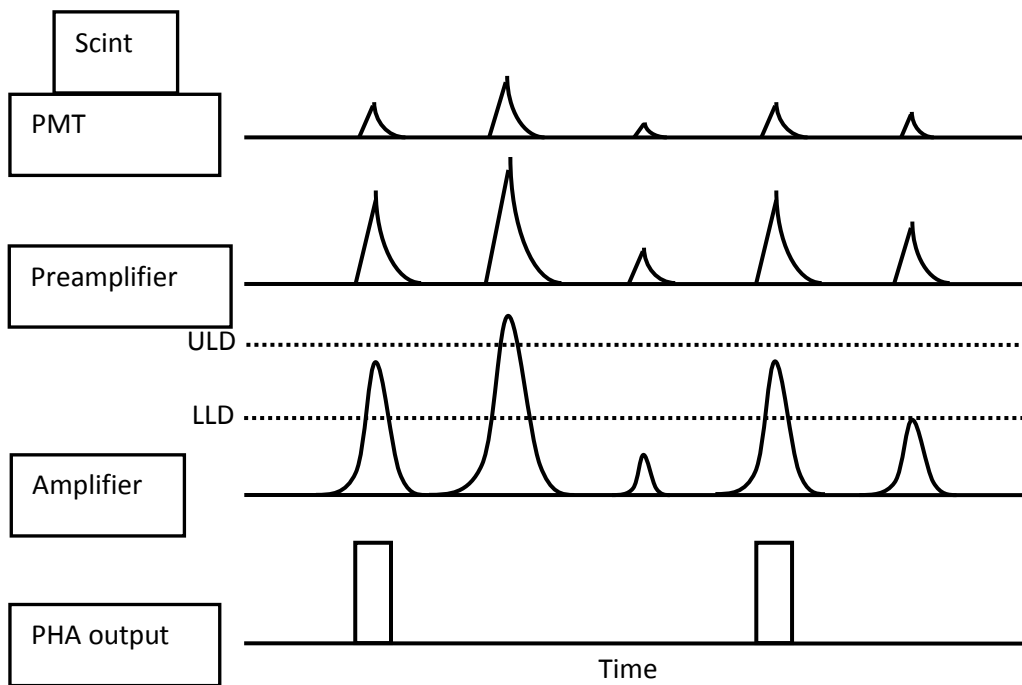


Figure 2.21: Signal processing in a scintillator detector.

2.4.1 Energy Spectrum and Energy Resolution

Scintillator based detectors are normally characterized using the ^{137}Cs isotope (^{137}Cs). ^{137}Cs decays by beta particle emission to ^{137}Ba . The ^{137}Ba is unstable and would attain a ground state by the emission of 662 keV gamma ray in 94% of the time, in the remaining 6%, a conversion electron is emitted followed by ~ 32 keV K-shell characteristic X-ray, as shown in Figure 2.22.

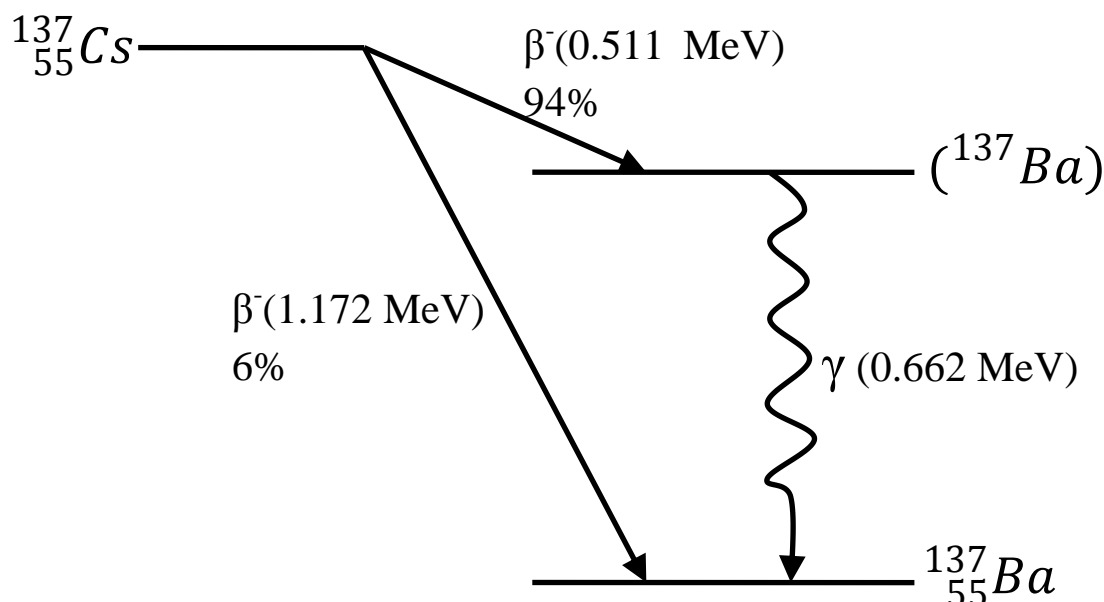


Figure 2.22: Nuclear level diagram of ^{137}Cs .

Detectors are normally contained in Lead-blocks during measurements to collimate the rays and also shield against strong background radiation. Figure 2.23 shows a typical arrangement and the paths normally taken by the rays with the source placed behind the scintillator. [Sturm 2010] has reported on the degradation of the energy resolution and increase on the photopeak position with decreasing irradiation source position to the PMT, due to the longer paths light photons travel to be reflected at the back of the detector, this means that irradiating from the back of the scintillator improves the energy resolution.

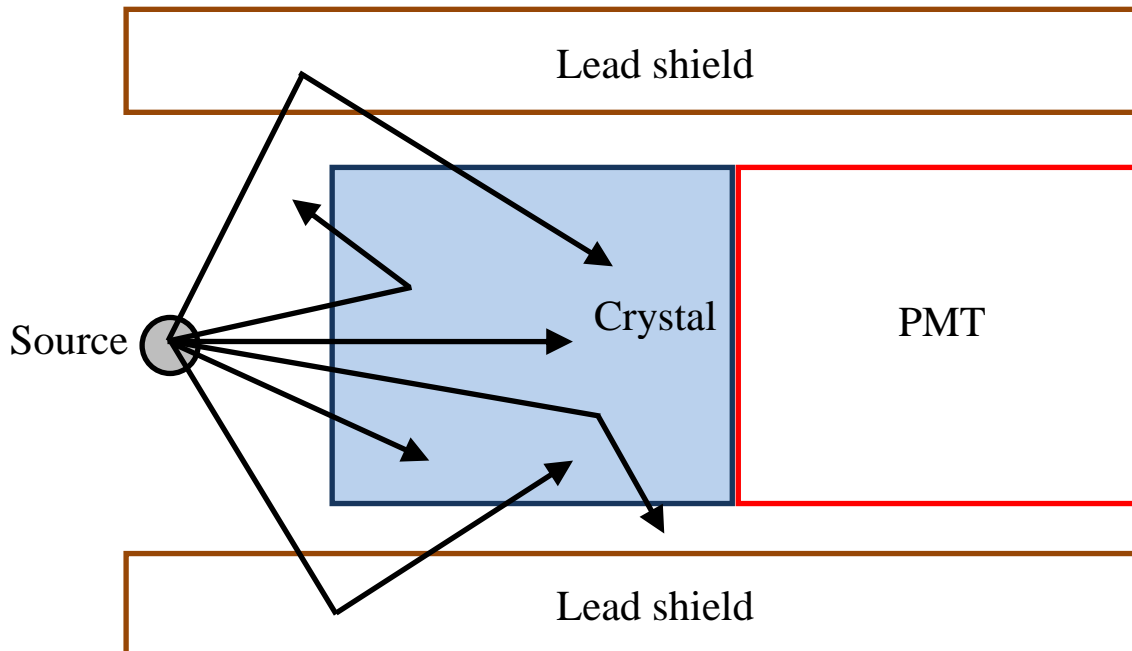


Figure 2.23: Scintillator crystal and PMT shielded by lead-blocks.

Figure 2.24 shows a typical pulse height spectrum of the ^{137}Cs – isotope. The spectrum is composed of the photopeak (A) corresponding to the complete absorption of 662 keV photon energy and normally Gaussian in shape; the Compton continuum (B) corresponds to Compton events with the scattered Compton photon escaping the crystal; the Compton edge (C) marks the upper limit of the Compton continuum; the backscatter peak (D) arises from photons that scatter from the lead-shield into the detector; barium X-ray photopeak (E) corresponds to the absorption of barium K-shell X-rays (31 – 37 keV) and the lead K-shell X-rays photopeak (F) from the shields.

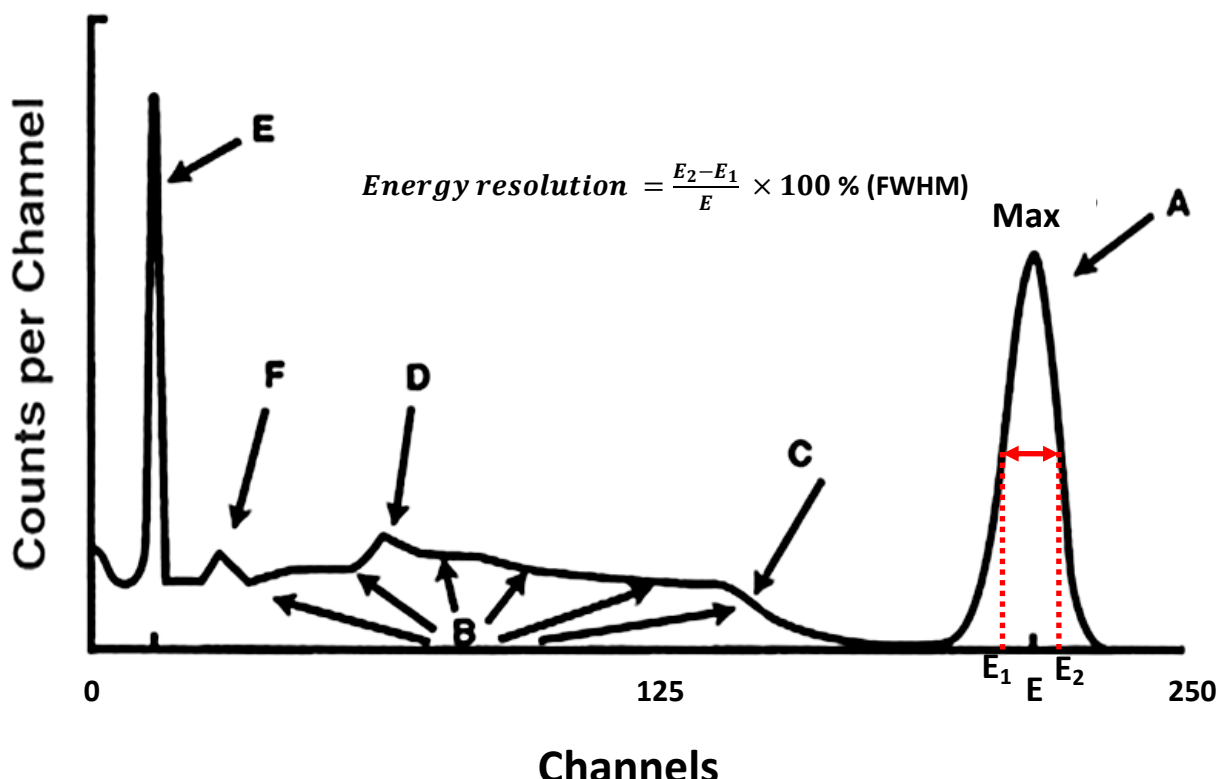


Figure 2.24: The components of a pulse height spectrum.

The energy resolution (FWHM) is measured at half the maximal height of the photopeak. According to [Leo 1994], the photopeak width arises because of fluctuations in the number of ionizations and excitations produced.

A good energy resolution of a scintillator is always associated with a high light yield; I personally think this should apply to a certain extent. There are few scintillators with low light yield and fantastic energy resolution. For example, the light yield of the LaBr₃:Ce is 65 000 ph/MeV compared to the SrI₂:Eu with more than 100 000 ph/MeV, but the energy resolution at 662 keV (FWHM) of the LaBr₃-scintillator (2.7%) is rivalling that of the SrI₂-scintillator (2.7%) as reported by [Shah 2010]. I think the energy resolution has much to do with the light collection efficiency of the scintillator; defined as the probability that a light photon produced in the scintillator, also leaves the scintillator, the efficiency of photon transfer to the PMT, fluctuations in PMT electron multiplication and scintillator non-proportionality. Experimentally, the energy resolution is calculated by fitting a Gaussian distribution function to the photopeak in the energy spectrum.

2.4.2 Light Yield

This is a very important scintillator property. A high light yield always translates into a high efficiency of a scintillator and in most cases also good energy resolution. It is a measure of the scintillator response to a particular radiation. The detectable scintillator light yield is strongly dependent on the total packaging (type of reflector and optical coupling), on the crystal

Theory and Scientific Background - 2

geometry (crystal size, form and surface finishing) and on the efficiency of photon transfer to the PMT. One also differentiates the absolute light yield from the relative light yield. The absolute light yield η is the ratio of total photon energy E_{ph} to the energy deposited in a scintillator E_γ

$$\eta = \frac{E_{ph}}{E_\gamma} \quad \text{eq. 2-33}$$

The absolute light yield of scintillators is difficult to determine due to the difficulties and errors associated with the measurement of the scintillator light collection efficiency (LCE). The relative light yield L is the ratio of total energy of scintillation photons T_{ph} detected at the photocathode to the energy E_γ , deposited in the scintillator by ionizing radiation

$$L = \frac{T_{ph}}{E_\gamma} \quad \text{eq. 2-34}$$

The light yield of scintillators reported in most literatures is the relative light yield. The relative light yield is calculated using the following methods

- I. Pulse method: the signal amplitude V at the PMT end is measured, T_{ph} can be calculated as

$$T_{ph} = \frac{V * \epsilon * C}{\Sigma_a * \mu * E * e} \quad \text{eq. 2-35}$$

C is output capacity of PMT, μ is the gain of the PMT, E is the energy of incident gamma-radiation, Σ_a is the anode sensibility of the PMT, e is the electron charge and ϵ the energy of light photon.

- II. PMT intrinsic resolution: measuring the number of photoelectrons N_{pe} produced at the photocathode and then calculating the number of photons N_p as

$$N_p = \frac{N_{pe}}{Q.E} \quad \text{eq. 2-36}$$

$Q.E$ is the PMT quantum efficiency.

- III. Single-electron method: comparing the measured signal amplitude to that of a single-electron distribution of the PMT.
- IV. Comparison: here the Q.E corrected signal amplitude is compared to that of a known scintillator. In most cases the NaI:Tl is used as a reference sample.

2.4.3 Decay Time

The scintillation decay time has been discussed in chapter 2.2.1.1. During this period, a second event cannot be accepted either because the detector is insensitive or because the second signal will pile up on the first [Leo 1994]. Figure 2.25 shows the typical scintillator decay time profile, the fast component arises mostly from excitonic emission and the slow component from sequential electron-hole capture or hole-electron capture and the excitation of certain metastable states that lead to emission.

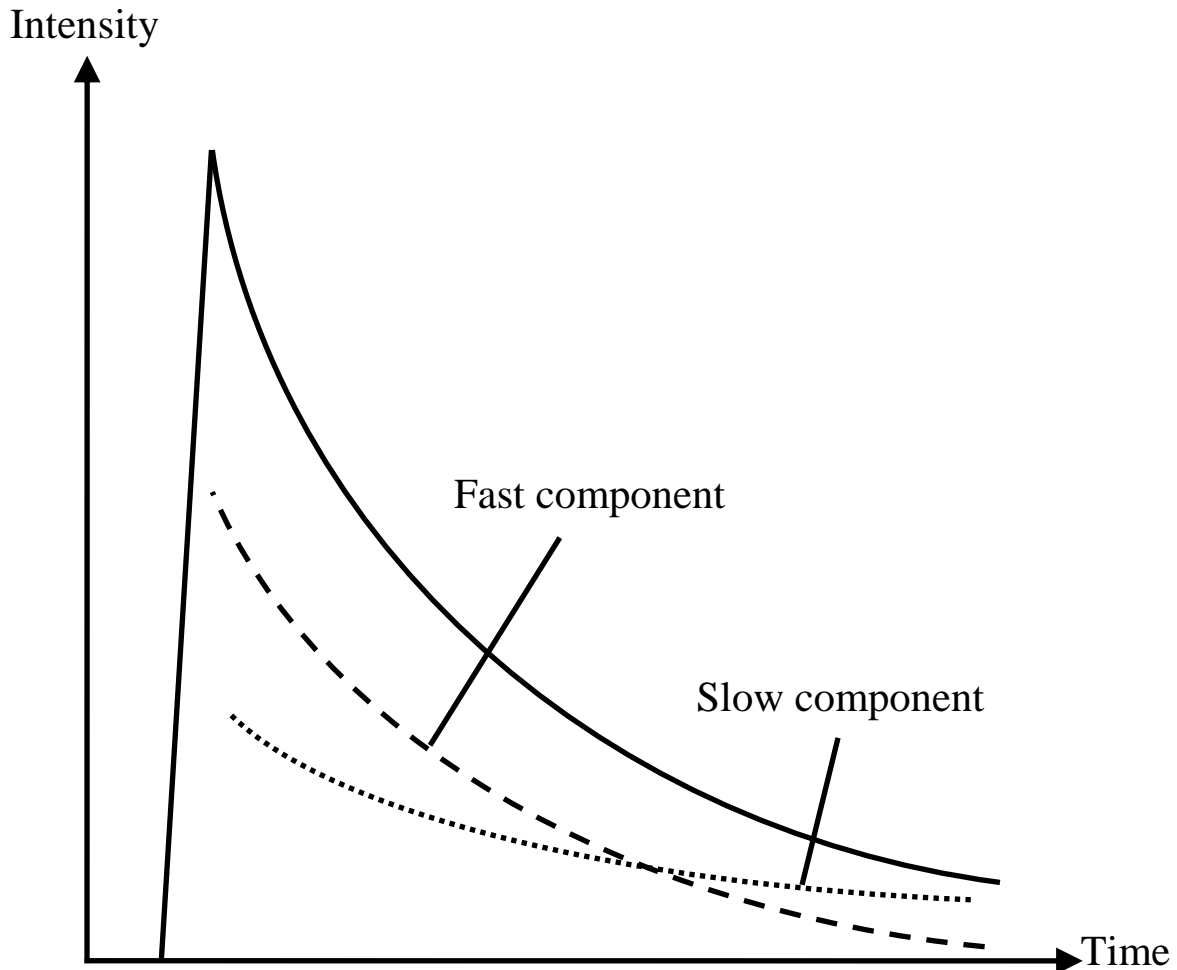


Figure 2.25: Typical pulse shape of scintillator detectors.

Decay time constants are calculated from single or double exponential decay functions fitted to the experimental data.

2.5 X-Ray Imaging

In this research work, the suitability of the $\text{SrI}_2(\text{Eu})$ -scintillator for X-ray imaging was tested for the first time ever. Considering the application of scintillators in X-ray imaging, especially for medical diagnostics, there is the need for more research work aimed at finding new scintillators with better performance: high spatial resolution, high conversion efficiency of X-rays into light images, high density and high Z_{eff} for better X-ray absorption in the thin scintillator material.

Some of the modalities of X-ray imaging that employ scintillators include: X-ray radiography, computed tomography CT, single photon emission computed tomography SPECT, positron emission tomography PET. X-ray radiography is a method that uses X-rays to view non-uniform density composed materials. It is a transmission based technique, where X-rays pass through material; the part of the X-ray stopped by material is converted in a scintillator screen into light with different spatial emission (optical) densities. Some of the scintillator characteristics for X-ray imaging include: high density ($> 5 \text{ gcm}^{-3}$) and high atomic number (> 50) in order to reduce the thickness of the scintillating screen, while maintaining a good X-ray absorption; good optical properties like high transmittance, no light scattering and emission in the wavelength of CCD detectors; low afterglow; high light emission ($> 15 \text{ ph/keV}$) and radiation hardness.

2.5.1 Image Formation

Scintillator based X-ray imaging detector systems consist of the X-ray source (X-ray generator), a scintillator, a light microscope optic and a charge-coupled device CCD, Figure 2.26. X-ray generation and interaction with matter have been discussed in chapter 2.1 and 2.1.1 respectively, the conversion of X-rays into light photons in an inorganic scintillator in chapter 2.3.

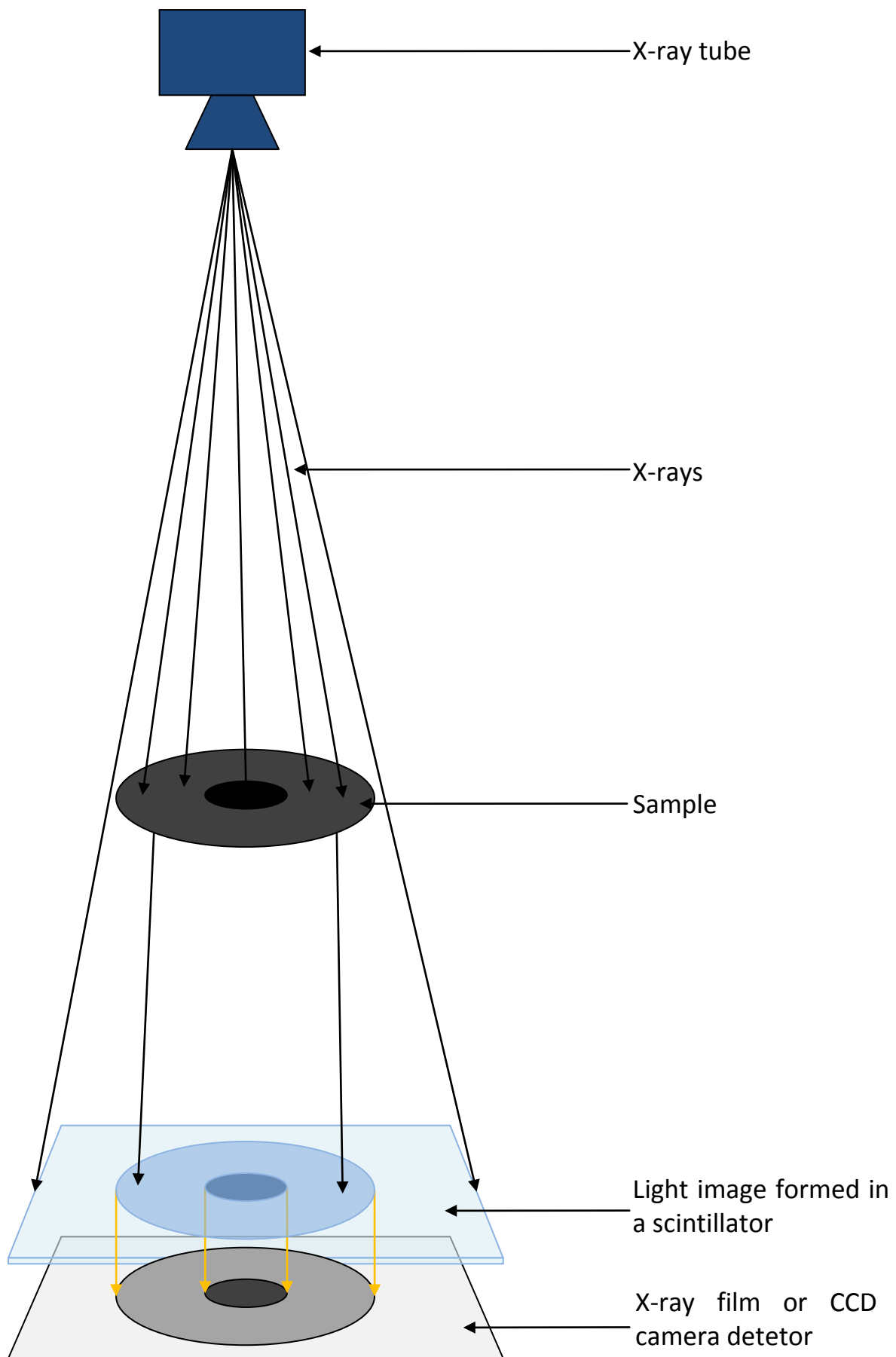


Figure 2.26: Basics of a scintillator based X-ray imaging detector system.

The X-rays from a source pass through the sample where they are differentially attenuated depending on the density, atomic number and thickness of the sample and its material composition. Figure 2.27 shows the mass attenuation coefficient of several materials in diagnostic X-ray imaging as an example.

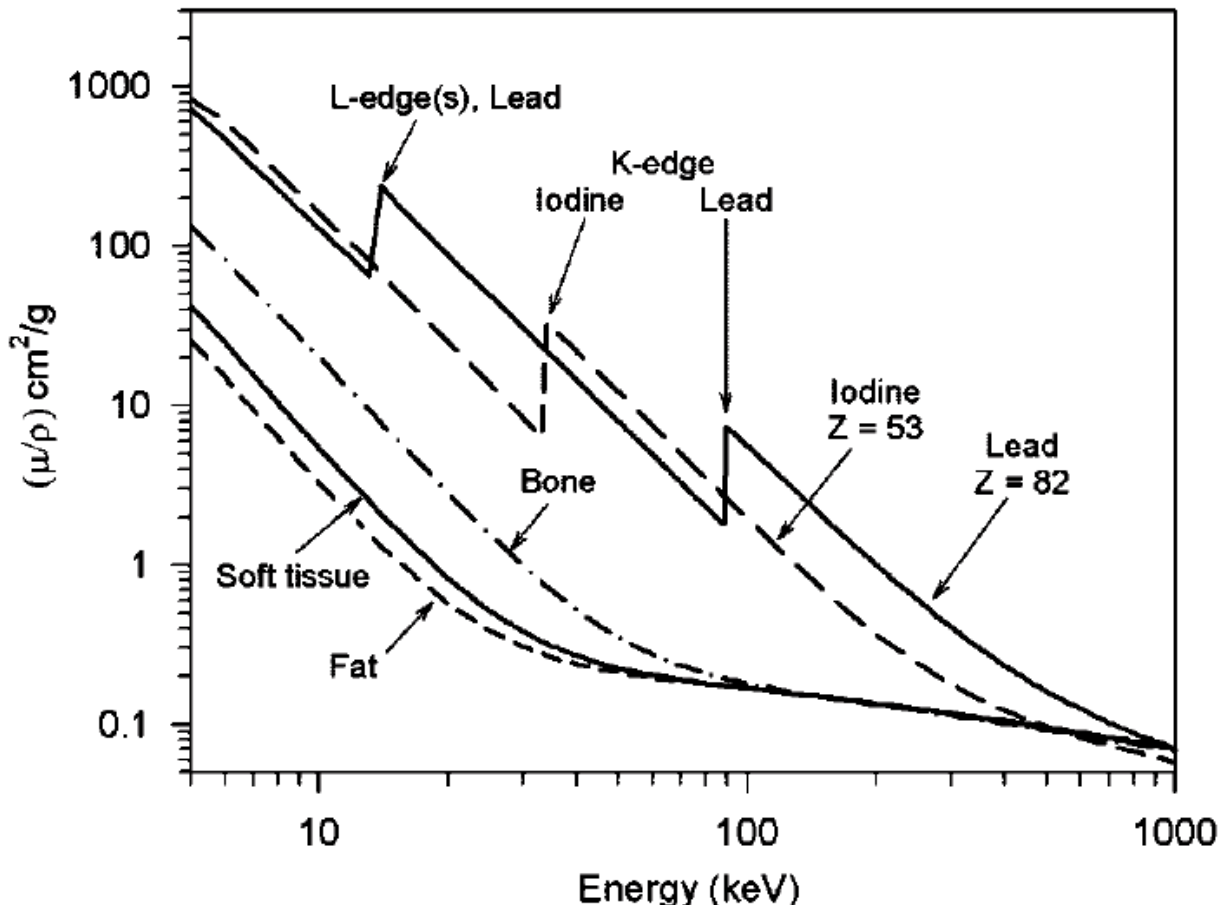


Figure 2.27: Mass attenuation coefficient (μ/ρ) of several materials encountered in diagnostic X-ray imaging [Seibert 2005].

Only a fraction of the initial X-rays will reach the scintillator crystal. Direct X-rays from the source portray the geometry of the sample onto the scintillator crystal and the partially attenuated X-rays portray the compositional image of the sample. Some of the X-rays reaching the crystal are absorbed in the crystal, some scatter from the crystal and some pass without interaction. The relative probability of these events depends on the energies of the photons and the thickness of the crystal. In the scintillator crystal, the X-rays are converted into a light image that is relayed by the optics to the CCD camera for recording.

According to [Martin and Koch 2006], the CCD camera is focused within the scintillator onto a certain object plane z_o in Figure 2.28, other planes in front of and behind z_o will be out of focus at the CCD but nevertheless contribute to the total light emitted in the thickness z of the scintillator projected onto the CCD. The image resolution R of such system depends on the defect of focus δz of the image outside the object plane z_o , on diffraction and spherical aberrations arising from the thickness of the scintillator z and the substrate t as follows

Resolution dependence on defect of focus

$$R \cong \delta z \cdot NA$$

eq. 2-37

Dependence on diffraction

$$R \cong \frac{\lambda}{NA}$$

eq. 2-38

Dependence on spherical aberration

$$R \cong t \cdot NA^3$$

eq. 2-39

δz is the depth of focus, λ is the wavelength of the light and NA is the numerical aperture.

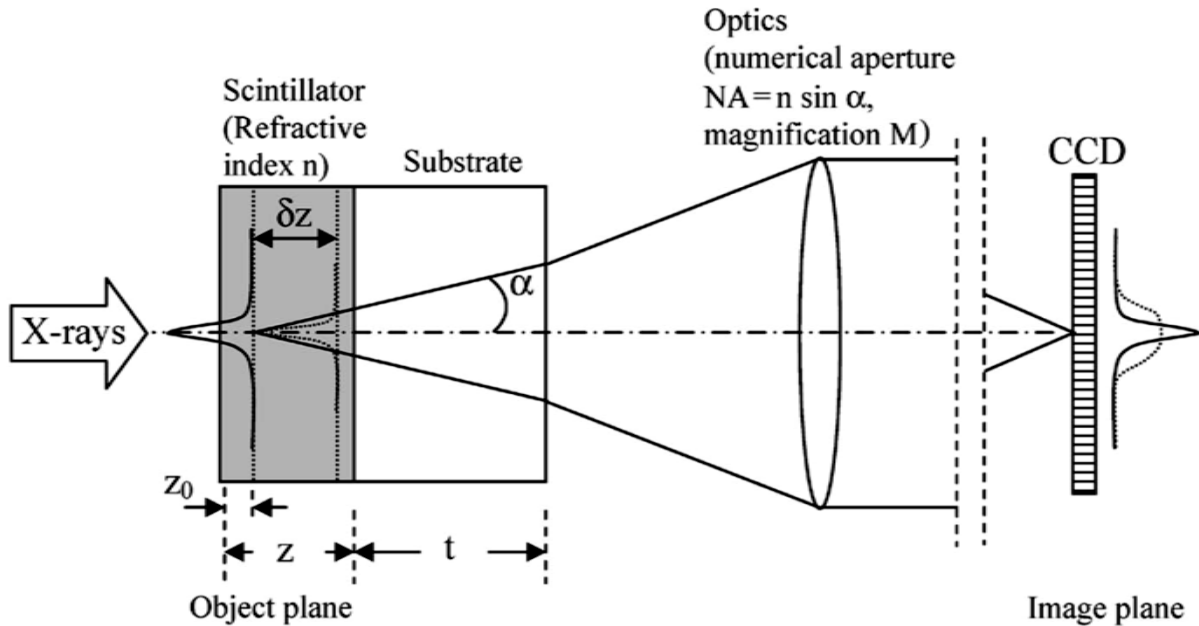


Figure 2.28: X-ray imaging with a scintillator and an optical system. An image in z_0 is focused on the CCD, an image in $z_0 + \delta z$ is out of focus at the CCD [Martin and Koch 2006].

2.5.2 Description of the Image

X-ray images are best described using three basic concepts: spatial resolution, detective quantum efficiency and contrast.

2.5.2.1 Spatial Resolution (Image Resolution)

[Seibert 2005] defined the spatial resolution as a measure of the detail visible in the output image, in other words spatial resolution is a measure of the smallest distance which two objects must have to be imaged clearly. The spatial resolution of an X-ray image is affected by the following factors:

1. The thickness of the scintillator screen: thick scintillators cause spreading of the emitted light leading to broad line spread function (LSF) width

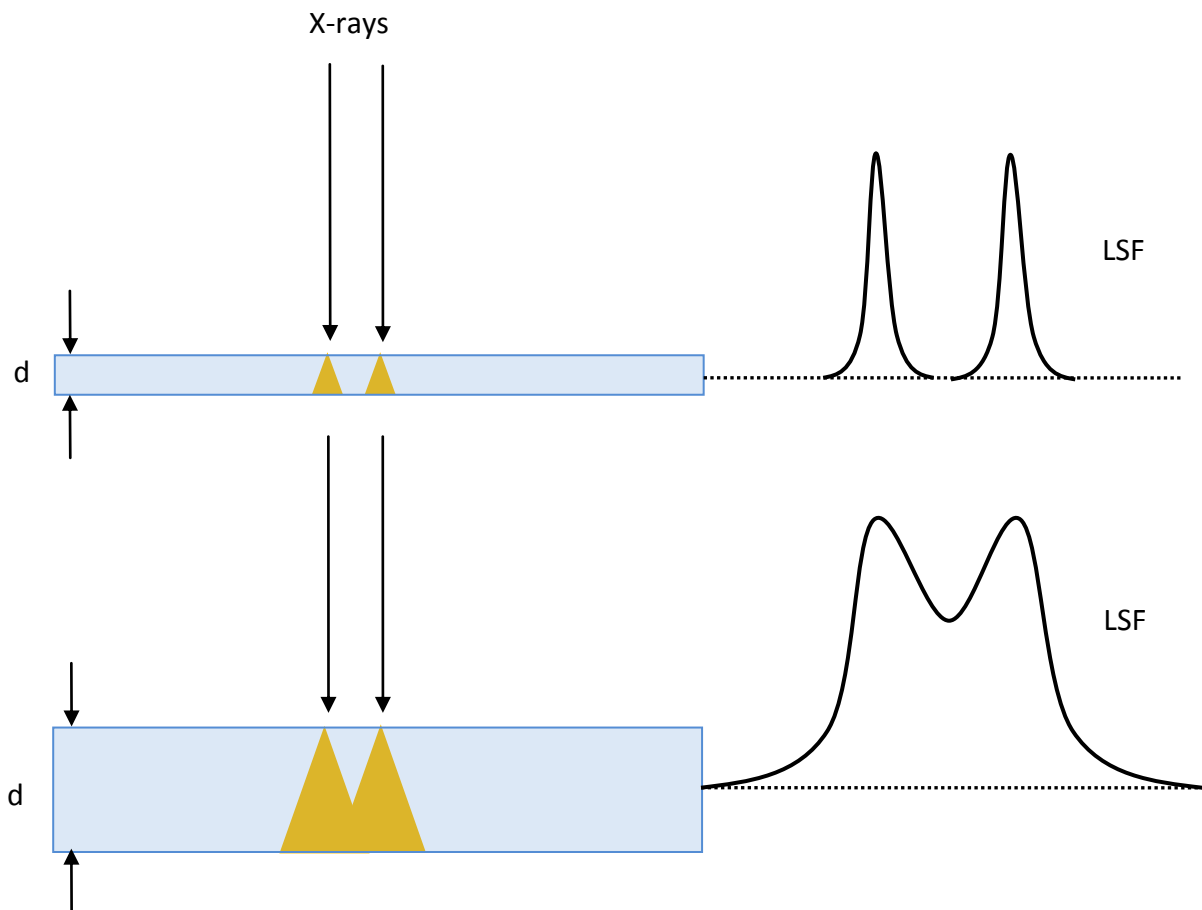


Figure 2.29: Degradation of spatial resolution caused by light spreading in the scintillator. d is the thickness of the scintillator screen.

2. The effective size of the X-ray focal spot: the X-ray focal spot is a collection of point sources, each producing its own view of the object, the summation of all views will result in blurring at the edge of the image; this effect is called the penumbra. The degree of image blurring depends on the effective focal spot size F , on the distance between the X-ray source and the object SOD and also on the distance between the X-ray source and the detector SID as in Figure 2.30. The penumbra region P is given by

$$P = \frac{F(SID - SOD)}{SOD} \quad \text{eq. 2-40}$$

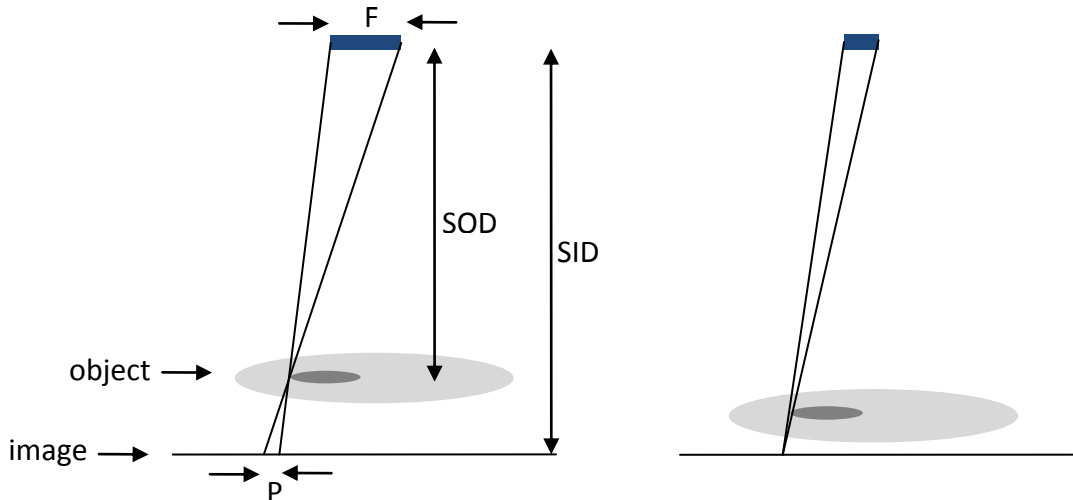


Figure 2.30: Formation of penumbra or geometric unsharpness at a finite value of the effective focal spot size. Decreasing the focal spot and the object-to-detector distance decreases the unsharpness (SOD is the source-to-object distance; SID is the source-to-image distance and P the penumbra region).

3. The absorption process: the quality of X-ray images depends on the type of X-ray absorption process in the scintillator. The limiting factors are the Rayleigh scattering which describes the deviation of photons from their direction with no energy loss, the Compton scattering where only a part of the energy is transferred to an electron and fluorescent X-rays produced during photoelectric effect.
4. The magnification factor: at fixed source-to-image distance SID in Figure 2.30, bringing the object closer to the source will increase the magnification m as follows

$$m = \frac{SID}{SOD} \quad \text{eq. 2-41}$$

This will lead to image blurring, to get a sharp image; the focal spot size of the source has to be as small as possible.

5. Problems of the optics: the microscope optics used in X-ray imaging is diffraction limited, meaning the obtainable resolution R depends on the wavelength of the light λ and the numerical aperture NA of the lens as follows

$$R = \frac{\lambda}{NA} \quad \text{eq. 2-42}$$

The spatial resolution of imaging systems is normally calculated from the point spread function (PSF) as in Figure 2.31 or the line spread function (LSF). These methods are based on measuring the optical density across the point image or line image. The graph of the measured optical density, when converted to relative exposure as a function of position will give the PSF or LSF. The modulation transfer function MTF is obtained from the PSF and

LSF as the magnitude of their two-dimensional Fourier transformation [Hasegawa 1987]. The spatial resolution can also be estimated using line-pair structures.

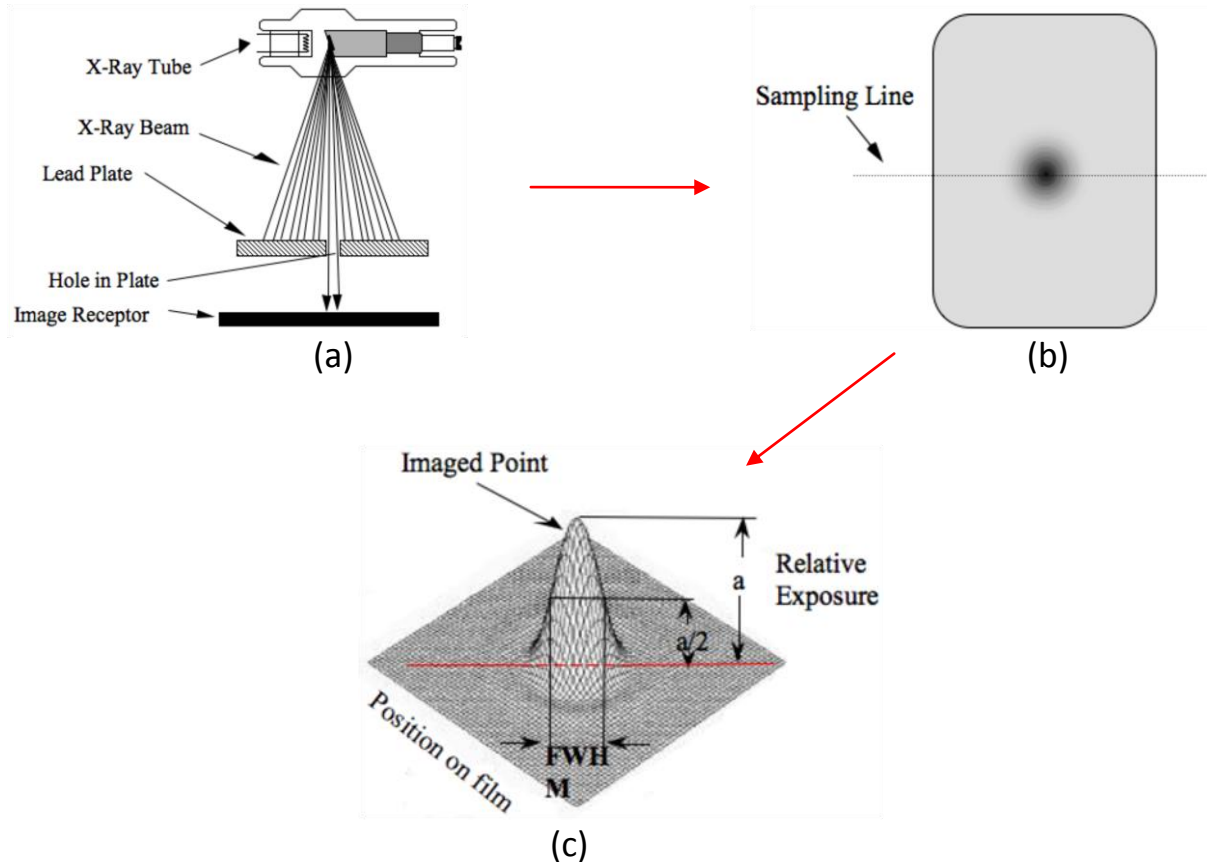


Figure 2.31: Spatial resolution measurement. a) imaging of a point; b) recording the optical density across the sample line; c) PSF calculated by converting the optical density to relative exposure as a function of position [Hasegawa 1987].

2.5.2.2 Detective Quantum Efficiency (DQE)

The DQE gives the ratio of the desired signal to the background noise.

$$DQE = \frac{SNR_{out}^2}{SNR_{in}^2} \approx \eta_{abs} \left[1 + \frac{1 + (1/\eta_{v/e})}{\eta_{coll}(E_x/E_v)\eta_{x/v}} \right]^{-1} \quad \text{eq. 2-43}$$

Where SNR_{out} and SNR_{in} are output and input signal-to-noise ratios respectively, η_{abs} is the scintillator absorption efficiency of X-rays, $\eta_{v/e}$ is the CCD quantum efficiency, E_x is the X-ray energy, E_v is the photon energy of the visible light, $\eta_{x/v}$ is the energy conversion efficiency of X-rays to visible light photons and η_{coll} is the collection efficiency of light by an objective.

The η_{coll} is given by

$$\eta_{coll} = \frac{(NA/n)^2}{4} \quad \text{eq. 2-44}$$

Where NA is the numerical aperture and n the scintillator refractive index.

$$\eta_{abs} \propto \frac{Z^4}{E_x^3} \rho_{scint} \quad \text{eq. 2-45}$$

Where Z is the effective atomic number and ρ the density of the scintillator.

2.5.2.3 Image Contrast

Image contrast is a measure of the difference between an image and its environment and is measured as shown in Figure 2.32. If a small plastic disk is radiographed, the X-ray flux (photons/area) is higher outside of the plastic disk than it is beneath it [Hasegawa 1987]. If the transmitted light intensity for the background is X_1 and that for the disk is X_2 , then the contrast C of the disk is related to the background as follows

$$C = \frac{X_2 - X_1}{X_1} \quad \text{eq. 2-46}$$

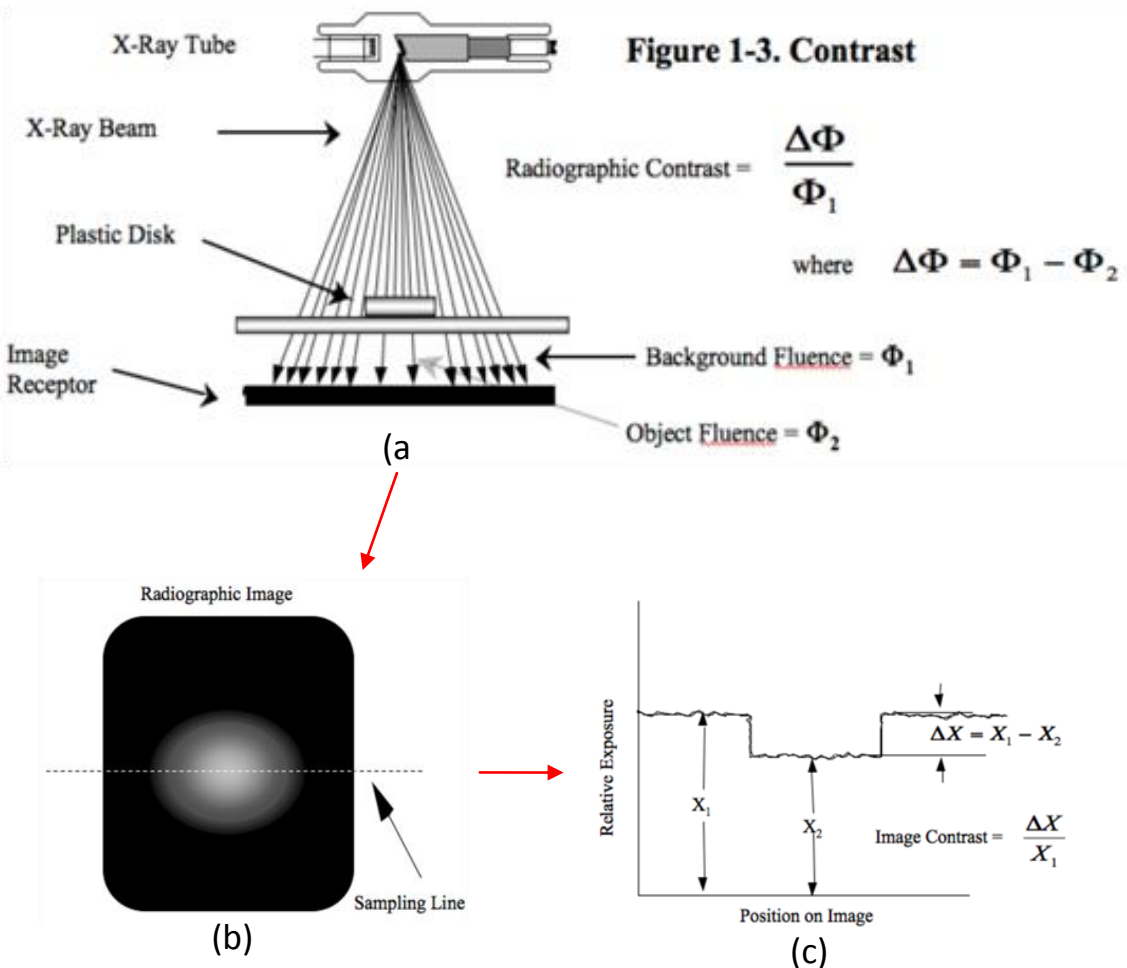


Figure 2.32: Image contrast [Hasegawa 1987].

2.5.3 X-Ray Tomography (Absorption Contrast and Phase Contrast)

In this work, the first ever X-ray tomography employing SrI₂ – thin screens were carried out. There are two different modalities for the formation of the transmission image: the absorption contrast and the phase contrast.

Treating X-rays as waves accounts for the attenuation and phase shifts when X-rays interact with materials. These changes are described by the materials complex refractive index

$$n = 1 - \delta + i\beta \quad \text{eq. 2-47}$$

δ is the refractive index decrement (real part). The wavelength of the scattered waves is the same as the incident wave, but with a wave shift of $\frac{\pi}{2}$ and reduced amplitude. β is the absorption coefficient (imaginary part) and corresponds to scattering at a phase difference of π compared to the incident wave. For materials with a weak absorption and at the diagnostic X-ray energy range (15 – 25 keV), δ is (the order of 10^{-7}) significantly greater than β (about 10^{-10}) [Zhou 2012].

How the refraction index affects the behaviour (phase shift and attenuation) of a wave traversing an object can be demonstrated in the wave propagation direction. If a monochromatic plane wave is assumed and the direction of travel is z , the wave at the exit surface of the object is given as

$$\psi(z) = e^{ikn\Delta z} = e^{i\frac{2\pi}{\lambda}n\Delta z} = e^{i\frac{2\pi}{\lambda}\Delta z} \cdot \underbrace{e^{-i\frac{2\pi}{\lambda}\delta\Delta z}}_{\text{phase shift}} \cdot \underbrace{e^{-\frac{2\pi}{\lambda}\beta\Delta z}}_{\text{attenuation}} \quad \text{eq. 2-48}$$

ψ is the incoming wave.

In general terms, the phase shift and amplitude of a wave propagating a distance z is calculated using the integrals

$$\text{Amplitude } A(x, y) = e^{-\frac{2\pi}{\lambda} \int \beta(x, y, z) dz} \quad \text{eq. 2-49}$$

$$\text{Phase } \varphi(x, y) = \varphi_0 - \frac{2\pi}{\lambda} \int \delta(x, y, z) dz \quad \text{eq. 2-50}$$

The principles of absorption contrast and phase contrast X-ray imaging are shown in Figure 2.33. The phase contrast technique has a lot of advantages over the absorption contrast technique. In the absorption contrast, the image contrast decreases with the energy. The phase contrast is used to investigate materials with weak or similar absorption, but different refractive indices. A higher spatial resolution is also achieved using the phase contrast technique.

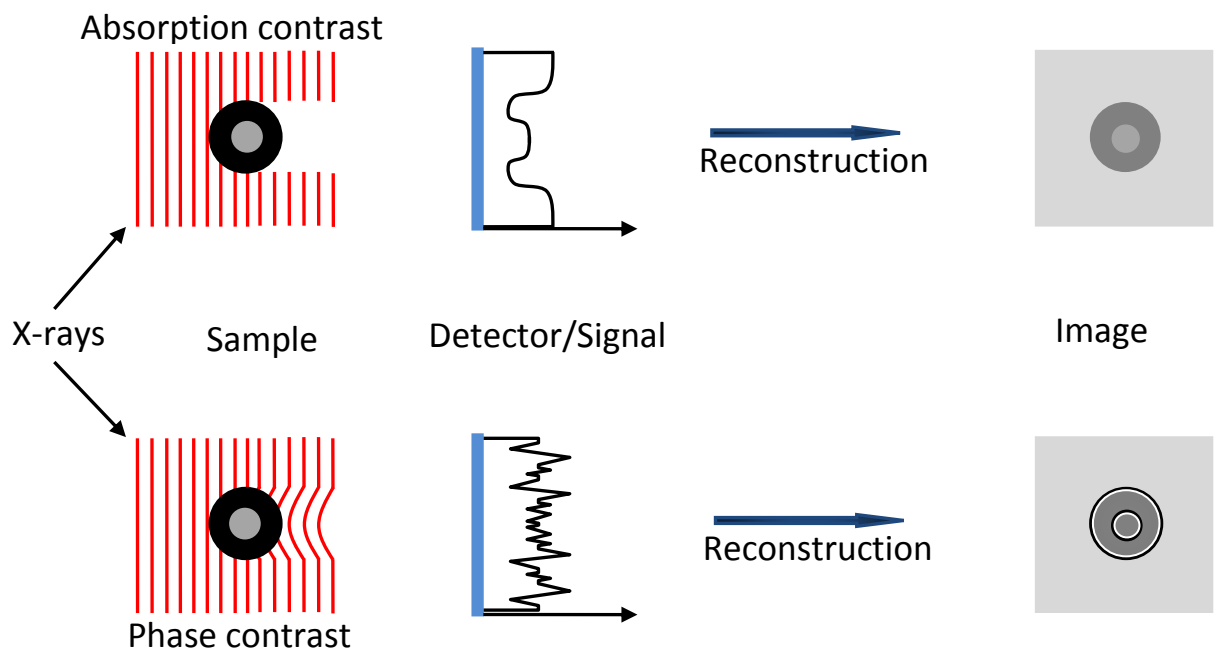


Figure 2.33: Principles of absorption contrast and phase contrast X-ray imaging.

Bibliography

[Kleber 1990]

Will Kleber: Einführung in die Kristallographie. 17., stark bearbeitete Auflage. Verlag Technik GmbH Berlin 1990.

[Alonso-Finn 1968]

Marcelo Alonso, Edward J. Finn: Quantum and statistical physics. Vol III. Addison-Wesley Publishing company. 1968.

[Leo 1994]

William R. Leo: Techniques for Nuclear and Particle Physics Experiments (A How-to Approach). 2nd Edition. Springer-Verlag Berlin Heidelberg 1994.

[XCOM]

<http://physics.nist.gov/cgi-bin/Xcom/xcom2>. Page accessed September 11, 2012.

[Birks 1964]

J. B. Birks: The Theory and Practice of Scintillation Counting. Pergamon Press LTD. 1964.

[Milbrath 2008]

B. D. Milbrath, A. J. Peurrung, M. Bliss and W. J. Weber: Radiation detector materials (An Overview). J. Mater. Res., Vol. 23, No. 10, Oct 2008.

[Kobayashi 2003]

M. Kobayashi: Introduction to scintillators. National Laboratory for High Energy Physics (KEK) Japan. November 17. 2003.

[Rodnyi 1997]

Piotr A. Rodnyi: Physical process in inorganic scintillators.CRC Press LLC. 1997.

[Mikhail 2011]

Mikhail S. Alekhin, Johan T. M. de Haas, Karl W. Krämer and Pieter Dorenbos: Scintillation Properties of and Self Absorption in SrI₂:Eu²⁺. IEEE TRANSACTIONS ON NUCLEAR SCIENCE, VOL. 58, NO. 5, OCTOBER 2011.

[Eijk 2001]

Carel W. E. van Eijk: Inorganic-scintillator development. Nuclear Instruments and Methods in Physics Research A 460 (2001) 1-4.

[HAMAMATSU]

HAMAMATSU: PHOTON COUNTING (using Photomultiplier Tubes). www.hamamatsu.com. Page accessed May 9. 2011.

Theory and Scientific Background - 2

[Cherepy 2010]

Nerine Cherepy, L. Boatner, A. Burger, K. Shah, Steve Payne, Alan Janos, Austin Kuhn: Overview of Strontium Iodide Scintillator Materials. LLNL presentation April 1, 2010. (LLNL-PRES-426327).

[Lecoq 2006]

P. Lecoq, A. Annenkov, A. Gekhtin, M. Korzhik, C. Pedrini: Inorganic Scintillators for Detector Systems (Physical Principles and Crystal Engineering). Springer-Verlag Berlin Heidelberg 2006.

[Weber 2004]

M. J. Weber: (Scintillation: mechanisms and new crystals). Nuclear Instruments and Methods in Physics Research A 527 (2004) 9-14.

[Pédrini 2005]

C. Pédrini: Scintillation Mechanisms and Limiting Factors on Each Step of Relaxation of Electronic Excitations. Physics of the Solid State, Vol. 47, No. 8, 2005, pp. 1406-1411.

[Bizarri 2010]

G. Bizarri: (Scintillation mechanism of inorganic materials: From crystal characteristics to scintillation properties). Journal of Crystal Growth 312 (2010) 1213-1215.

[Sturm 2010]

Benjamin W. Sturm, Nerine J. Cherepy, Owen B. Drury, Peter A. Thelin, Scott E. Fisher, Stephen A. Payne, Arnold Burger, Lynn A. Boatner, Joanne O. Ramey, Kanai S. Shah, Rastgo Hawrami: Effects of packaging SrI₂ (Eu) scintillator crystals. Nucl. Instr. And Meth. A (2010).

[Seibert 2005]

J. Anthony Seibert, PhD; and John M. Boone, PhD: X-Ray Imaging Physics for Nuclear Medicine Technologists. Part 2: X-Ray Interactions and Image Formation. Journal of Nuclear Medicine Technology, Volume 33, Number 1, March 2005.

[Martin and Koch 2006]

Thierry Martin and Andreas Koch: Recent developments in X-ray imaging with micrometer spatial resolution. J. Synchrotron Rad. (2006). 13, 180-194.

[Hasegawa 1987]

Bruce Hasegawa: The physics of Medical X-Ray Imaging. Medical Physics Pub Corp; 2 edition (June 1987).

Theory and Scientific Background - 2

[NDT 2012]

<http://www.ndted.org/EducationResources/HighSchool/Radiography/xraygenerators.htm>. Page accessed September 2012.

[Shah 2010]

Kanai Shah, Jarek Glodo, Edgar van Loef, William Higgins, Rastgo Hawrami, Urmila Shirwadkar: Advances in Scintillator and Related Technologies. FRIB Equipment Workshop, Feb 20 – 22, 2010.

[Kleber 1990]

Kleber, Bautsch, Bohm: Einführung in die Kristallographie. 17. Auflage, Verlag Technik GmbH Berlin. 1990.

[Zhou 2012]

Yu Zhou, Alfred K. Louis, Tie Zhou, Ming Jiang: Partial coherence theory for x-ray phase contrast imaging technique with gratings. Optics Communications 285 (2012) 4763 – 4774.

3 Material Properties of SrI₂

Chapter Overview

Abstract

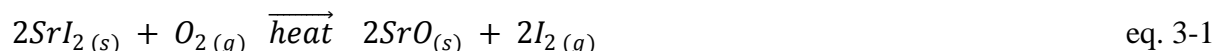
3.1 Physical and Chemical Properties	47
3.1.1 Hydration Levels and the Melting Point of SrI ₂	49
3.2 Structural Properties	51
3.2.1 Doping with Europium (Eu ²⁺)	53
Bibliography	58

Abstract

A good knowledge of the material properties of the SrI₂ is very important for its application as a scintillator. The structural, physical and chemical properties of the SrI₂ are presented in this chapter. Some of these material properties are responsible for the excellent scintillation properties, while others make every step of working with SrI₂ very challenging. An insight into the material properties of the dopant EuI₂ is provided. It was noticed that the EuI₂ shares similar structural and chemical properties with the SrI₂.

3.1 Physical and Chemical Properties

Strontium iodide (SrI₂) is an inorganic salt of the alkaline earth halide. It is colourless as crystalline and white as powder. A freshly exposed surface of the SrI₂ was noticed here to turn whitish or milky, under the sun yellowish and after a longer time pinkish due to decomposition and release of iodine gas. The hardness of this material was determined in this research work to be approximately 3 on the Mohs scale; this is based on the readiness of this material to be scratched by copper penny and a knife. This material property is important in choosing the right materials for polishing the SrI₂. The solubilities of SrI₂ in water and alcohol are 177.8 g/100 ml (20°C) and 3.1 g/100 ml (4°C) respectively [Seidell 1919]. [Singh 2008] calculated the refractive index of SrI₂ at 435 nm for a-, b- and c- crystallographic axes to be 2.05, 2.07 and 2.05 respectively. When heated in the presence of oxygen, SrI₂ decomposes to strontium-oxide according to the equation below.



In this work, SrI₂ from two producers (Alfa Aesar and Sigma-Aldrich) was characterized. The starting materials were anhydrous SrI₂, 99.99% (4N-purity: metal basis). The density of SrI₂ is given as 4.55 g/cm³ at 25 °C by the producers. This is a very important material parameter of the SrI₂ considering its application as a scintillator. A high density scintillator would absorb

Material Properties of SrI₂ - 3

the total energy of the incoming gamma quanta in a small volume. A high density combined with a high effective atomic number (Z_{eff}) is necessary for strong interactions through photoelectric effect. The bandgap of SrI₂ is 5.3 eV [Derenz 2011]. The Z_{eff} of SrI₂ is 49.4, this value is from calculations using the equation below.

$$Z_{\text{eff}} = \sqrt[2.94]{f_1 x (Z_1)^{2.94} + f_2 x (Z_2)^{2.94}} \quad \text{eq. 3-2}$$

$f_1 = 0.33$ is the fraction of Sr in SrI₂; $f_2 = 0.67$ is the fraction of I₂
 $Z_1 = 38$ is the atomic number of Sr; $Z_2 = 53$ is the atomic number of iodine

The phase diagram of SrI₂ in Figure 3.1 (created using the software Tapp V2.2 from E. S. Microware) shows a binary system that has a gap in miscibility in the liquid phase between 751 and 1056 °C. It also gives information about the different phases of the strontium (α and β), SrI₂, iodine and their compositions.

When a melt of this binary system is cooled, at 769 °C (strontium solidus temperature) pure strontium will start crystallizing and the composition of the melt will shift towards the iodine. Two modifications of the strontium are known, α -Sr exists between 0 and 527 °C while β -Sr exists between 547 and 751 °C. Both have the same chemical composition but different crystal structures [Massalski 1990] [Okamoto 2000]. The composition of the SrI₂ that is of utmost importance here has 66.7 at.% iodine and 33.3 at.% strontium. According to the phase diagram below, SrI₂ will start forming below 537 °C. The solidus temperature of iodine is 113.6 °C, below this temperature iodine crystals will be formed.

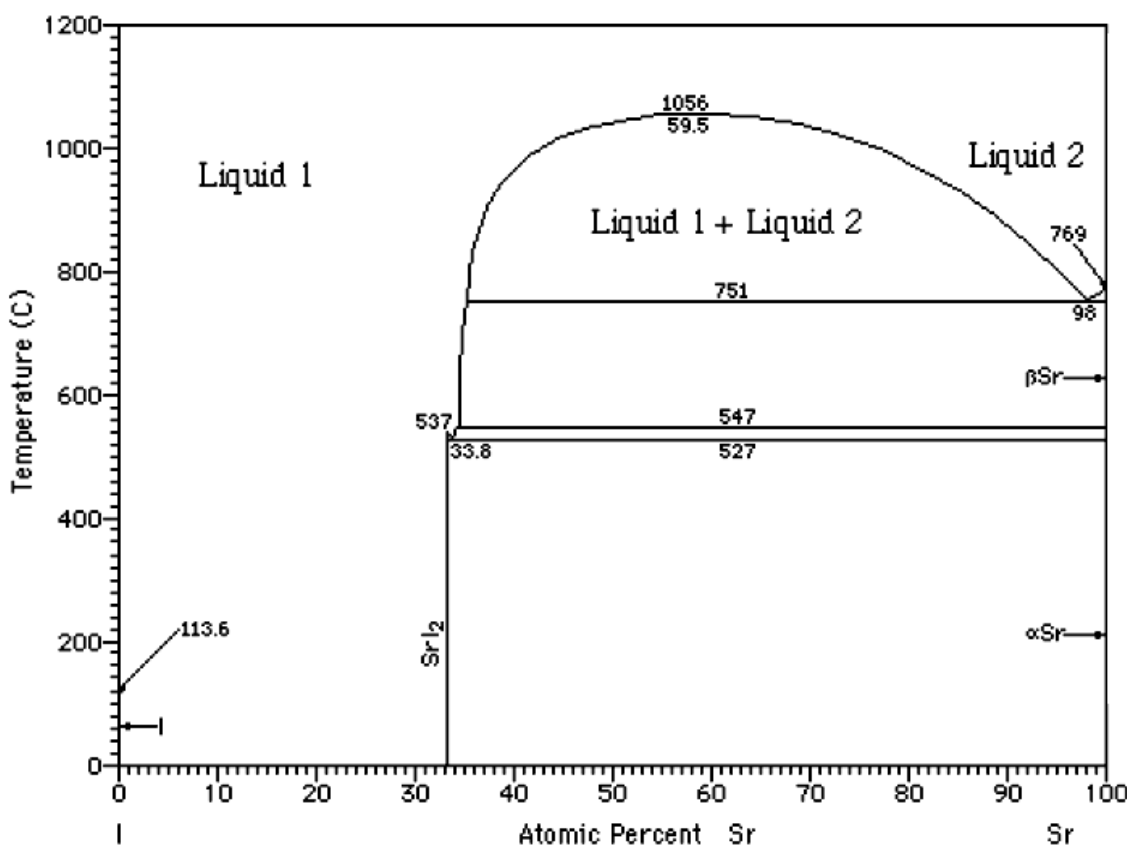


Figure 3.1: Phase diagram of SrI₂ created using the software: Tapp V2.2 (E S Microware).

The phase diagram of a material system for crystal growth is important in choosing the best growth temperatures to prevent material dissociation in the melt. Two literatures [Massalski 1990] [Okamoto 2000] summarized the I-Sr binary system phase diagram as follows, Table 3.1.

Phase	Composition at.% I	Pearson symbol	Space group	Strukturbericht designation	Prototype
β-Sr	0	<i>cI2</i>	<i>Im</i> $\bar{3}m$	A2	W
α-Sr	0	<i>cF4</i>	<i>Fm</i> $\bar{3}m$	A1	Cu
SrI ₂	66.7	<i>oP24</i>	<i>Pbca</i>
I	100	<i>oC8</i>	<i>Cmca</i>	A14	I

Table 3.1: Summary of the I-Sr binary system phase diagram [Massalski 1990] [Okamoto 2000].

3.1.1 Hydration Levels and the Melting Point of SrI₂

Here the thermogravimetric method (TG) and differential scanning calorimetry (DSC) were used to determine the melting point of the SrI₂, the level of hydration and the possible dehydration temperature of the charge materials prior to the crystal growth. See [Alaribe 2010] for more on the principles of TG and DSC.

The temperature program used for all measurements was 10 °C/minute from 20 to 600 or 700 °C. Studies have been done in the past especially by [Gere 1975] and [Gere 1978] on the thermal dehydration of SrI₂ hydrates containing 6, 2 and 1 molecules of water of crystallization. The thermal dehydration of the hexahydrate occurs between 40 and 80 °C, the dihydrate between 104 and 160 °C and the monohydrate between 280 and 370 °C depending on the experimental conditions [Gere 1975] [Gere 1978] [Cherepy 2010].

Figure 3.2 shows the result of a TG/DSC-measurement done on the first SrI₂ batch (Alfa Aesar, 99.99%-metal basis) used for crystal growth. This image shows thermal processes (blue line) accompanied by changes in weight (green line). The onset gives the temperature at the beginning of these endothermic processes that are accompanied by a decrease in weight. There are two possible explanations for the decrease in weight at these temperatures, either contained water of crystallization or volatile (impurity) components are being released. The release of contained water of crystallization at the onset-temperatures in all the TG/DSC – diagrams in this work is confirmed by the correlation of these temperatures with literature values. In Figure 3.2 there is an endothermic peak at 323.1 °C, according to [Gere 1978] the peak is related to the percentage of a hydrate containing a lower number of water molecules combined and the melting point is denoted in all diagrams with M.P.

See Figure 3.3, Figure 3.4, Figure 3.5 and Figure 3.6 for analysis done on materials from Sigma Aldrich. The melting point of SrI₂ lies between 510 and 545 °C. The melting point was found to change with the impurity concentrations which were different for different material batches.

Material Properties of SrI₂ - 3

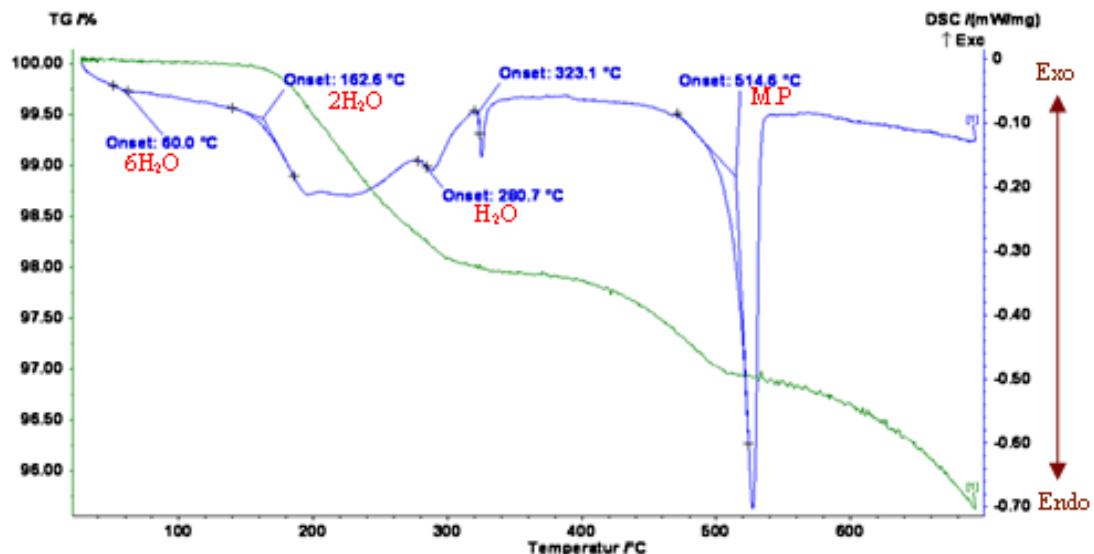


Figure 3.2: TG/DSC result of the SrI₂ - first batch (Alfa Aesar, 99.99%-metal basis).

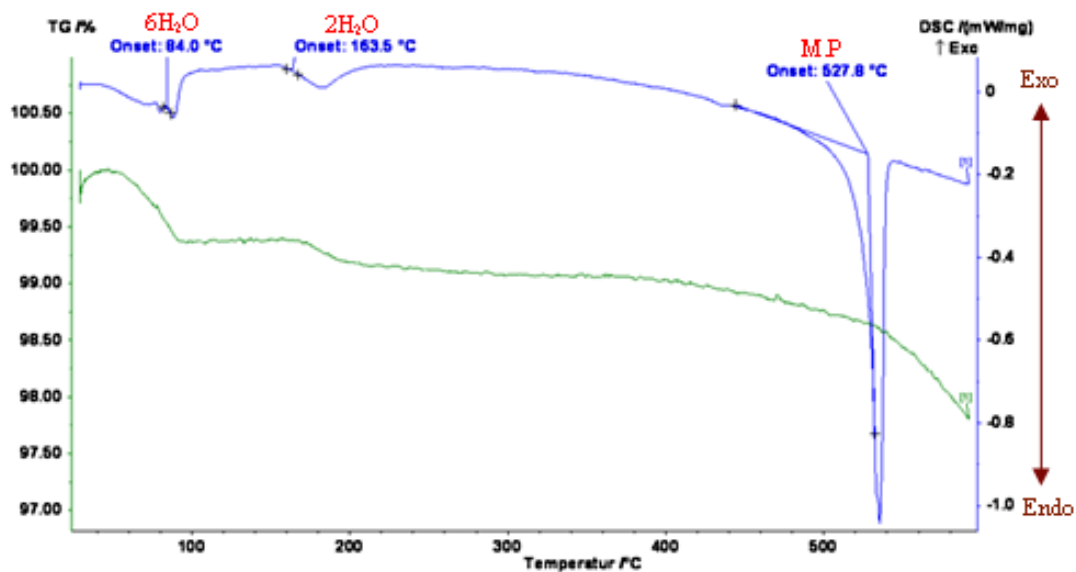


Figure 3.3: TG/DSC result of SrI₂ – second batch (Sigma Aldrich, 99.99%-metal basis)

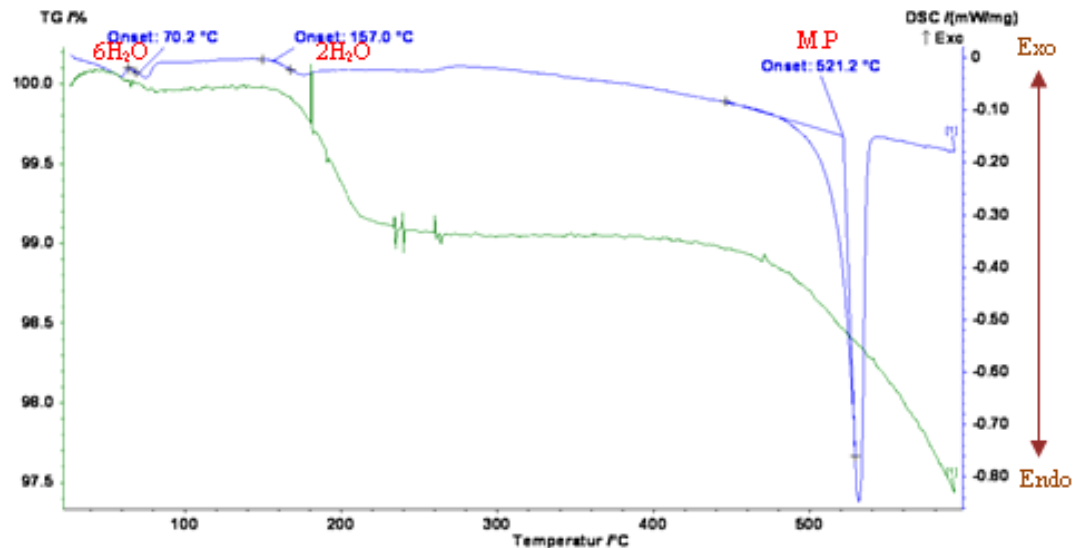


Figure 3.4: TG/DSC result of SrI₂ – third batch (Sigma Aldrich, 99.99%-metal basis)

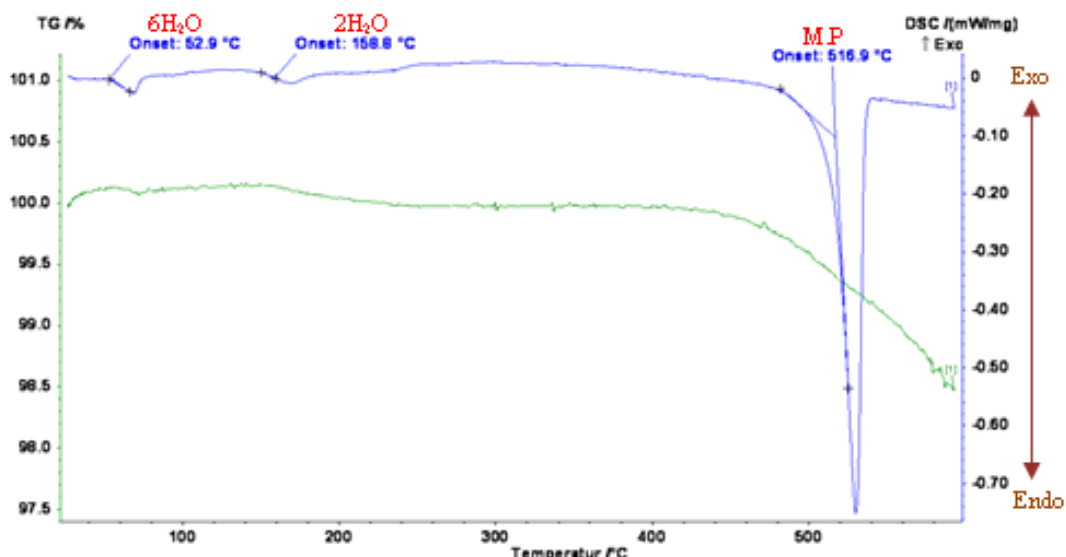


Figure 3.5: TG/DSC result of SrI₂ – fourth batch (Sigma Aldrich, 99.99%-metal basis)

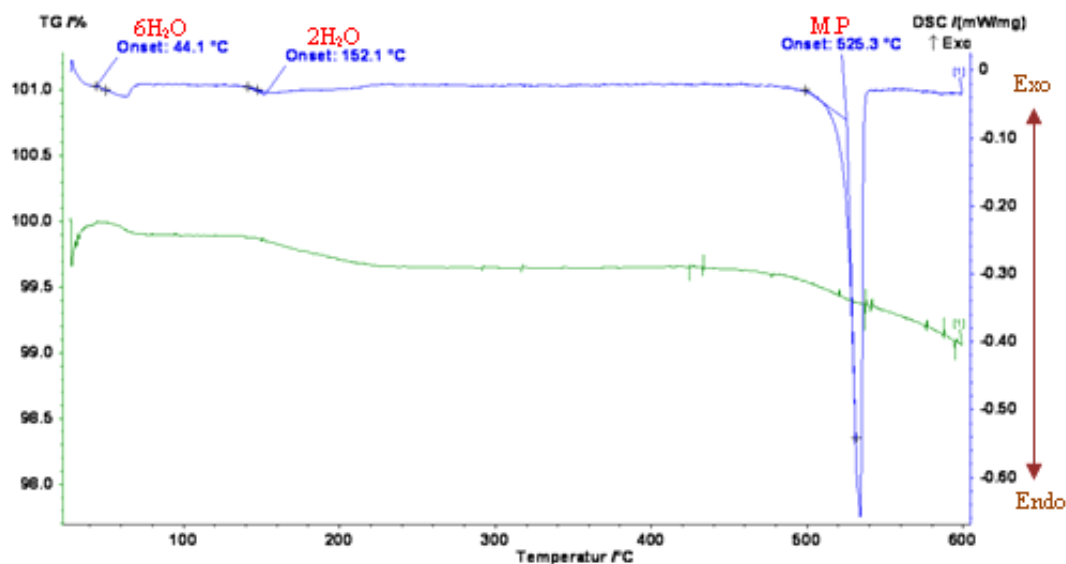


Figure 3.6: TG/DSC result of SrI₂ – fifth batch (Sigma Aldrich, 99.99%-metal basis)

3.2 Structural Properties

SrI₂ crystallizes in the orthorhombic crystal system (space group: Pbca) and the lattice constants in [Å] are: a = 15.22, b = 8.22 and c = 7.90. A SrI₂ unit cell contains a sum of 8 formula units [Bärnighausen 1967], one central strontium-ion with seven neighbouring iodine-ions. The coefficients of thermal expansion along the crystallographic axes are: a = 1.552x10⁻⁵/°C; b = 2.164x10⁻⁵/°C; c = 0.924x10⁻⁵/°C [Cherepy 2010]. This is a very important material property to consider before the crystal growth. The values presented here for SrI₂ are fairly similar. Materials with large differences in thermal expansion along the different axes would definitely have a problem with cracking due to anisotropy during the crystal growth. A look at the crystal structure of SrI₂ shows two different coordinations of the iodine ions in Figure 3.7.

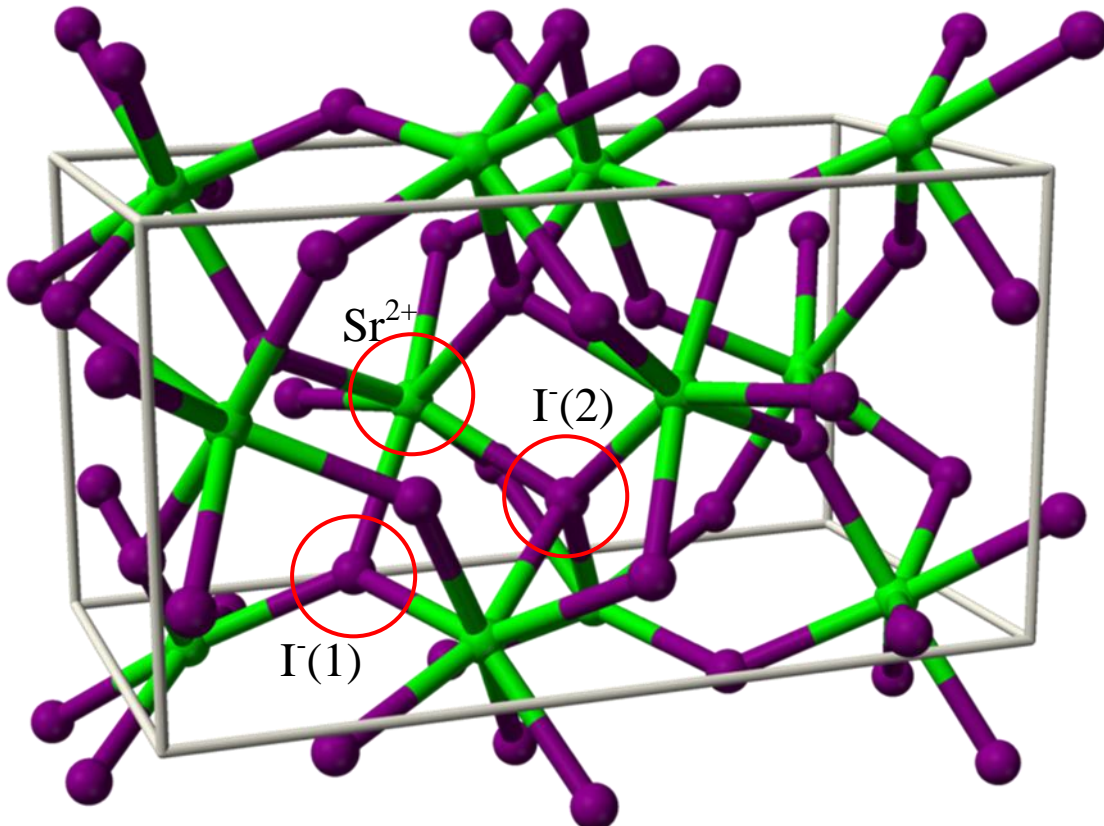


Figure 3.7: A 3D projection of the SrI₂ crystal structure, green is the Strontium-ion and violet are the Iodine-ions [Wikipedia].

The central Sr²⁺-ion has seven neighbouring I⁻-ions that are arranged in two parallel planes, in one plane they form a square and in the other plane a triangle. One of the (I⁻) Ions is coordinated with three Sr²⁺-ions in such way that it forms the peak of a flat trigonal pyramid and the second I⁻-ion is coordinated with four Sr²⁺-ions that form a distorted tetrahedron around it as shown in Figure 3.8 [Rietschel 1969].

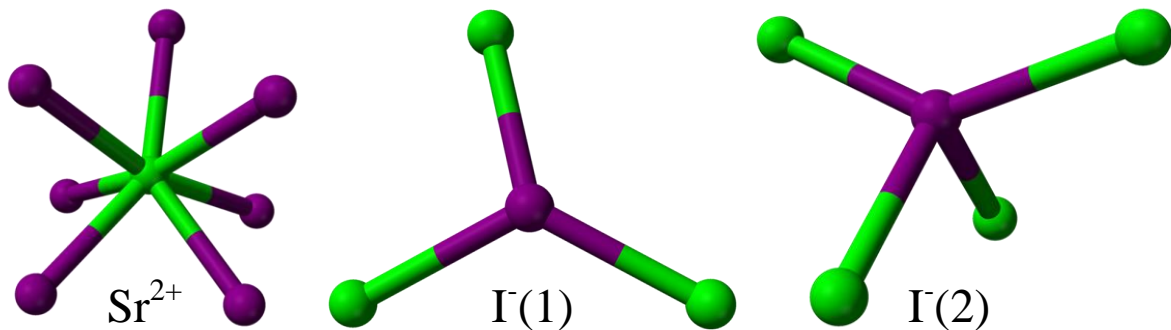


Figure 3.8: The coordination of the units making up the SrI₂ crystal structure [Wikipedia].

3.2.1 Doping with Europium (Eu²⁺)

The SrI₂-scintillators characterized here were all doped with Eu²⁺. Most scintillators are doped in order to increase the photon yield, see Figure 3.9. In pure crystal scintillators, the energy of the photon released when an electron recombines with a hole is similar to the energy required to form an electron-hole pair. When scintillators are doped, luminescence centres with emission wavelength much less than the electron – hole pair energy are produced. The host matrix will become transparent to its scintillation light due to less self-absorption.

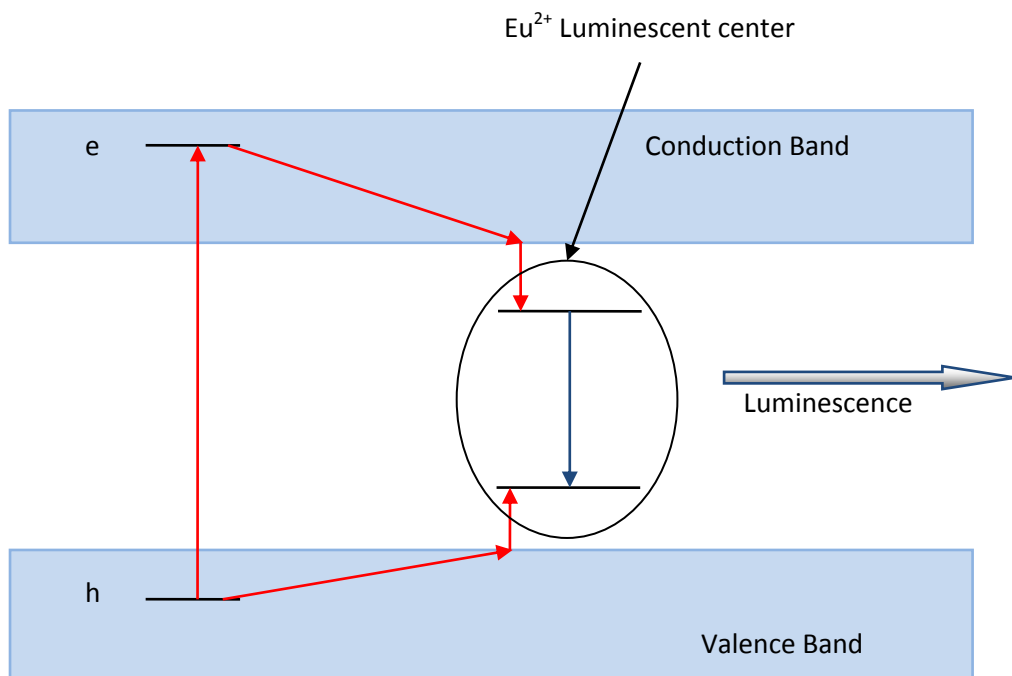


Figure 3.9: A luminescence centre in the bandgap of a scintillator.

The luminescence centres (mostly transition elements of the lanthanides) are energy levels contained within the bandgap of the host materials. There have been research works in the past and present to predict the energy level of the Eu²⁺-ion and other divalent lanthanide ions ground and excited states relative to the valence band and the conduction band of the host materials. Figure 3.10 shows the energy-level of divalent lanthanides in an ionic crystal with a bandgap of approximately 6.5 eV (ideal scenario).

The position of the 5d excited state relative to the conduction band determines the stability of an electron trapped against photo- and thermal ionization back to the conduction band and thus the quantum efficiency of the luminescence centre. The 5d excited states are influenced by crystal-field interactions and sometimes degenerated into the conduction band. The position of the luminescence centre ground and excited states relative to the valence band and the conduction band is very important in choosing the best activator ion for a given host material.

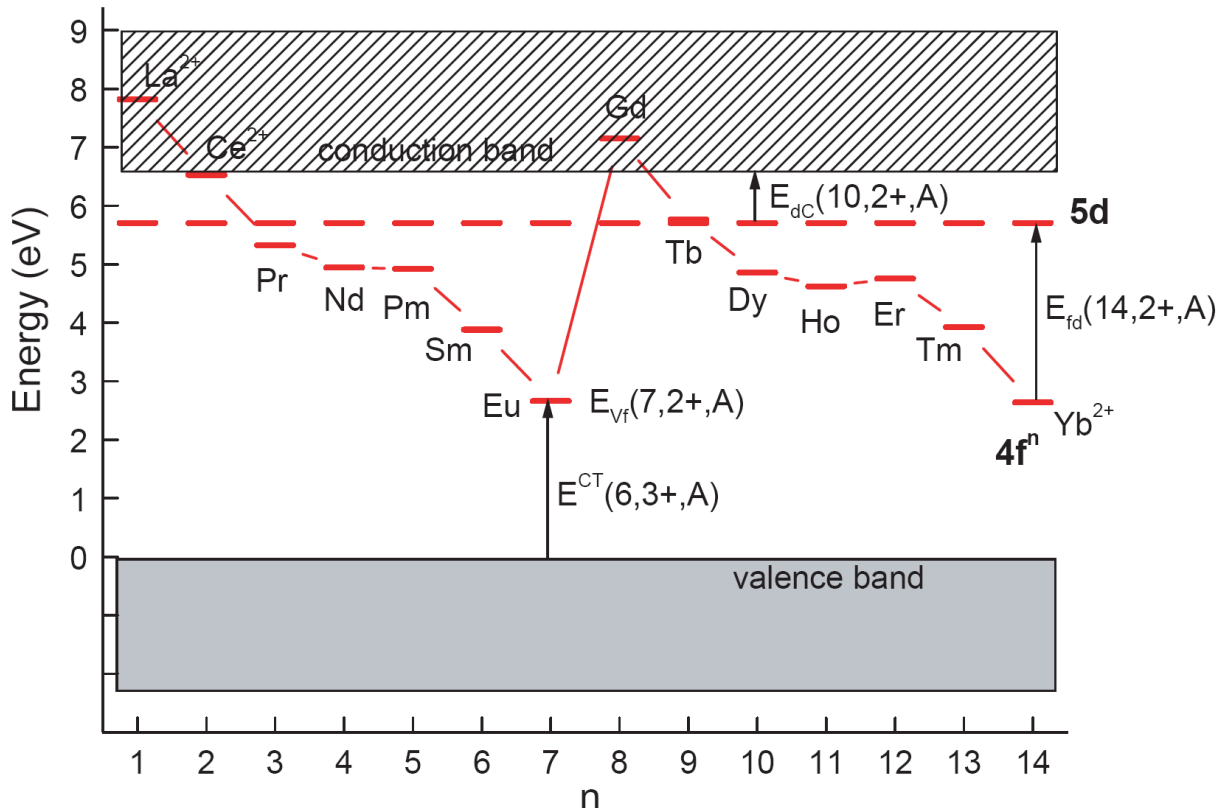


Figure 3.10: Energy-level positions of divalent lanthanides in a wide bandgap ionic crystal (ideal scenario). The first digit in bracket is the number of electrons in f-orbital, second digit the oxidation state and letter A is host material [Dorenbos 2004].

Well studied is also the emission of the Eu²⁺ in different materials. The ground state electronic configuration of Eu²⁺ is the half filled 4f-shell (4f⁷6s²) corresponding to the 4f⁷8S_{7/2} ground state. Absorption spectra of Eu²⁺ activated scintillators show the transition from the ground state to the excited state as given by the equation below

$$4f^n \rightarrow 4f^{n-1}5d \quad \text{eq. 3-3}$$

This corresponds to the electronic transitions in Eu²⁺

$$4f^7 \rightarrow 4f^65d \quad \text{eq. 3-4}$$

Emission spectra of Eu²⁺ activated scintillators or phosphors show a broad emission band from the d → f transition as given by the equation below

$$4f^{n-1}5d \rightarrow 4f^n \quad \text{eq. 3-5}$$

Corresponding to de-excitation from the excited state as shown by the equation below for the Eu²⁺

$$4f^65d \rightarrow 4f^7 \quad \text{eq. 3-6}$$

[Thomas 1992], [Blasse 1973] and [Rodnyi 1997] have also reported on parity forbidden f→f transitions in Eu²⁺ and other divalent lanthanide activated compounds leading to the emission of sharp lines corresponding to

$$4f(6P_i) \rightarrow 4f(8S_{7/2}) \quad \text{eq. 3-7}$$

With $i = 3/2, 5/2$ and $7/2$

[Thomas 1992] attributed the presence of both $5d \rightarrow 4f$ and $4f \rightarrow 4f$ transitions to the proximity of the lowest excited $5d$ and $4f^7(6P_{7/2})$ levels with the $6P_i$ level located above the $4f^65d$ in SrS as shown Figure 3.11, while [Blasse 1973] reported on the $6P_i$ level being located below the $4f^65d$ in BaAlF₆.

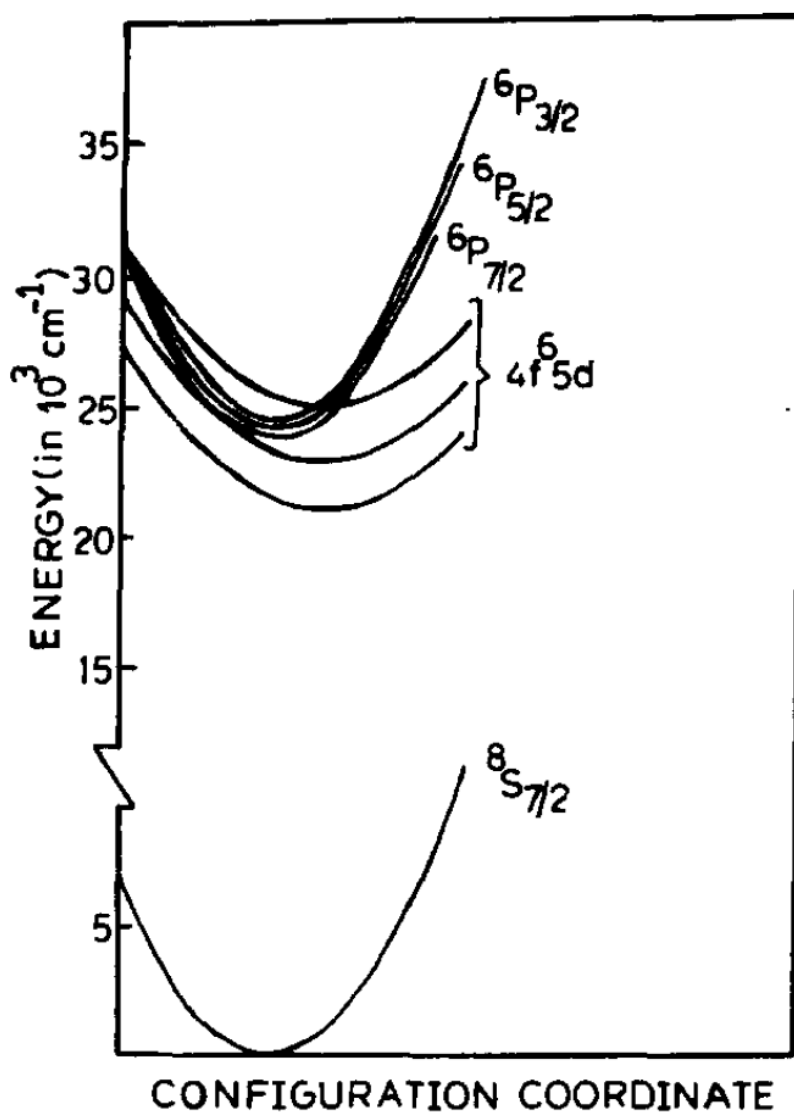


Figure 3.11: Schematic configuration coordinate diagram of Eu²⁺ [Thomas 1992].

Unlike the $4f$ electrons that are well shielded from external charge by $5s^2$ and $5p^6$ shells, there is a strong crystal field effect on the $4f^65d$ levels so that their relative positions to the

Material Properties of SrI₂ - 3

⁶P_i levels would depend on the host material. The crystal field effect normally leads to the splitting of the 5d -orbitals into two components t_{2g} and e_g [Gahane 2009].

The melting point of the EuI₂ used in this research work was also determined using the TG/DSC method as shown in Figure 3.12 to be 534.9 °C. Thermal dehydration of EuI₂ has not been studied extensively, in this work it was noticed that the EuI₂ – hydrates were evolved at temperatures similar to SrI₂ – hydrates and we attributed this to the structural similarities between the SrI₂ – and EuI₂ - materials.

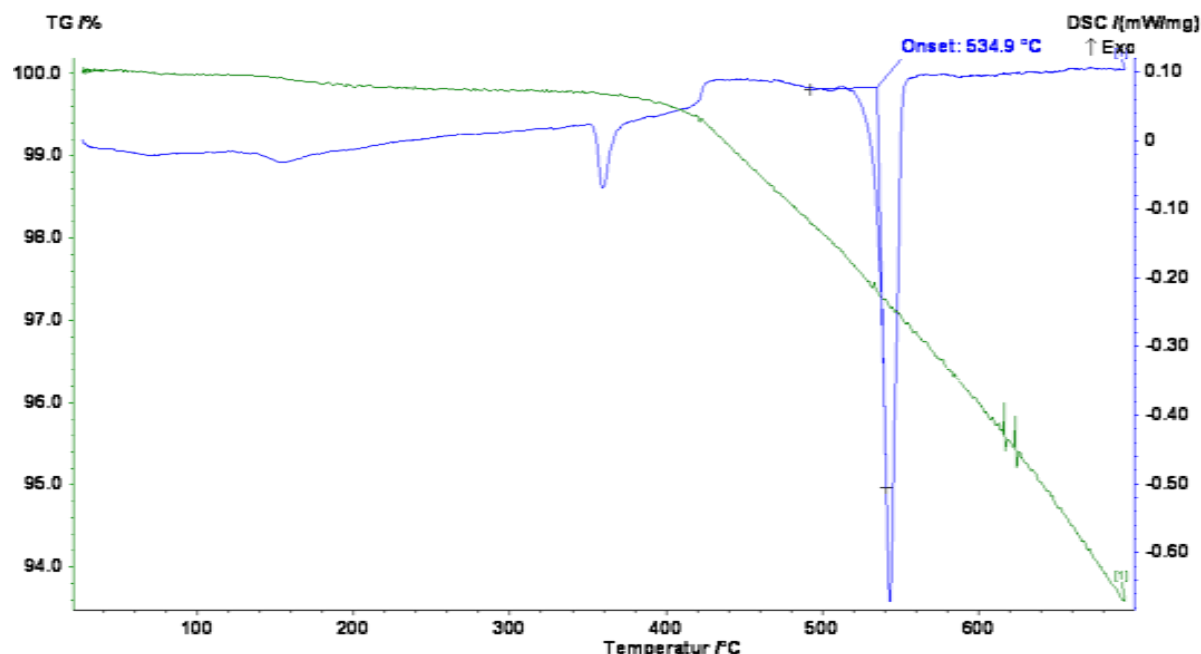


Figure 3.12: Result of the TG /DSC measurement on the EuI₂.

The EuI₂ is weighed and introduced into the ampoule prior to the crystal growth. The dopant concentrations used here were based on the work of [Glodo 2010], Figure 3.13. The SrI₂-scintillator shows strongest emission for the 5 and 6 mol% Eu²⁺ concentration.

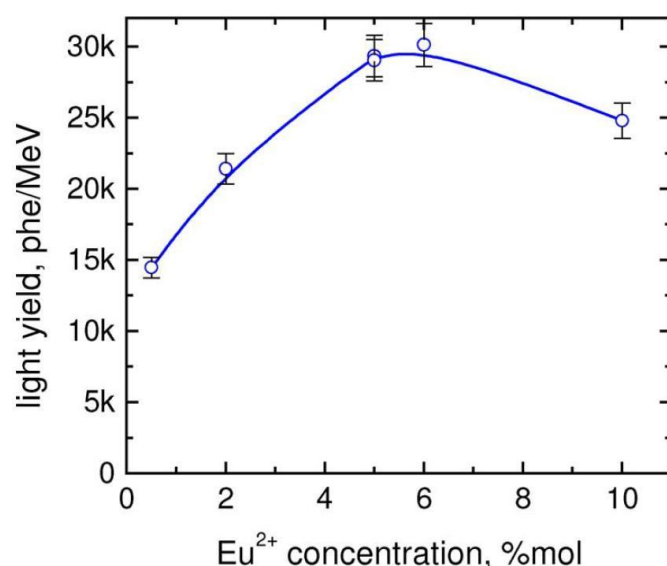


Figure 3.13: Dependence of light yield on Eu²⁺-concentration in SrI₂ [Glodo 2010].

Material Properties of SrI₂ - 3

The structural properties of SrI₂ and EuI₂ are so similar that segregation is not a problem during the crystal growth. Studies have also shown the distribution coefficient of Eu in SrI₂ to be approximately 1 [Cherepy 2010]. This is expected considering the lattice constants of EuI₂ [\AA]: a = 15.12; b = 8.18 and c = 7.83 [Bärnighausen 1969], which are similar to that of the SrI₂. This means that the Eu atoms can easily replace the Sr atoms in the crystal lattice without causing much distortion of the SrI₂ crystal lattice. The material properties of SrI₂ and EuI₂ are summarized in Table 3.2 below.

Material properties	SrI₂	EuI₂
Colour	White as powder, colourless as crystal	Brownish-white as powder
Colour (when exposed in air)	Whitish or milky (yellowish if accompanied by dissociation)	-
Colour after a long storage	Brownish	Shiny metallic black
Hardness (Moh's scale)	~ 3	-
Crystal system	Orthorhombic	Orthorhombic
Space group	Pbca	Pbca
Ionic radii (\AA)	Sr: 1.40	Eu: 1.41
Lattice constants (\AA): a	15.22	15.12
b	8.22	8.18
c	7.90	7.83
Solubility in H₂O (g/100 ml) 20°C	177.8	-
Solubility in alc. (g/100 ml) 4°C	3.1	-
Refractive index at 435 nm: a	2.05	-
b	2.07	-
c	2.05	-
Z_{eff}	49.4	-
Bandgap (eV)	5.3	-
Coeff. Of thermal expansion ($^{\circ}\text{C}^{-1}$): a	1.552×10^{-5}	-
b	2.164×10^{-5}	-
c	0.924×10^{-5}	-
Melting point (°C)	510 - 545	535

Table 3.2: Structural properties of SrI₂ and EuI₂.

Bibliography

[Seidell 1919]

Atherton Seidell, Ph.D.: Solubilities of Inorganic and Organic Compounds. Second Edition, D. Van Nostrand Company, New York (1919).

[Singh 2008]

D. J. Singh: Near optical isotropy in noncubic SrI₂: Density functional calculations. Applied Physics Letters 92, 201908 (2008).

[Derenzo 2011]

Stephen Derenzo and Gregory Bizarri: Scintillator Discovery and Development for Security and Safeguards. Oral Presentation at Scint 2011, Gießen, Germany, Sept 12-16, 2011.

[Massalski 1990]

Thaddeus B. Massalski, Hiroaki Okamoto, P.R. Subramanian, Linda Kacprzak: Binary Alloy Phase Diagrams. ASM International; Second Edition (December 1990).

[Okamoto 2000]

Hiroaki Okamoto: Desk handbook: Phase Diagrams for Binary Alloys. ASM international (2000).

[Alaribe 2010]

Leonard Alaribe: Charakterisierung von LaCl₃-Kristallen. Diplom Thesis, Albert-Ludwigs-University Freiburg (2010).

[Gere 1975]

É. BUZÁGH-GERE, J. SZTATISZ, S. GÁL: Investigation of dehydration process II. Processes preceding dehydration of alkaline earth halides. Journal of Thermal Analysis, Vol. 10 (1976) 89-98.

[Gere 1978]

É. BUZÁGH-GERE, J. SZTATISZ, S. GÁL: Investigation of dehydration process III. Thermal dehydration of strontium iodide hydrates. Journal of Thermal Analysis, Vol. 17 (1979) 501-505.

[Cherepy 2010]

Nerine Cherepy, L. Boatner, A. Burger, K. Shah, Steve Payne, Alan Janos, Austin Kuhn: Overview of Strontium Iodide Scintillator Materials. LLNL presentation April 1, 2010. (LLNL-PRES-426327).

Material Properties of SrI₂ - 3

[Bärnighausen 1967]

H. Bärnighausen and E. Th. Rietschel: Die Elementarzelle und Raumgruppe von SrI₂. Z. anorg. allg. Chem. Band 354. 1967.

[wikipedia]

http://en.wikipedia.org/wiki/Strontium_iodide. Page accessed August 27, 2012.

[Rietschel 1969]

E. Th. Rietschel and H. Bärnighausen: Die Kristallstruktur von SrI₂. Z. anorg. allg. Chem. Band 368. 1969.

[Dorenbos 2004]

P. Dorenbos: Locating lanthanide impurity levels in the forbidden band of host crystals. Journal of Luminescence 108 (2004) 301-305.

[Thomas 1992]

Thomas Baby and V. P. N. Nampoori: Fluorescence emission of SrS:Eu²⁺ Phosphor-energy splitting of Eu²⁺. Solid State Communications, Vol. 81, No. 4, pp. 367-369, 1992.

[Blasse 1973]

G. Blasse: On the Nature of the Eu²⁺ Luminescence. Phys. Stat. Sol. (b) 55, K131 (1973).

[Rodnyi 1997]

Piotr A. Rodnyi: Physical process in inorganic scintillators.CRC Press LLC. 1997.

[Gahane 2009]

D. H. Gahane, N. S. Kokode, P. L. Muthal, S. M. Dhopte, S. V. Moharil: Luminescence of Eu²⁺ in some iodides. Optical Materials 32 (2009) 18-21.

[Glodo 2010]

Jarek Glodo, Edgar V. van Loef, Nerine J. Cherepy, Stephen A. Payne, Kanai S. Shah: Concentration Effects in Eu Doped SrI₂. IEEE TRANSACTIONS ON NUCLEAR SCIENCE, VOL. 57, NO.3, JUNE 2010.

[Bärnighausen 1969]

H. Bärnighausen and N. Schultz: Die Kristallstruktur der monoklinen Form von Europium(II)-Iodid. Acta Cryst. (1969). B25, 1104.

4 Crystal Growth

Chapter Overview

Abstract

4.1	Growth Ampoules and Preparations	60
4.2	Thermal Dehydration of SrI ₂ (EuI ₂)	65
4.3	Thermodynamics and Kinetics of Nucleation and Crystal Growth	65
4.4	Bridgman/Stockbarger Crystal Growth Technique	71
	Bibliography	76

Abstract

In this work a method referred to as spontaneous crystallization or self-seeding was used due to the difficulties associated with integrating seed-crystals into the growth ampoules for the hygroscopic SrI₂. This means that the work of seed-crystal formation and the subsequent translation of the seed-crystal faces into a bulk crystal were carried out in the same ampoule. The disadvantage of this method is the inability to use a seed-crystal with known crystal orientation.

At the beginning of crystallization, millions of seed-embryos are formed, those that reach the critical radius become stable seed-crystals, but at the end only one seed-crystal is thermodynamically favoured to grow into a bulk single crystal. The ability of one seed-crystal outgrowing the rest does not depend only on the prevailing thermodynamic conditions, but also on the use of grain selectors to suppress multiple grain growth.

This chapter will discuss the thermodynamics of nucleation and crystal growth, and also other arrangements to achieve the growth of single crystals. Single crystals are prerequisites for further use as scintillators in order to avoid light scattering at the grain boundaries.

4.1 Growth Ampoules and Preparations

The growth of SrI₂-single crystals and most alkaline halide and alkaline earth halide scintillator crystals require some arrangements to prevent the hydration and oxidation of the melt during the crystal growth process. The decision to use silica ampoules for the crystal growth was based on the relatively low melting point and contraction of SrI₂ on crystallization. The ampoules were made from dry fused silica (Herasil® from Heraeus). A couple of ampoule designs (grain selectors) on first to freeze region were tested here to help subdue the growth of multiple grains (seed-crystals), Figure 4.1.

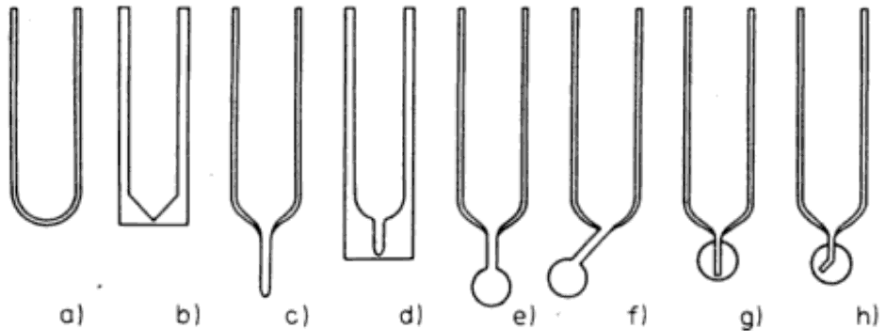


Figure 4.1: Different grain selector designs [Wilke 1973].

In this work three grain selector models were tested (c, e and f), Figure 4.2. The diameter of the capillaries varied between 3 and 5 mm and the length between 3 and 5 cm. The capillary diameter was increased from 3 to 5 mm to make sure that surface tension doesn't prevent the melt from flowing into the first to freeze region, the length was increased from 3 to 5 cm so that the first to freeze region is properly separated from the growth region to avoid the whole material crystallizing at the same time. The diameter of the crystal growth ampoules also increased from 1 to 2.54 cm (1``) which was the set target for this crystal growth research work. All the ampoules were manufactured in the glass laboratory of the crystallography department; an oxyhydrogen flame is used for the shaping and sealing work.

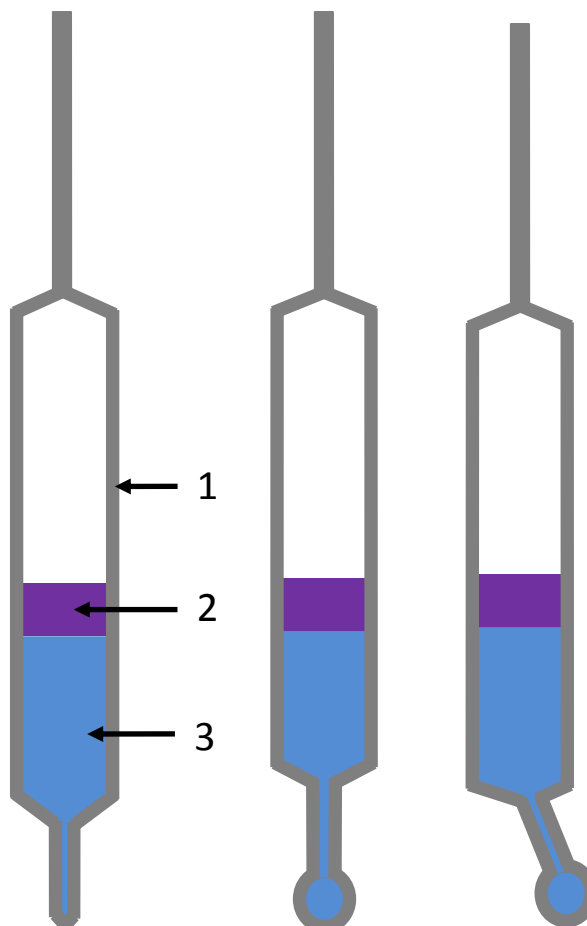


Figure 4.2: Ampoule designs (grain selectors) tested in this work: 1) Silica glass; 2) Iodine or Boron oxide; 3) SrI_2 .

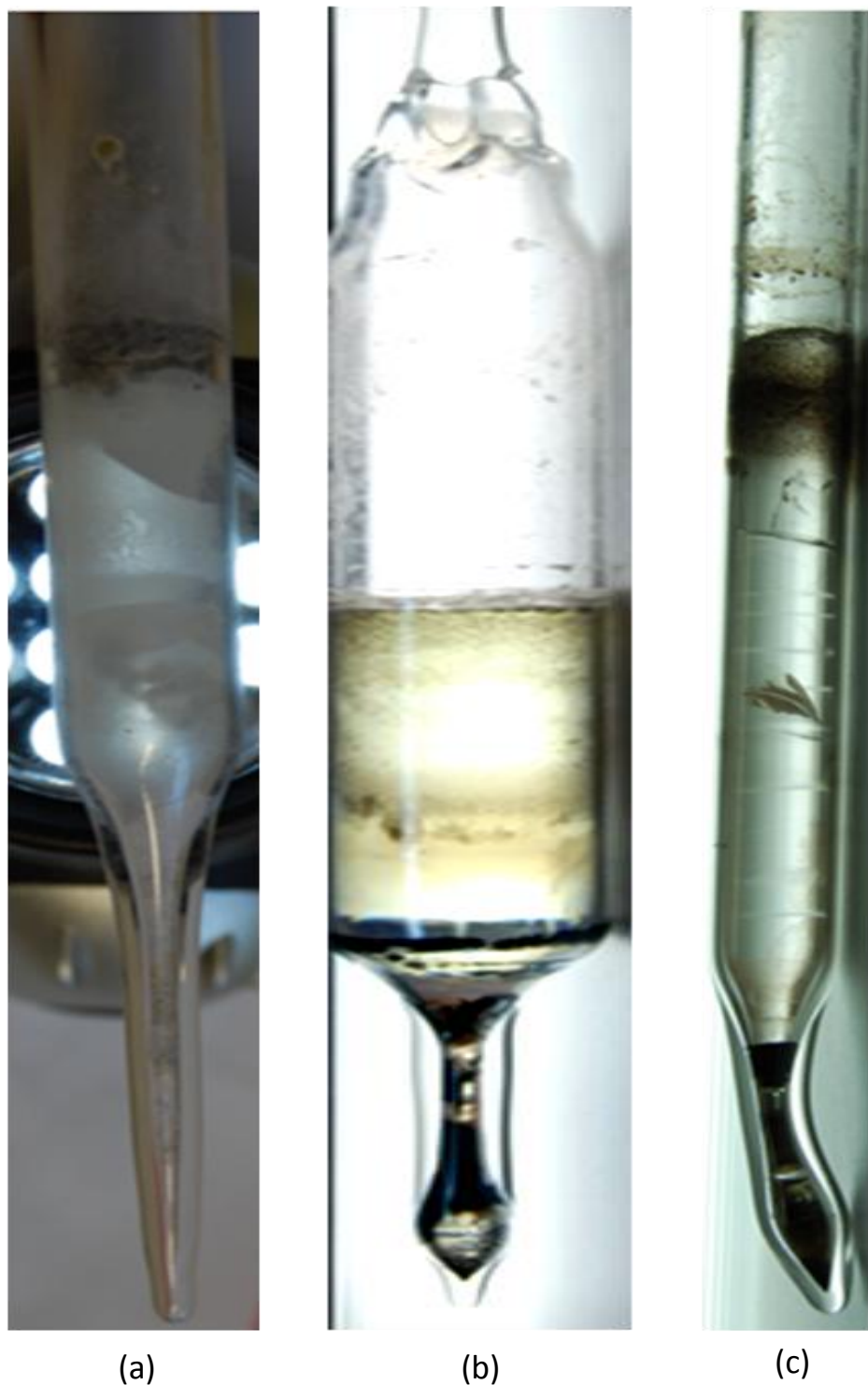


Figure 4.3: Some of the manufactured ampoules. a) 1.5 cm diameter; b) 2.54 cm (1[“]) diameter; c) 1 cm diameter. Dark colour in the grain selector region is the iodine-gas growth atmosphere.

After manufacturing, the ampoules are cleaned with acetone to remove any residual grease and impurities, and then rinsed with distilled water. Ampoules are baked at 1000°C and evacuated for a couple of hours to remove residual gases like oxygen and moisture. For transportation, empty ampoules are normally covered with a paraffin-tape to prevent oxygen diffusion.

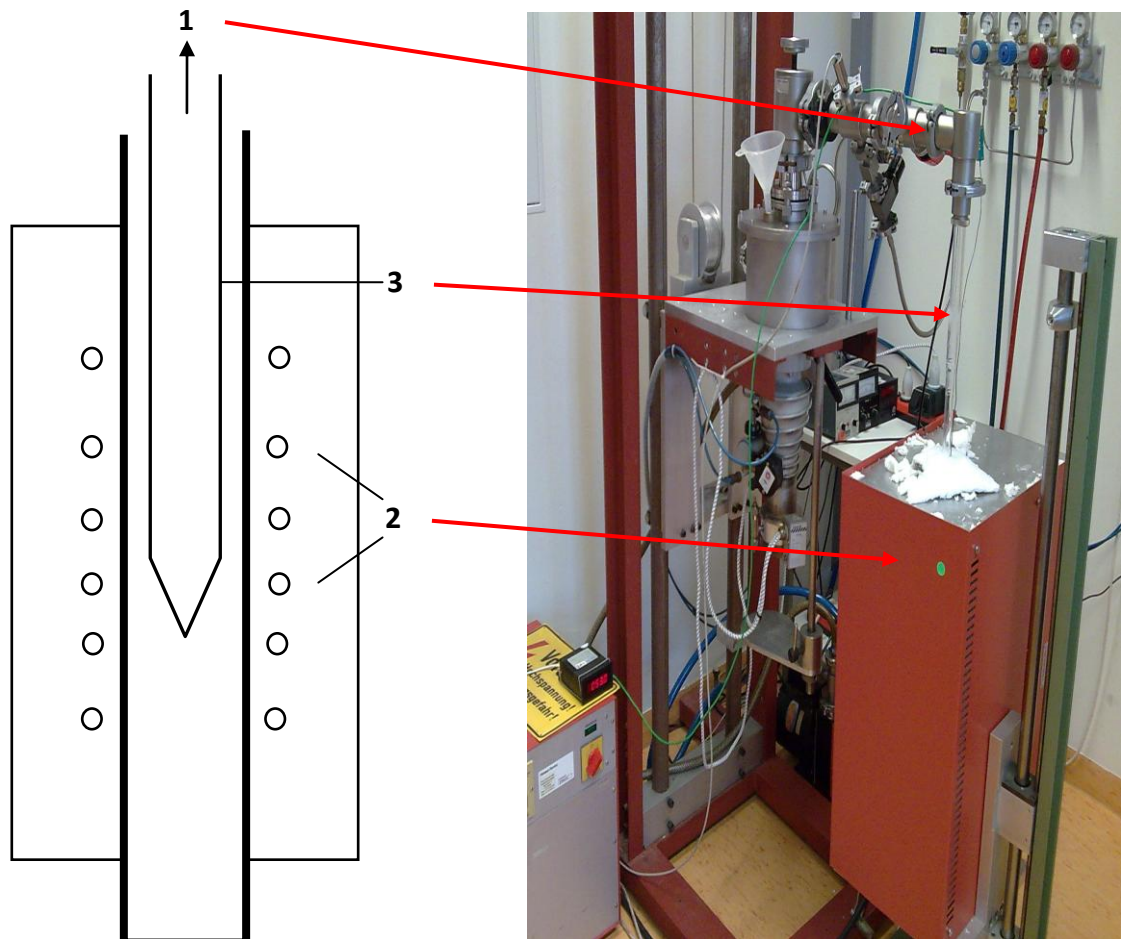


Figure 4.4: Baking and evacuation of ampoules prior to the crystal growth: 1) Vacuum-pump system; 2) Furnace and heating elements; 3) The ampoule.

The transfer of growth materials (SrI_2 and EuI_2) into the ampoule for dehydration and subsequent crystal growth, the opening of the ampoules after the crystal growth and the crystal preparation processes (saw cutting, grinding, polishing and hermetic encapsulation) are done in an argon gas purged glove box. The argon gas in the glovebox is dried by continuously circulating it through an absorber tower containing molecular sieve and copper metal, Figure 4.5. The molecular sieve absorbs moisture while copper metal reacts with oxygen to copper oxide.



The absorber tower is regenerated monthly by flushing a forming gas (95% N_2 and 5% H_2) through it and at the same time heating it at 240 °C for 8 hours to get rid of the absorbed moisture and also reduce the copper oxide to copper as follows



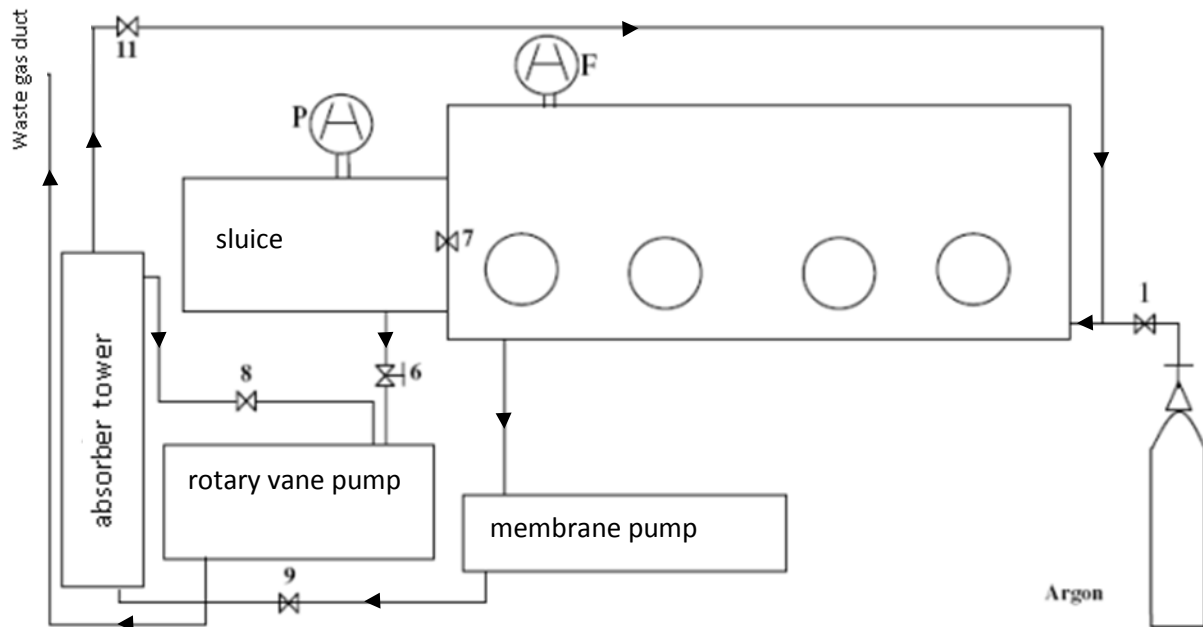


Figure 4.5: Circulation of the argon gas for drying: P is the pressure gauge; F is the moisture meter; 1 – 12 are valves.



Figure 4.6: The glovebox in the synthesis laboratory of the crystallography department, all preparation work on the SrI_2 – material/crystal is done here. The moisture content is always maintained at $< 1 \text{ ppm}$.

Ampoules are normally closed with a vacuum valve in the glovebox after loading with the crystal growth materials. This is to prevent exposure to ambient environment during the transport from the glovebox to the preparation laboratory.

4.2 Thermal Dehydration of SrI₂ (EuI₂)

Because of the hygroscopic nature of SrI₂ and EuI₂, the crystal growth materials must be physically dehydrated prior to the crystal growth. Hygroscopicity is the ability of a substance to absorb moisture from the atmosphere. SrI₂ is strongly hygroscopic; this is not a surprise considering its solubility in H₂O:177.8 g/100 ml at 20 °C. This material property is believed to be responsible for the decolouration of SrI₂ crystals in ambient environments (white to milky).

The loaded ampoule is connected to a high vacuum pump, heated at 350 °C for many hours and at the same time evacuated to ~10⁻⁶ Torr. The hydration levels of the SrI₂ and EuI₂ used in this work and the dehydration temperature were determined using the thermogravimetric method; see chapter 3.1.1. Ampoules are sealed off at the high vacuum pump when the vacuum stabilizes at 10⁻⁶ Torr and then attached to a glass rod for the crystal growth.

4.3 Thermodynamics and Kinetics of Nucleation and Crystal Growth

Crystal growth is a process of repeatedly arranging the same atoms, ions or molecules into a three dimensional body known as a crystal.

A solid -, liquid - or vapour phase is transformed by this process into a solid state. Solid – solid phase transformations are mostly used for post-growth annealing processes and vapour – solid phase transformations in epitaxial layer growth processes. Liquid – solid phase transformations are used mainly to grow bulk crystals from solutions or melts.

Liquid and solid phases are said to be in thermodynamic equilibrium, when the free energies of both phases are equal and no growth can occur.

$$G_{\text{liquid}} = G_{\text{solid}} \quad \text{eq. 4-3}$$

For a crystal growth, the thermodynamic equilibrium has to be disturbed by intentionally changing either the concentration, saturation or the temperature [Dhanaraj 2010]. This would result in a change in the free energy of the system given by the Gibbs equation

$$G = H - TS \quad \text{eq. 4-4}$$

H is the enthalpy; *S* is the entropy and *T* the temperature.

So the driving force for crystallization especially in a self-seeding crystal growth process as used in this work comes from lowering the free energy of the system to form unit volumes of seed-embryos according to the equation below

$$\Delta G_V = \Delta H_V - T\Delta S_V \quad \text{eq. 4-5}$$

Where: $\Delta H_V = H_{solid} - H_{liquid}$; $\Delta S_V = S_{solid} - S_{liquid}$

ΔG_V is the Gibbs free energy, ΔH_V enthalpy and ΔS_V entropy per unit volume of seed-embryo formed.

At equilibrium T_e

$$\Delta G_V = \Delta H_V - T_e \Delta S_V = 0 \quad \text{eq. 4-6}$$

Meaning

$$\Delta H_V = T_e \Delta S_V \quad \text{eq. 4-7}$$

Solving for ΔS_V

$$\Delta S_V = \frac{\Delta H_V}{T_e} \quad \text{eq. 4-8}$$

Gibbs free energy at a temperature T lower than the melting temperature T_m can be calculated as follows

$$\Delta G_V = \Delta H_V - T \frac{\Delta H_V}{T_m} \quad \text{eq. 4-9}$$

Simplifying eq. 4-9 gives

$$\Delta G_V = \frac{\Delta H_V \Delta T}{T_m} \quad \text{eq. 4-10}$$

$$\Delta T = T_m - T$$

At crystallization, energy is released in the form of “heat of crystallization” as the crystal building units (atoms, ions or molecules) move closer and the entropy decreases too due to higher ordering of the units in a crystal.

Crystallization can be divided into two stages, the nucleation and the growth of a nucleus into a single crystal.

Nucleation is the accumulation of atoms, ions or molecules to form the first sub-microscopic nuclei (seed - embryos). Seed-embryos are formed due to fluctuations in the supersaturation of the melt caused by supercooling. According to [Goodman 1978], the probability that a seed-embryo will grow to form a stable nucleus depends on the change in free energy associated with its formation. The change in free energy associated with the formation of a spherical seed-embryo of radius r for a homogeneous system is given by

$$\Delta G = -\frac{4}{3}\pi r^3 \Delta G_V + 4\pi r^2 \sigma \quad \text{eq. 4-11}$$

σ = is the interfacial (surface) energy per unit area

This means that the energy of a system would decrease by ΔG_V and increase by σ for each unit volume seed-embryo formed. Thermodynamically, the seed-embryos are not stable and would re-dissociate as long as their radius is less than the critical radius (r^*). Critical radius is the minimum size seed-embryos must reach to become stable and is obtained by differentiating equation 4-11 with respect to r .

$$r^* = \frac{2\sigma}{\Delta G_V} \quad \text{eq. 4-12}$$

The free energy change ΔG^* at the critical radius can be calculated by substituting r in the equation 4-11 as follows

$$\Delta G^* = \frac{16\pi\sigma^3}{3(\Delta G_V)^2} \quad \text{eq. 4-13}$$

Substituting for ΔG_V in equations 4-12 and 4-13 would give

$$r^* = \left(\frac{2\sigma T}{\Delta H_V} \right) \frac{1}{\Delta T} \quad \text{eq. 4-14}$$

And

$$\Delta G^* = \left(\frac{16\pi\sigma^3 T^2}{3(\Delta H_V)^2} \right) \frac{1}{(\Delta T)^2} \quad \text{eq. 4-15}$$

Figure 4.7 shows the free energy of a system as a function of the seed-embryo radius

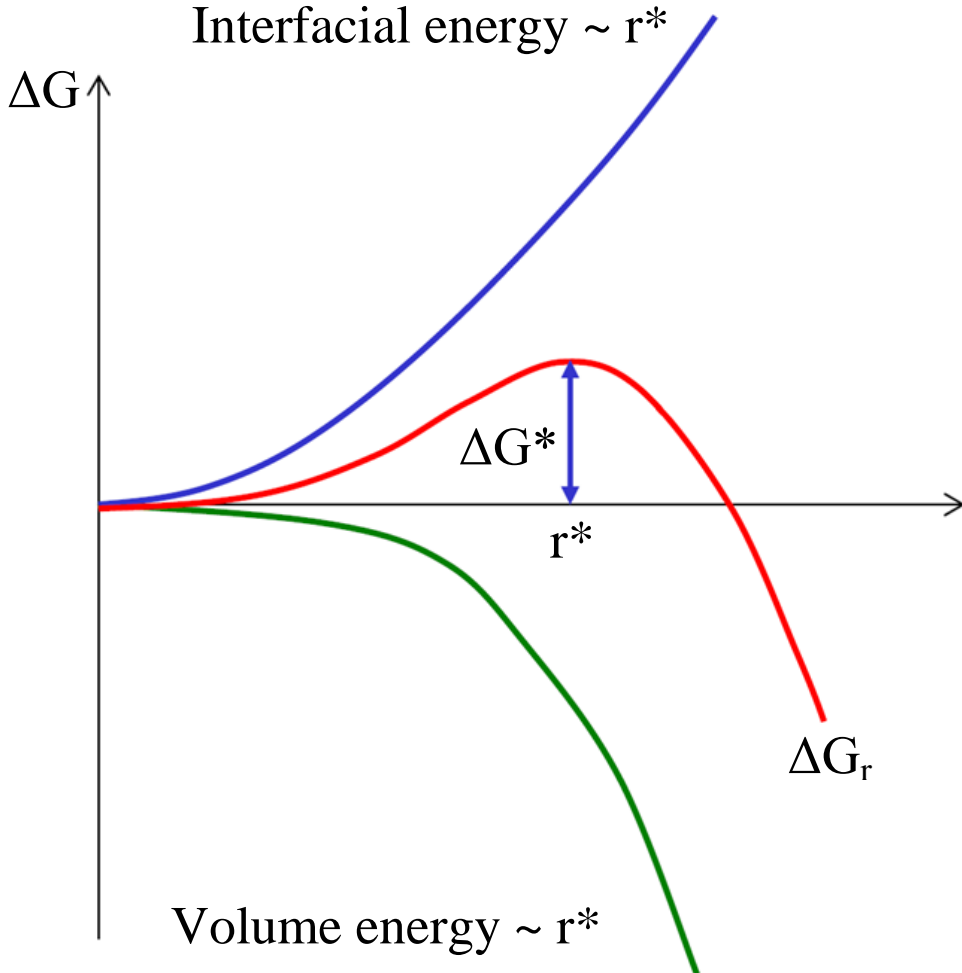


Figure 4.7: Dependence of the free (Gibbs) energy on the seed-embryo radius.

The rate of homogeneous nucleation for a given supercooling can be calculated using the Arrhenius equation as follows

$$\dot{N} = f_0 N_0 \exp\left(-\frac{\Delta G^*}{kT}\right) \text{ nuclei per m}^3 \text{ per s} \quad \text{eq. 4-16}$$

\dot{N} is the number of seed-embryos that have reached a critical size, N_0 is the number of atoms per unit volume, f_0 is the frequency of forming seed-embryos with critical radius, K is the Boltzmann constant.

Substituting for ΔG^* in equation 4-16 would give

$$\dot{N} = f_0 N_0 \exp\left(-\frac{16\pi\sigma^3 T^2}{3kT(\Delta H_V)^2(\Delta T)^2}\right) \text{ nuclei per m}^3 \text{ per s} \quad \text{eq. 4-17}$$

Figure 4.8 shows a strong dependence of the nucleation rate on the temperature. There are no nuclei until the critical temperature is reached which is then followed by an explosive nucleation. The free energy released by this process is proportional to the supercooling below the melting temperature [Imai and Oaki 2010].

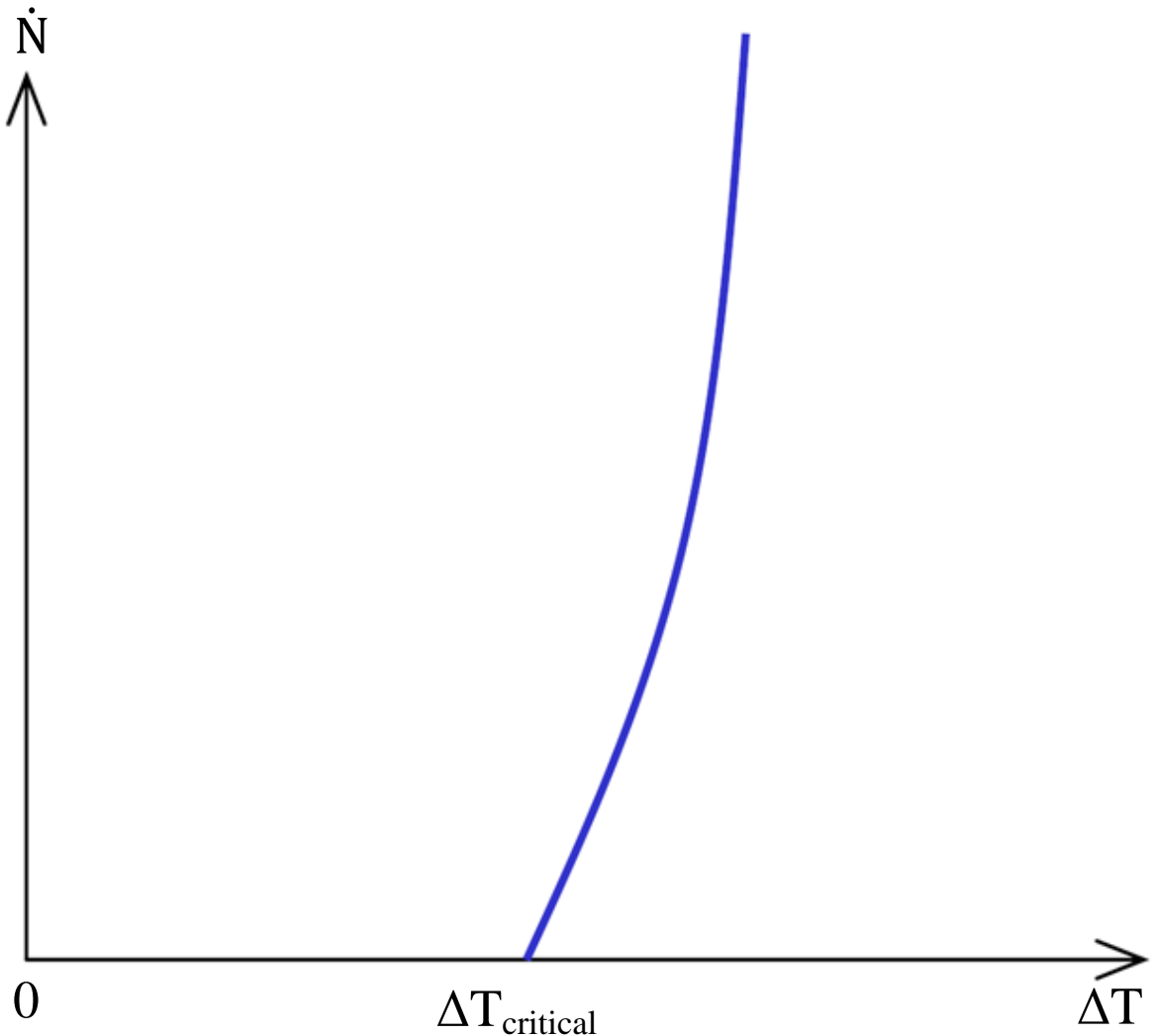


Figure 4.8: Dependence of the nucleation rate on temperature.

The growth of a nucleus into a single crystal can be explained using crystal growth theories that give insight into the mechanism and kinetics of growth. The important crystal growth theories are the surface energy theory, diffusion theory, adsorption layer theory and screw dislocation theory [Dhanaraj 2010] [Goodman 1978].

The surface energy theory is based on the thermodynamic treatment of equilibrium states put forward by Gibbs where the growing surface is assumed to take the shape with the minimum surface energy [Gibbs 1928]. This idea was applied by many researchers like [Curie 1885] to calculate the shapes and morphologies of crystals in equilibrium with a solution or vapour. [Wulff 1901] deduced correlations of growth rate of different faces and the corresponding surface free energies. [Marc 1911] stated that different faces have different solubilities; when the difference in solubility is small, growth is mainly influenced by surface energy and the change in one form takes place at the expense of the other. [Bravais 1866] suggested that the velocities of the growth of the different crystal faces depend on the reticular density.

The diffusion theories were proposed by [Noyes 1897] and [Nernst 1904] based on the following assumptions:

1. There exists a concentration gradient in the vicinity of a growing surface.
2. Crystal growth is the reverse process of dissolution.

They gave the amount of solute that will be deposited over the surface of a growing crystal in a supersaturated solution as

$$\frac{dm}{dt} = \left(\frac{D}{\delta}\right) A (c - c_0) \quad \text{eq. 4-18}$$

Where dm is the mass of solute deposited in a time interval dt over the crystal surface area A . D is the diffusion coefficient of the solute, c and c_0 are the actual and equilibrium concentrations of the solute and δ the thickness of the stagnant layer adjacent to the growing crystal surface.

The adsorption layer theory suggested the existence of terrace, ledge and kink sites on the surface of a growing crystal; a growth unit on reaching a crystal surface is not integrated immediately into the lattice, but becomes adsorbed and migrate over the surface until it is incorporated at a kink site [Stranski 1928]. According to [Nesse 2000], adding the growth units at the terrace and ledge sites would be difficult because they have many unsatisfied chemical bonds, on the other hand adding a growth unit at the kink site is easier because more chemical bonds are satisfied. The adsorption layer theory is demonstrated in Figure 4.9.

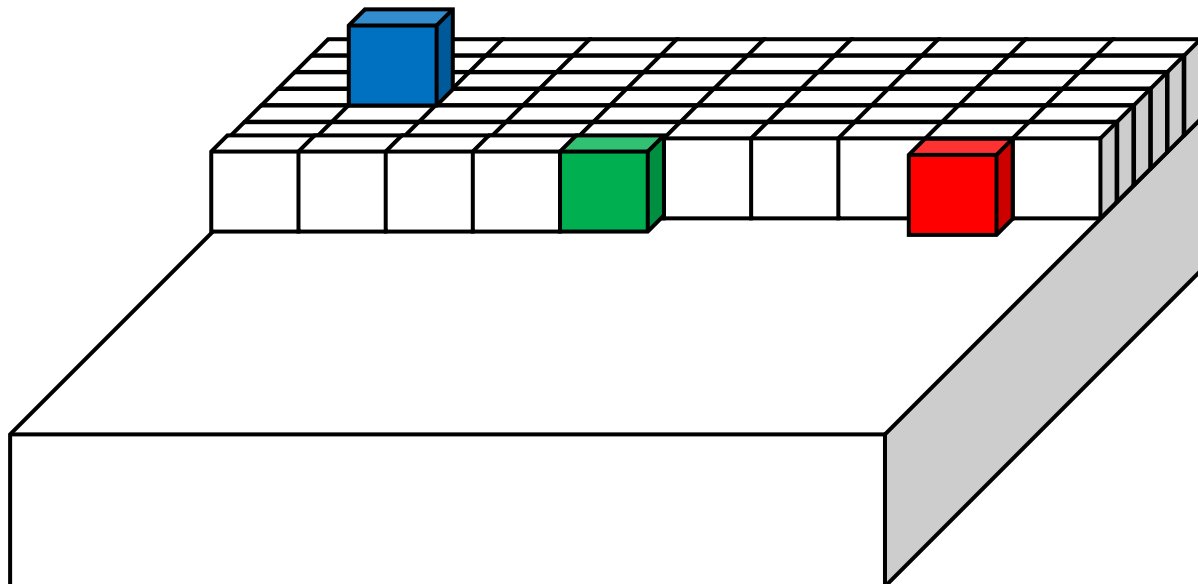


Figure 4.9: The adsorption layer theory of crystal growth.
(Blue and red are growth units at terrace site and ledge site respectively. Green is a growth unit at a kink site).

The screw dislocation theory by [Frank 1949] proposed that a screw dislocation at any point on the surface of the crystal could act as a continuous source of steps for the crystal growth. This means that crystal growth is through the rotation of the steps around the dislocation point as demonstrated in Figure 4.10. Growth on a screw dislocation ensures that an edge always remains available for growth [Nesse 2000].

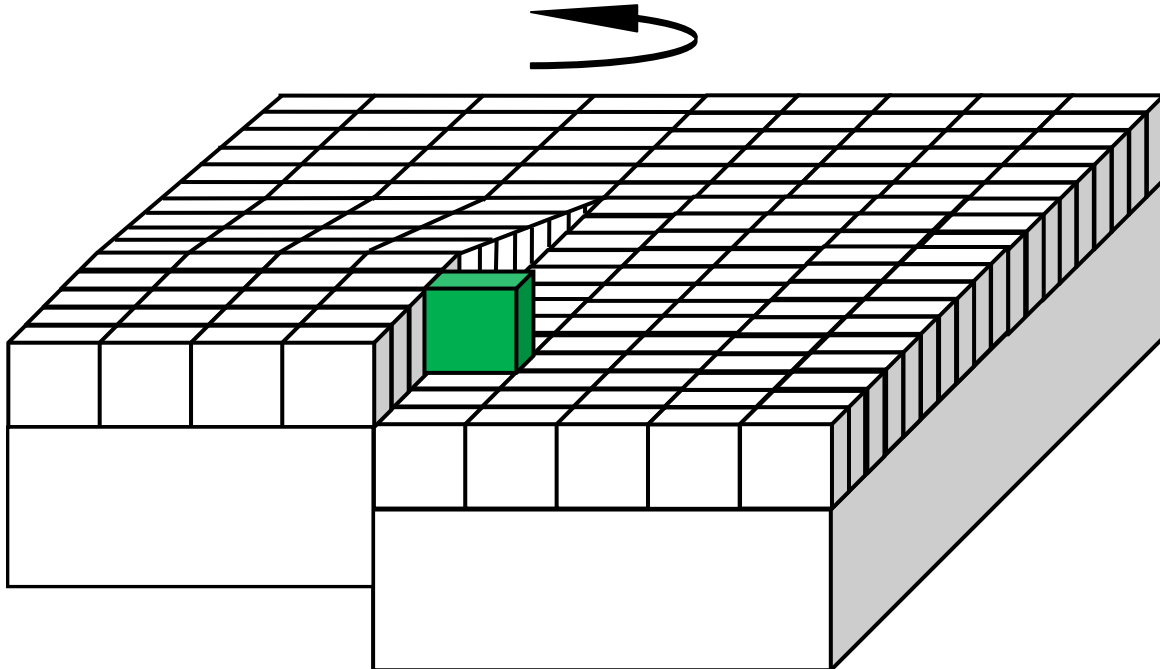


Figure 4.10: The screw dislocation theory of crystal growth.
(Green is a growth unit incorporated at the screw dislocation site)

4.4 Bridgman/Stockbarger Crystal Growth Technique

There are many techniques to grow single crystals from the solid-, vapour- or liquid (solution or melt) phase. Crystal growth from the melt was used in this work. The choice of the Bridgman/Stockbarger was necessitated by the hygroscopic nature of the SrI_2 and its oxygen sensitivity. [Alaribe 2010] described in detail methods of crystal growth from the melt, therefore the discussion here would be limited to the Bridgman/Stockbarger technique.

The Bridgman/Stockbarger technique is applied to the growth of semiconductors, alkaline halide and alkaline earth halide crystals due to their hygroscopic nature.

The advantage of the Bridgman/Stockbarger technique is the ability to seal hygroscopic materials and volatile melts in silica ampoules, to prevent melt hydration and also maintain its stoichiometry during the crystal growth.

The disadvantages are the direct contact between the growing crystal and the ampoule with different thermal conductivities and expansion coefficients that in most cases lead to cracking in crystals and the inability of in-situ monitoring of the crystal growth process.

The Bridgman technique is based on the movement of a crucible containing the melt through the axial temperature gradient of a furnace. In cases where the vibration of the ampoule is a problem, the furnace can be moved on a linear track assembly. This can be done using a vertical configuration as in Figure 4.11 or horizontal configuration of the furnace.

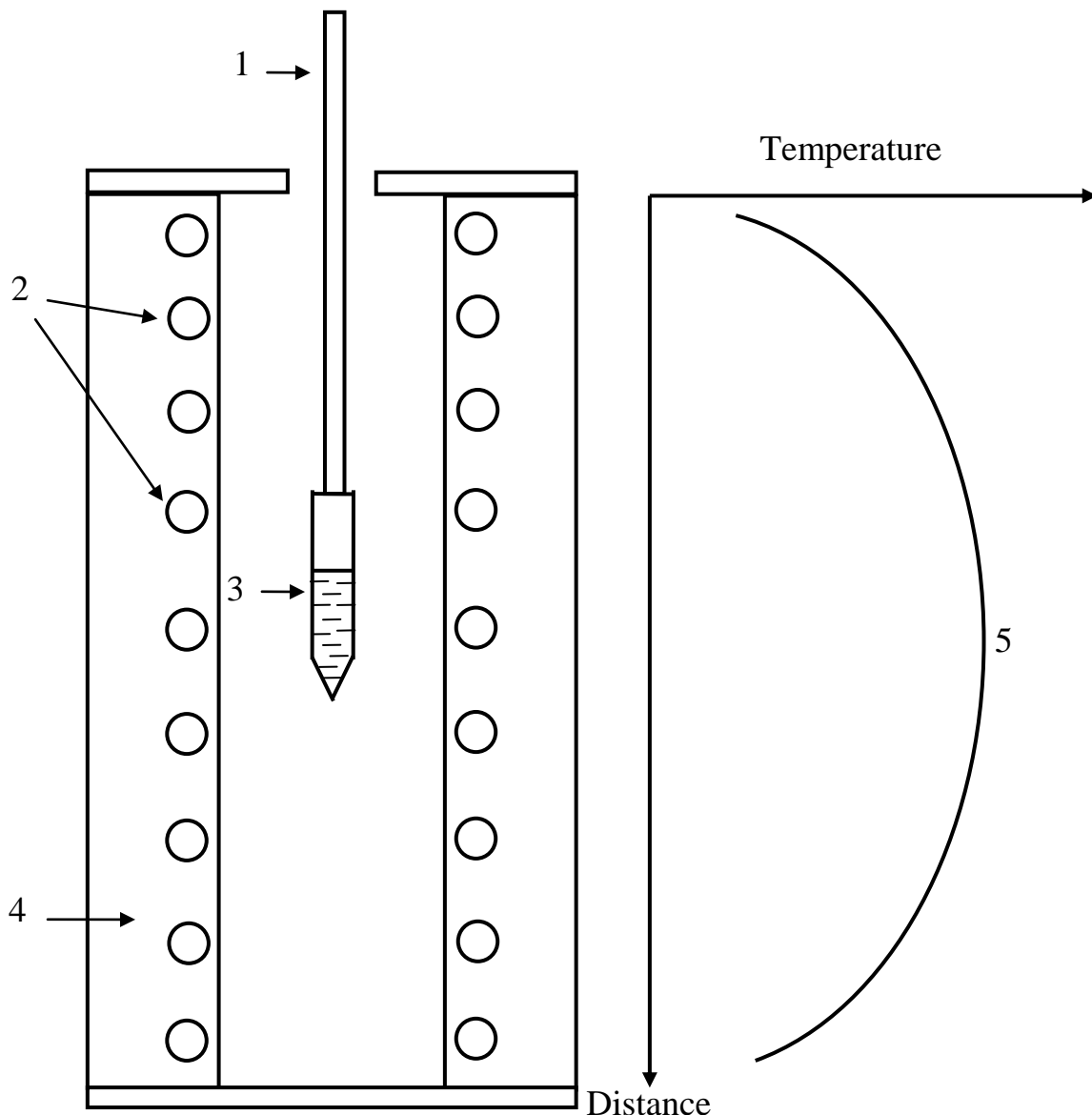
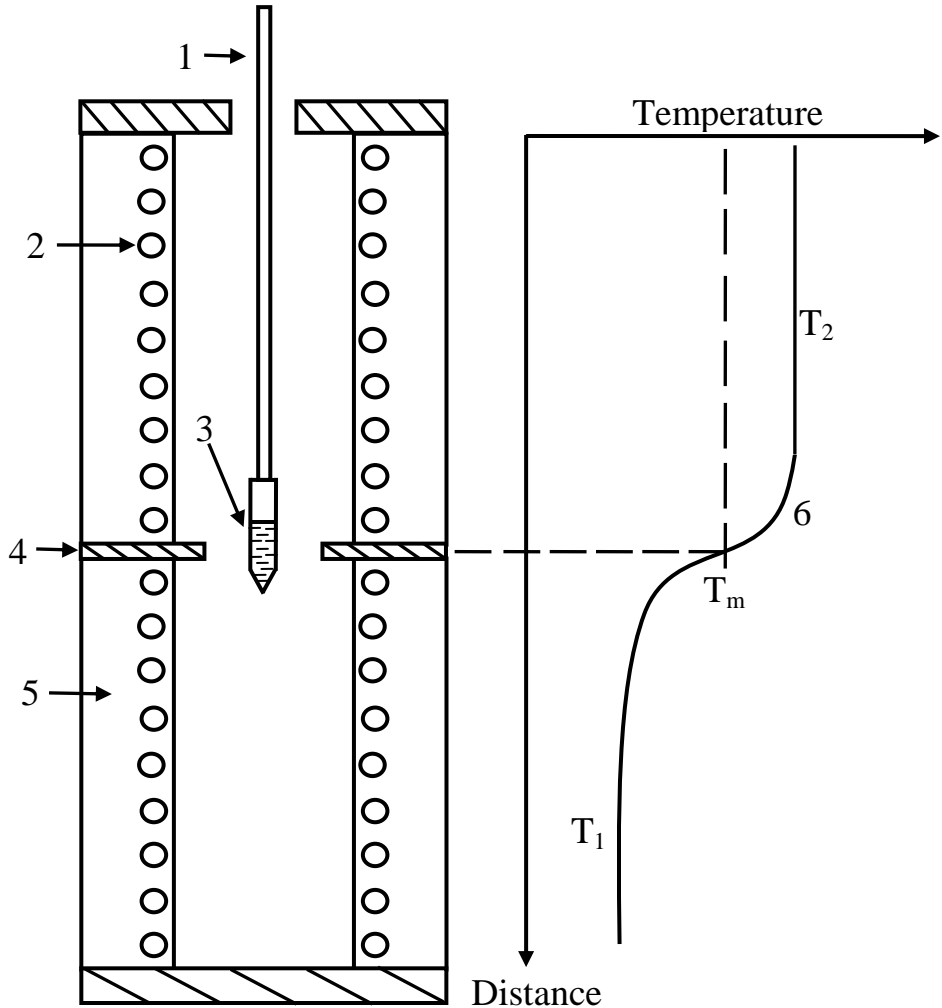


Figure 4.11: Vertical Bridgman furnace configuration
 1. Ampoule holder, 2. Heater, 3. Ampoule, 4. Thermal insulator, 5. Temperature profile.

The difference between the Bridgman technique and the Stockbarger technique is the presence of a temperature gradient in the Bridgman furnace. Stockbarger technique is a sophisticated modification of the Bridgman technique with a high temperature zone, an adiabatic loss zone and a low temperature zone [Hurle 1994] as in Figure 4.12.

The advantages of the Stockbarger technique are the ability to modify the temperature gradient through independent heating of the two zones and the use of the second zone for post-growth annealing.

**Figure 4.12:** Vertical Stockbarger furnace configuration

1. Crucible/Ampoule holder, 2. Heater, 3. Crucible/Ampoule, 4. Baffle, 5. Thermal insulator,
6. Temperature profile.

During the crystal growth experiments using the two different Bridgman configurations described above, the growth materials were contained in silica ampoules. [Wilke 1973] has reported on the formation of parasitic seed-crystals through interaction of the melt with the ampoule walls and also on the chances of eliminating these parasitic seed-crystals by maintaining a convex growth front (from the viewpoint of the solid). The position and shape of a growth front depend on the temperatures T_1 and T_2 , and also on the heat conductivity of the melt and crystal [Wilke 1988]. The condition for a convex growth using the vertical Bridgman-Stockbarger technique was given by [Chang 1974] as

$$\theta = \frac{(T_M - T_1)}{(T_2 - T_1)} > 0,5 \quad \text{eq. 4-19}$$

T_M is the melting point, T_1 is the low temperature zone and T_2 the high temperature zone.

This can be said to be the ideal case scenario because [Chang 1974] assumed the same thermal diffusivity ($k/\rho C_p$; k is the thermal conductivity; ρ is the density and C_p is the heat capacity) for the crucible material, the solid and the melt. This is not always the case in

practical applications, where the melt, the crystal and the crucible have different thermal diffusivities. Nevertheless, the [Chang 1974] condition was considered in choosing the crystal growth parameters (temperatures) in this work.

In the course of this work, crystal growth experiments were carried out using both single-zone Bridgman furnace and two-zone Bridgman-Stockbarger furnace. Figure 4.13 shows the single-zone Bridgman setup used. Simulations were done on this single zoned growth furnace to check the temperature distribution in the furnace and also to extract some information about the crystallization process (i.e. the rate at which the growth front is moved and its shape), since it was not possible to carry out an in-situ monitoring during the growth. The simulation results are discussed in chapter 5.1.1, while the simulated temperature profile is also compared to the measured in Figure 5.4.

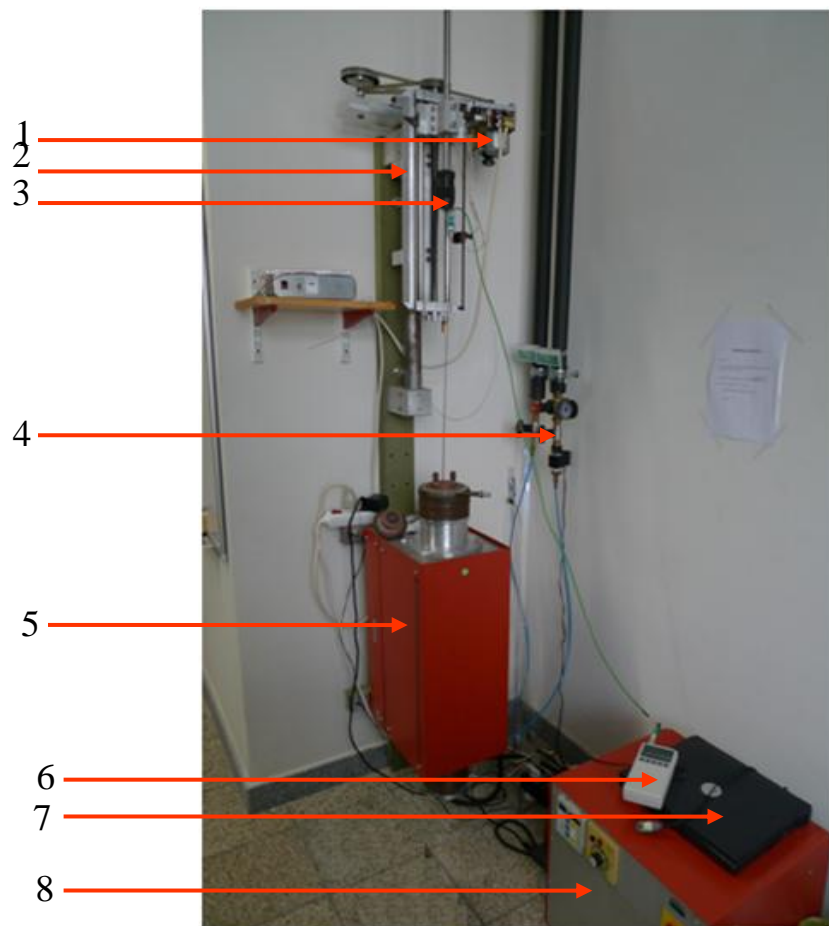


Figure 4.13: The single-zone Bridgman furnace

1. The pulling mechanism; 2. Scale (cm); 3. Ampoule holder; 4. Cooling water; 5. The single-zone Bridgman furnace; 6. Almemo (records the ampoule temperature); 7. Laptop (for automatic plotting of the ampoule temperature); 8. Furnace controller.

A two zone Bridgman/Stockbarger furnace was constructed in the course of this work to have a better control over the temperature gradient and also for post-growth annealing of crystals. Figure 4.14 shows an image of the Bridgman/Stockbarger furnace (not to scale) before construction. The images were created using Autodesk Inventor Professional 2010.

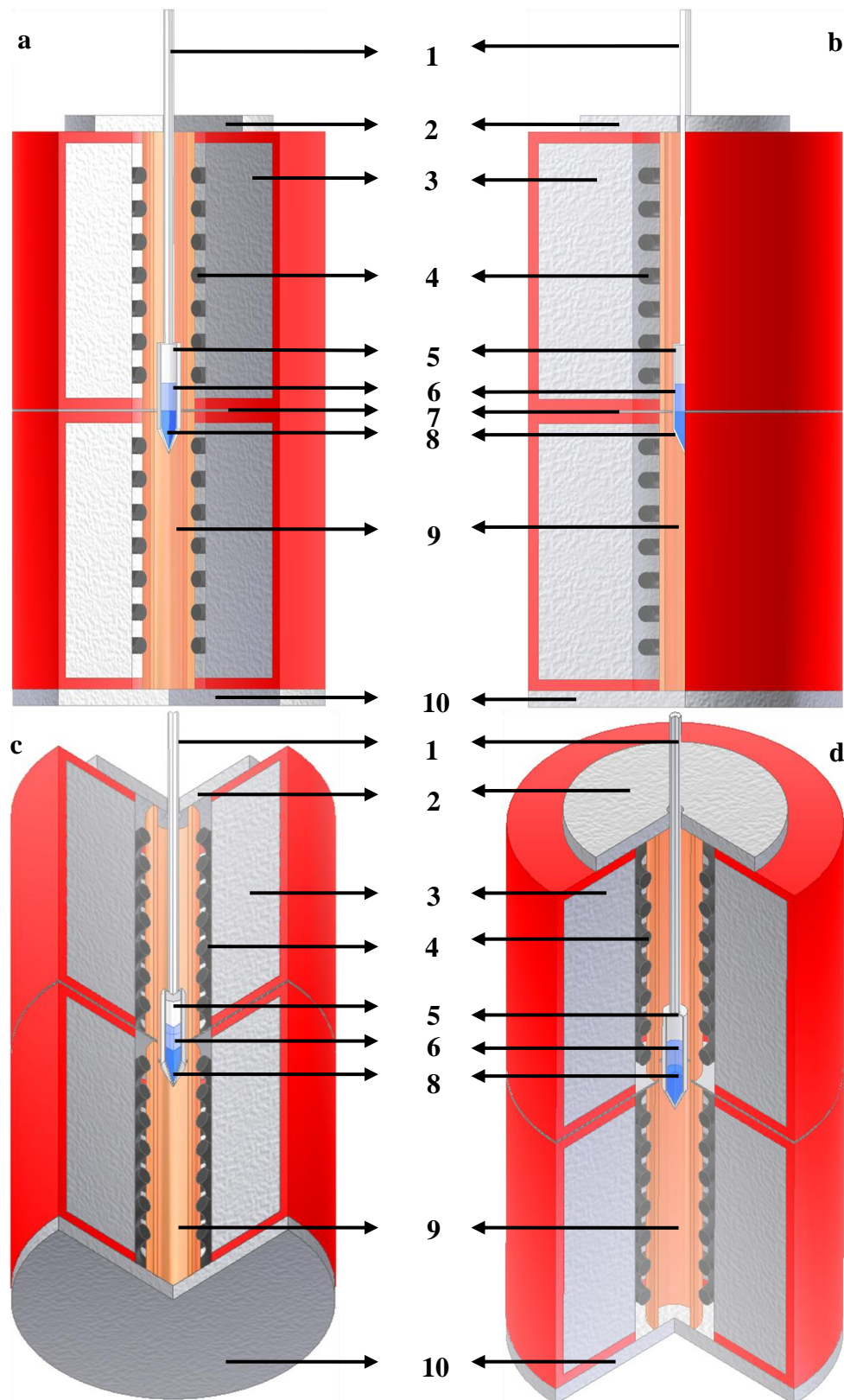


Figure 4.14: The designed Bridgman/Stockbarger setup before construction (not to scale).
a) front view b) side view c) bottom view d) top view.

1) glass rod for attaching the growth ampoule to the pulling mechanism
 2) covering thermal insulation with an opening for the ampoule
 3) thermal insulation for the heating elements
 4) heating elements
 5) ampoule
 6) melt
 7) thermal insulation preventing heat exchange between the two furnace zones
 8) crystal
 9) growth chamber (copper)
 10) bottom thermal insulation.

Bibliography

[Wilke 1973]

K. –Th. Wilke (unter Mitarbeit von J. Bohm): Kristall Züchtung. VEB Deutscher Verlag der Wissenschaften. Berlin 1973.

[Dhanaraj 2010]

Govindhan Dhanaraj, Kullaiah Byrappa, Vishwanath Prasad, Michael Dudley: Springer Handbook of Crystal Growth. Springer – Verlag Berlin Heidelberg 2010.

[Imai and Oaki 2010]

H. Imai, Y. Oaki: Nucleation and growth kinetics. MRS Bulletin 35, February issue, 138-144 (2010).

[Goodman 1978]

C. H. L. Goodman: Crystal Growth: Theory and Techniques. Plenum Press (1978).

[Gibbs 1928]

J. W. Gibbs: On the Equilibrium of Heterogeneous Substances. Collected Works, Longmans Green, New York (1928).

[Curie 1885]

P. Curie: Sur la formation des criteaux et sur les constantes capillaires de leurs differentes faces. Bull. Soc. Franc. Mineral. 8, 145-150 (1885).

[Wulff 1901]

G. Wulff: Zur Frage der Geschwindigkeit des Wachstums und der Auflösung von Kristallflächen. Z. Kristallogr. 34, 449 (1901).

[Marc 1911]

R. Marc, A. Ritzel: Über die Faktoren, die den Kristallhabitus bedingen. Z. Phys. Chem. 76, 584 (1911).

[Bravais 1866]

A. Bravais, A. Etudes: Crystallographiques. Gauthier Villers, Paris 1866.

[Noyes 1897]

A. A. Noyes, W. R. Whitney: Über die Auflösungsgeschwindigkeit von festen Stoffen in ihren eigenen Lösungen. Z. Phys. Chem. 23, 689 - 692 (1897).

[Nernst 1904]

W. Nernst: Theorie der Reaktionsgeschwindigkeit in heterogenen Systemen. Z. Phys. Chem. 47(1), 52 – 55 1904.

[Stranski 1928]

I. N. Stranski: Zur Theorie des Kristallwachstums. Z. Phys. Chem. 136, 259 – 278 (1928).

[Nesse 2000]

William D. Nesse: Introduction to Mineralogy. OXFORD UNIVERSITY PRESS 2000.

[Frank 1949]

F. C. Frank: The Influence of Dislocations on Crystal Growth. Discussions Faraday Soc. 5 48 – 54. 1949.

[Alaribe 2010]

Leonard Alaribe: Charakterisierung von LaCl₃-Kristallen. Diplom Thesis, Albert-Ludwigs-University Freiburg (2010).

[Hurle 1994]

D. T. J. Hurle: Handbook of Crystal Growth 2 (Basic Techniques). Elsevier Science B.V. 1994.

[Wilke 1988]

K. –Th. Wilke (Neu verfaßt und herausgegeben von Joachim Bohm): Kristallzüchtung. Verlag Harri Deutsch, Thun. Frankfurt/Main 1988.

[Chang 1974]

Chong E. Chang, William R. Wilcox: Control of Interface Shape in the vertical Bridgman-Stockbarger Technique. Journal of Crystal Growth 21 (1974) 135-140.

5 Experiments and Results

Chapter Overview

Abstract

5.1	Crystal Growth	79
5.1.1	Simulation of the single-zone furnace	80
5.1.2	Construction of a Two-Zone Bridgman/Stockbarger Furnace	85
5.1.3	Crystal Growth Experiments and Results	87
5.2	Crystal Preparations and Packaging	102
5.2.1	Crystal Preparations	102
5.2.2	Crystal Packaging	102
5.3	Spectroscopic Measurements	107
5.3.1	SrI_2 : 5% Eu^{2+} - 1	107
5.3.2	SrI_2 : 6% Eu^{2+} - 3	110
5.3.3	SrI_2 : 6% Eu^{2+} - 5	117
5.3.4	SrI_2 : 5% Eu^{2+} - 6	122
5.3.5	SrI_2 : 2% Eu^{2+} - 7	136
5.4	X-ray Imaging Measurements	139
5.4.1	Flat Field Image Recording	143
5.4.2	Mesh Image Recording	147
5.4.3	Radiographic Images	151
5.4.4	First X-Ray Tomography Images using SrI_2	159
	Bibliography	169

Abstract

The experiments in this research work were done systematically. Prior to the crystal growth experiments, some investigations were carried out on this relatively new scintillator material (SrI_2) to get some information on the structural properties, and also to check if other easier crystal growth methods are applicable and so on.

This chapter will present the results achieved so far on the crystal growth, polishing, packaging, scintillation performance and X-ray imaging application. With SrI_2 – thin screens in X-ray imaging, the integration time was reduced by factor 4, this was attributed to its high light yield as will be presented. Correlation between the obtained results and the experimental conditions is presented, so also some aspects of this work, where more improvement is needed.

5.1 Crystal Growth

Prior to the crystal growth experiments, thermogravimetric measurements were done on the starting materials to determine their level of hydration and their melting points. The results of these measurements were presented in chapter 3.1.1. X-ray diffraction measurements were also carried out on the starting materials prior and after dehydration to identify the compositional phases. For X-ray diffraction measurements, SrI_2 powder was filled in 0.5 mm diameter borosilicate glass capillaries. Due to the high X-ray absorption of the SrI_2 and the glass capillaries no signals were recorded at the detector.

Initial crystal growth experiments were done using the single-zone Bridgman furnace shown in Figure 4.13. First, the temperature profile of this furnace was recorded at different set temperatures, Figure 5.1.

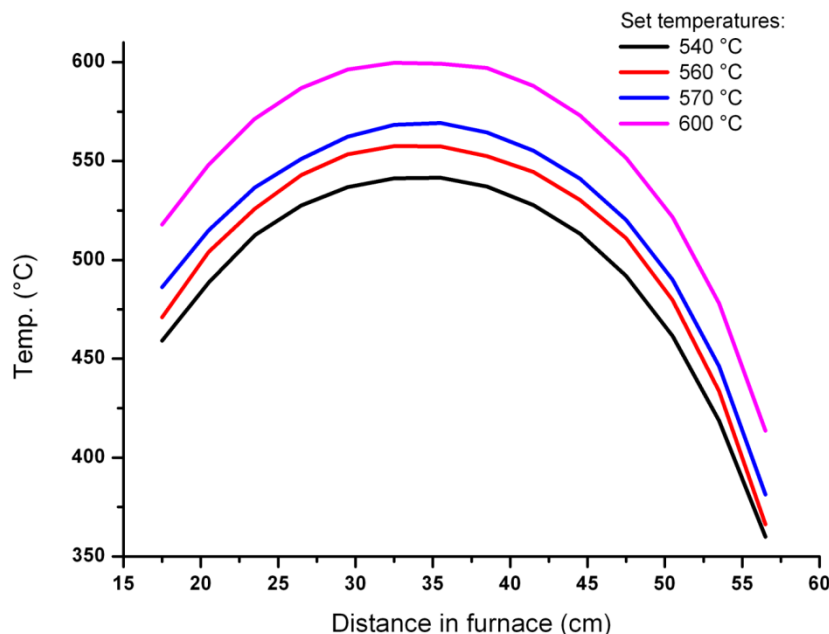


Figure 5.1: Measured temperature profiles of the single zone vertical Bridgman furnace.

The temperature gradient calculated from recorded experimental data is summarized in Table 5.1 below. The temperature gradient did not change much with the furnace temperature, so there was not much control over it. For a self – seeded growth as used here, a steep temperature gradient at the interface region is very important, so there was every need for at least a two-zone Bridgman furnace. At 600 °C set temperature, the temperature gradient decreased to 7.7 °C/cm, this can be attributed to experimental errors like shifting of the thermocouple during the measurement.

Furnace set temperature [°C]	Calculated temperature gradient in furnace [°C/cm]
540	7.5
560	8
570	9
600	7.7

Table 5.1: Temperature gradient of the single-zone Bridgman furnace.

5.1.1 Simulation of the single-zone furnace

In order to understand the prevailing temperature field during crystallization, the shape of the growth front and maybe the rate at which it is moved, some simulations were done using the computer software ANSYS Fluent®. Figure 5.2 shows the simulated furnace configuration.

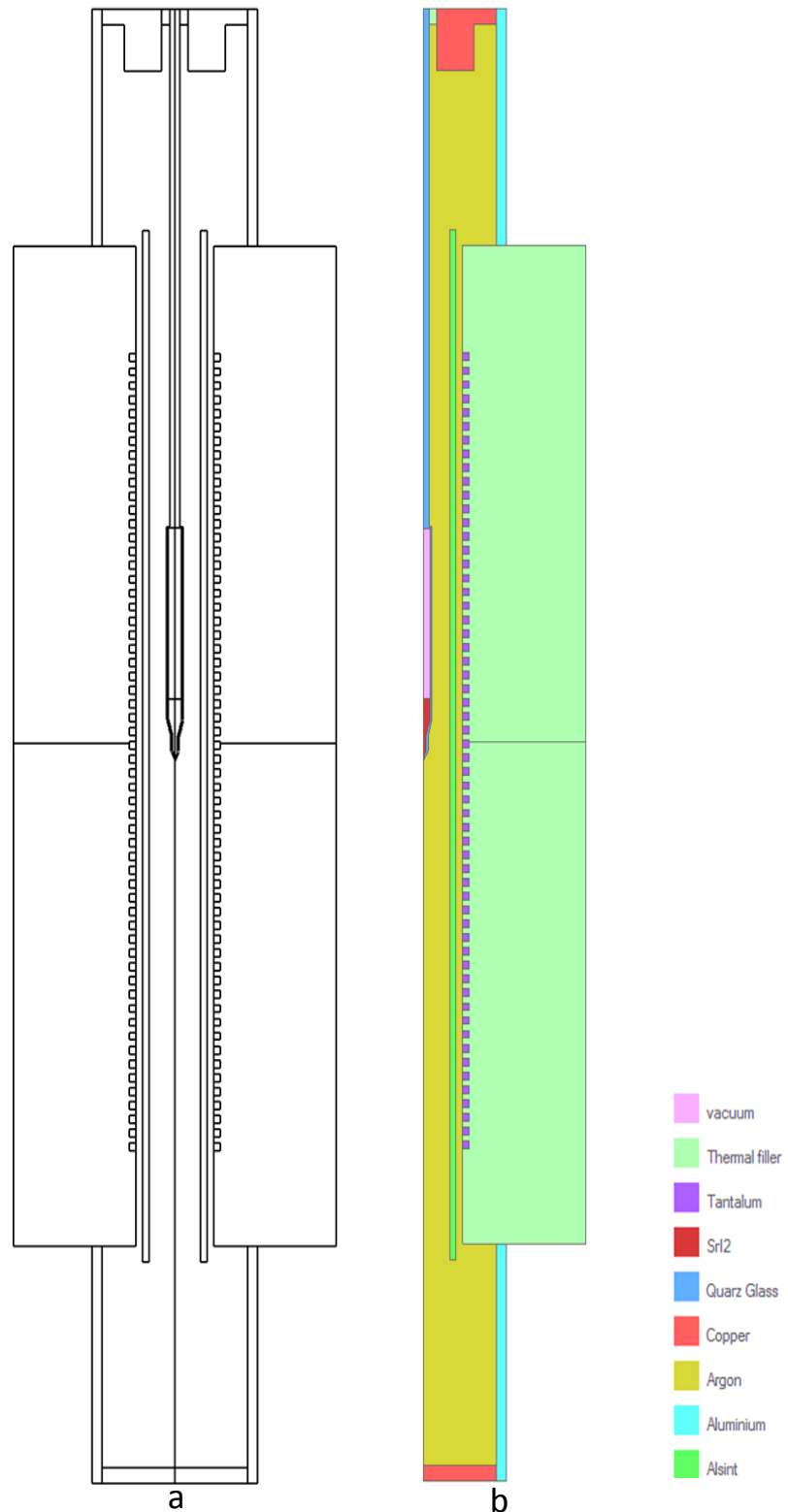


Figure 5.2: Image of the simulated furnace and its components.

Experiments and Results - 5

Figure 5.3 shows the temperature field distribution in the furnace. The middle of the furnace is the hottest region. During crystal growth processes, ampoules are lowered through the temperature gradient at the bottom region of the furnace.

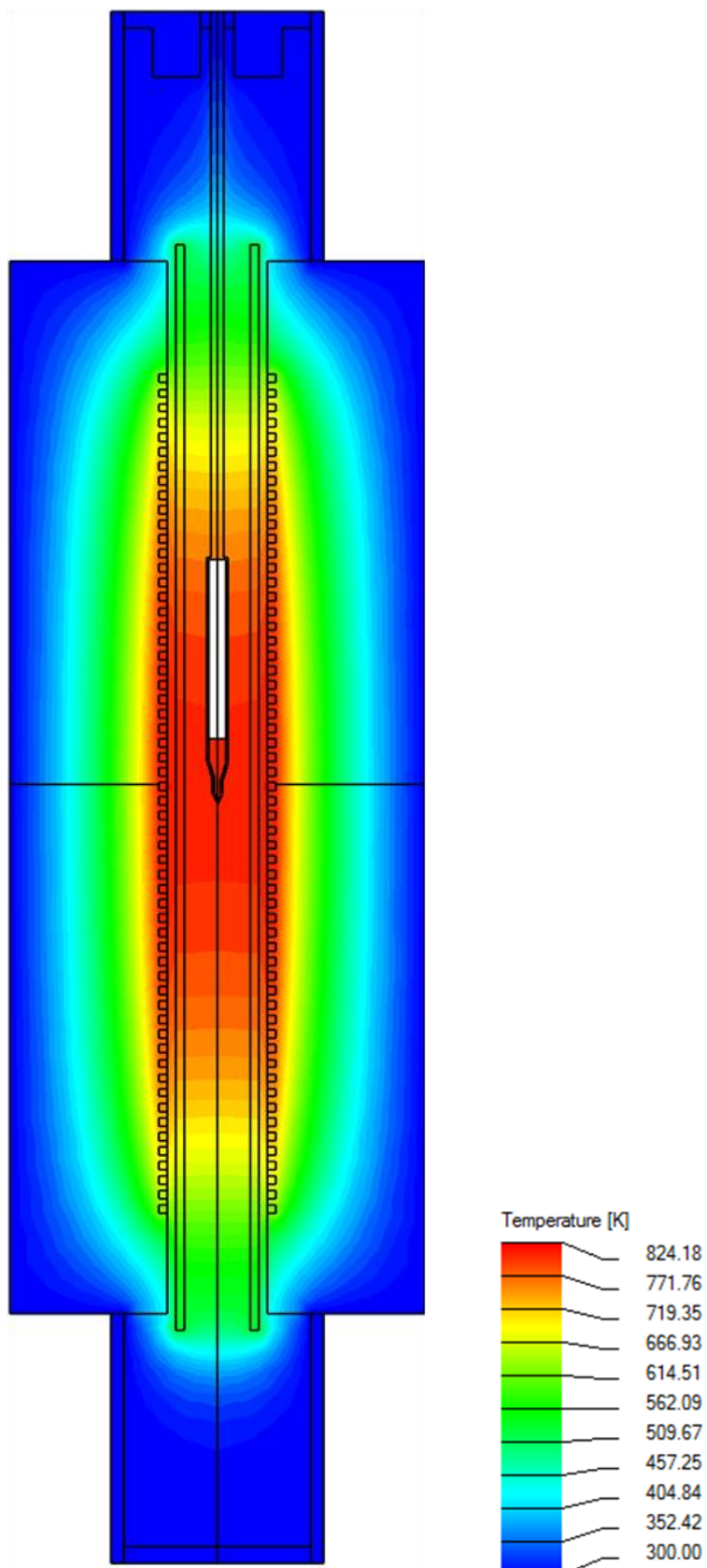


Figure 5.3: Simulated temperature field in the furnace.

Experiments and Results - 5

The simulated and measured temperature profiles are plotted in Figure 5.4 at 550 °C furnace set temperature. Both curves show a similar trend with the experimentally recorded temperature values slightly higher, which could mean that the furnace was well thermally insulated, another possible explanation could be that the used thermocouple was very close to the furnace wall. There is a slight distortion of the experimental curve around 17 cm which resulted in the shifting of the maximum of the experimental curve, this is due to the shifting of the thermocouple during the measurement.

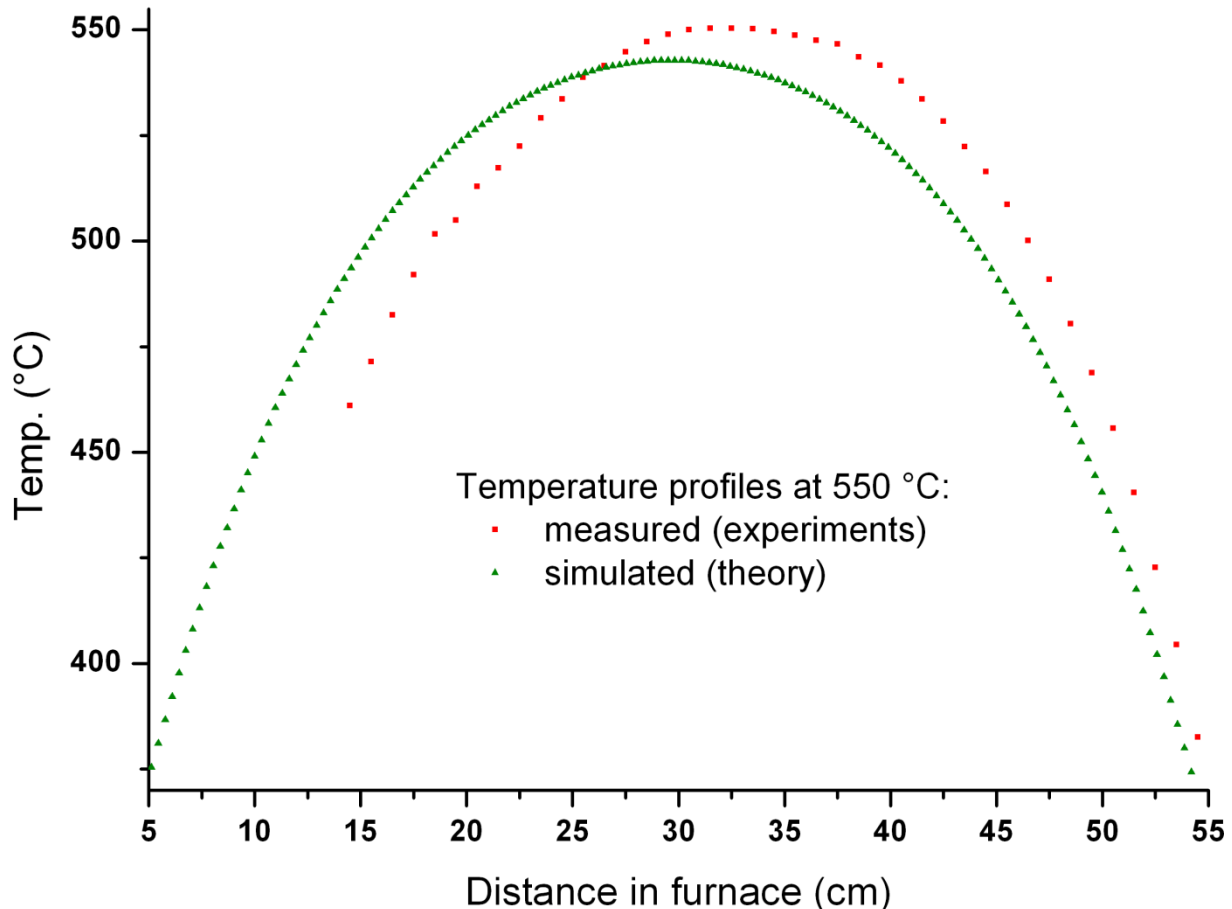


Figure 5.4: Comparison of the simulated and the measured temperature profiles.

The simulation helped understand how the growth ampoules interact with the spatial temperature field in the Bridgman furnace. The behaviour of the temperature fields is best described using the word elastic, Figure 5.5. The ampoule, on leaving a temperature field, deforms it. When the field's elastic limit is reached, it breaks and moves with a certain velocity from the peak of the ampoule to the height of the melt. Simulated here was a melt height of 5 cm. In order not to have the entire melt crystallize at once during the real growth, the length of the grain selector region was changed from 3 cm to 5 cm. The aim was to make sure the growth front stabilizes in the capillary region before moving over to the crystal growth region.

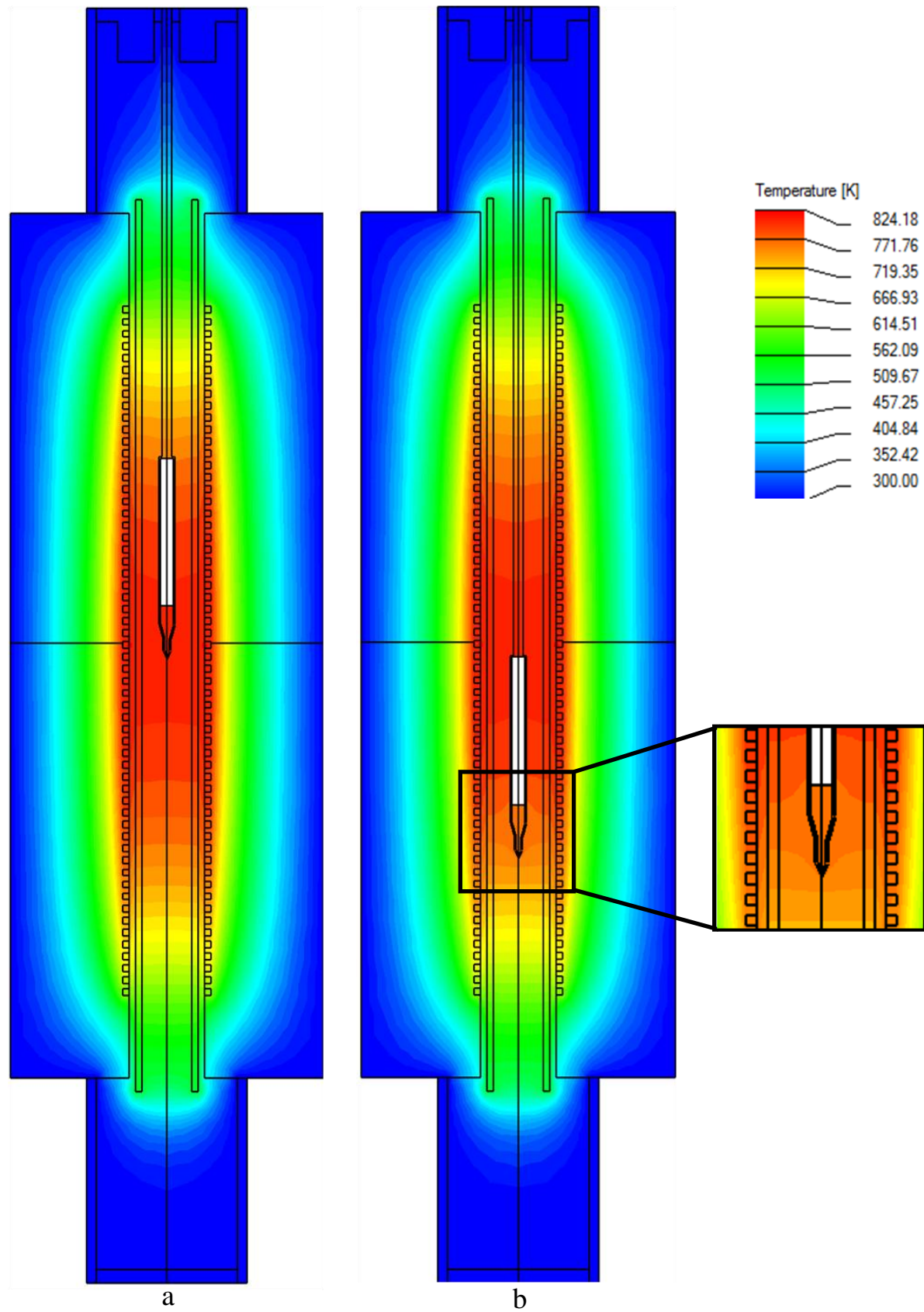


Figure 5.5: Lowering of the growth ampoule through the furnace. Inset in (b) shows the deformation of the spatial temperature field by the ampoule.

Experiments and Results - 5

Other informations deduced from the simulations are: the changes in the shape of the growth front and the different rates at which the temperature front and the growth front move through the ampoule. It was also possible to calculate the crystal growth rate from the movement of the growth front.

The shape of the growth front in the capillary region is slightly concave (from the viewpoint of the solid), but this changed to convex (also from the viewpoint of the solid) in the growth region. A convex growth front to the growing crystal is necessary in order to achieve single crystals, but a strong convex growth front as in Figure 5.6 image (h), would lead to stress in the crystal. It is better to maintain a flat growth front which is difficult here because the [Chang 1974] equation does not apply; it is valid for at least a two-zone Bridgman furnace configuration.

The simulations show that the crystallization process would be over after 9 mm as in Figure 5.6. The pulling rates used during the experiments were 0.25 – 0.5 mm/hr, meaning that between 18 and 36 hours, the crystal growth would be over for a 5 cm melt height. For the simulations here, the thermal conductivity of CaF_2 (16 watt/mK) was used, the thermal conductivity of SrI_2 is still unknown and we are making arrangements to measure it.

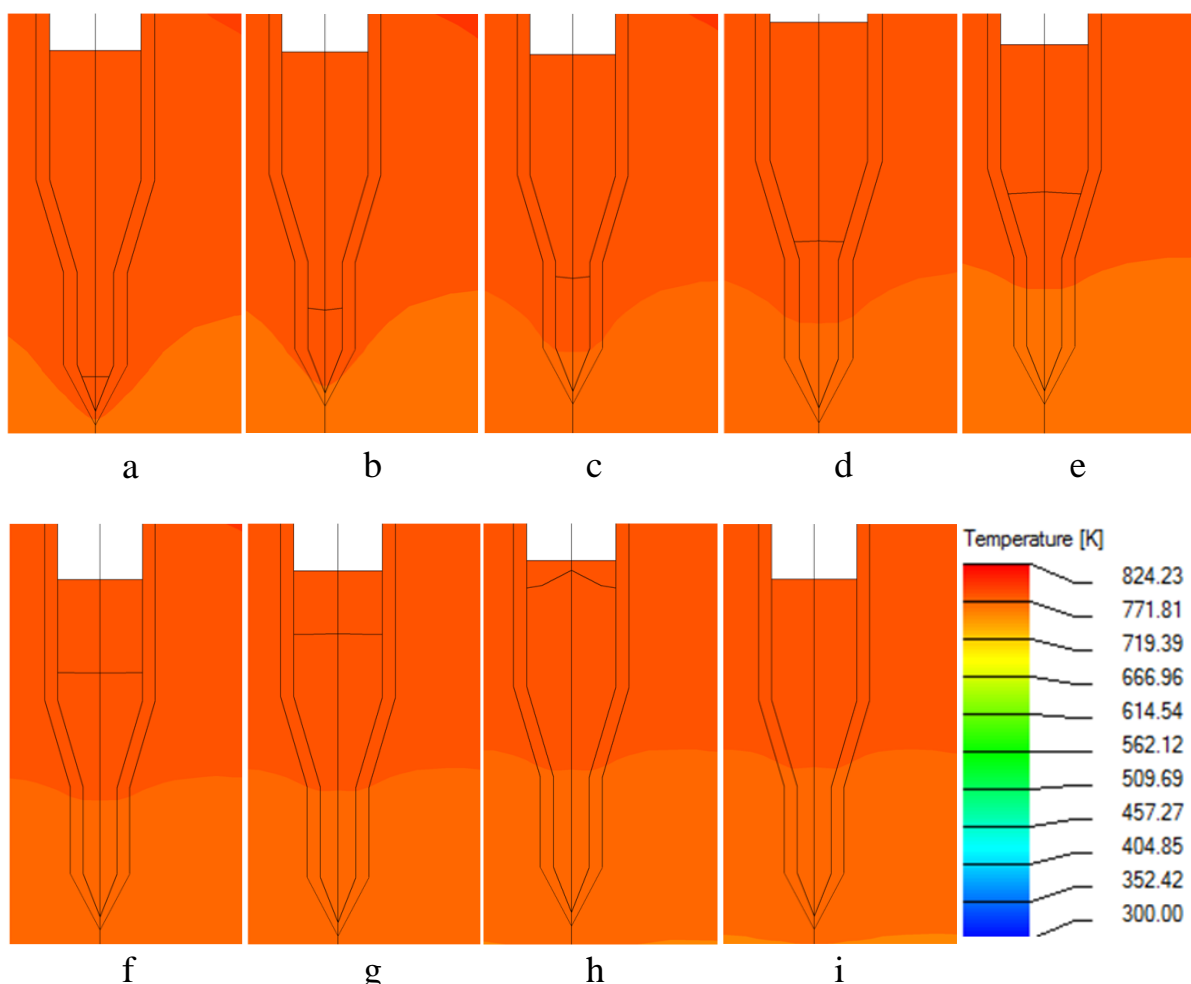


Figure 5.6: Simulation showing the crystallization process. a) Self-seeding process, b) – h) notice the changes in the shape of the crystal growth front, i) is the end of crystallization.

5.1.2 Construction of a Two-Zone Bridgman/Stockbarger Furnace

In order to exercise better control over the temperature gradient, apply the [Chang 1974] equation for a convex growth front and also carry out post-growth annealing of the crystals down to room temperature, a two-zone Bridgman/Stockbarger furnace was constructed. Figure 5.7 shows the vertical Bridgman/Stockbarger furnace as constructed. Two tubular resistance furnace segments manufactured by Gero, the F 70-400 and the F 70-500 were used. According to [Gero 2013], the heating tubes consist of an uncovered CrFeAl heating coil that is mounted on a ceramic fibre module. Other technical information on the furnace coating are tabulated below. The furnace is controlled using MODCON, which allows for independent heating of the different segments.

Type	F 70-400	F 70-500
T _{MAX} (°C)	1300	1300
Rated voltage (V)		55
Power (kW)	2.94	3.1
Year built	12/92	12/92

Table 5.2: Data on the two Gero furnace segments used.

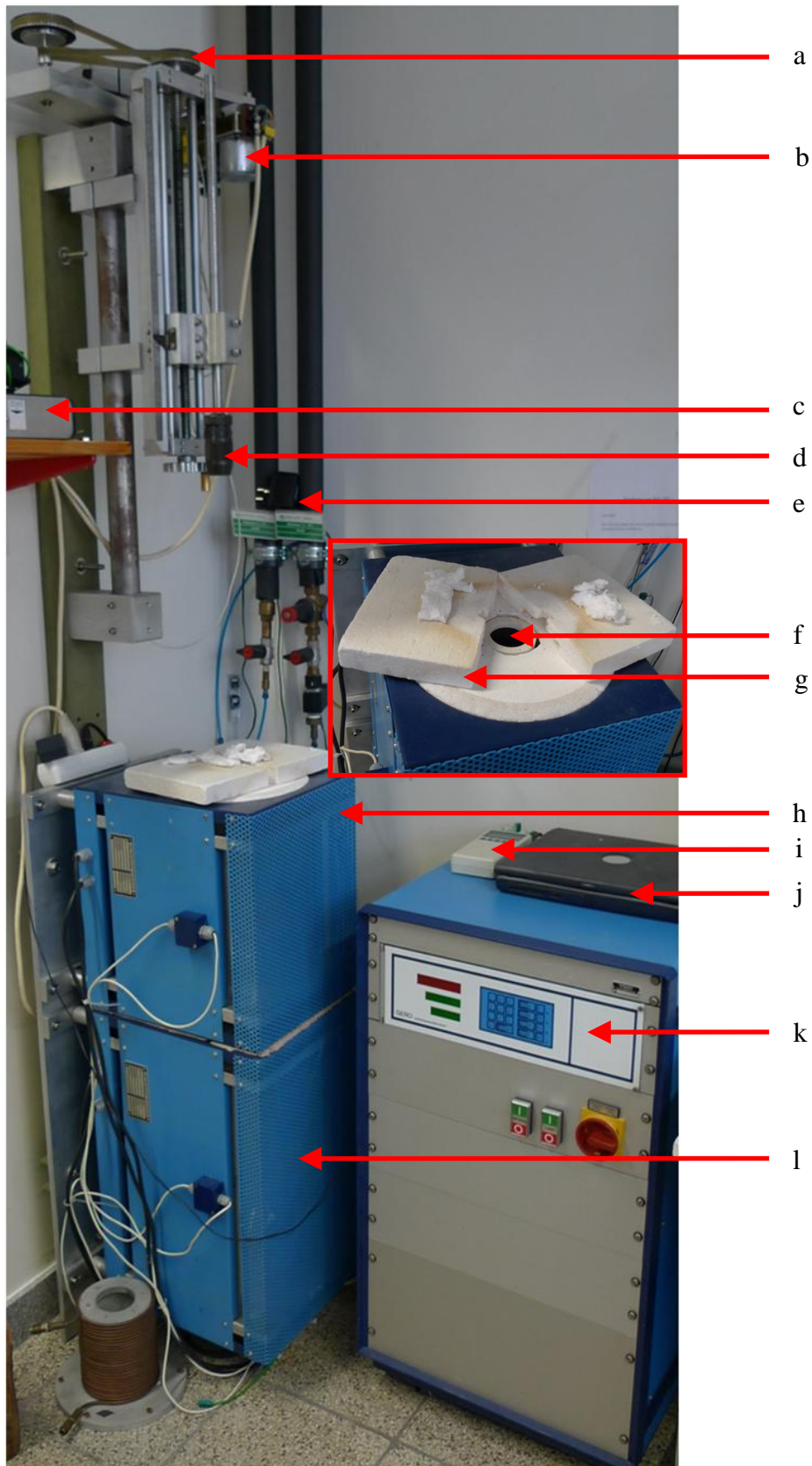


Figure 5.7: The constructed Bridgman/Stockbarger furnace. a) the pulling gears, b) the pulling motor, c) switch for the pulling unit, d) the pulling finger, e) water cooling supply, f) inset: the growth chamber, g) inset: Fiberfrax, h) upper zone, i) Almemo for automatic temperature recording, j) laptop for monitoring the growth temperature, k) furnace control unit, l) the lower zone.

Experiments and Results - 5

The temperature profiles of this new furnace were measured as shown in Figure 5.8. For the first measurement, the upper zone was set at 600 °C and the lower zone at 200 °C, resulting in a temperature gradient of 39.08 °C/cm. For the second measurement, the upper zone was set at 575 °C and the lower zone at 350 °C, resulting in a temperature gradient of 20.86 °C/cm.

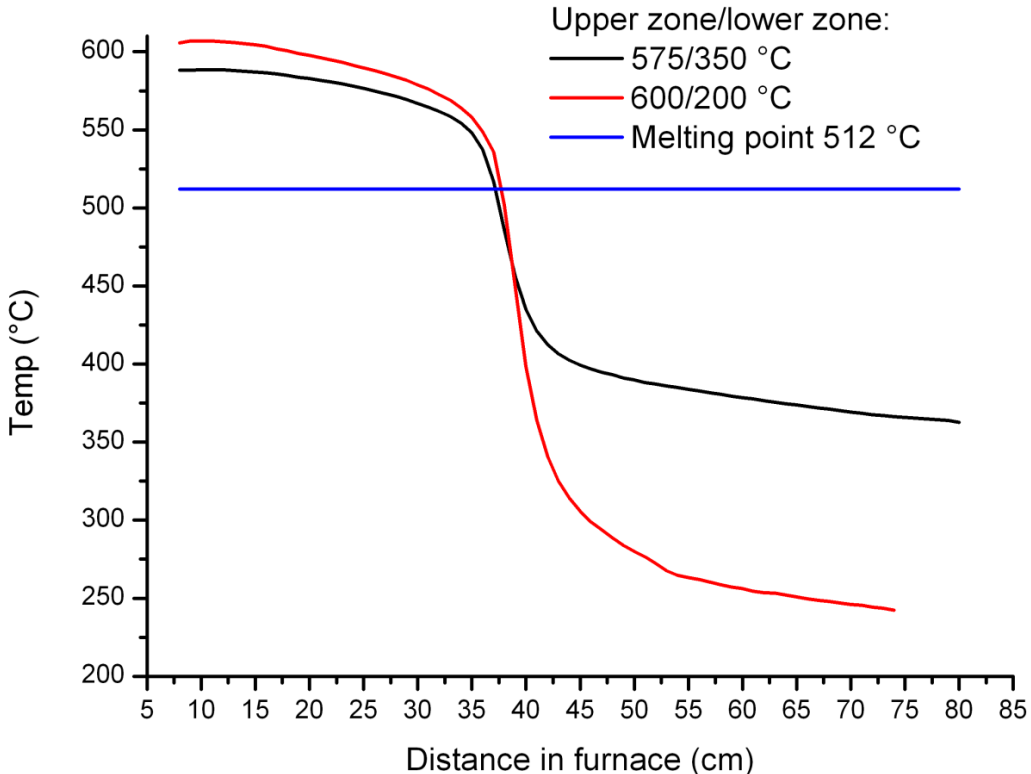


Figure 5.8: Measured temperature profiles of the vertical Bridgman/Stockbarger furnace.

5.1.3 Crystal Growth Experiments and Results

A lot of things were tried out, all aimed at achieving the growth of high quality bulk single crystals. How some of these factors like liquid encapsulated Bridgman, ampoule designs and the addition of a growth gas influenced the end results, is discussed below.

Prior to the crystal growths, the degree of supercooling of the SrI₂ was determined to be ~60°C for zone-refined materials, Figure 5.9. This can be said to be moderate, meaning the material is self-seeding. This also helped us to know where to expect crystallization peaks during the crystal growth experiments. For this measurement, a temperature program of 10 °C/minute was used in the heating process, from 20 to 600 °C and also in the cooling process, from 600 to 20 °C.

It is important to mention here that the differential scanning calorimetry method uses an open system, meaning there is material and energy interaction with the surrounding. The crystal growth is a closed system where you have only energy interaction with the surrounding. This means that there could be a slight deviation of the values if the measurement is done using a closed system. This will be investigated.

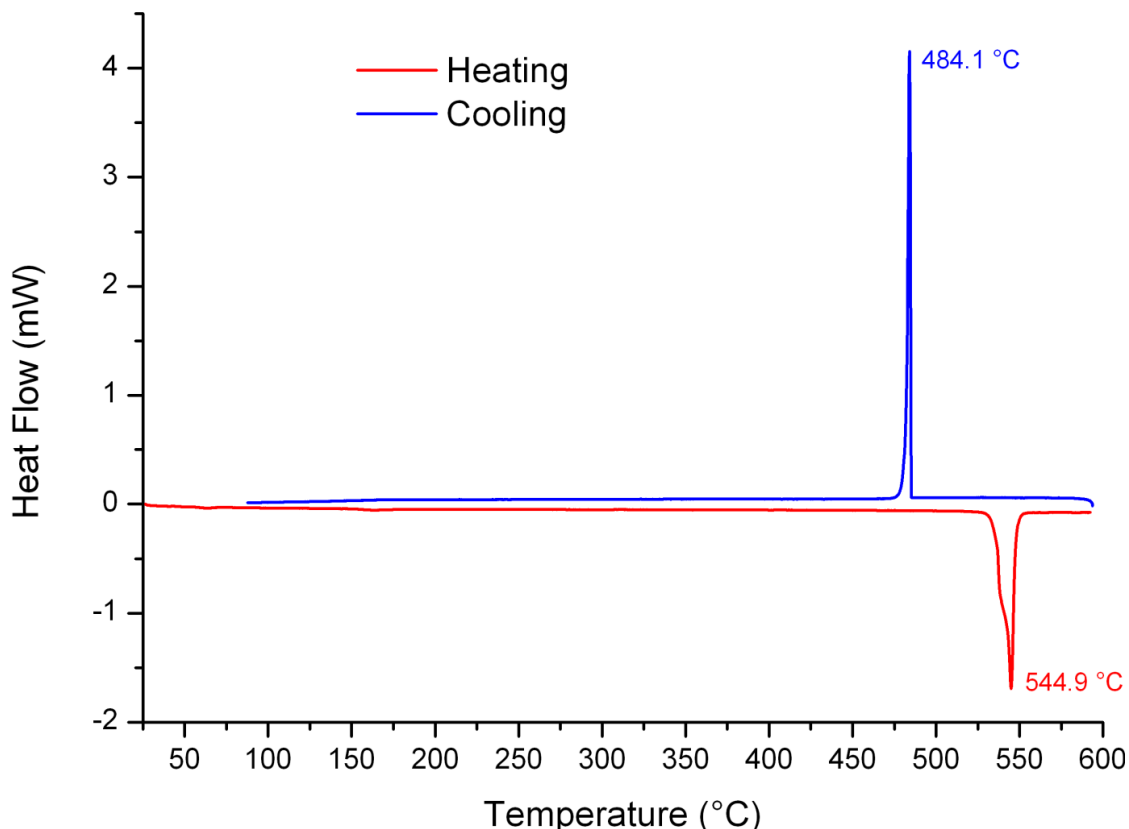


Figure 5.9: Differential scanning calorimetry curves of SrI_2 . An endothermic process in red shows the melting and the exothermic process in blue shows the crystallization.

5.1.3.1 SrI_2 : 5% Eu – 1

This first ampoule was aimed at finding out the problems (material and technical) associated with the growth of the SrI_2 and how these could be addressed to achieve a single crystal growth.

Notice in Figure 5.10 and Figure 5.11 the thickness of the ampoule at first to freeze region marked (a) and the crystallinity of the material inside. This region is polycrystalline and is thought to be caused by the accumulation of heat due to the ampoule thickness at the first to freeze region.

As growth proceeded, the crystallinity of the material also improved from region (b) to region (c). The sample shown in Figure 5.12 is from the (c)-region.

The region (d) shows dark colorations, possible explanations are: segregated impurities contained in the starting material or decomposed part of the material. This ampoule was sealed under vacuum, during melting processes; the vapours of the compositional materials will have to fill the empty space. This might lead to slight changes in the stoichiometry of the SrI_2 , since iodine gas has to escape in order to fill the vacuum. At this point, the addition of a growth gas to fill up the space and the purification of the starting materials were considered.

Experiments and Results - 5

Under white light, defects were visible in the ampoules (b)-region. These defects were first thought to be grain boundaries. Because they reflect light in different directions and upon opening of the ampoule; the crystals fell apart, suggesting that the defects must have originated from post-growth cracking, as grain boundary would only reflect light in one direction only.

The colour of the crystal in the ampoule is slightly white, but high purity SrI₂ should be colourless in a crystalline form. There was no zone-refining prior to this crystal growth, and the coloration is thought to be caused by impurities.

One can say that SrI₂ wets glass as a liquid, but pulls from the walls on crystallization. Figure 5.13 shows a polished sample from this ampoule. The pulling rate used here was 0.5 mm/hr, with ~ 10 °C/hr cooling rate down to the room temperature.

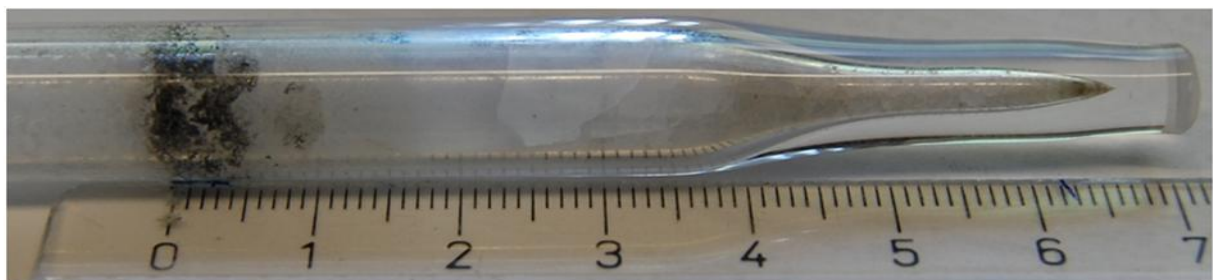


Figure 5.10: The SrI₂: 5% Eu – ampoule as grown. 1 cm diameter.

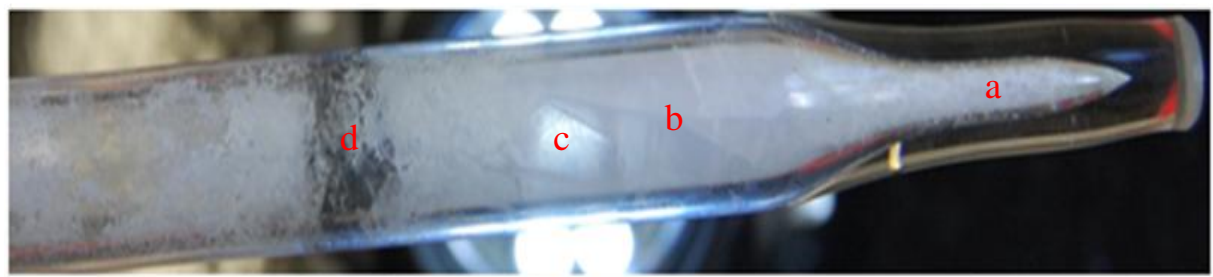


Figure 5.11: SrI₂: 5% Eu – ampoule showing different regions marked in red.

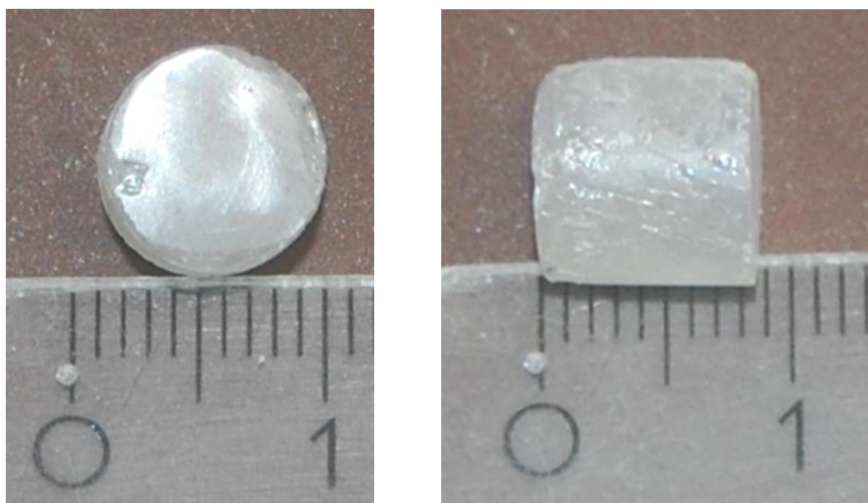


Figure 5.12: Harvested crystals.

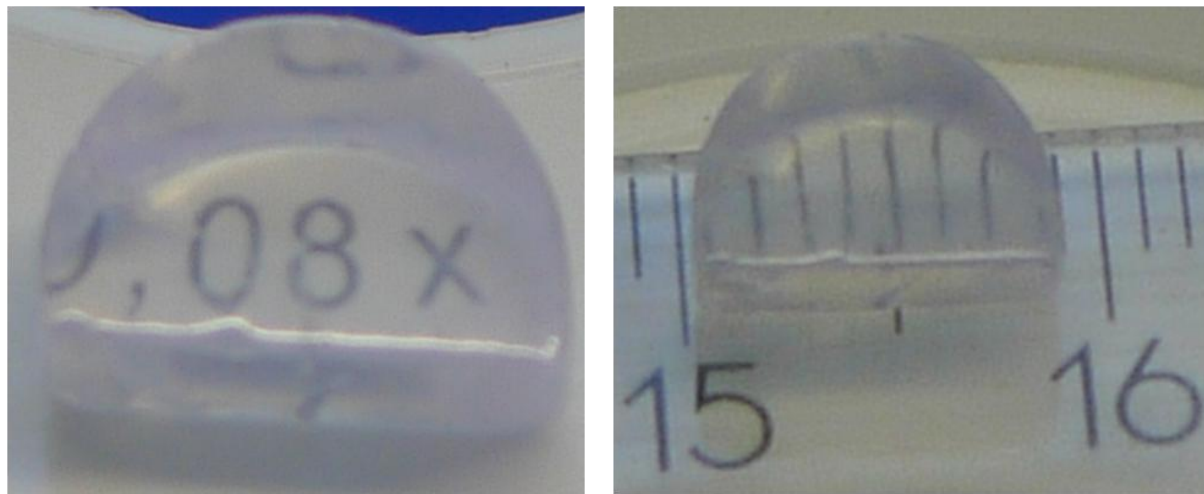


Figure 5.13: A polished sample.

5.1.3.2 SrI₂: 5% Eu – 2

With this growth no.2, attempt was made to address a couple of problems noticed in growth no.1. It was thought that the defects in crystal no.1 were caused by different thermal conductivities of the SrI₂ and the quartz ampoule. To address this problem, the liquid encapsulated Bridgman technique was tested.

The technique is simple as shown in Figure 5.14; a material with a low melting point that doesn't react with the SrI₂ was introduced into the growth ampoule. After the crystallization of the SrI₂, the melt of this encapsulant material will flow between the SrI₂ crystal and the ampoule wall, thereby reducing the direct thermal contact between them. The decision to use Boron trioxide B₂O₃ was based on its low melting point 450 °C and its chemical inertness. During the loading of ampoule no. 2, few pellets of B₂O₃ were also introduced into the ampoule as in Figure 5.15. Figure 5.16 shows the ampoule after the crystal growth.

Notice in Figure 5.17 the cracks on the ampoule wall and the coloration of the materials inside. It is difficult to say for sure what destroyed the ampoule; a possible explanation is that the pressure exerted on the SrI₂ crystal and the ampoule wall by the B₂O₃ on crystallization was very high, B₂O₃ is known to be one of the most difficult compounds to crystallize. Upon opening of the ampoule, it was discovered that the material stuck to the ampoule wall. The coloration is from escaping iodine gas. More analysis is still to be carried out, in order to see to what extent the melt was oxidized. After this, the use of the B₂O₃ for encapsulated Bridgman technique was discouraged, leaving open the search for a replacement. The same crystal growth parameters as in growth no.1 were used here.

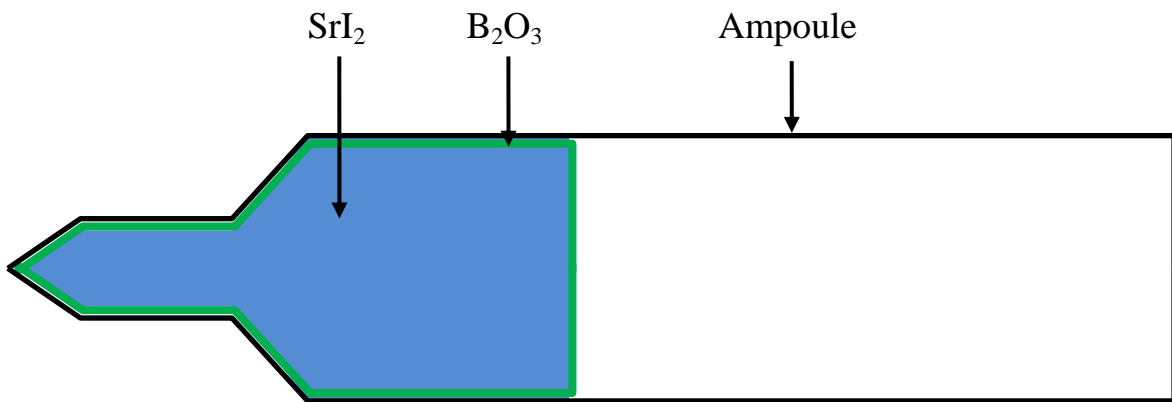


Figure 5.14: Liquid encapsulated Bridgman-ampoule.



Figure 5.15: The ampoule before the crystal growth. Notice the two regions; (a) is SrI_2 and (b) B_2O_3 .



Figure 5.16: The ampoule after growth. 1 cm in diameter.



Figure 5.17: Cracks seen on the ampoule wall. Red colouration is due to escaping iodine gas.

5.1.3.3 SrI₂: 6% Eu – 3

Figure 5.18 shows the ampoule no.3 after growth. Notice the dark coloration in Figure 5.19 and also the white colour of the crystal. Under white light, one would notice that this ampoule shows less defects of the crystal than ampoule no.1, Figure 5.20.

The thickness of the ampoule at the first to freeze region was reduced to avoid heat accumulation and the length prolonged to make sure the whole material doesn't crystallize at once. Figure 5.21 shows a good work of nucleation, the single crystal growth started from the grain selector region. It was thought that this improved the crystallinity of the whole crystal, but the need for optimization of the crystal growth process, in order to avoid the cracking of the crystals during post-growth cooling processes remained.

Figure 5.22 and Figure 5.23 shows the harvested crystals and polished samples respectively. The pulling rate used here was 0.25 mm/hr followed by a cooling rate of 5 °C/hr down to room temperature.



Figure 5.18: The ampoule no. 3 after growth. 1 cm in diameter.



Figure 5.19: Dark coloration visible in the ampoule.



Figure 5.20: Single crystal blocks visible due to cracking of the crystal during the cooling process.



Figure 5.21: First to freeze region showing a good nucleation work.

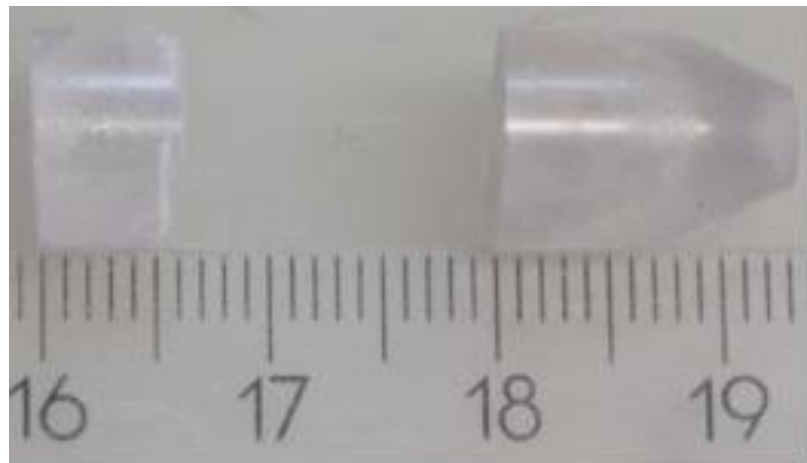


Figure 5.22: Some of the harvested crystals.



Figure 5.23: Polished samples from ampoule no.3.

5.1.3.4 SrI₂: 5% Eu – 4

The idea to introduce argon gas into the growth ampoule for better heat transport and distribution in the ampoule came after a long search for an adequate growth gas, especially since the B₂O₃ in growth no.2 proved futile. The need for a growth gas has been discussed under crystal growth no.1.

Notice the yellowish coloration of the EuI₂ in the ampoule in Figure 5.24, this image was taken after the dehydration of the crystal growth charge materials at the high vacuum pump. Figure 5.25 and Figure 5.26 show a strong distribution of this yellowish coloration in the ampoule after growth.

It was already noticed in the glovebox already where the SrI₂ and EuI₂ were stored, that the colour of the EuI₂ had changed from light-brown as bought to brown. At first, it was thought that the EuI₂ was exposed to low level moisture in the glove box. But because the yellowish coloration remained after dehydration, it suggested a kind of reaction or decomposition of the EuI₂.

Experiments and Results - 5

The level of yellowish coloration of the ampoule in Figure 5.27 suggested strong decomposition of the material during growth. Later it was found that the argon gas used here was not the purest and needed some purification prior to use for crystal growth purposes. The need for zone-refining of the materials prior to the crystal growth also became clearer after the growth no. 4. The ampoule no.4 was used for zone-refining experiments.



Figure 5.24: Ampoule no. 4 before the crystal growth. Notice the yellowish coloration in the ampoule.



Figure 5.25: The first to freeze region showing some colorations.

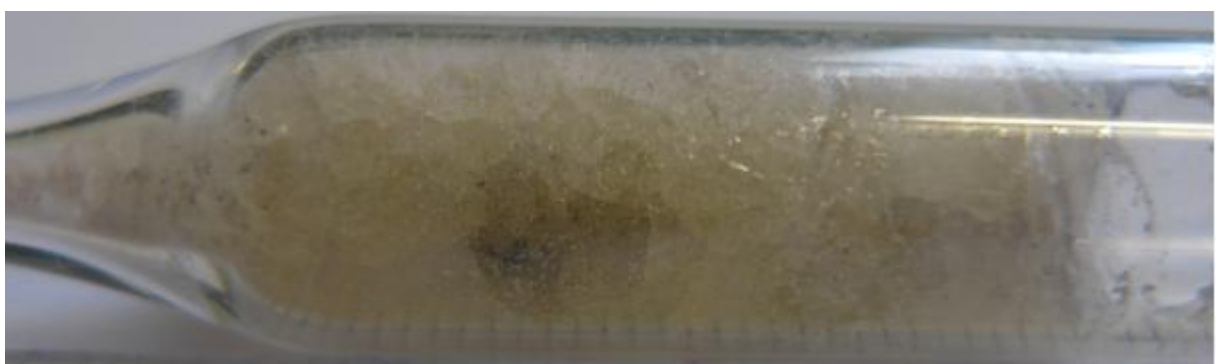


Figure 5.26: Yellowish to dark colorations in the ampoule.

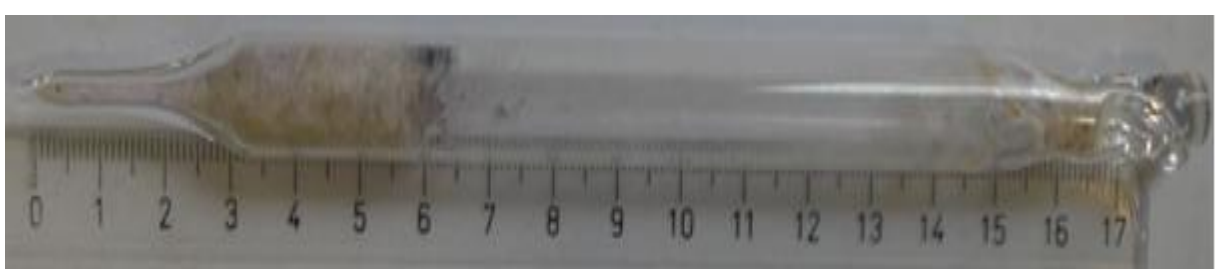


Figure 5.27: The ampoule no.4. 1 cm in diameter.

5.1.3.5 SrI₂: 6% Eu – 5

One of the aims of this work is the growth of 1-inch crystals. Here the diameter of the ampoule was increased to 1.5 cm. The grain selector at first to freeze region was redesigned to subdue the growth of multiple grains.

For the first time, an attempt was also made at purifying the materials prior to the crystal growth. The method used here is simple. The charge materials for a crystal growth are loaded in an ampoule, heated up to the melting point and cooled very fast to room temperature. This was repeated two or three times, the ampoule is opened and the better part of the material is cut and loaded in a new ampoule for the crystal growth. Figure 5.28 and Figure 5.29 show some improvement in the purity of the material. Figure 5.30 and Figure 5.31 show the harvested and the polished samples respectively with better crystallinity. The pulling rate of the ampoule was 0.25 mm/hr and 7 °C/hr cooling rate after the crystal growth.

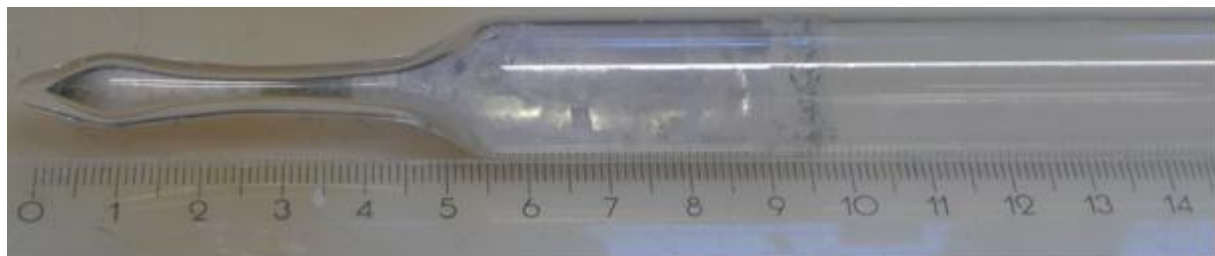


Figure 5.28: The ampoule no.5. Notice the design of the grain selector.



Figure 5.29: Ampoule no.5 under a white light.

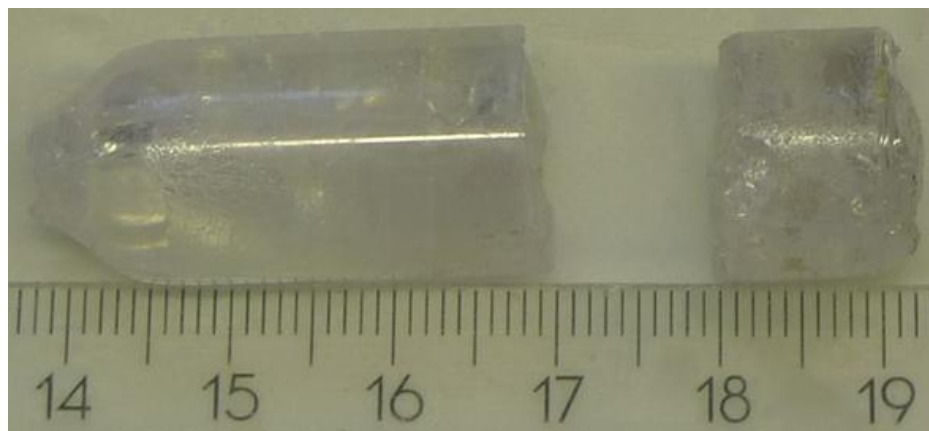


Figure 5.30: Harvested crystals.

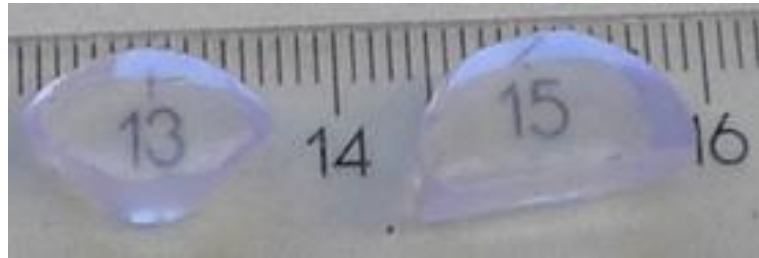


Figure 5.31: Polished samples.

5.1.3.6 SrI₂: 5% Eu – 6

Owing to the result of growth no.5, materials for growth no.6 were zone-refined prior to the crystal growth.

Figure 5.9 showed the degree of supercooling of the SrI₂ melt to be 60 °C. To check if the supercooling effect could be reduced through better heat dissipation, a 3 cm glass rod was attached to the first to freeze region shown in Figure 5.32.

Notice the attachment of a thermocouple to the growth ampoule in Figure 5.32 for the recording of the growth temperature. Figure 5.33 shows the ampoule under a white light with improved crystal quality. Notice also the pattern of the boundaries; they seem to originate from the side of the thermocouple. At this point, it was thought that the 3 mm diameter thermocouple could be disturbing the temperature distribution in the furnace, especially at the growth interface region. For the next crystal growth experiments, no thermocouple was used.

Figure 5.34 and Figure 5.35 show some of the harvested and polished crystals. The pulling rate used here was 0.25 mm/hr and a cooling rate of 7 °C/hr after the crystal growth.

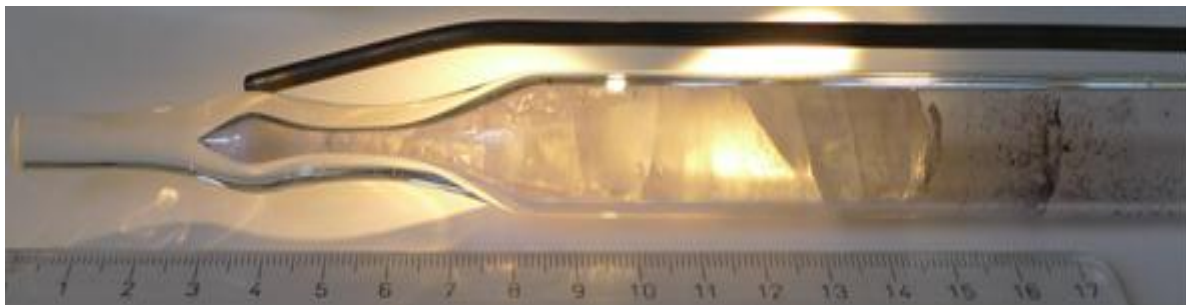


Figure 5.32: Ampoule no. 6. Notice here the glass rod at first to freeze region.



Figure 5.33: Ampoule under light. 1.5 cm in diameter.

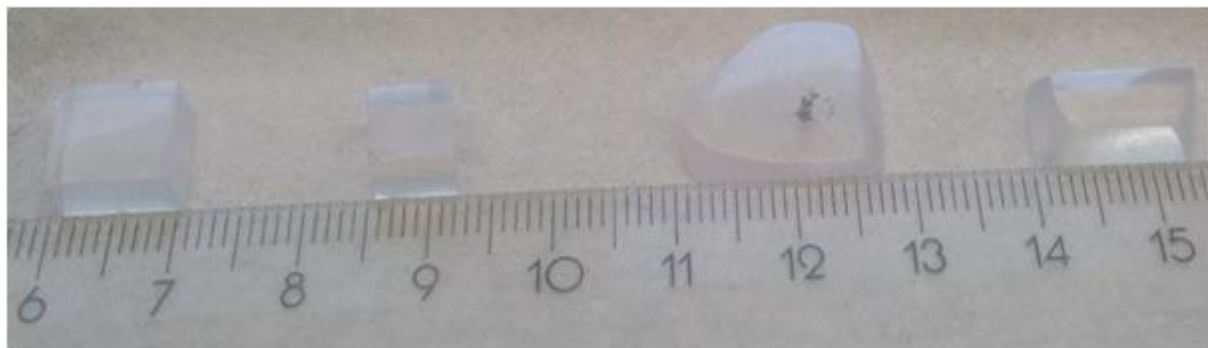


Figure 5.34: Some harvested and polished crystals.



Figure 5.35: Polished samples optically coupled to the quartz glass window using epotek opt. adhesive.

5.1.3.7 SrI₂: 2% Eu – 7

All the experiences won from previous experiments so far were invested in this particular crystal growth experiment. It was noticed that despite storing both EuI₂ and SrI₂ in air-tight bottles in the glovebox, the decomposition of these materials could not be stopped. The EuI₂ was also noticed to be sensitive to light, with the colour changing to shiny-violet/shiny metallic black. The materials showed strong yellowish coloration after dehydration (Figure 5.36), so they were zone-refined prior to the crystal growth.

For the zone refining a temporary floating-zone setup was put in place. It consisted of a 15 cm long horizontal Bridgman furnace and a pulling mechanism as shown in Figure 5.37 – a, Figure 5.37 – b shows the SrI₂ – melt and the iodine atmosphere during the zone refining. The zone-refining was done in excess iodine gas atmosphere, in order to restore the stoichiometry of the partly decomposed material. In order to maintain a small molten zone for a better cleaning effect, both sides of the furnace were kept open. In Figure 5.38, one can see the impurity concentration at the lower part of the ampoule. For the crystal growth, the zone-refined material was loaded in a new ampoule.

Figure 5.39, Figure 5.40 and Figure 5.41 show the ampoule after growth. Notice here the strong dark coloration at the first to freeze region and the top of the crystal. After a long search, we decided to grow this material in the excess atmosphere of one of its compositional materials, the iodine gas. The functions of iodine in the growth ampoule are:

Experiments and Results - 5

1. Restoration of any change in the material stoichiometry from dehydration.

It is well known that iodine containing compounds are very unstable. The analysis data sheet from the producer showed the SrI_2 and EuI_2 to contain various trace elements, especially alkaline metals and other alkaline earth metals. These trace materials are present as iodine-compounds; while most of them decompose during dehydration with iodine gas leaving the ampoule. Any change in the stoichiometry of the SrI_2 due to iodine deficit from dehydration is to be corrected during the crystal growth.

2. Improvement of the heat conductivity and distribution in the ampoule.

The SrI_2 pulls from the ampoule walls upon crystallization. It was thought that excess iodine gas in the ampoule could fill up the gap between the crystal and the ampoule, thereby regulating the heat dissipation of the crystal.

3. To fill up the vacuum in the ampoule and prevent material decomposition during melting process.

Vacuum in the growth ampoule would create room for material decomposition. A vapour of the material components would fill up this empty room, so the idea was to make sure this room doesn't exist. The excess iodine is not incorporated into the crystal lattice of the SrI_2 .

The dark coloration seen at the top of other crystals is not present in Figure 5.40. No grain boundaries or cracks and defects visible in the crystal in Figure 5.42 and Figure 5.43 under UV-light.

The success of this crystal growth experiment proved the notion that the 3 mm diameter thermocouple was responsible for the defects (grain boundaries) in all the crystals, and not the pulling or cooling rates used during the crystal growth experiments. The pulling rate was 0.25 mm/hr, the cooling rate 5 °C/hr. The temperature gradient in the buffer region of the furnace was 20.86 °C/cm.



Figure 5.36: 1“ (1-inch) diameter ampoule after dehydration. Notice the yellowish coloration.

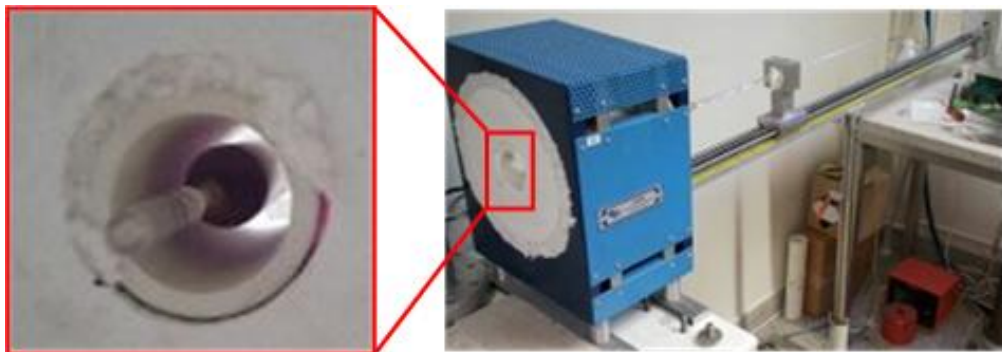


Figure 5.37: a) A 15 cm long furnace used for zone-refining and the pulling mechanism. b) SrI_2 -melt during the zone-refining.



Figure 5.38: The ampoule after zone-refining.

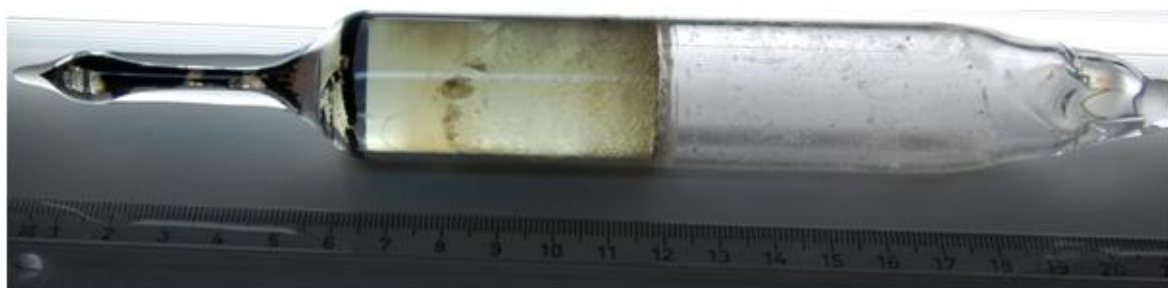


Figure 5.39: 1-inch ampoule after the crystal growth.



Figure 5.40: The ampoule under white light. Notice the dark coloration at the first to freeze region.



Figure 5.41: The first to freeze region showing the excess iodine growth gas.

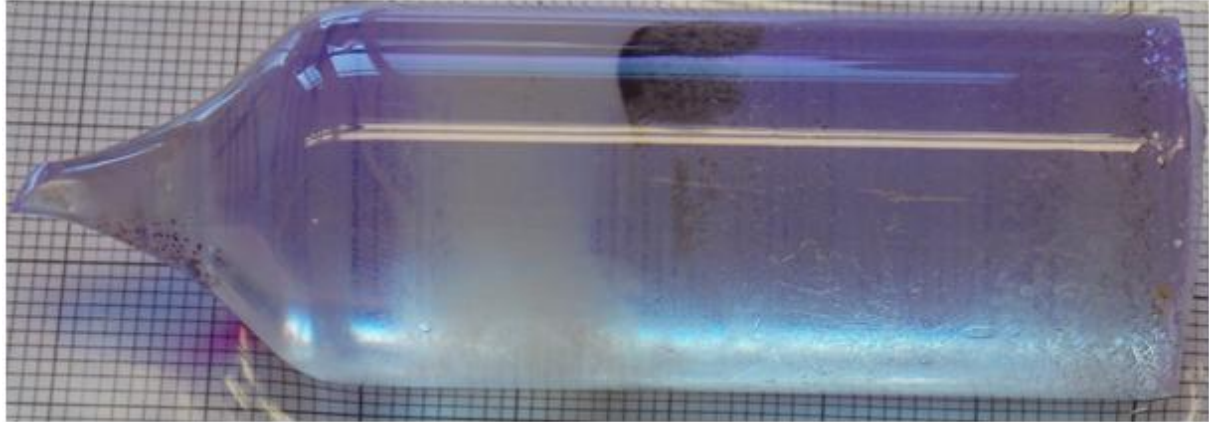


Figure 5.42: The harvested crystal.

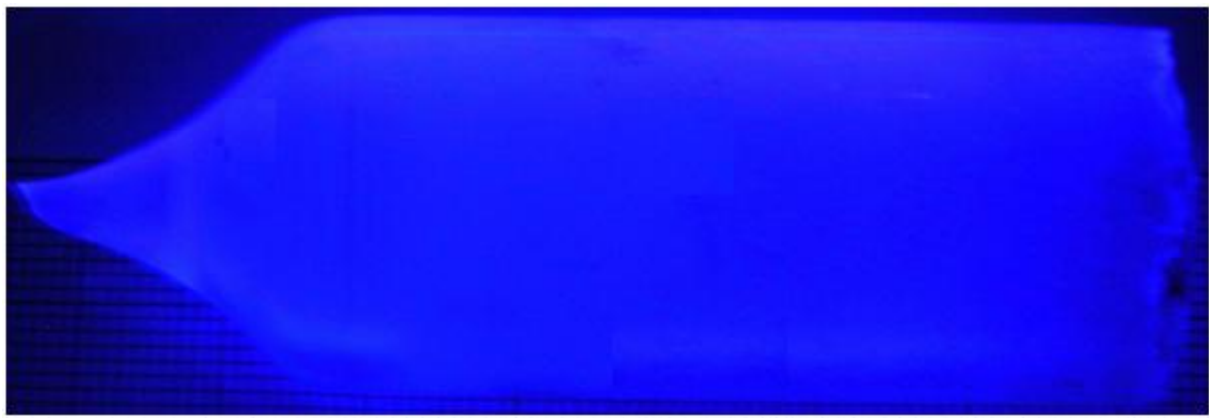


Figure 5.43: Homogenous crystal emission under UV-light. No defects visible.

5.1.3.8 SrI₂ – 8

Growth no.8 was aimed at reproducing the growth no.7. The optical absorption spectra and UV-diffuse reflectivity of the SrI₂ would be measured using this crystal. A better knowledge of these parameters would help to estimate the band gap of the SrI₂ and increase the photon yield. The material used here is undoped SrI₂.

Notice in Figure 5.44 the dark coloration in the middle of the ampoule, the red marked areas in Figure 5.45 and the design of the grain selector in Figure 5.46. The dark coloration are impurities as there was no zone-refining of the SrI₂ material prior to the crystal growth.

Marked in red are defects, the first defect in the middle of the crystal could only propagate half way through the crystal diameter, the second propagated all through the crystal. These defects were attributed to the oxide layers of the copper-metal growth chamber shown in Figure 5.47 and Figure 5.48. These oxide layers were found to lie on the ampoule at the end of the crystal growth. The design of the grain selector was also modified to subdue the growth of multiple grains.



Figure 5.44: The ampoule after growth. 1 cm diameter.



Figure 5.45: The ampoule under white light. Marked in red are defects.



Figure 5.46: Notice the design of the grain selector, this was done to subdue multiple grain growth.

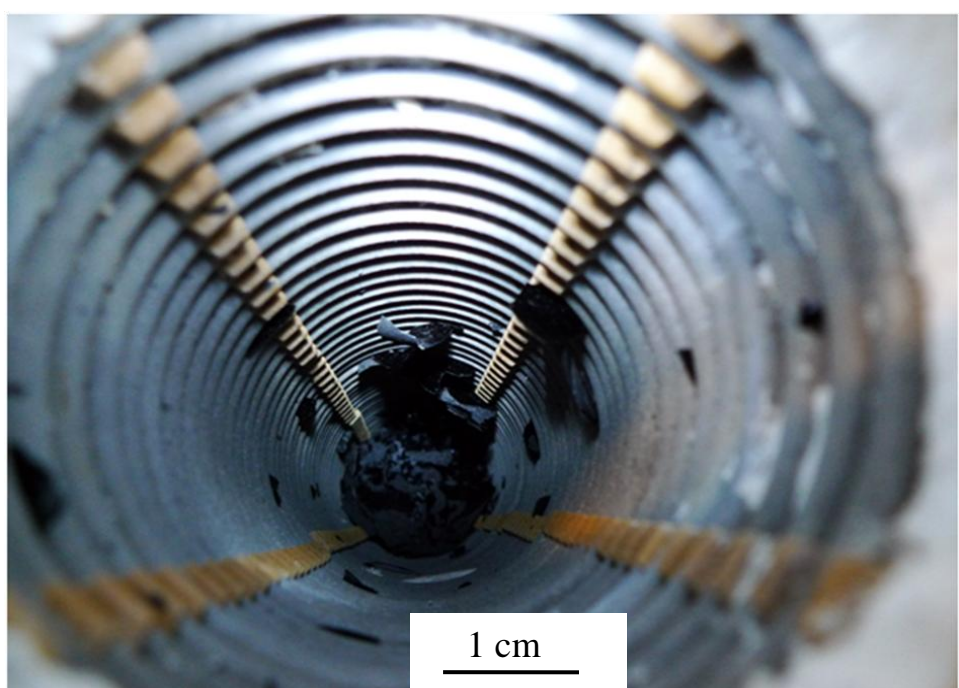


Figure 5.47: Inside of the Bridgman/Stockbarger furnace after the crystal growth.



Figure 5.48: The oxidized copper-metal growth chamber.

5.2 Crystal Preparations and Packaging

5.2.1 Crystal Preparations

All the preparation work before and after the crystal growth is done in an argon-gas purged glovebox with moisture content always $< 1 \text{ ppm}$. Crystal cutting is done using 0.3 mm diameter diamond wire manufactured by well. The cutting is normally done in paraffin oil. Crystals are ground on Buehler, LECO and Struers SiC grinding papers (p400, p800, p1200 and p4000). The polishing is done in paraffin oil using $1 \mu\text{m}$ ($1 \mu\text{Grit}$) Al_2O_3 from (Pieplow & Brandt) on a Buehler Texmet lap. At the end of polishing, crystals are washed with kerosene.

5.2.2 Crystal Packaging

5.2.2.1 Samples for Spectroscopic Measurements

For spectroscopy measurements, crystals were hermetically encapsulated in aluminum containers with quartz glass optical window. Figure 5.49 shows the materials used for the first set of encapsulations, a normal Teflon tape served as the reflector. The basics of the first packaging technique are shown in Figure 5.50. Crystals were wrapped with the Teflon tape and then enclosed in the hermetic capsule as shown in Figure 5.51.



Figure 5.49: Materials for the crystal encapsulation.

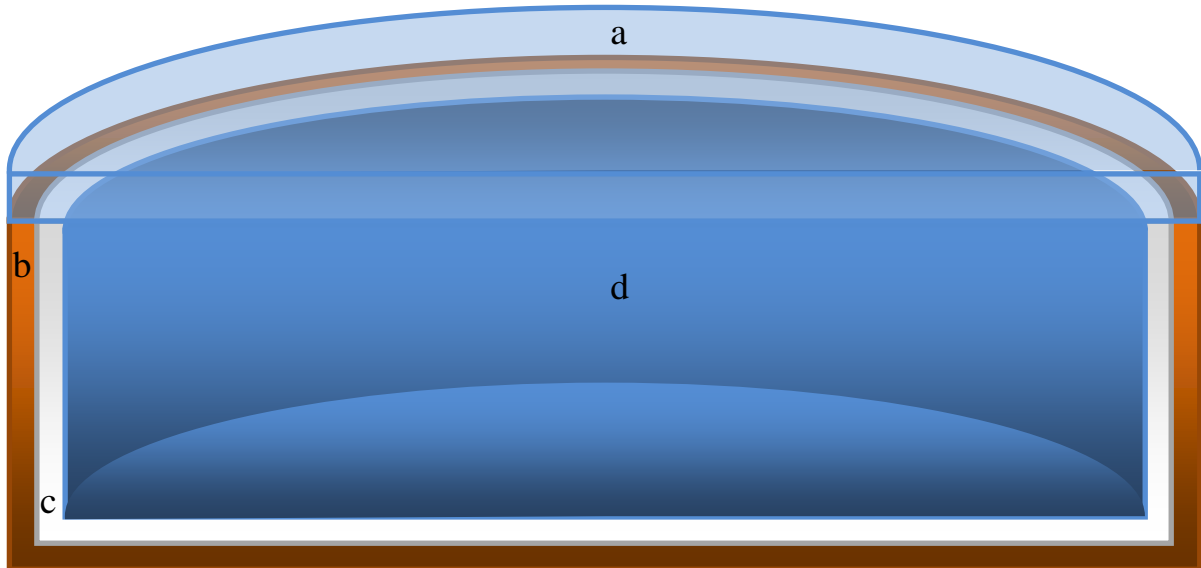


Figure 5.50: The basics of the first packaging used in this work with (a) the quartz glass detector window; (b) the aluminium container; (c) the reflector and (d) the crystal. This was modified in the second packaging by applying an optical coupler between the crystal and detector window.

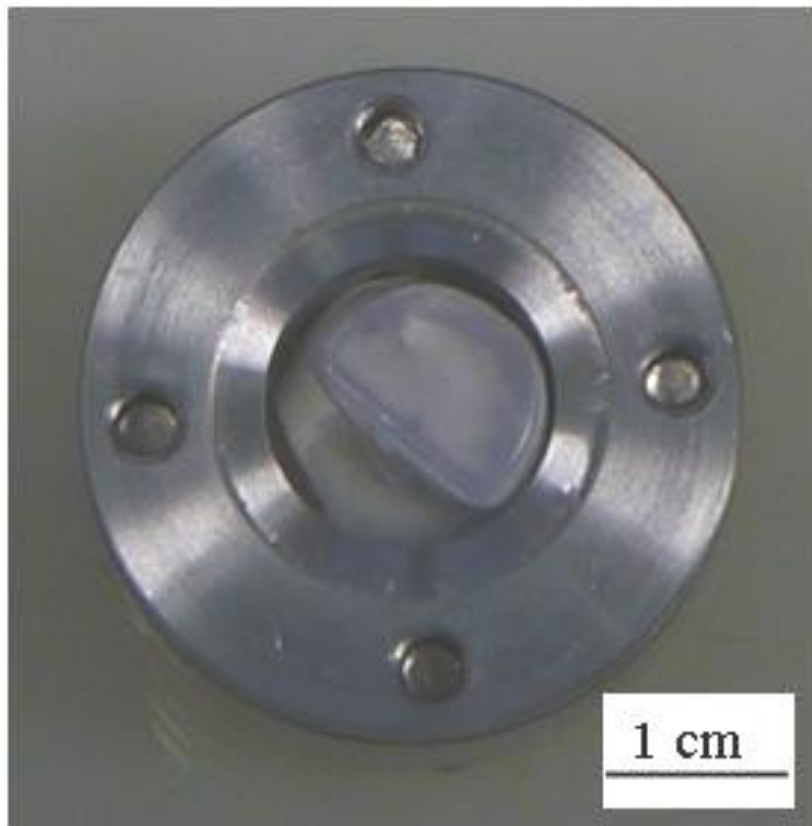


Figure 5.51: The first encapsulation with the crystal wrapped in a Teflon tape reflector.

Later, the thickness of the aluminium container was reduced with an optical coupler applied between the crystal and the detector glass window. The optical coupler tested here is the Bicron BC-630 from Saint-Gobain. This optical coupler was noticed to bleed after encapsulations as shown in Figure 5.52, which is not good for the scintillation photons. We started searching for another optical coupler, that doesn't react with the SrI_2 .

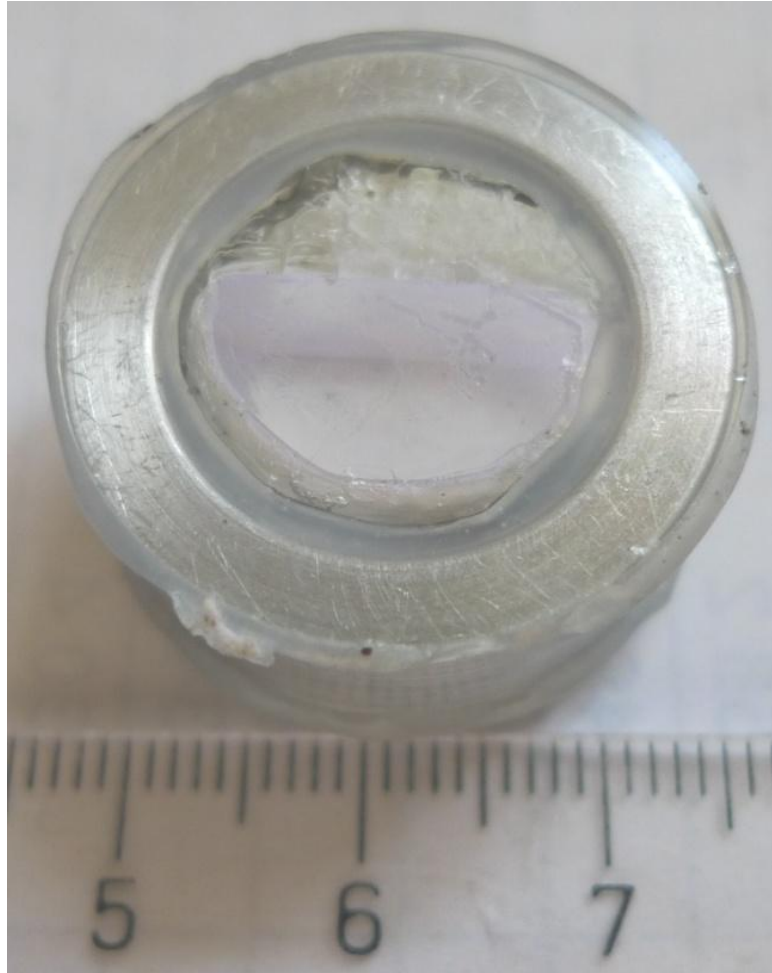


Figure 5.52: The second technique with the thickness of the Al-container reduced and the crystal optically coupled to the quartz glass using Bicron BC-630. Notice the bleeding between the crystal and the quartz glass.

Later the complete packaging process was modified. The aluminium container became very thin (1.5 mm thickness), an epoxy was used as optical coupler. The epoxy is the EPO-TEK 305/B4 Opt. Adhesive. It is a two component colourless optical coupler with transmission range 248 - 1600 nm and index of refraction of 1.4763 at 589 nm.

Figure 5.53 shows the basics of the third packaging technique. This was developed and tested in this work. The idea behind it is the reflector used in bicycle light as demonstrated in Figure 5.54. The light photons leaving the crystal from the sides are reflected towards the PMT. Normally crystals are wrapped in the reflector and light photons emitted from the sides are reflected back into the crystals. These light photons don't stay in the crystal forever. There is a certain probability that they might be absorbed in the crystal.

Another problem is the issue of light trapping; a high ratio of the refractive indices between the scintillator and its environment would lead to trapping of the light between the scintillator and the reflector. Figure 5.55 shows a sample after assembling. Instead of a Teflon tape, aluminium foil served here as the reflector because it can be formed into a particular shape. The decision to use aluminium foil as reflector was based on the work of [Birks 1964], which gave the reflectivity to be ~ 90% down to 300 nm.

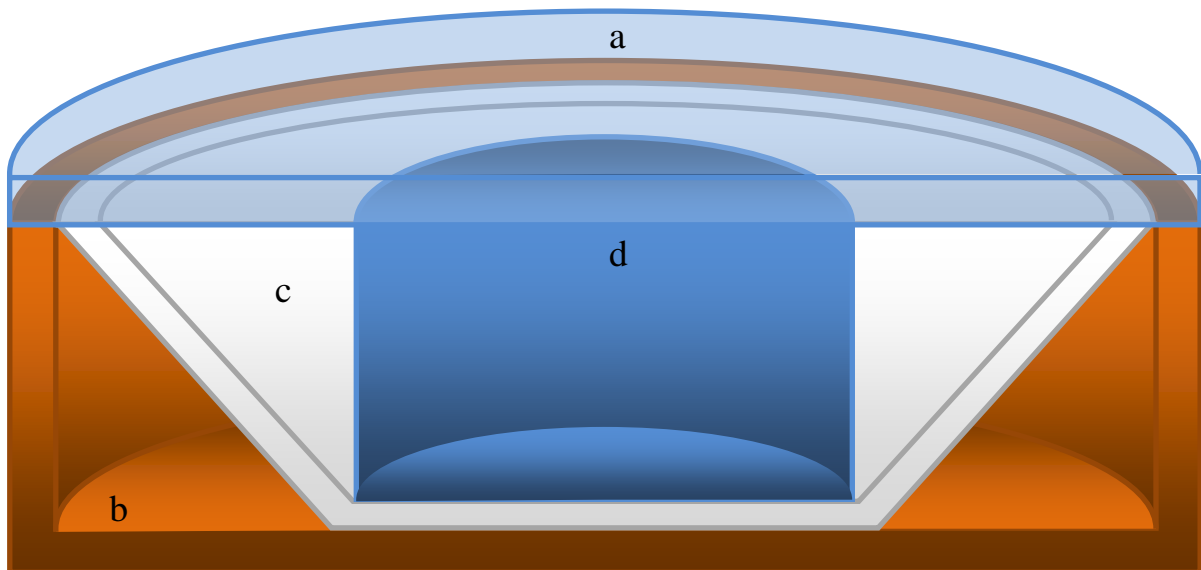


Figure 5.53: The basics of the third packaging technique developed and tested in this work. Notice the form of the aluminium reflector. (a) is the quartz-glass detector window, (b) is the aluminium container, (c) is the reflector and (d) the crystal.

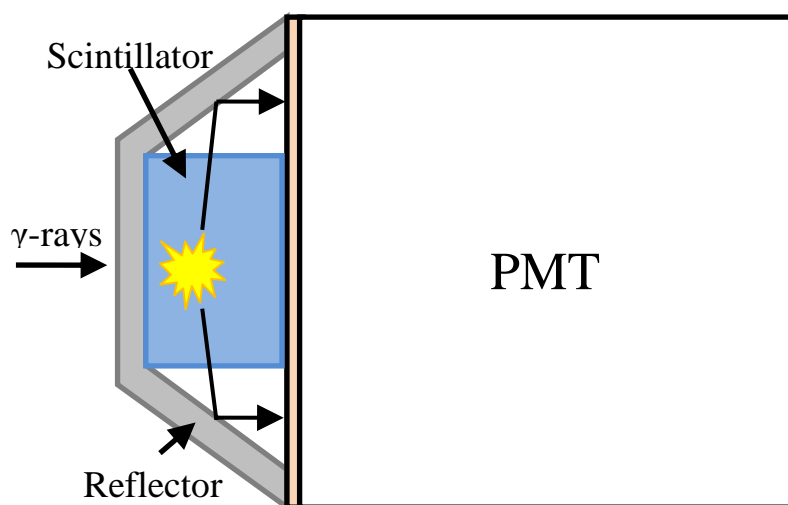


Figure 5.54: Paths taken by light photons leaving the crystal from the side.

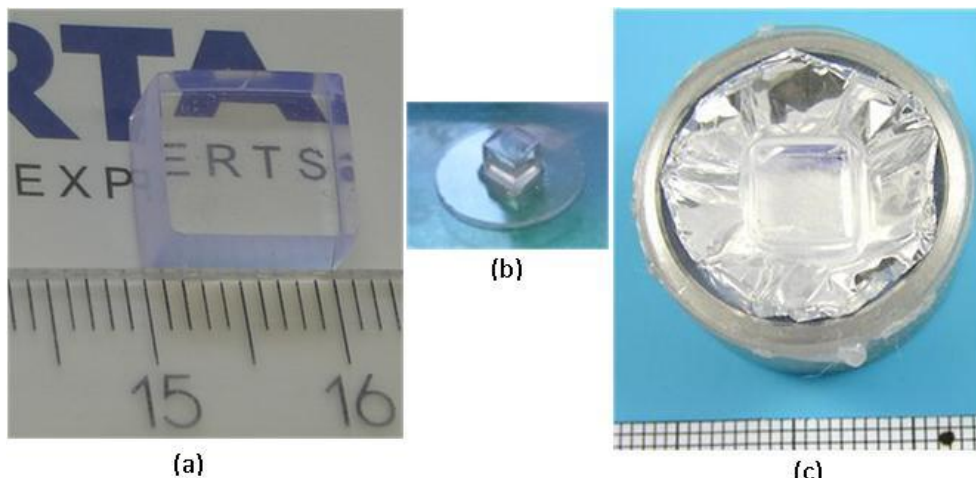


Figure 5.55: The third packaging technique. (a) polished crystal, (b) crystal glued to the quartz glass using (EPO-TEK 305/B4 Opt. Adhesive). (c) Aluminium foil used as a reflector.

5.2.2.2 Samples for X-Ray Imaging

Thin SrI₂-scintillator screens were tested in this work for X-ray imaging applications. The micrometer samples (maximum thickness 400 µm) were glued to an aluminium slide ~ 210 µm thick, the aluminium slide is optically polished in order to reduce the scattering of the scintillation light photons, which would affect the quality of the obtainable image. A quartz glass ~ 170 µm is used to cover the samples in order to prevent the oxidation of the surface. The quartz glass is glued to the aluminium slide using an epoxy kit (KL-320K) from Lesker. The packaging technique is demonstrated in Figure 5.56, while Figure 5.57 shows a 360 µm thick screen ready for X-ray imaging measurements.

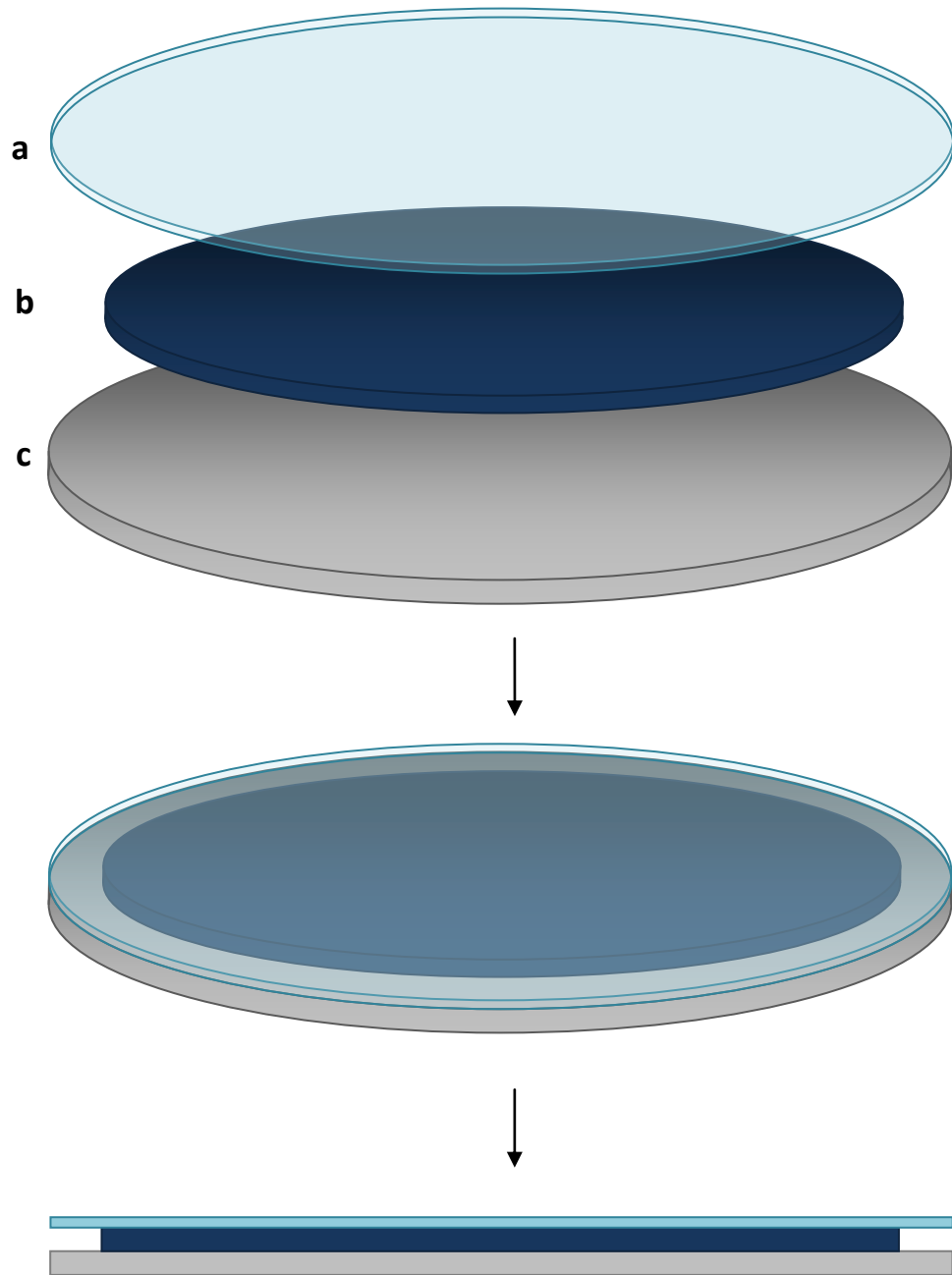


Figure 5.56: Packaging of the SrI₂-scintillator thin screens for X-ray imaging. (a) is 150 – 170 µm quartz glass slide; (b) is the scintillator screen 400 µm max. thickness; (c) is the aluminium back slide ~ 210 µm thick.



Figure 5.57: A 360 μm SrI_2 -scintillator thin screen for X-ray imaging.

5.3 Spectroscopic Measurements

During the spectroscopic measurements, the energy spectra, decay time spectra and radioluminescence spectra were recorded. The energy resolution of the scintillator crystals was calculated from the Gaussian distribution function fitted to the photopeak of the energy spectrum. The light yield of the samples were estimated by comparing the current-pulse-height of the $\text{SrI}_2:\text{Eu}^{2+}$ - scintillator samples to that of a $\text{NaI}:\text{Tl}$ - scintillator reference sample.

Much detail about the experimental conditions would not be given here, because the measurements were done at the research center, Jülich and at the FISK University, Tennessee as will always be indicated. Below the performance of each sample will be presented.

Radioluminescence spectra were recorded at the synchrotron light source ANKA (TopoTomo beamline) in Karlsruhe. The synchrotron light source is operated at 2.5 GeV ring electron energy and 180-80 mA beam current. The available energy spectrum ranges between 1.5 and 50 keV [Cecilia 2009]. The light was passed through a *Jobin Yvon CP140-104* spectrograph working in the 250-800 nm range and detected with a high resolution cooled CCD camera (*PCO4000*) positioned in the focal plane of the spectrograph.

5.3.1 SrI_2 : 5% Eu^{2+} - 1

The sample-1 was wrapped in Teflon tape and hermetically encapsulated in an aluminium container using quartz glass as detector window, Figure 5.58.

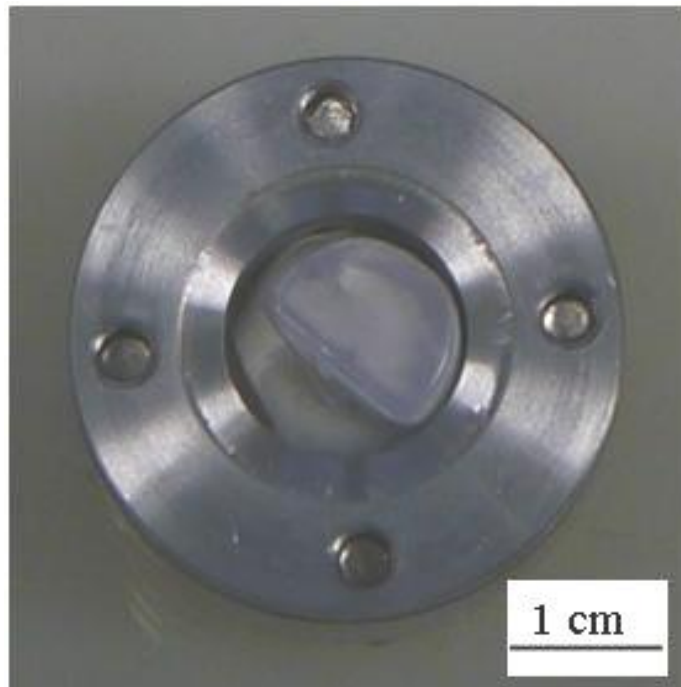


Figure 5.58: The measured crystal slightly $< 1 \text{ cm}^3$.

The energy resolution of this sample is 15.9% at 662 keV (FWHM), Figure 5.59. No doubt the packaging and polishing must have strongly influenced the results obtained, especially the energy resolution which depends on the transfer efficiency of the photons from the scintillator to the PMT, among other factors.

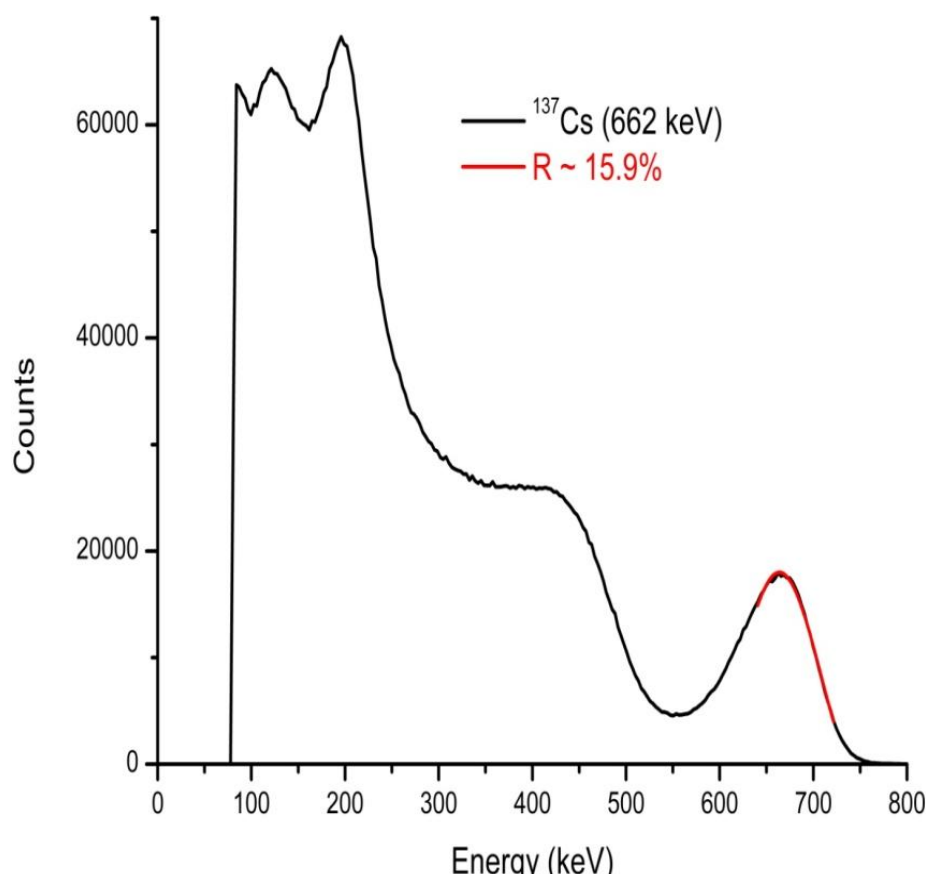


Figure 5.59: Pulse height spectrum of ^{137}Cs -isotope recorded with the sample - 1.

Experiments and Results - 5

Figure 5.60 shows the output signal of the PMT anode, the decay constant calculated after fitting the curve with a single exponential decay function (ExpDec1) was $1.39 \mu\text{s}$.

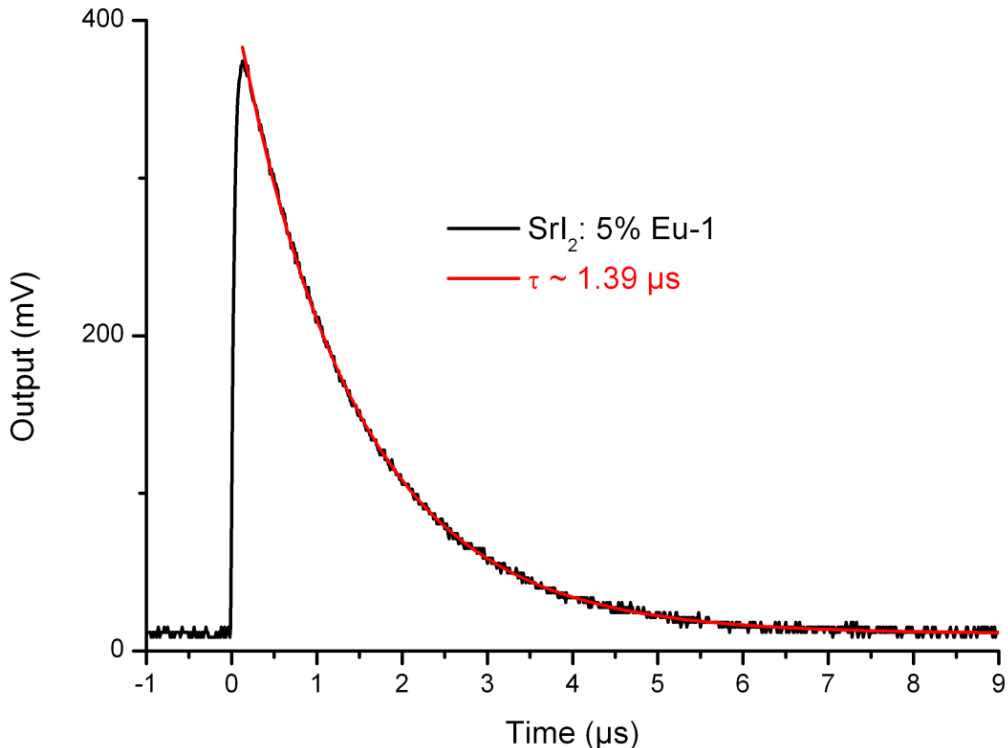


Figure 5.60: The recorded scintillation light decay curve with a decay constant of $1.39 \mu\text{s}$.

The recorded radioluminescence spectrum in Figure 5.61 shows a single broad band emission from $\text{Eu}^{2+} 4f^6 5d \rightarrow 4f^7$ transitions peaking at 431 nm.

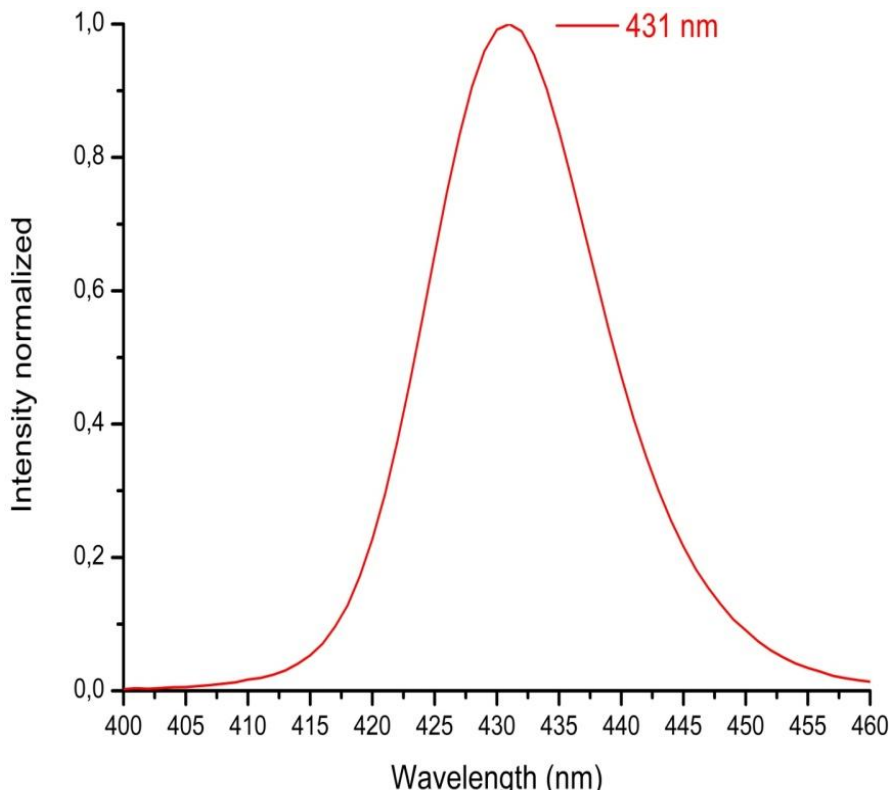


Figure 5.61: The radioluminescence spectrum showing a 431 nm emission wavelength.

5.3.2 SrI₂: 6% Eu²⁺ - 3

There was some improvement in the polishing and packaging of sample 3. Gluing the samples during polishing helped improve the surface finishing. It took some time to find out the right glue for this purpose, that doesn't react with the material and also easy to remove after polishing.

Sample 3a (First Measurement)

The first packaging of the sample-3a is shown in Figure 5.62. Here an optical coupler was tested, the Bicron BC-630.

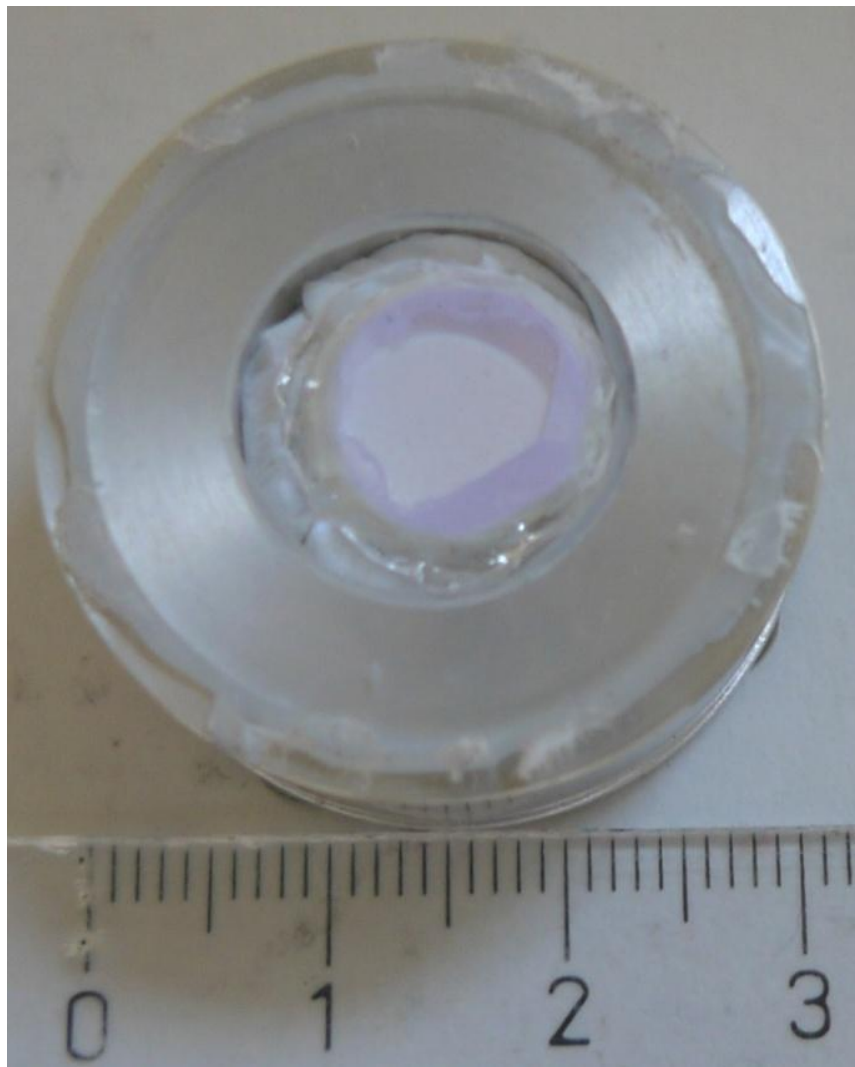


Figure 5.62: The first packaging and the first measurement of sample 3a (< 1 cm³). Bicron BC-630 optical coupler applied between crystal and detector window and Teflon tape served as a reflector.

With this packaging, an energy resolution of 15.4% for the (FWHM) was achieved which is shown in Figure 5.63. After the measurements, a kind of bleeding of the optical coupler was noticed, that might have affected the results.

Experiments and Results - 5

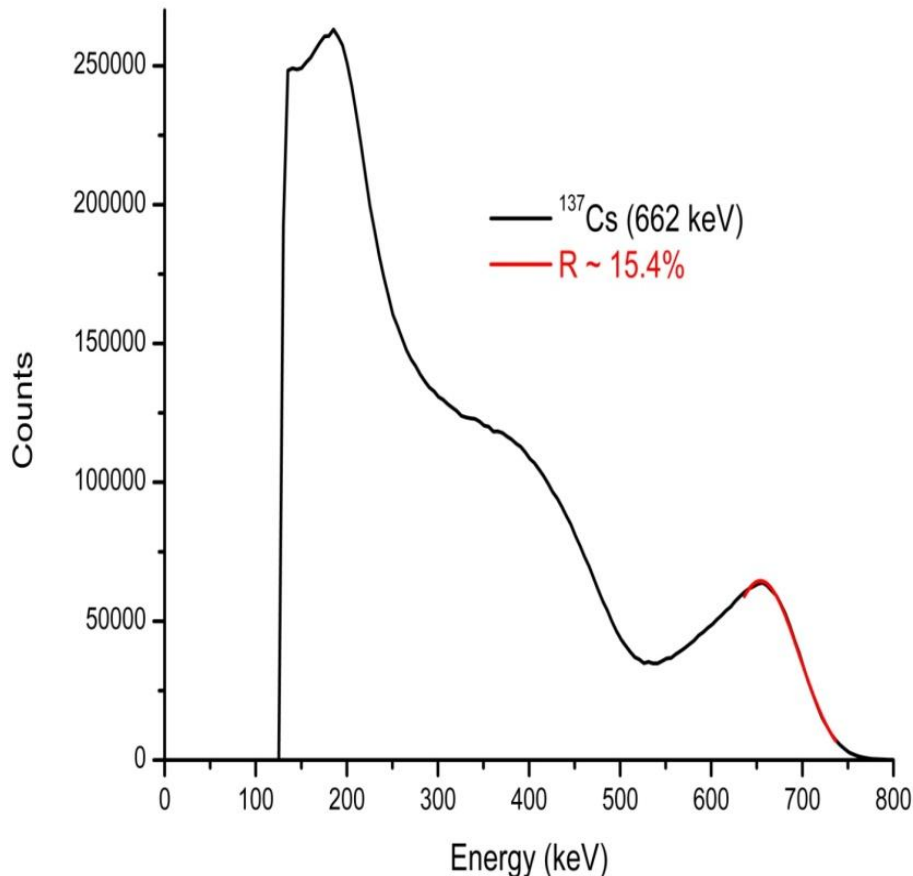


Figure 5.63: Pulse height spectrum of ^{137}Cs recorded with this sample.

The signal output here was also fitted with a single exponential decay function (ExpDec1) yielding a decay constant of 1.38 μs , Figure 5.64.

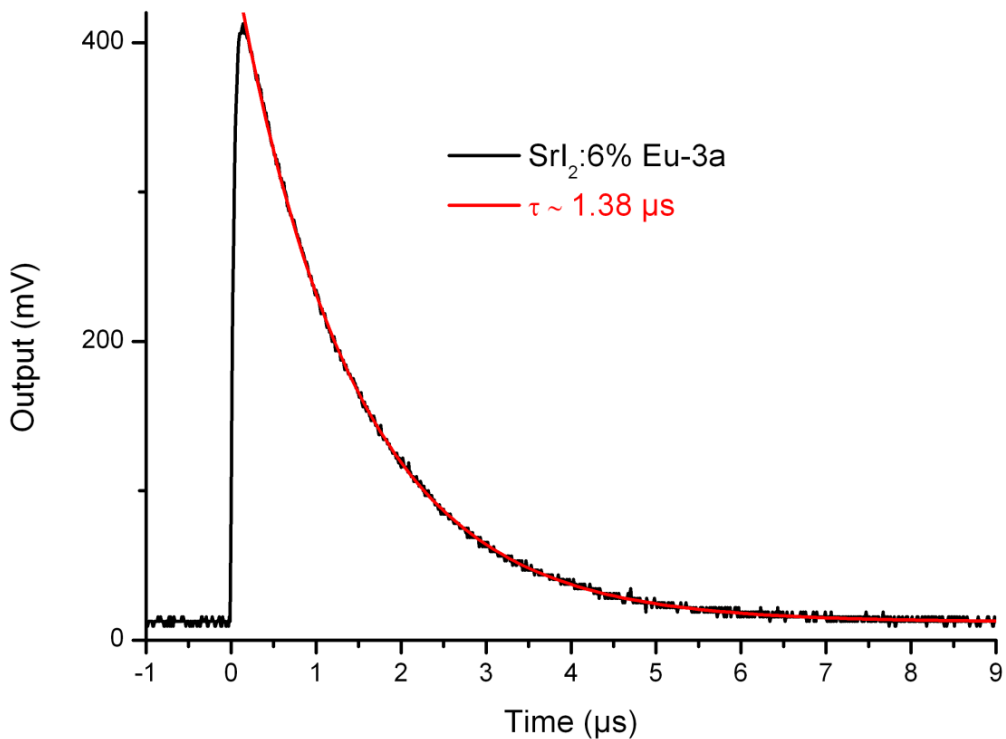


Figure 5.64: Scintillation light decay curve with a decay constant of 1.38 μs .

Second Measurement

The sample-3a was repackaged. This time EPO-TEK 305/B4 Opt. Adhesive was used. The packaging is shown in Figure 5.65, with aluminium foil serving as the reflector.



Figure 5.65: The second packaging using EPO-TEK 305/B4 Opt. Adhesive and aluminium foil as reflector.

An image of the sample-3a emission under UV-light is shown below. The emission of this sample is homogenous. Unfortunately, there are also few bubbles visible, which were produced during the mixing of the two component optical coupler.

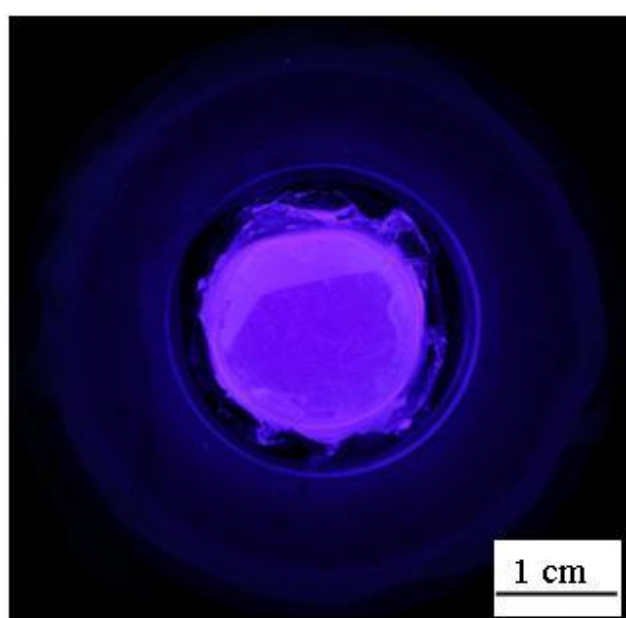


Figure 5.66: The sample emission under UV-light.

Experiments and Results - 5

With this second packaging, the energy resolution improved from 15.4% to 11.7% at 662 keV as shown below. This improvement is attributed to better light collection efficiency of the scintillator through improved packaging.

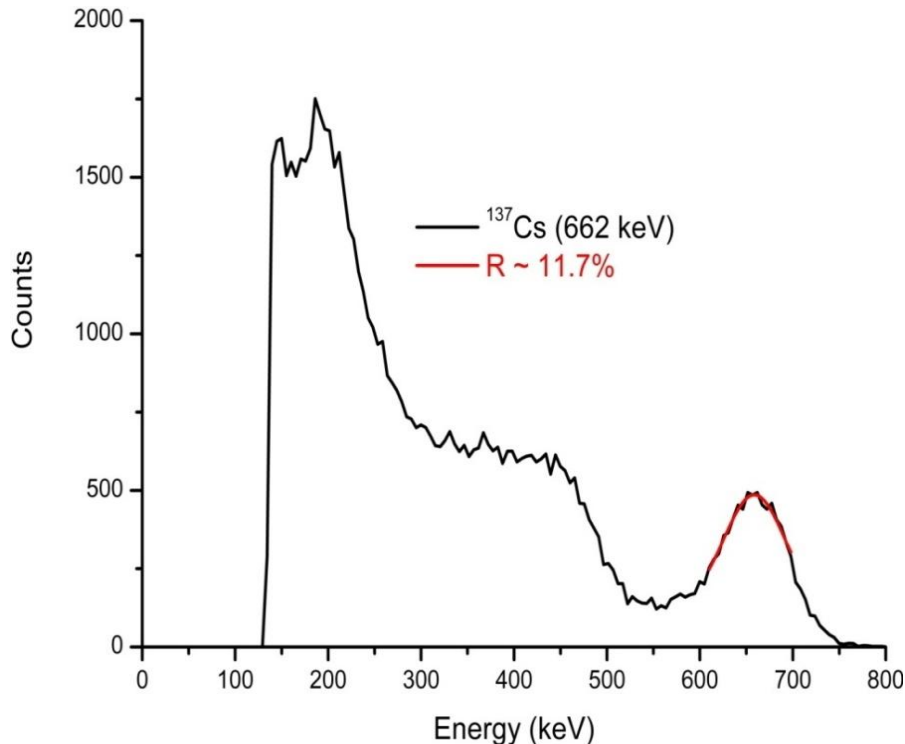


Figure 5.67: Pulse height spectrum of the ^{137}Cs -isotope recorded after the second packaging showing improvement in the energy resolution.

Not only did the energy resolution improve, the signal output also improved. The scintillation decay constant reduced from 1.38 μs to 1.18 μs , Figure 5.68.

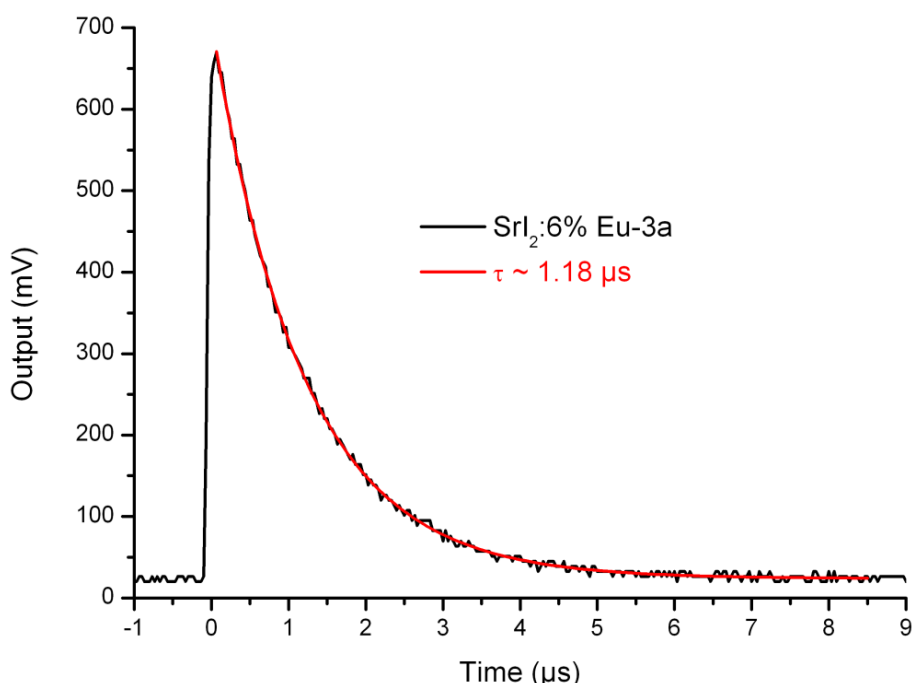


Figure 5.68: Scintillation light decay curve showing a reduced decay constant of 1.18 μs .

Measurement at FISK University

The sample-3a was measured using another experimental setup. This measurement was carried out at the physics department of the FISK University, Tennessee. For the measurements, optical grease was applied between detector and PMT, which is a remarkable difference compared to the experimental conditions used at the research centre, Jülich. Figure 5.69 shows the pulse height spectrum recorded with this sample, a tremendous improvement in the energy resolution is observed.

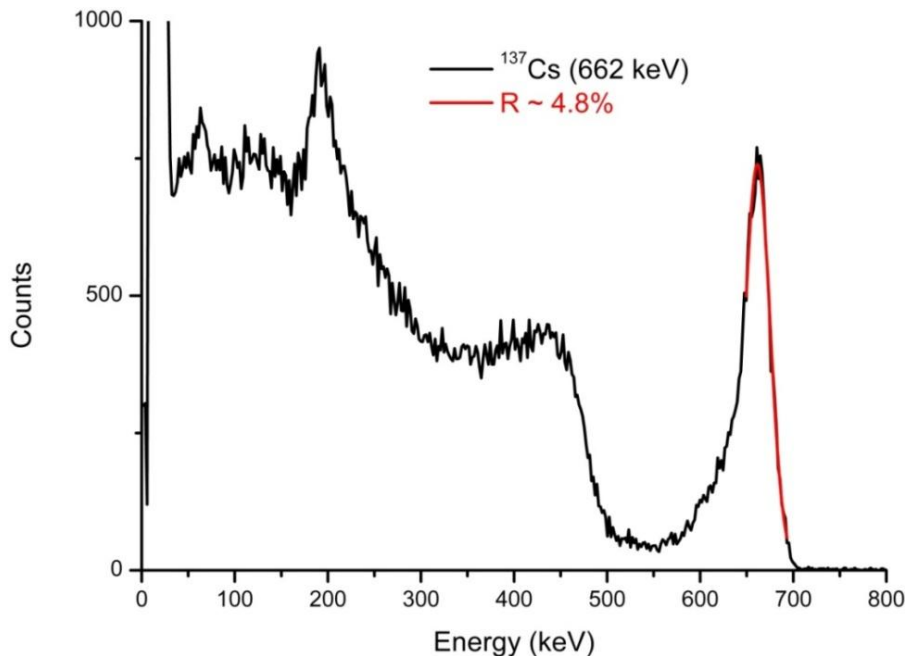


Figure 5.69: Pulse height spectrum of the ^{137}Cs -isotope recorded at the FISK University with a 4.8% energy resolution (FWHM).

A single exponential decay function was also fitted to the recorded output signal yielding a decay constant of $1.58 \mu\text{s}$.

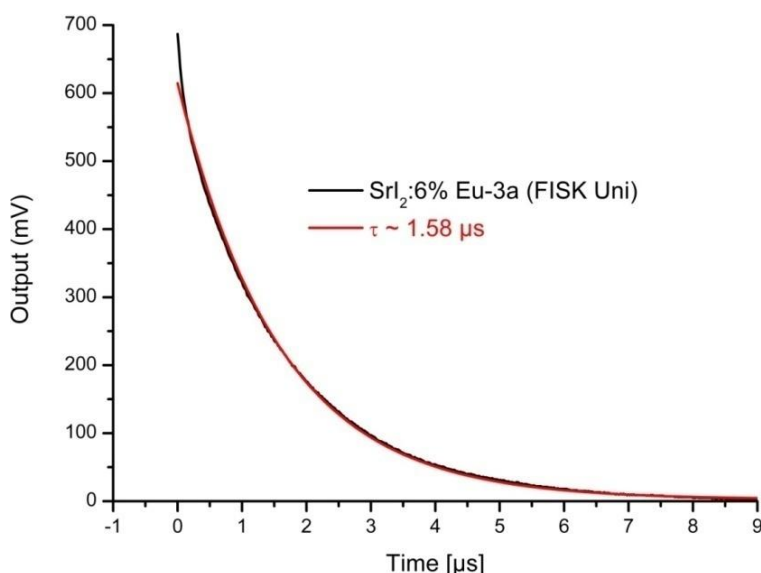


Figure 5.70: The decay curve recorded at the FISK University ($1.58 \mu\text{s}$ decay constant).

Experiments and Results - 5

The radioluminescence spectrum of this sample also shows a single broad emission band typical of Eu^{2+} d \rightarrow f transitions, peaking at 432 nm.

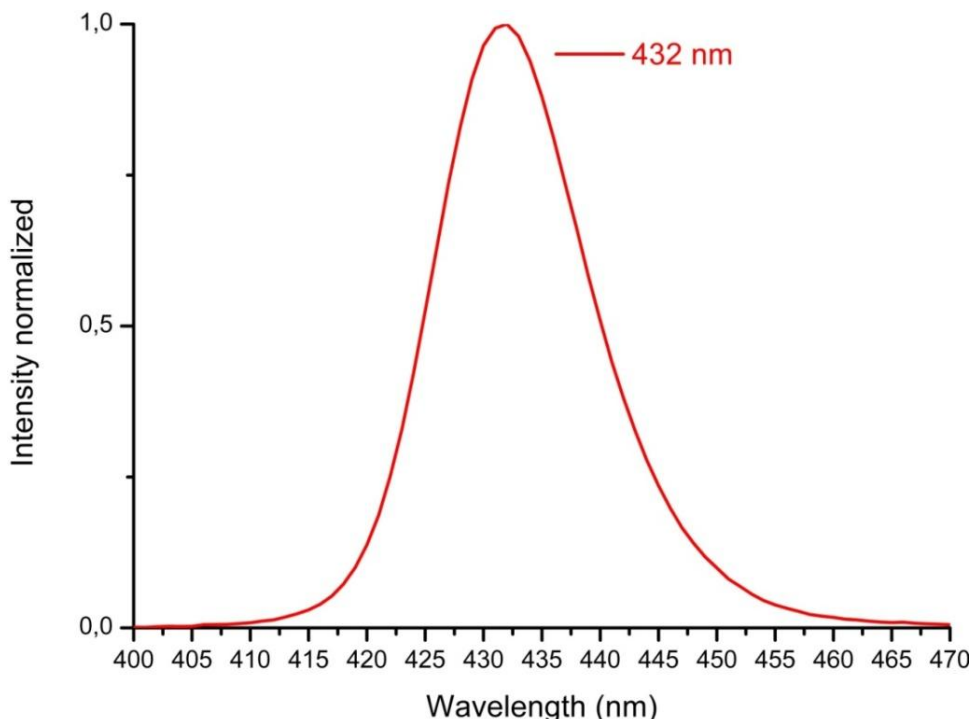


Figure 5.71: The radioluminescence spectrum showing a 432 nm emission wavelength.

Sample 3b

The sample-3b was wrapped in Teflon tape and optically coupled to the detector window using Bicron BC-630 as shown below.

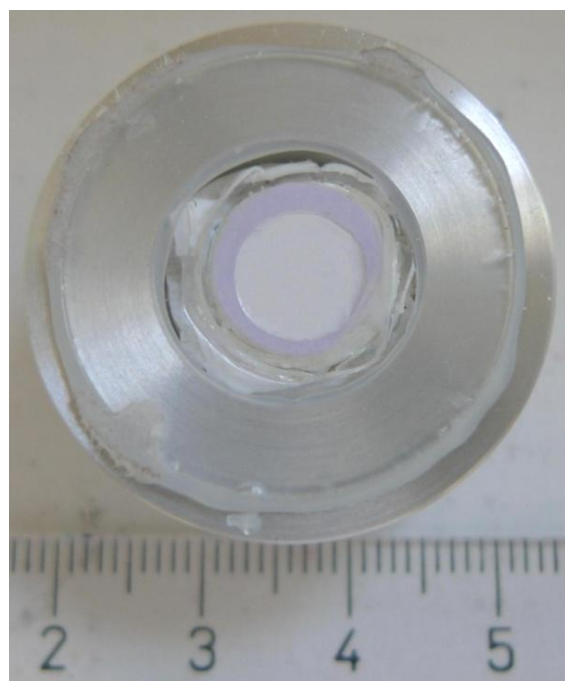


Figure 5.72: Sample 3b packaged with Bicron BC-630 opt. Coupler.

Experiments and Results - 5

This sample could only be measured once. It showed signs of hydration and decomposing after the measurements, thereby turning yellowish. The energy resolution of this sample was 20% at 662 keV (FWHM).

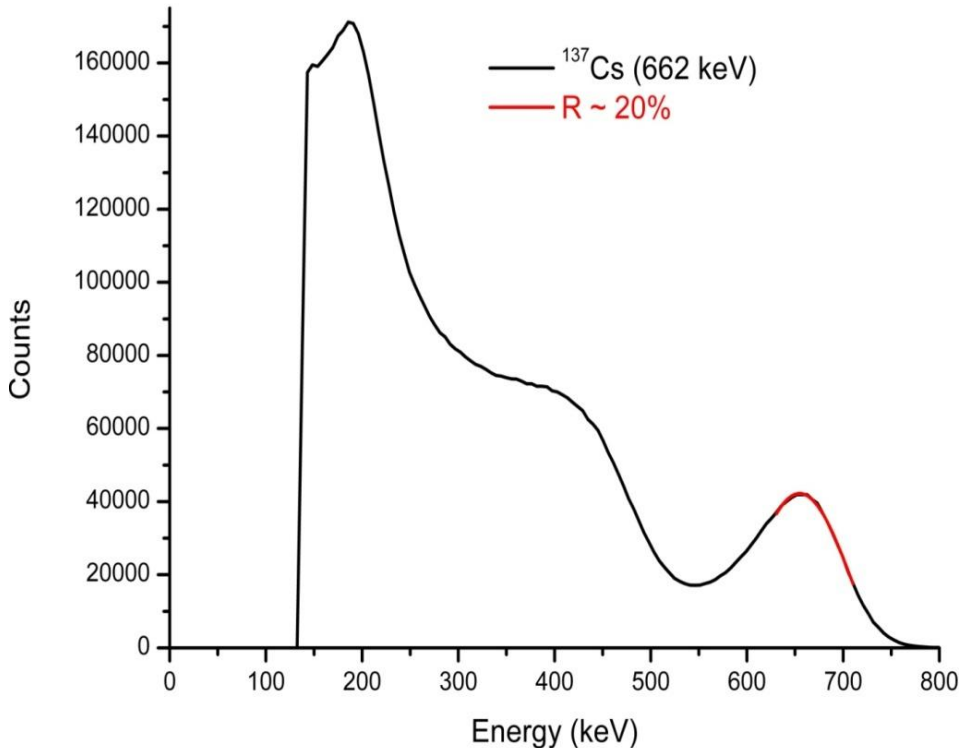


Figure 5.73: Pulse height spectrum of the ^{137}Cs -isotope observed with this sample.

The decay time constant of this sample obtained after fitting with a single exponential decay function was $1.38 \mu\text{s}$.

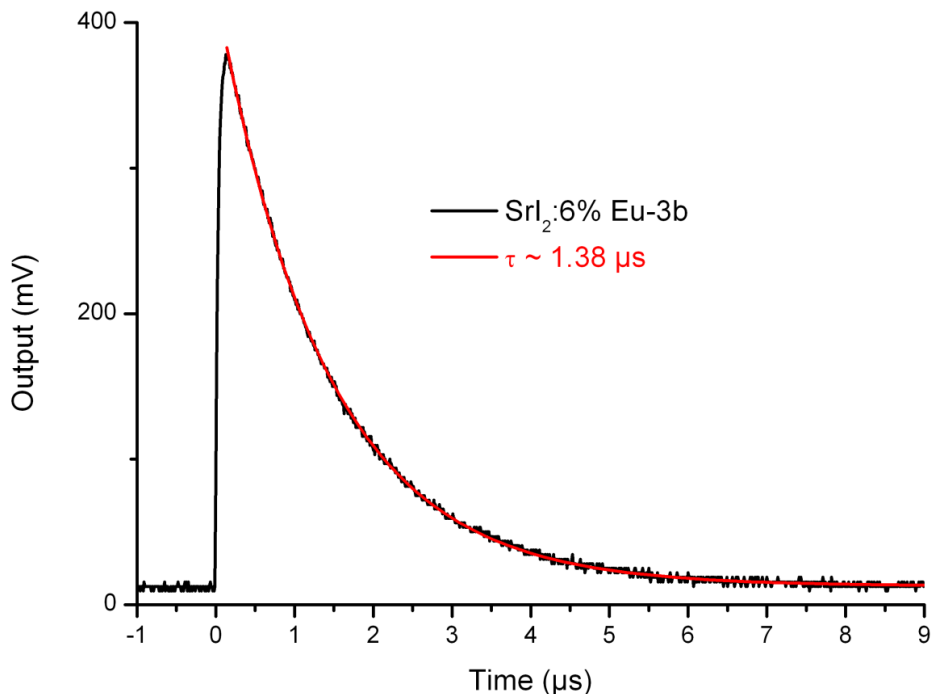


Figure 5.74: The scintillation decay time curve.

Experiments and Results - 5

The emission wavelength of this sample is 432 nm like sample-3a. This was expected since both samples originated from the same crystal ingot.

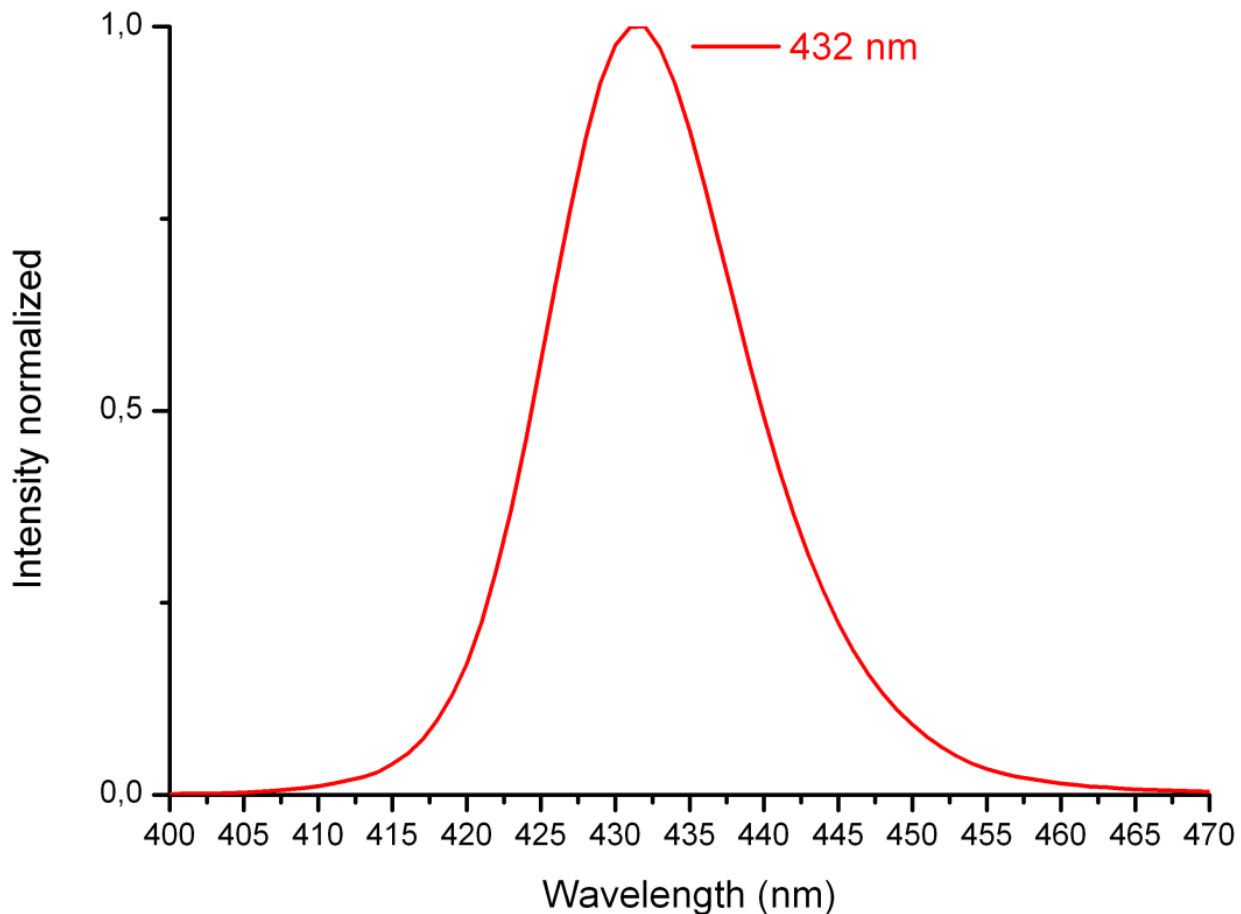


Figure 5.75: The emission spectrum peaking at 432 nm.

5.3.3 SrI₂: 6% Eu²⁺ - 5

Due to the sizes of the crystal samples so far, it was easier packaging them with aluminium foil as a reflector than with a Teflon tape. Wrapping the Teflon tape around the crystals in the glovebox was very difficult. So the sample 5 crystals were wrapped in aluminium foil and optically glued to the detector window using EPO-TEK 305/B4 Opt. Adhesive.

Sample 5a

Figure 5.76 shows the sample-5a after the optical coupling to the detector quartz glass window. In the next step, this sample was wrapped in aluminium foil and hermetically encapsulated in aluminium container.

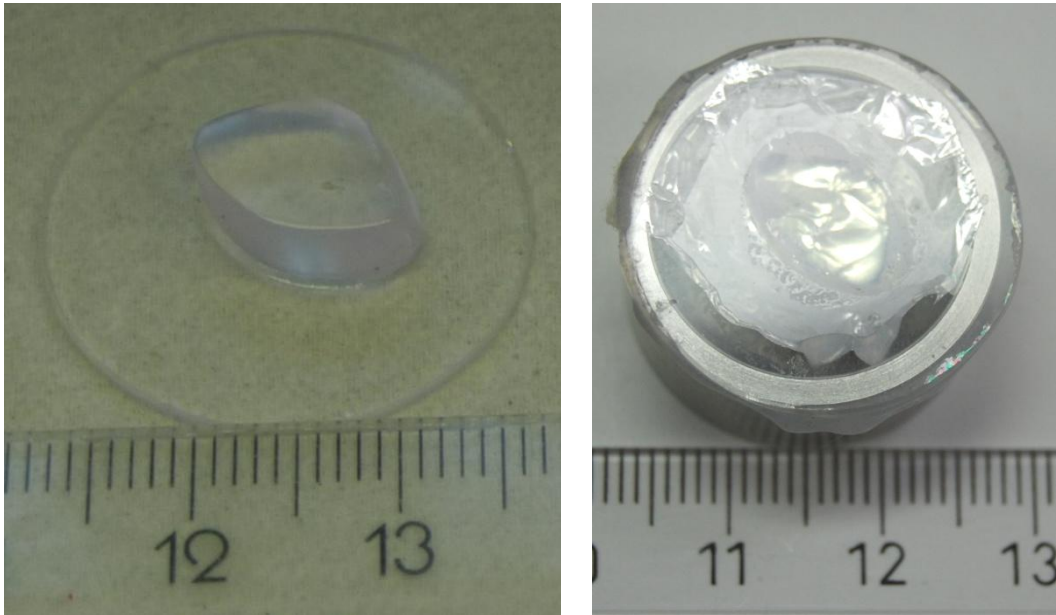


Figure 5.76: Sample 5a ($\sim 1 \text{ cm}^3$) optically coupled using EPO-TEK 305/B4 Opt. Adhesive and aluminium foil served as a reflector.

The sample-5 crystals were zone-refined prior to the crystal growth. The pulse height spectrum recorded with the sample-5a shows an energy resolution of 12% at 662 keV (FWHM) which was some progress compared to the other samples measured using the same experimental setup.

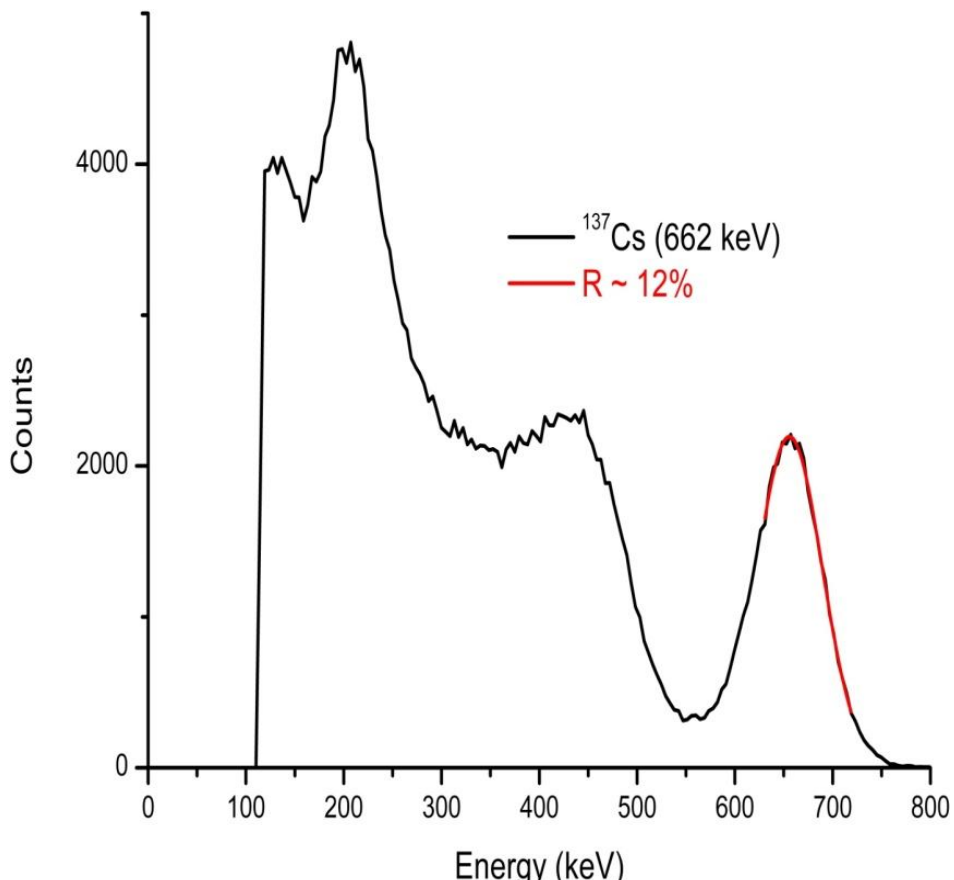


Figure 5.77: Pulse height spectrum of the ^{137}Cs -isotope observed with this sample.

Experiments and Results - 5

The signal output of this sample was also recorded and fitted with a single exponential decay function (ExpDec1). The decay constant of this sample was $0.7 \mu\text{s}$ as shown in Figure 5.78. This is however not a characteristic feature of the $\text{SrI}_2:\text{Eu}$ scintillator, therefore it is being investigated.

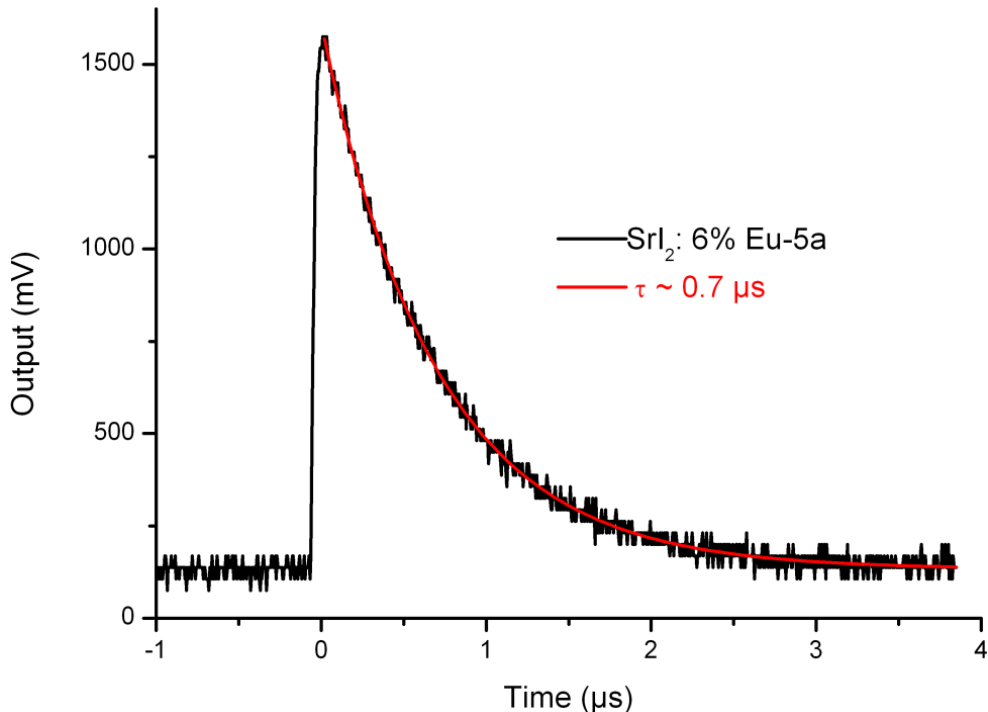


Figure 5.78: The scintillation decay time spectrum.

The emission of this sample also shows a single broad emission band typical of Eu^{2+} d \rightarrow f transitions with peak at 427 nm, Figure 5.79.

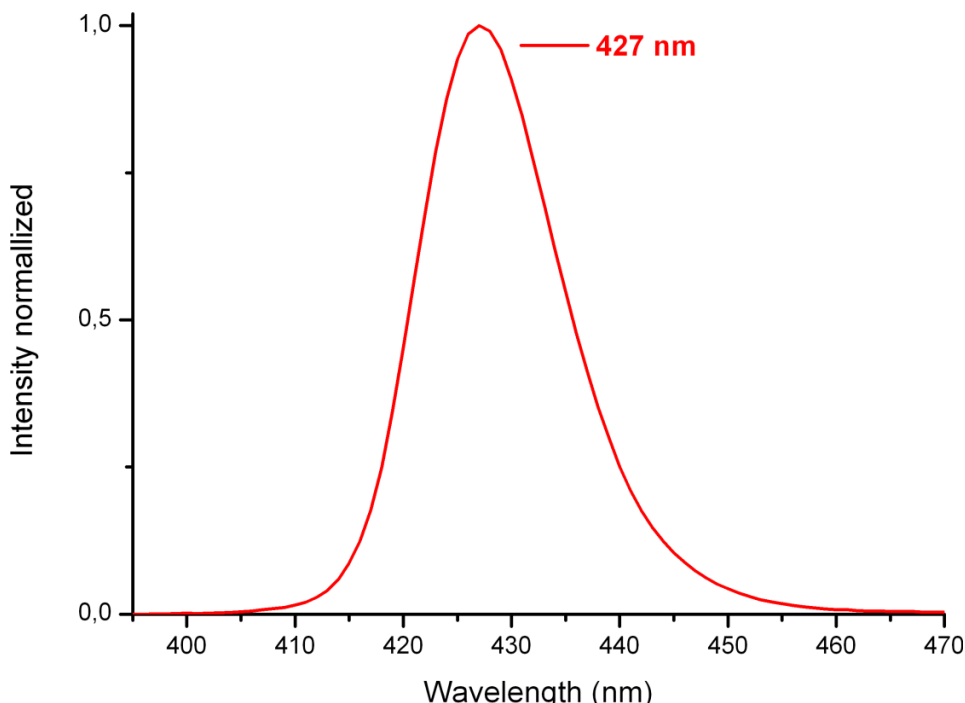


Figure 5.79: The emission spectrum showing a 427 nm emission peak.

Sample 5b

The packaging of the sample-5b is similar to the sample-5a and other samples wrapped in aluminium foil. The sample-5b is shown in Figure 5.80, this is the biggest sample till date with more than one cubic centimetre volume.

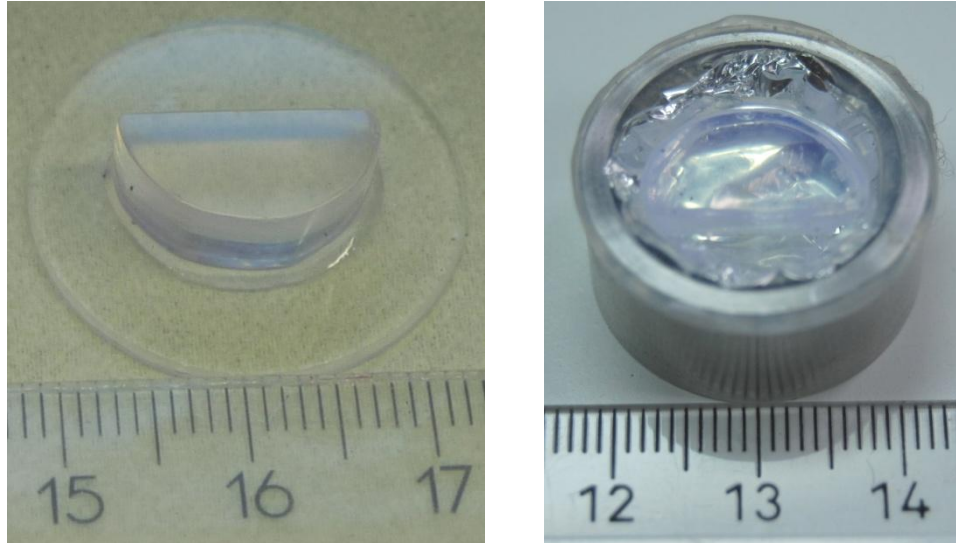


Figure 5.80: Sample 5b ($> 1 \text{ cm}^3$) optically coupled using EPO-TEK 305/B4 Opt. Adhesive and aluminium foil served as a reflector.

The pulse height spectrum recorded with this sample yielded an energy resolution of 14.6% at 662 keV (FWHM).

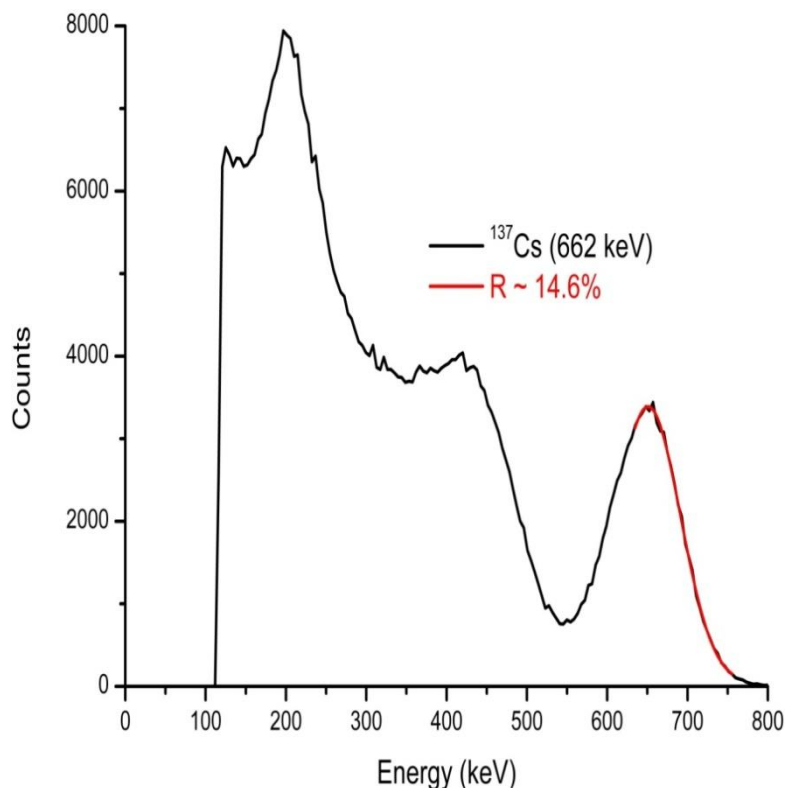


Figure 5.81: Pulse height spectrum of ^{137}Cs observed with this sample.

Experiments and Results - 5

The recorded signal output of this sample is shown in Figure 5.82, a decay time constant of $0.69 \mu\text{s}$ was calculated after fitting with a single exponential decay function. This decay time constant is also untypical of $\text{SrI}_2:\text{Eu}$ scintillator. It is being investigated too, to determine if it has anything to do with the crystal or an experimental error.

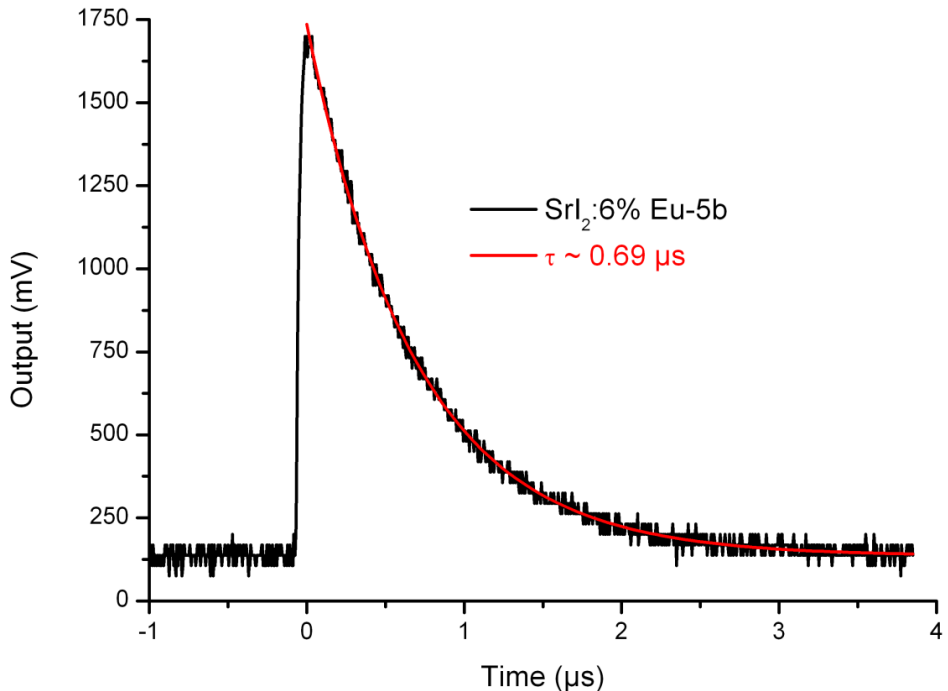


Figure 5.82: The scintillation decay time spectrum.

The emission of this sample shows a single broad emission band of Eu^{2+} d \rightarrow f transitions, peaking at 427 nm, Figure 5.83.

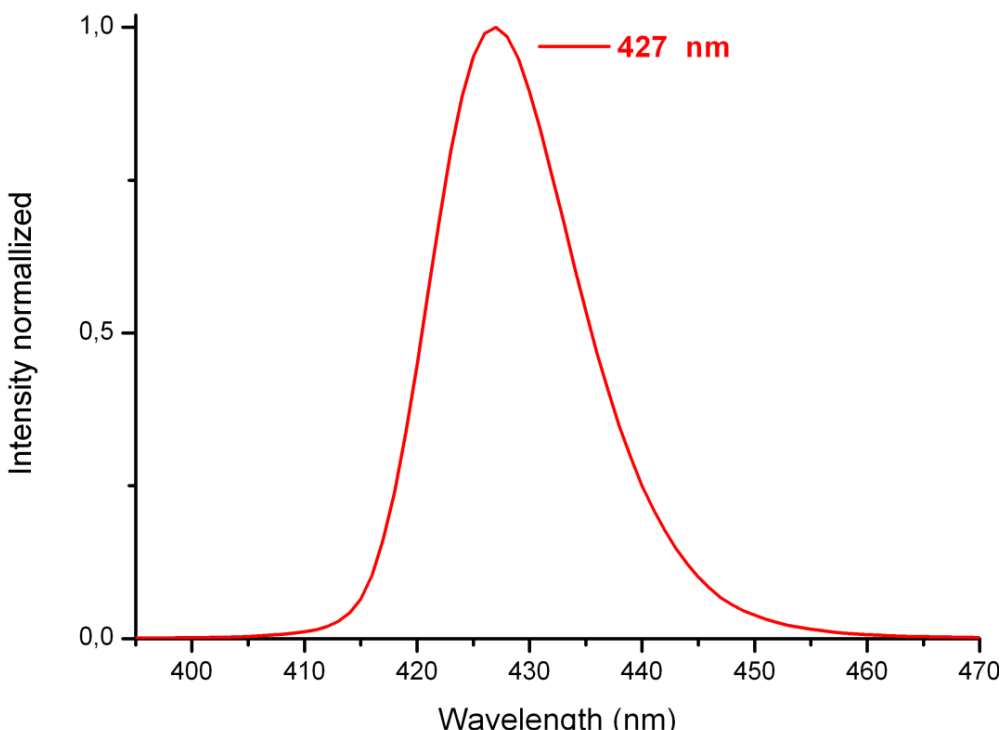


Figure 5.83: The 427 nm emission of the sample-5b.

5.3.4 SrI₂: 5% Eu²⁺ - 6

The sample-6 crystals are the best performing so far. The measurements done with these samples at the FISK University, confirmed their quality to be equivalent to that of commercial SrI₂ scintillators.

Sample 6a

The sample-6a is ~ 1cm³. The sample is packaged as shown in Figure 5.84. This image was taken shortly before the measurement at the FISK University.

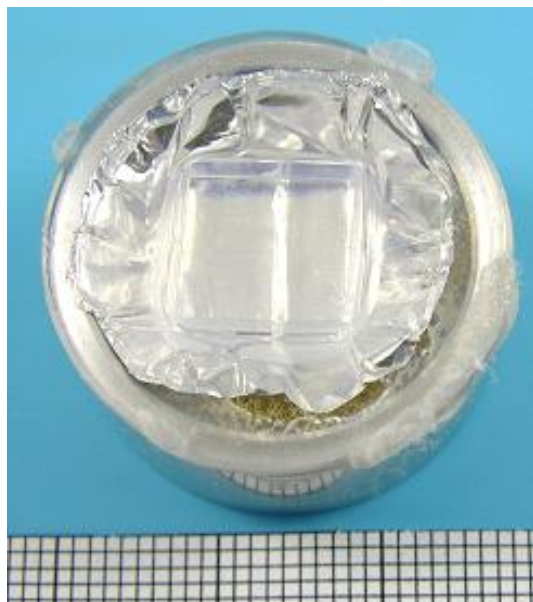


Figure 5.84: Sample 6a (~ 1 cm³) packaging. Optical coupler: EPO-TEK 305/B4 Opt. Adhesive and aluminium foil served as the reflector.

The emission of this sample under UV-light is homogenous and the aluminium foil also shows a good reflectivity of the light from the sides of the crystal towards the detector window.

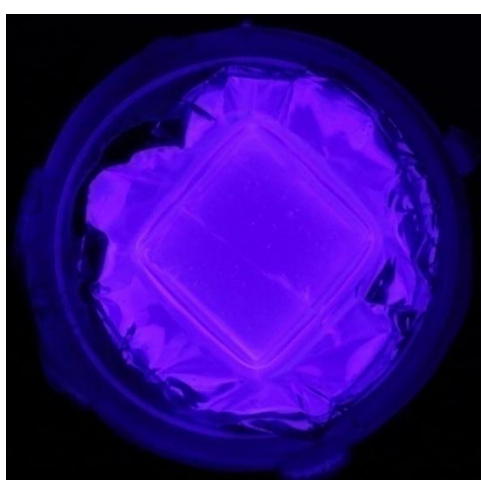


Figure 5.85: Emission of sample 6a under UV-light.

Experiments and Results - 5

The pulse height spectrum of the ^{137}Cs -isotope recorded with this sample at the research centre Jülich yielded an energy resolution of 9.8% at 662 keV (FWHM) as shown in Figure 5.86. The improvement in the energy resolution was a good indication that the sample packaging and crystal quality were improving.

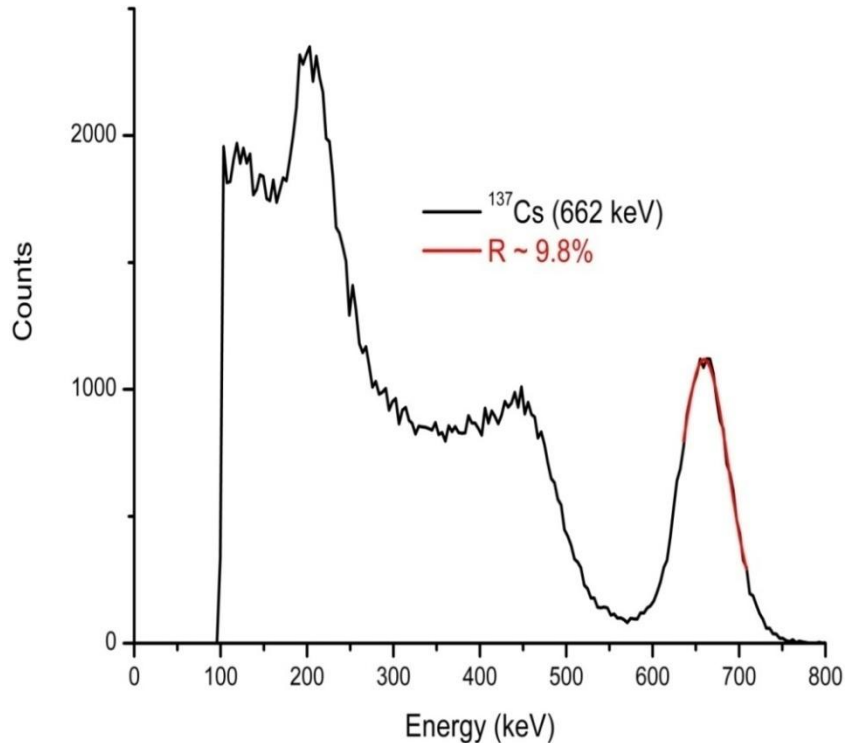


Figure 5.86: Pulse height spectrum of the ^{137}Cs -isotope recorded with 9.8% energy resolution (FWHM).

A scintillation decay time constant of 1.15 μs was calculated from the output signal of this sample, Figure 5.87.

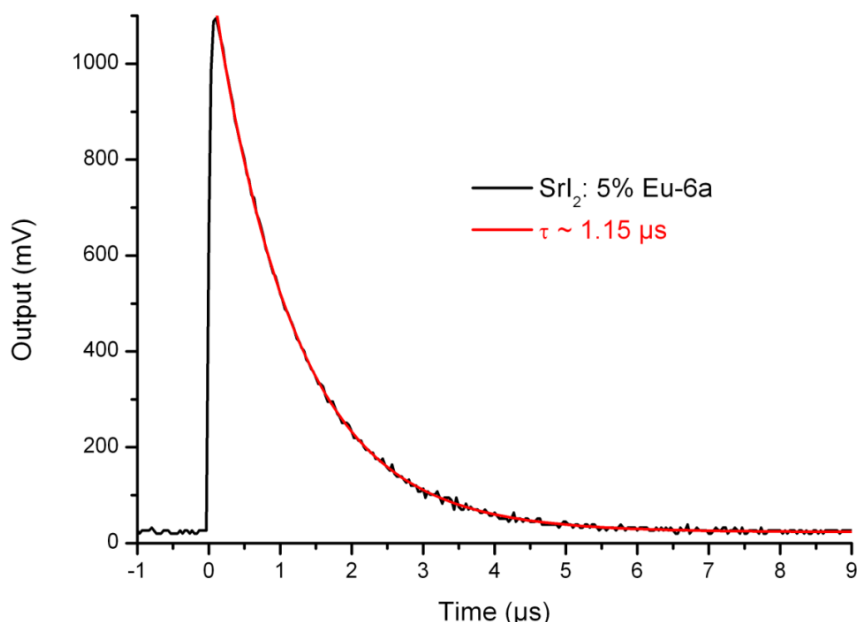


Figure 5.87: The scintillation decay time spectrum.

Measurement at FISK University

The measurement was repeated at the FISK University and gave rise to an energy resolution of 4.7% at 662 keV (FWHM).

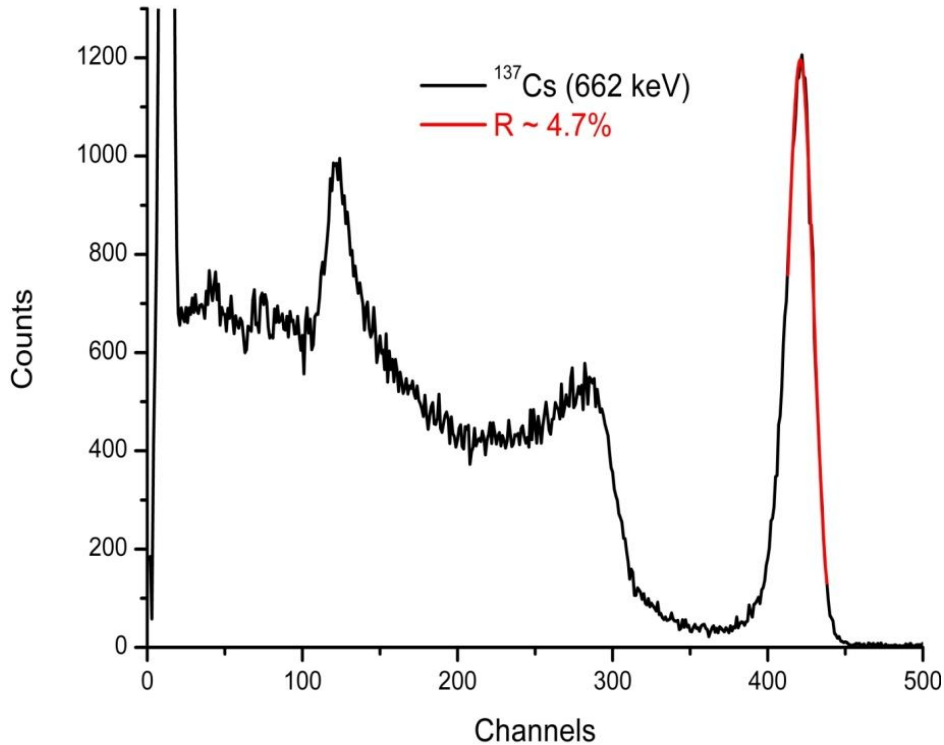


Figure 5.88: Pulse height spectrum of the ^{137}Cs -isotope observed with this sample at the FISK University.

The calculated scintillation decay time constant from the recorded experimental data was 1.47 μs .

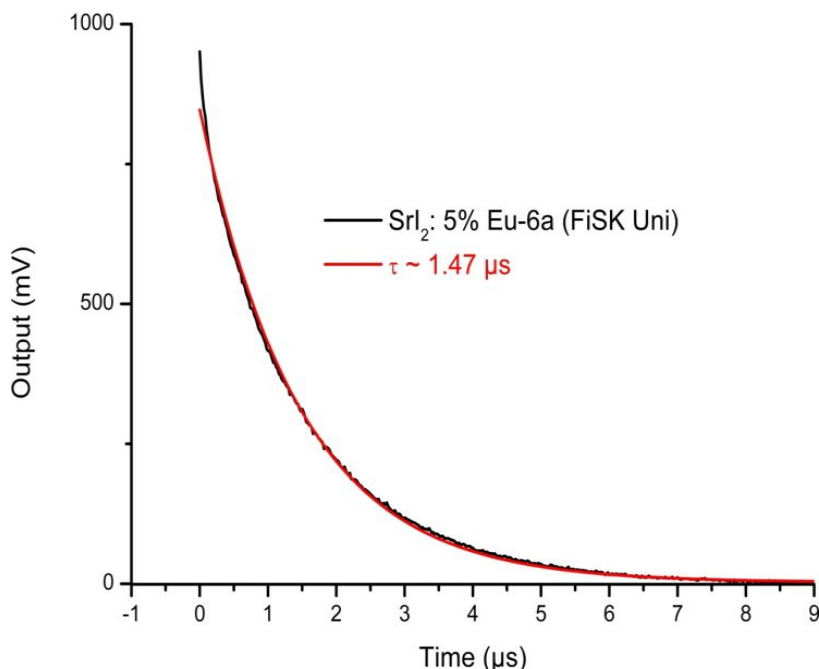


Figure 5.89: Decay time spectrum recorded at the FISK University.

Experiments and Results - 5

The emission wavelength of this sample lies at 427 nm and also comprises of a single broad emission band typical of Eu^{2+} d \rightarrow f transitions, Figure 5.90.

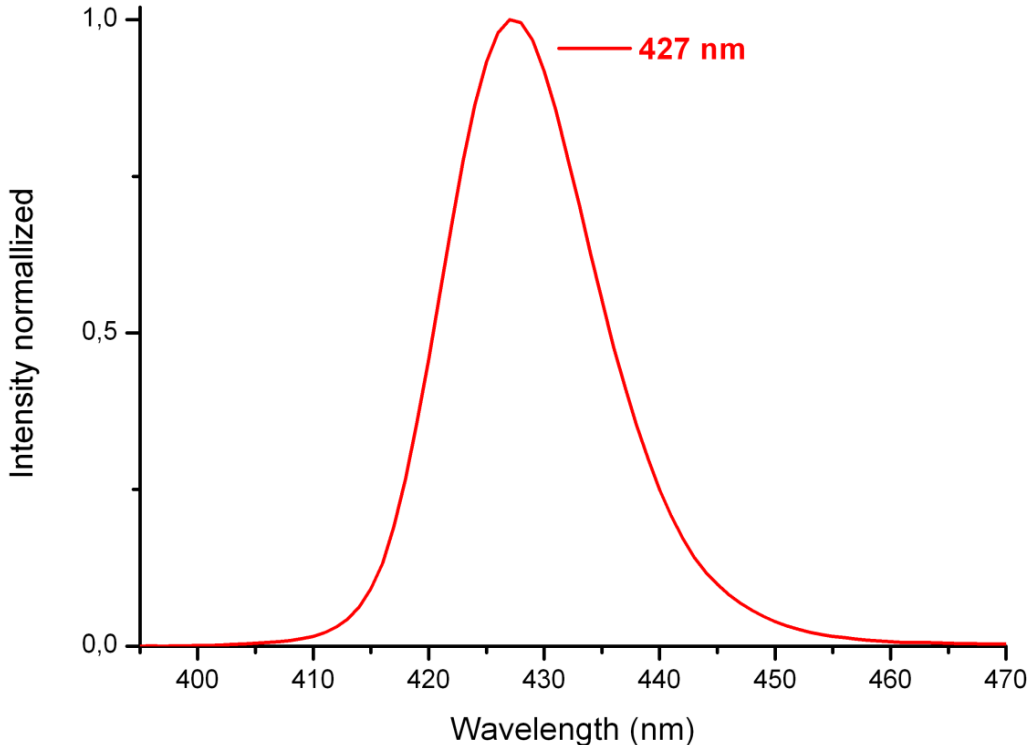


Figure 5.90: The 427 nm emission wavelength.

Sample 6b

Figure 5.91 shows the sample-6b and the aluminium foil reflector after packaging.



Figure 5.91: Sample 6b ($< 1 \text{ cm}^3$) packaging. Optical coupler: EPO-TEK 305/B4 Opt. Adhesive. Reflector: aluminium.

Experiments and Results - 5

The energy resolution of the first measurement was 10.6% at 662 keV (FWHM) as shown below.

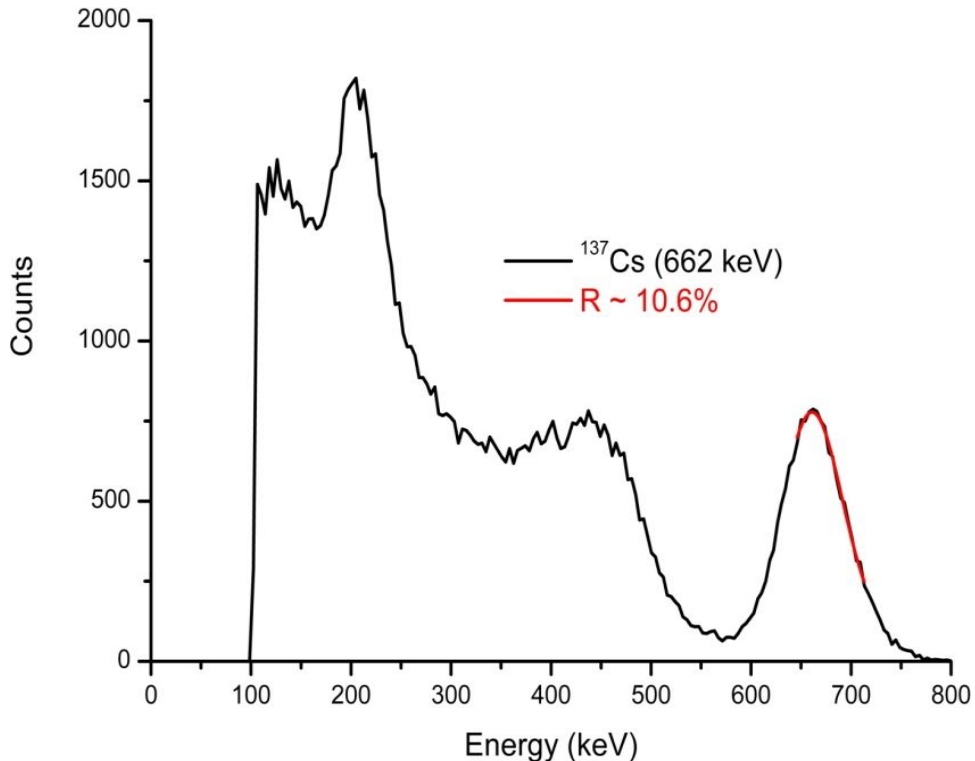


Figure 5.92: Pulse height spectrum of the ^{137}Cs -isotope observed with this sample.

The scintillation decay time constant of the sample-6b was $1.17 \mu\text{s}$, this is shown in Figure 5.93.

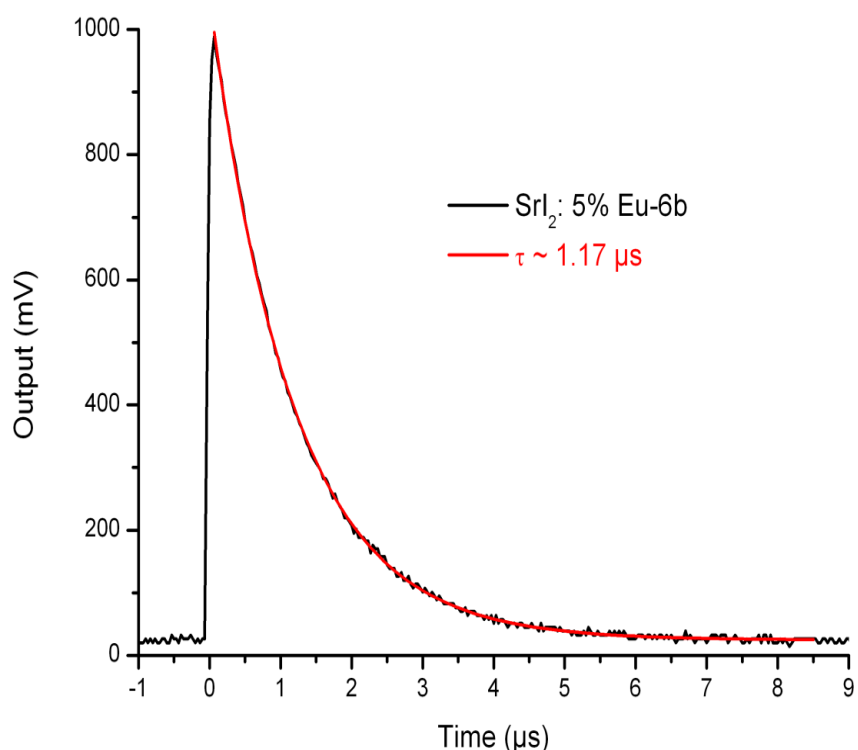


Figure 5.93: The decay time spectrum recorded.

Measurement at FISK University

This sample was also measured with the experimental setup at the FISK University, resulting to a better energy resolution of 5.2% at 662 keV (FWHM).

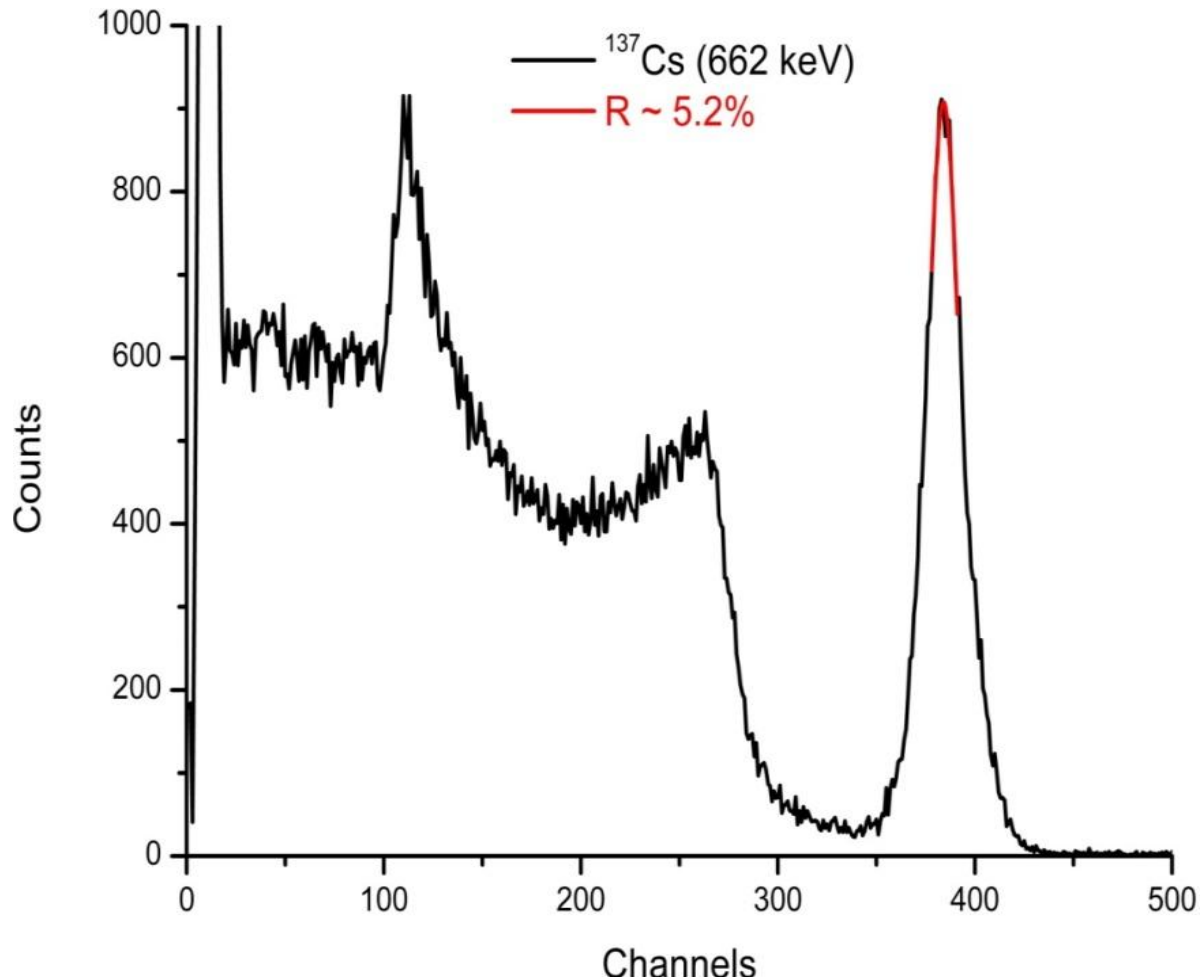


Figure 5.94: Pulse height spectrum of the ^{137}Cs -isotope observed with this sample at the FISK University.

The decay time constant of the scintillation light was determined to be 1.28 μs ; this is shown in Figure 5.95.

Experiments and Results - 5

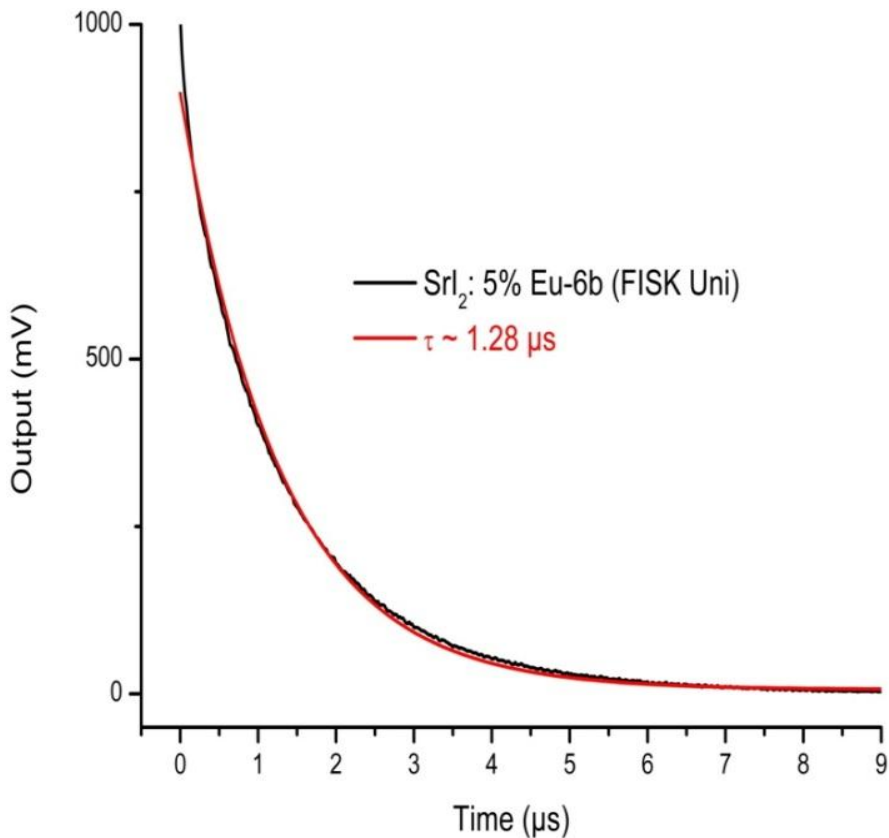


Figure 5.95: The decay time spectrum.

The radioluminescence spectrum of this sample also peaked at 427 nm as shown in Figure 5.96, this was expected because this sample originated from the same crystal ingot as sample-6a.

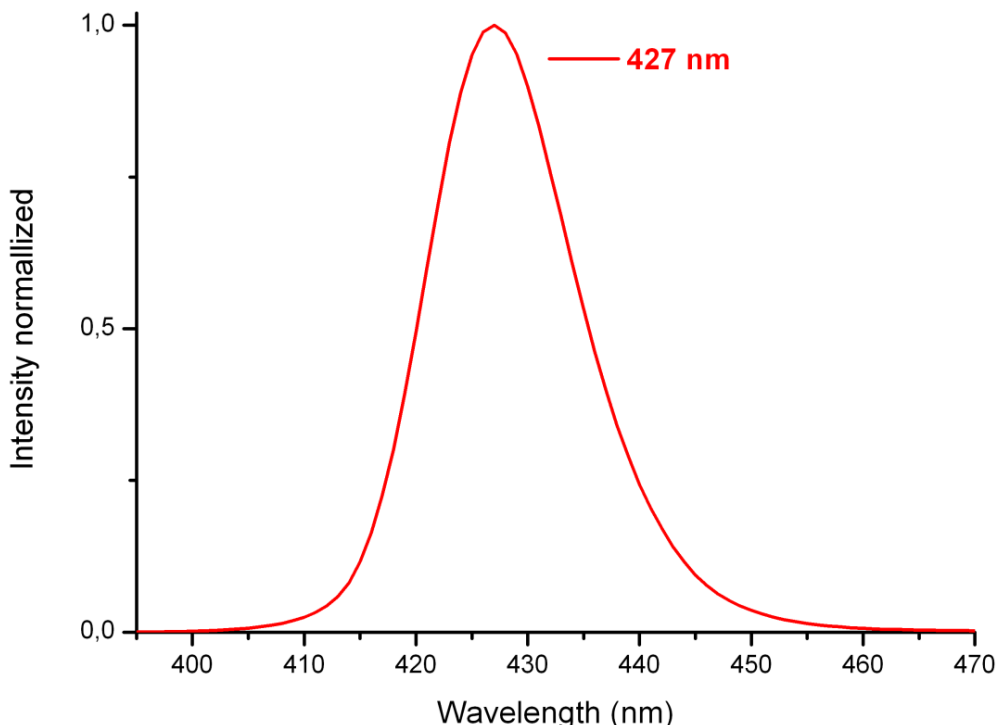


Figure 5.96: Sample-6b emission spectrum with peak at 427 nm.

Sample 6c

The sample-6c shown as packaged in Figure 5.97 is $> 1 \text{ cm}^3$.

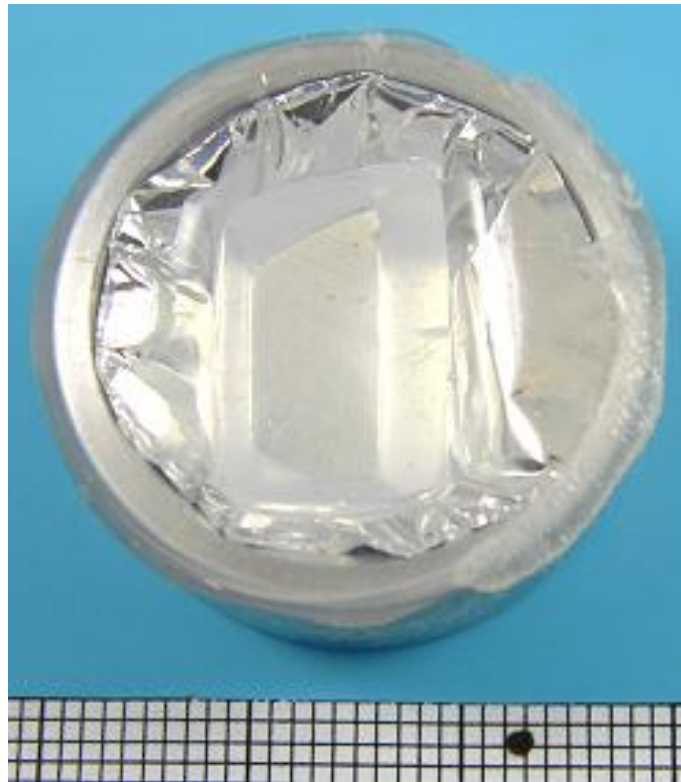


Figure 5.97: Sample 6c ($> 1 \text{ cm}^3$) packaging. Optical coupler: EPO-TEK 305/B4 Opt. Adhesive. Reflector: aluminium.

This sample shows a homogeneous emission under UV-light with some bubbles on the surface. This was investigated and found to be produced during the mixing of the two components of the EPO-TEK 305/B4 optical Adhesive and will be addressed in the next experiments.

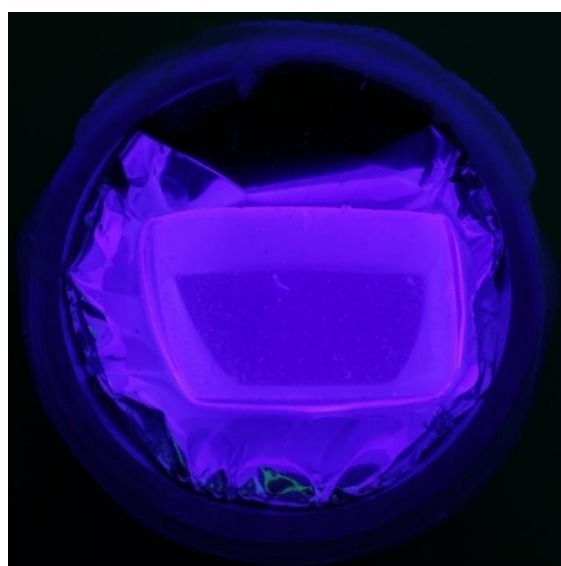


Figure 5.98: Emission of sample 6c under UV-light.

Experiments and Results - 5

The pulse height spectrum observed with this sample show an energy resolution of 9.9% at 662 keV (FWHM), Figure 5.99.

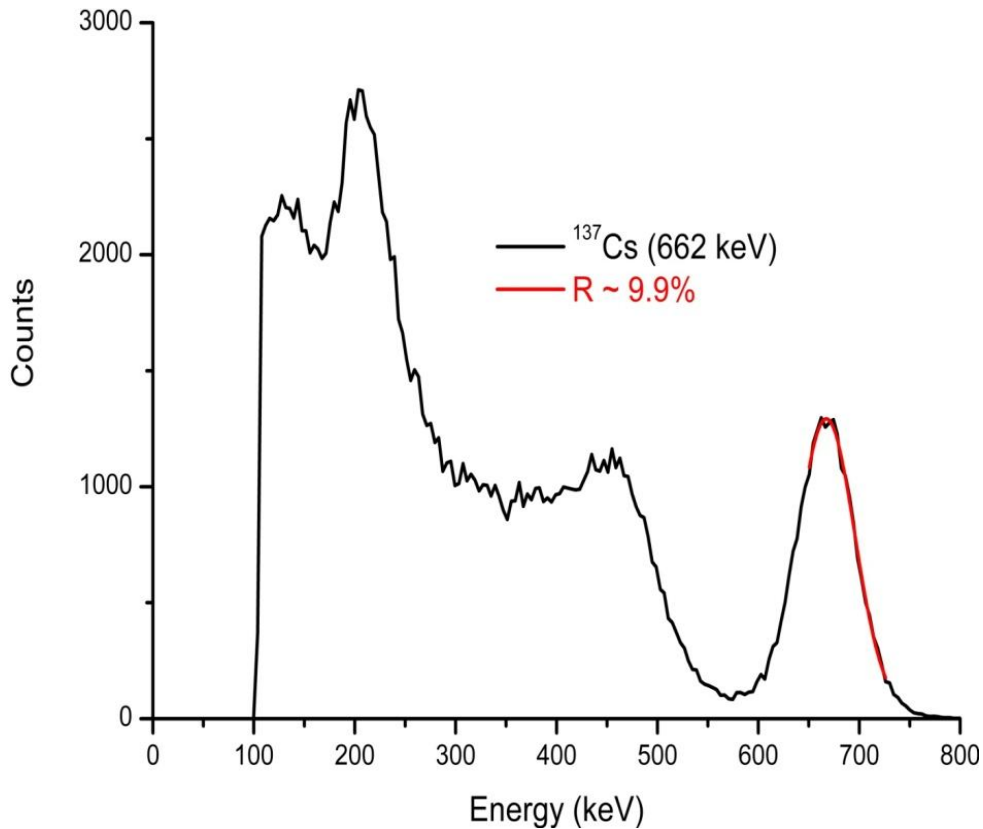


Figure 5.99: The pulse height spectrum of the ^{137}Cs -isotope.

The scintillation decay constant of this sample from the first measurement was 1.18 μs ; this is shown in Figure 5.100.

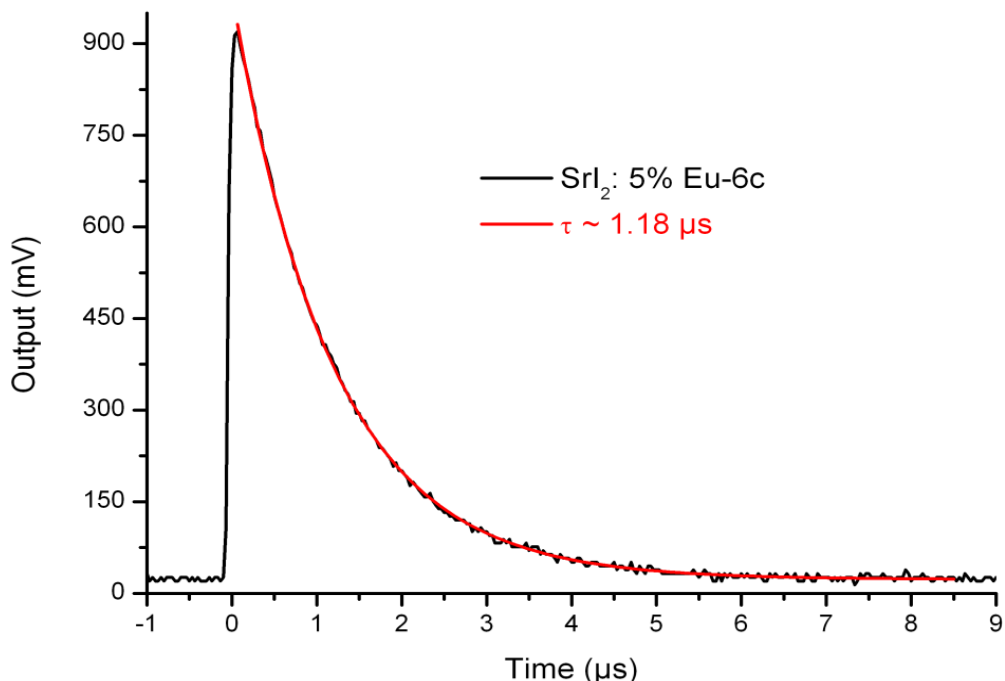


Figure 5.100: The scintillation decay time profile.

Measurement at FISK University

The second measurement was done at the FISK University. The energy resolution after fitting a Gaussian distribution function to the photopeak of the pulse height spectrum was 4.1% at 662 keV (FWHM).

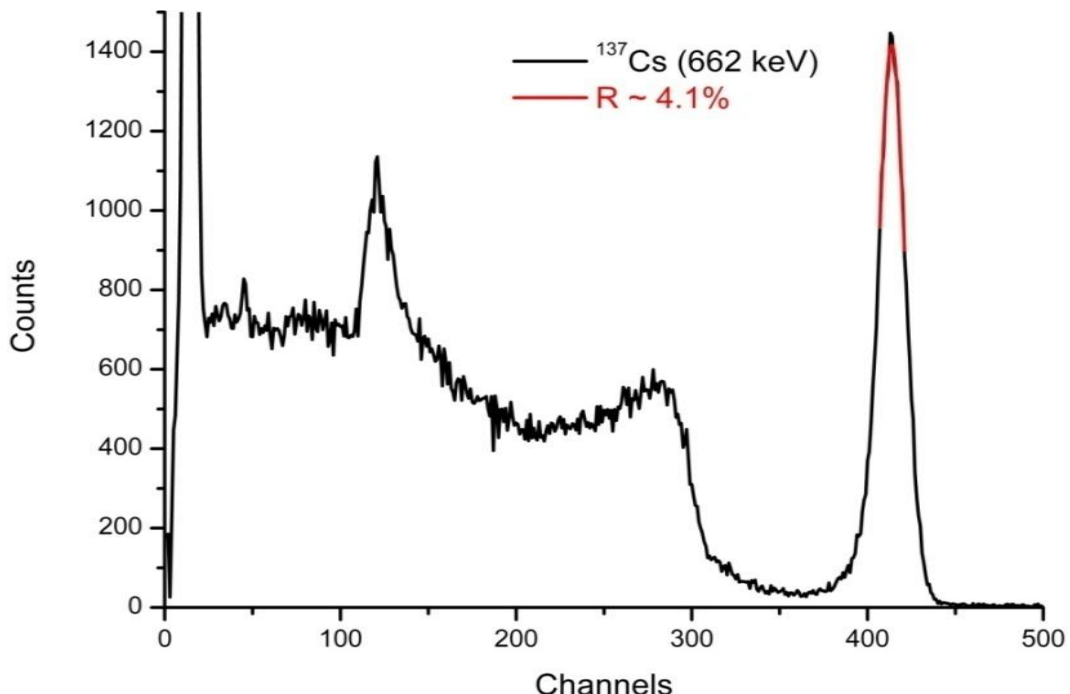


Figure 5.101: Pulse height spectrum of the ^{137}Cs -isotope observed with this sample at the FISK University.

The signal output was also fitted with a single exponential decay function (ExpDec1), the decay time constant calculated from the fitted function was $1.57 \mu\text{s}$.

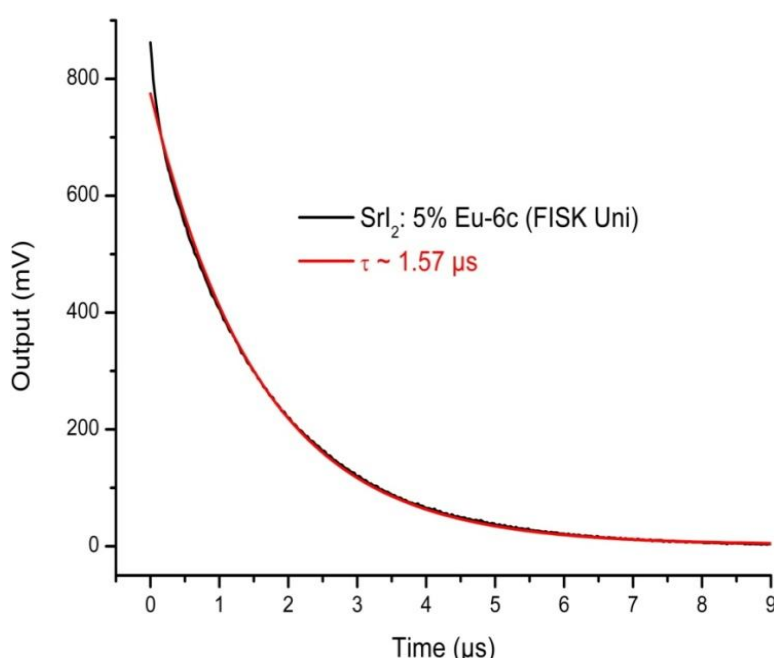


Figure 5.102: The scintillation decay time profile.

Experiments and Results - 5

The 427 nm emission wavelength of this sample is shown below in Figure 5.103.

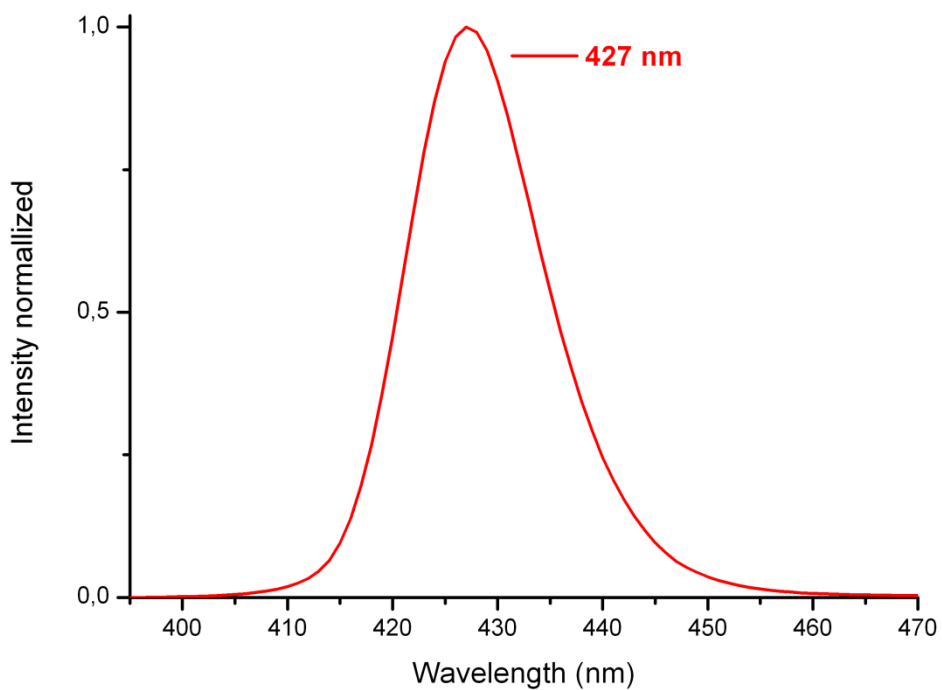


Figure 5.103: Radioluminescence spectrum of sample-6c with emission peak at 427 nm.

Sample 6d

The sample-6d was $> 1 \text{ cm}^3$, an image of the sample and packaging is shown in Figure 5.104. There are some black spots in the sample; these are inclusions in the crystal.

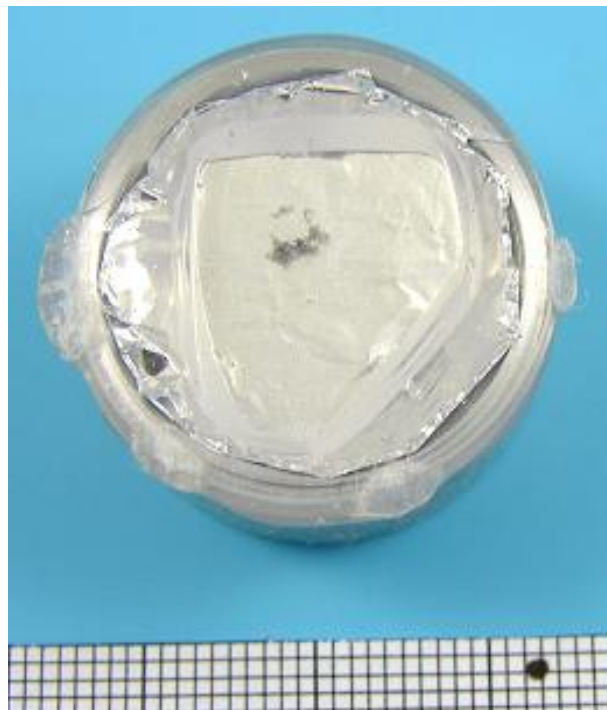


Figure 5.104: Sample 6d ($> 1 \text{ cm}^3$) packaging. Optical coupler: EPO-TEK 305/B4 Opt. Adhesive. Reflector: aluminium.

Experiments and Results - 5

The emission of this sample under UV-light is shown in Figure 5.105. The region with dark spots is slightly darker, this is probably due to light trapping and absorption.

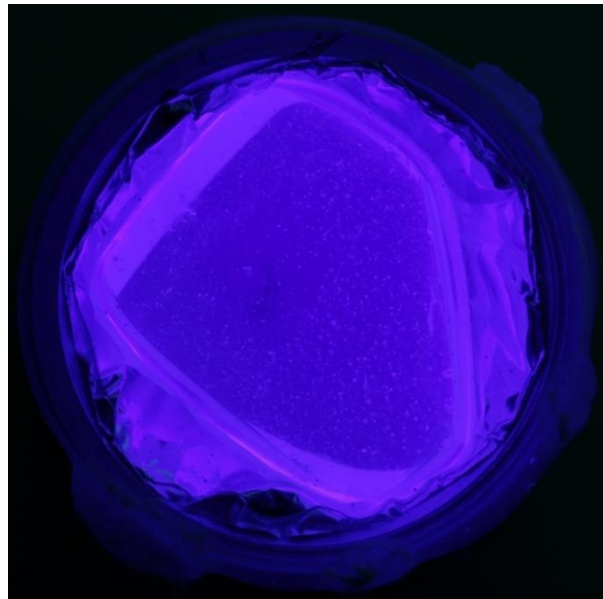


Figure 5.105: Emission of sample 6d under UV-light.

This sample was also measured twice. Figure 5.106 shows the pulse height spectrum from the first measurement. The energy resolution achieved here was 13% at 662 keV (FWHM).

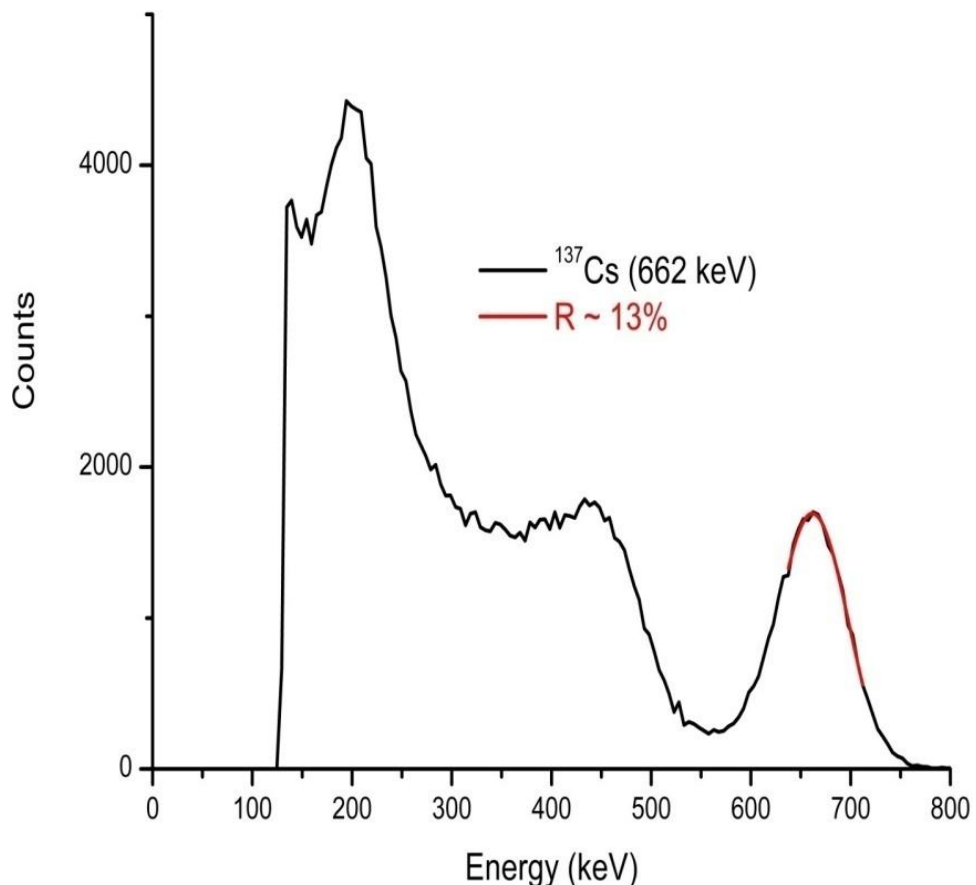


Figure 5.106: The pulse height spectrum of the ^{137}Cs -isotope.

Experiments and Results - 5

The scintillation decay time constant of this sample was determined to be $1.18 \mu\text{s}$ as shown in Figure 5.107

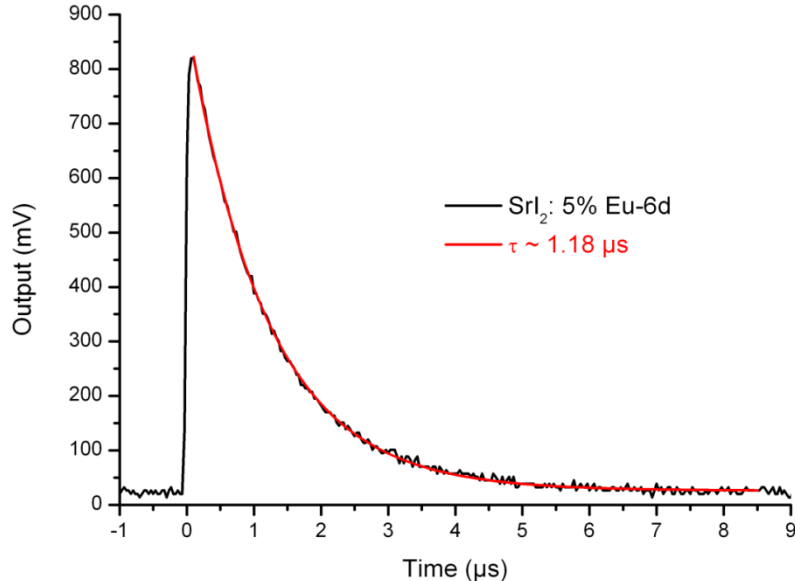


Figure 5.107: The scintillation decay time profile.

Measurement at FISK University

The pulse height spectrum of the ^{137}Cs -isotope observed at the FISK University shows an energy resolution of 6.6% at 662 keV (FWHM). The sample was made from the same crystal ingot as samples 6a, 6b and 6c with 4.1% energy resolution. We think high impurity concentration in this part of the crystal might have strongly affected the energy resolution here.

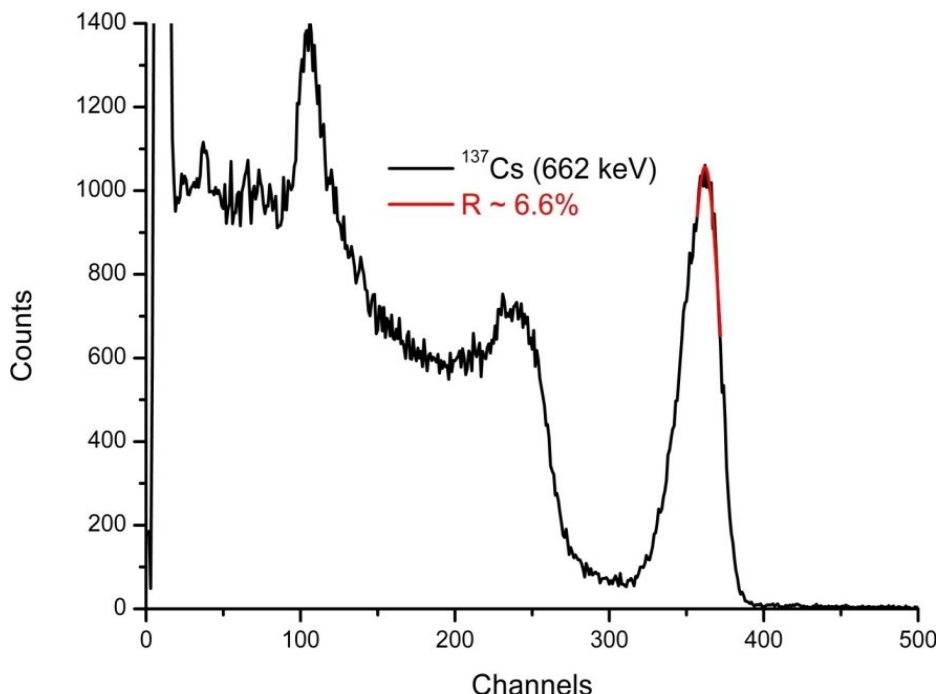


Figure 5.108: The pulse height spectrum of the ^{137}Cs -isotope (FISK University).

Experiments and Results - 5

The scintillation decay time constant of this sample was $1.52 \mu\text{s}$. This corresponds to the decay constant of other samples made from the same crystal ingot and measured at FISK University.

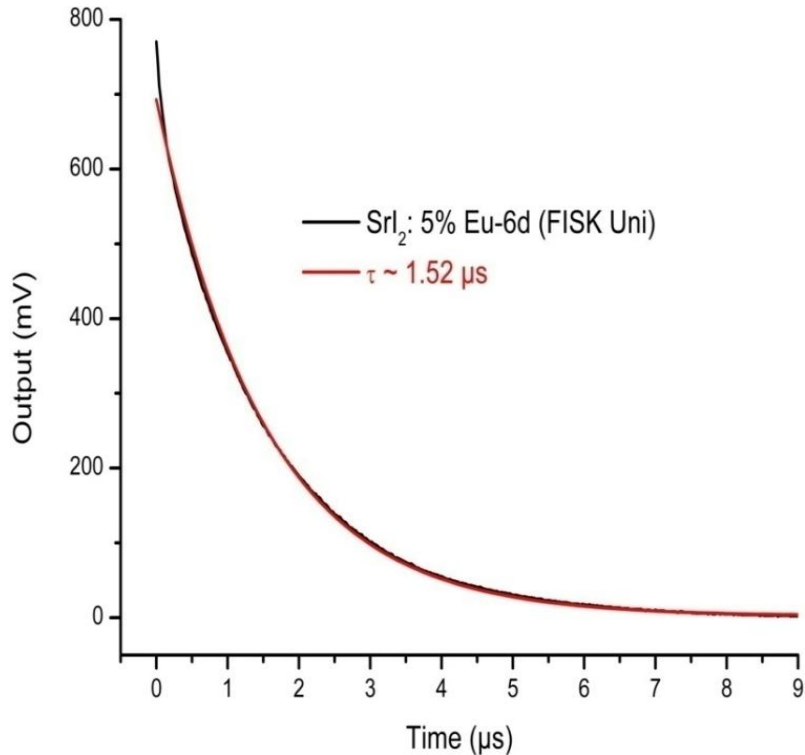


Figure 5.109: The scintillation decay time spectrum.

The radioluminescence spectrum of this sample also shows a 427 nm emission wavelength like other samples from the same crystal ingot.

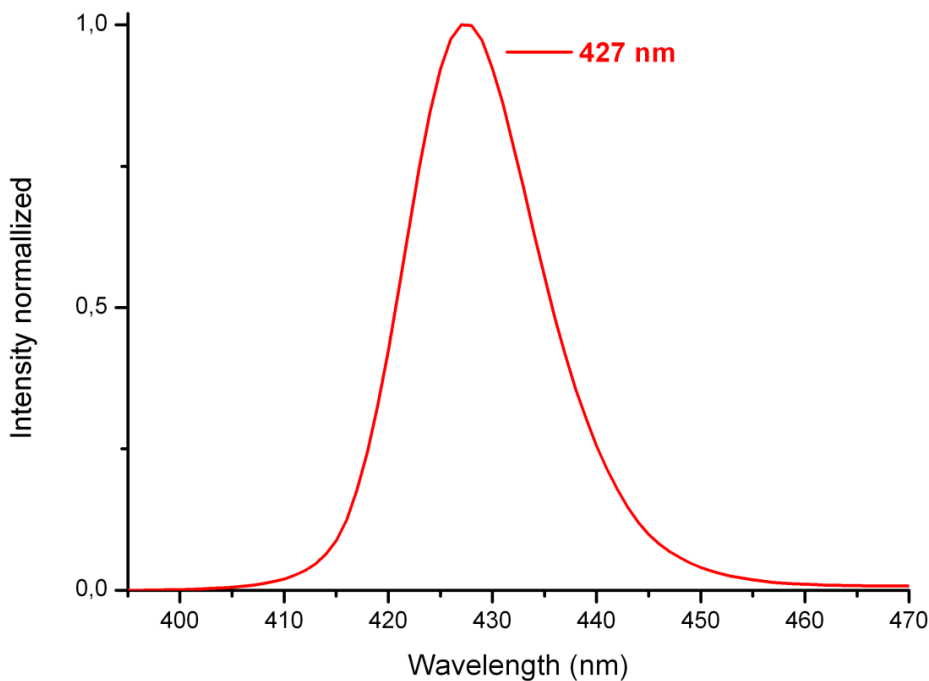


Figure 5.110: Radioluminescence spectrum of the sample-6d showing a 427 nm emission.

5.3.5 SrI₂: 2% Eu²⁺ - 7

The sample – 7 was made from the region A in Figure 5.111.

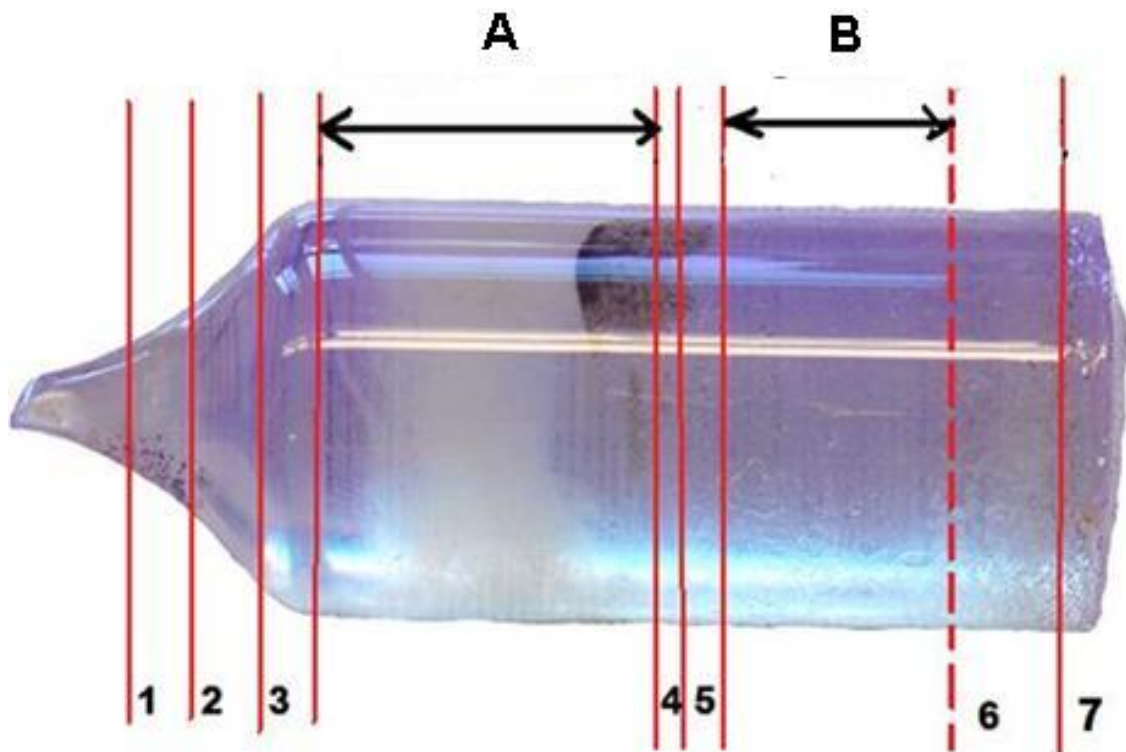


Figure 5.111: Different slices of this crystal were made for γ – ray spectroscopy, X-ray imaging and structural analysis, only the spectroscopic results recorded using region – A regarded here as sample – 7 will be reported.

There were three measurements using the sample – 7; the geometry was cylindrical for the first measurement (Figure 5.112), tapered for the second measurement (Figure 5.114), tapered and canned for the third measurement (Figure 5.116).

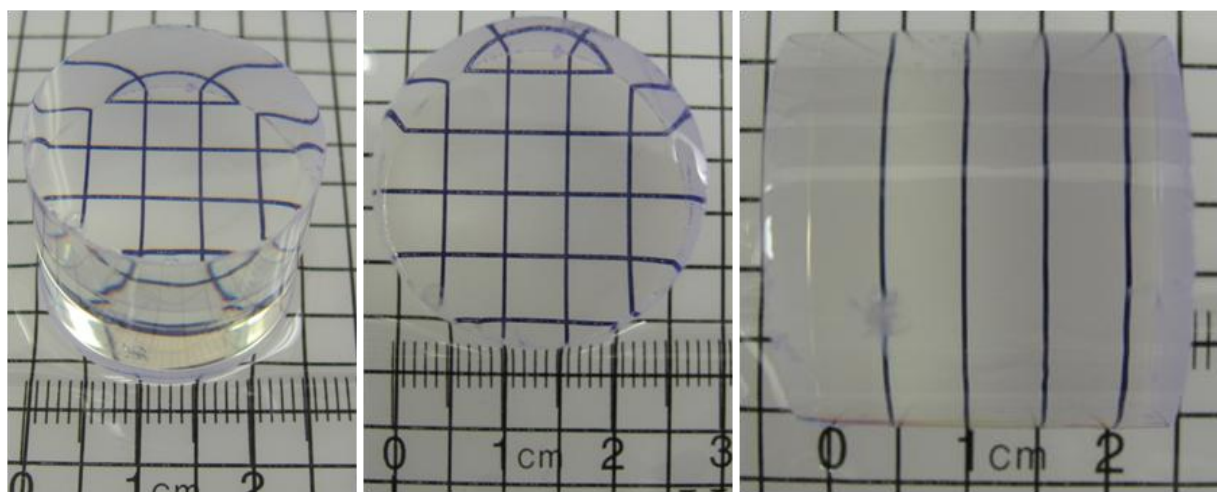


Figure 5.112: The sample – 7 after polishing and cylindrical in geometry.

Experiments and Results - 5

The energy spectrum recorded with the sample – 7 having a cylindrical geometry is shown in Figure 5.113. An energy resolution of 3.99% at 662 keV was calculated after fitting a Gaussian distribution function to the photopeak.

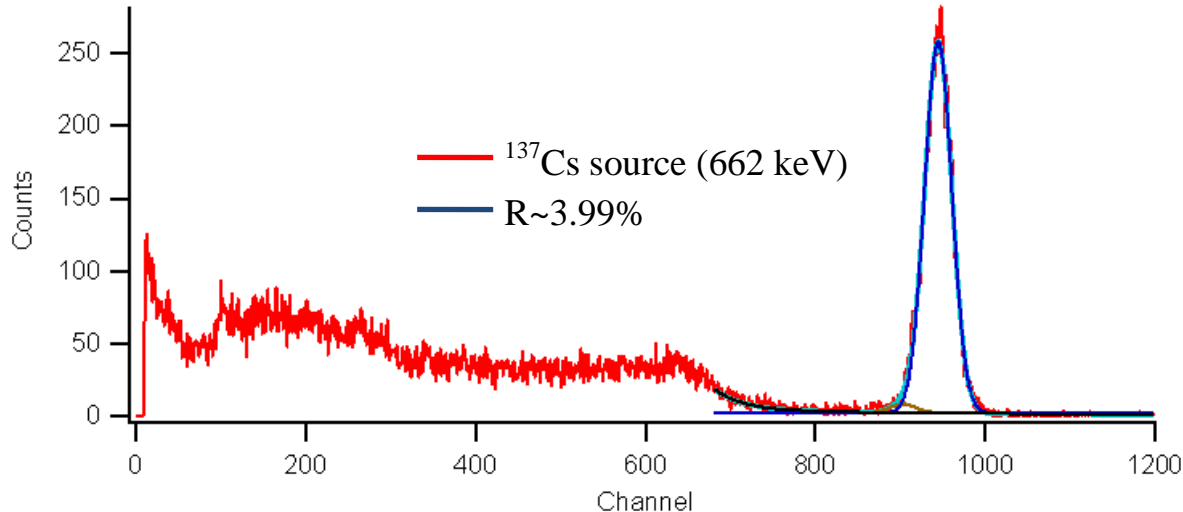


Figure 5.113: Pulse height spectrum observed with the cylindrical sample – 7.

[Sturm 2010] has reported on higher efficiency of collection of scintillation photons in crystals having the geometry of a tapered cylinder. The sample – 7 was ground into a tapered cylinder (Figure 5.114), polished and measured again.

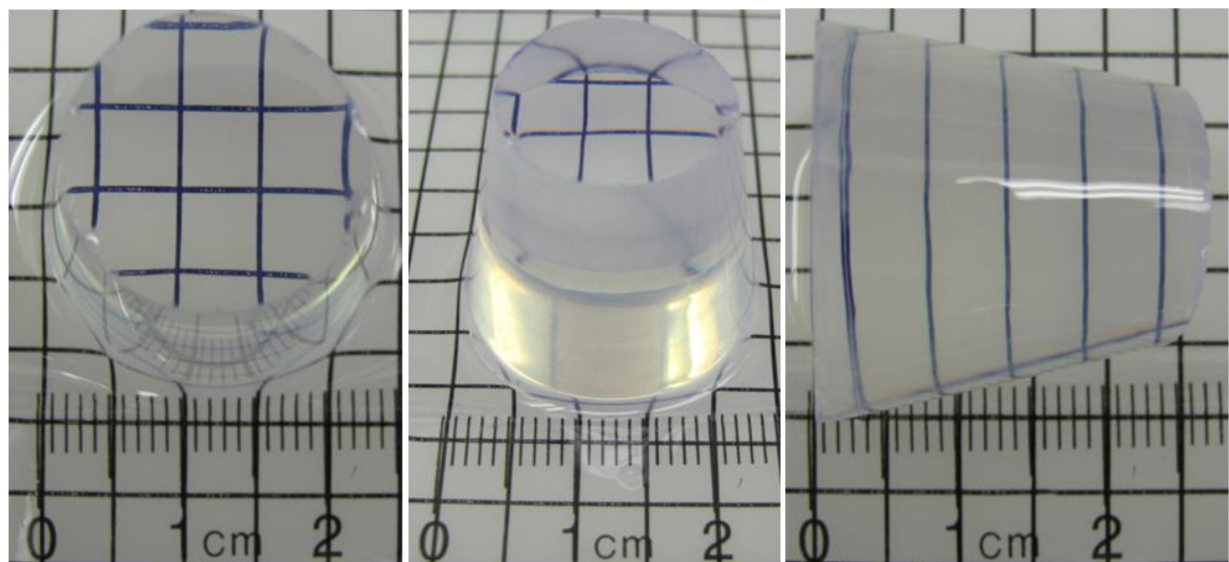


Figure 5.114: The sample – 7 having a tapered geometry for the second measurement.

Figure 5.115 shows the energy spectrum observed with this sample. The energy resolution improved from 3.99% to 2.76% at 662 keV. This confirmed that the crystal geometry has strong effects on the performance of scintillator detectors.

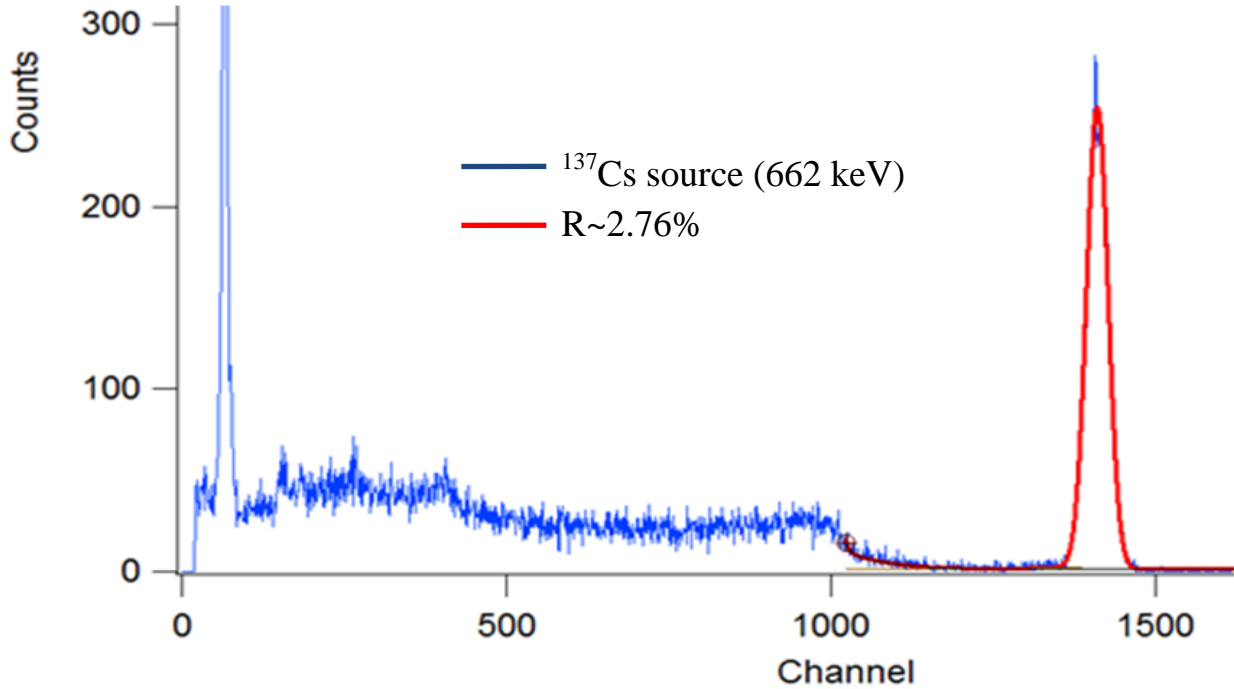


Figure 5.115: The pulse height spectrum observed with the tapered sample – 7.

The third measurement was done with the tapered sample – 7 canned in aluminium containers as shown in Figure 5.116. The hermetic encapsulation is very important for longer field use.

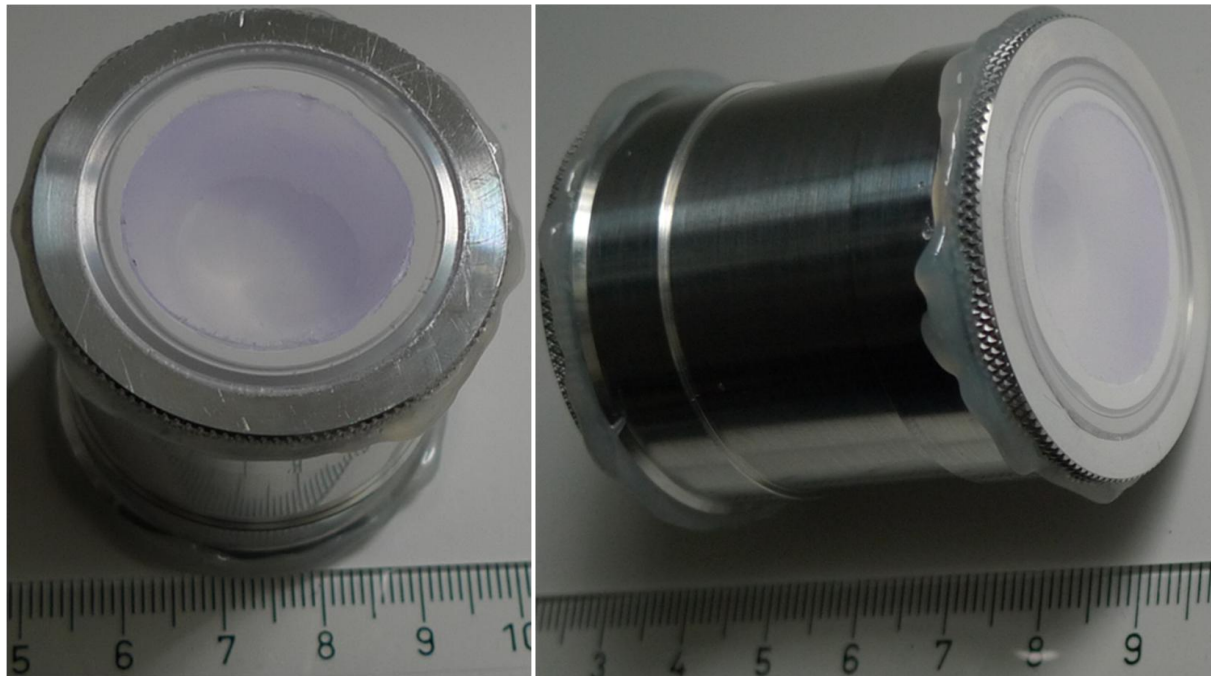


Figure 5.116: The sample – 7 canned for longer field use.

The recorded energy spectrum with the sample – 7 canned is shown in Figure 5.117. A slight improvement in the energy resolution 2.73% at 662 keV was noticed.

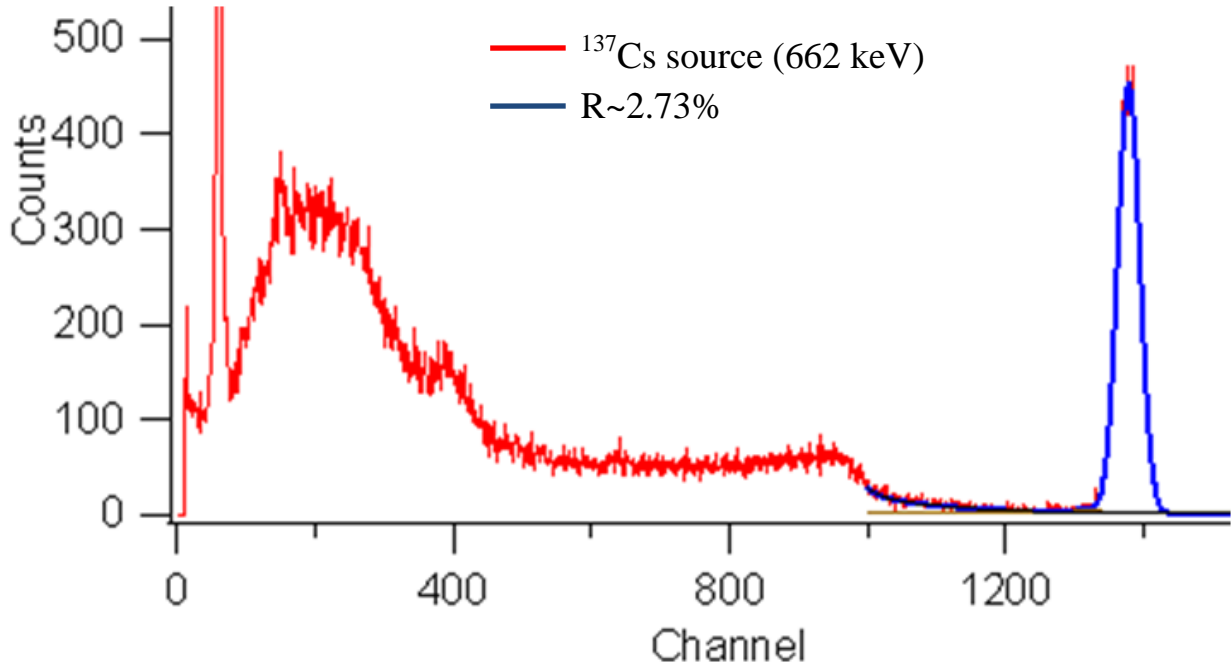


Figure 5.117: The pulse height spectrum observed with the tapered and canned sample – 7.

5.4 X-ray Imaging Measurements

The application of SrI_2 - scintillators in high X-ray imaging was investigated in this work for the first time ever. The application of scintillator screens in high resolution X-ray imaging is not new. At present, mostly non-hygroscopic scintillators are used, due to the difficulties associated with hermetic encapsulation of hygroscopic thin screen scintillator samples such as the SrI_2 - scintillator.

Not only is the sample packaging process a problem; the obtainable image quality depends also on the packaging. For example, covering the scintillator screen with a thick glass slide would lead to lateral spreading of the light, thereby reducing the spatial resolution and contrast of the recorded image.

The scintillator requirements for high resolution X-ray imaging has been discussed in the theory part of this work. Here the scintillation properties of the SrI_2 – scintillator was compared to that of the YAG – scintillator used mostly for X-ray imaging purposes, Table 5.3. The YAG – scintillator has been used in combination with microscope objectives and a CCD-detector to achieve a spatial resolution down to $0.8 \mu\text{m}$ [Martin and Koch 2006].

The density of both materials is the same, SrI_2 has a higher effective atomic number and higher light output that could result in reducing the integration time needed to acquire the images during measurements. The emission wavelengths of both scintillators lie in the spectral response of most CCD cameras. The SrI_2 – scintillator has other advantages over the YAG – scintillator, like the low melting point and the readiness to be grown into single crystals. Unfortunately, it is hygroscopic.

Experiments and Results - 5

Property	$\text{Y}_3\text{Al}_5\text{O}_{12}:\text{Ce}$	$\text{SrI}_2:\text{Eu}$
Density (g/cm ³)	4.55	4.55
Z_{eff}	32	49.4
Light output (ph/MeV)	40000 - 50000	80000 – 120000
Emission wavelength (nm)	550	435
Hygroscopic	No	Yes
Refraction index	1.82	~ 2.05
Crystal structure	Cubic	Orthorhombic
Melting point °C	1940 - 1970	510 – 545

Table 5.3: Scintillator characteristics of YAG- and SrI_2 – scintillators.

A look at the absorption efficiencies calculated for 5 μm SrI_2 – and YAG – scintillators show a better absorption efficiency of the YAG – scintillator due to the yttrium k-absorption shell, Figure 5.118.

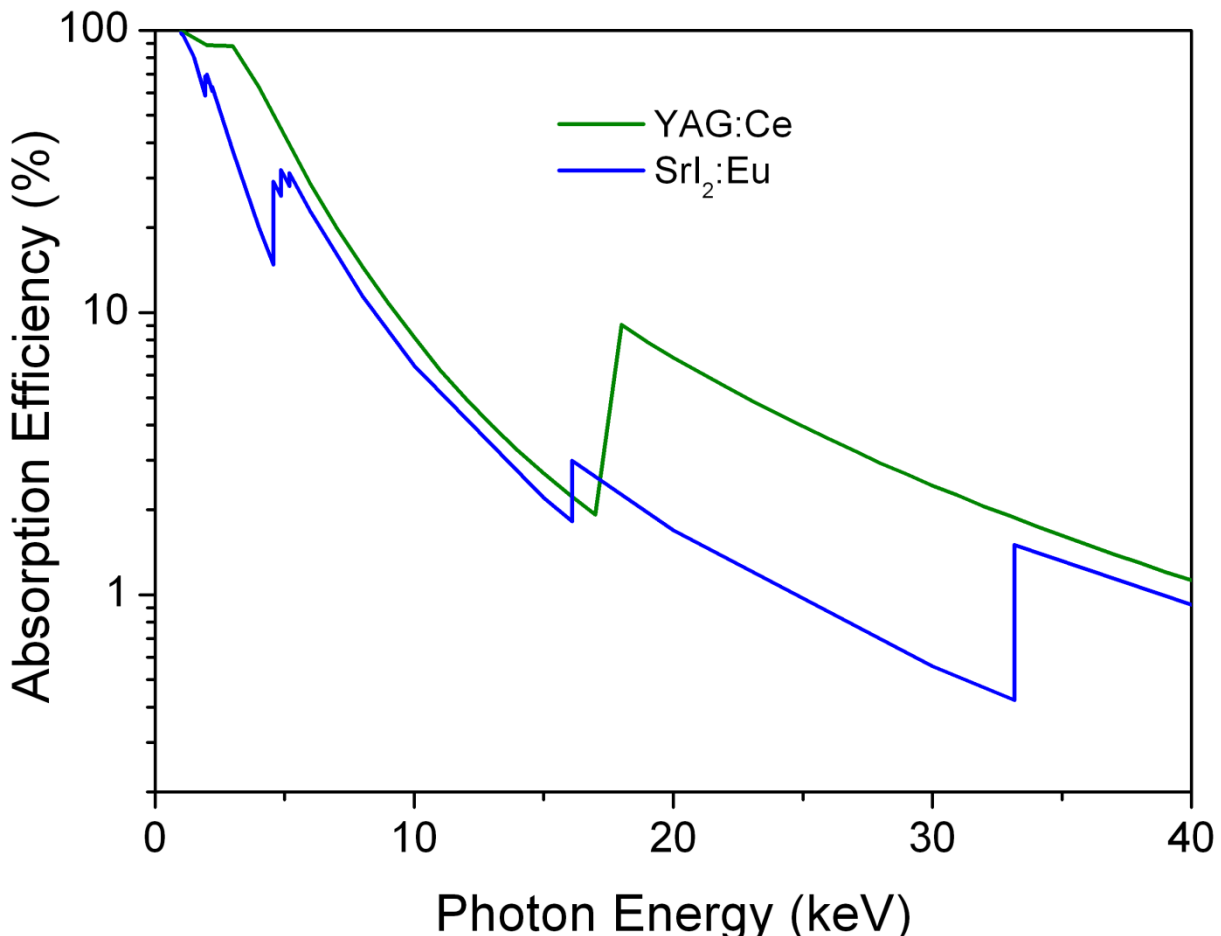
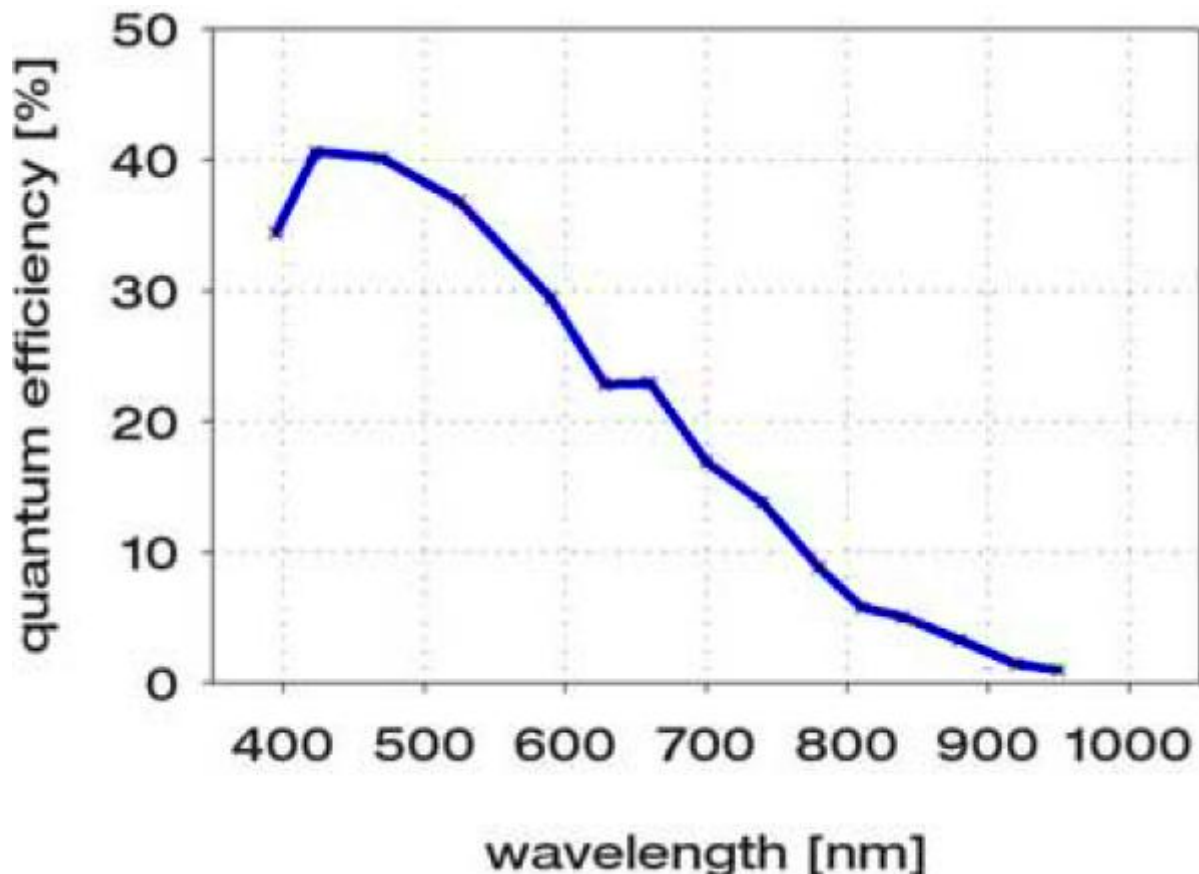


Figure 5.118: Calculated absorption efficiencies of 5 μm SrI_2 and YAG – scintillators.

The maximum sample thickness needed for the given parameters of the optical system used in the measurements here was 400 μm . The high resolution X-ray imaging detector setup available at the ANKA/ Topo Tomo beamline comprises of a high resolution microscope (Optique Peter, France) coupled to a PCO 4000 CCD camera. The technical data and quantum efficiency of the PCO 4000 camera are shown in Table 5.4 and Figure 5.119 respectively.

resolution (hor × ver)	pixel	4008×2672
pixel size	(hor × ver) μm^2	9.0 × 9.0
peak quantum efficiency	%	50 @ 500 nm
image sensor		KAI-11000
full well capacity	e^-	60000
dynamic range A/D	bit	14
readout noise	$e^- \text{ rms}$	12 / 22 @ 8/32 MHz
imaging frequency, frame rate	fps	5 @ full frame
spectral range	nm	normal 320..1000 UV sensitive 200..1000
dark current	$e^- / \text{pixel}\cdot\text{s}$	@ 20° C typical 0.7 @ -20° C typical 0.02

Table 5.4: PCO 4000 technical data [Baumbach 2007].**Figure 5.119:** PCO 4000 quantum efficiency [Baumbach 2007].

An image of the experimental setup is shown in Figure 5.120. The total magnification was equal to 5x (objective 2x /NA = 0.08 and eye piece 2.5x). The resolution limit according to the Rayleigh criterion was equal to 3.8 μm . The effective pixel size used was 1.8 μm .

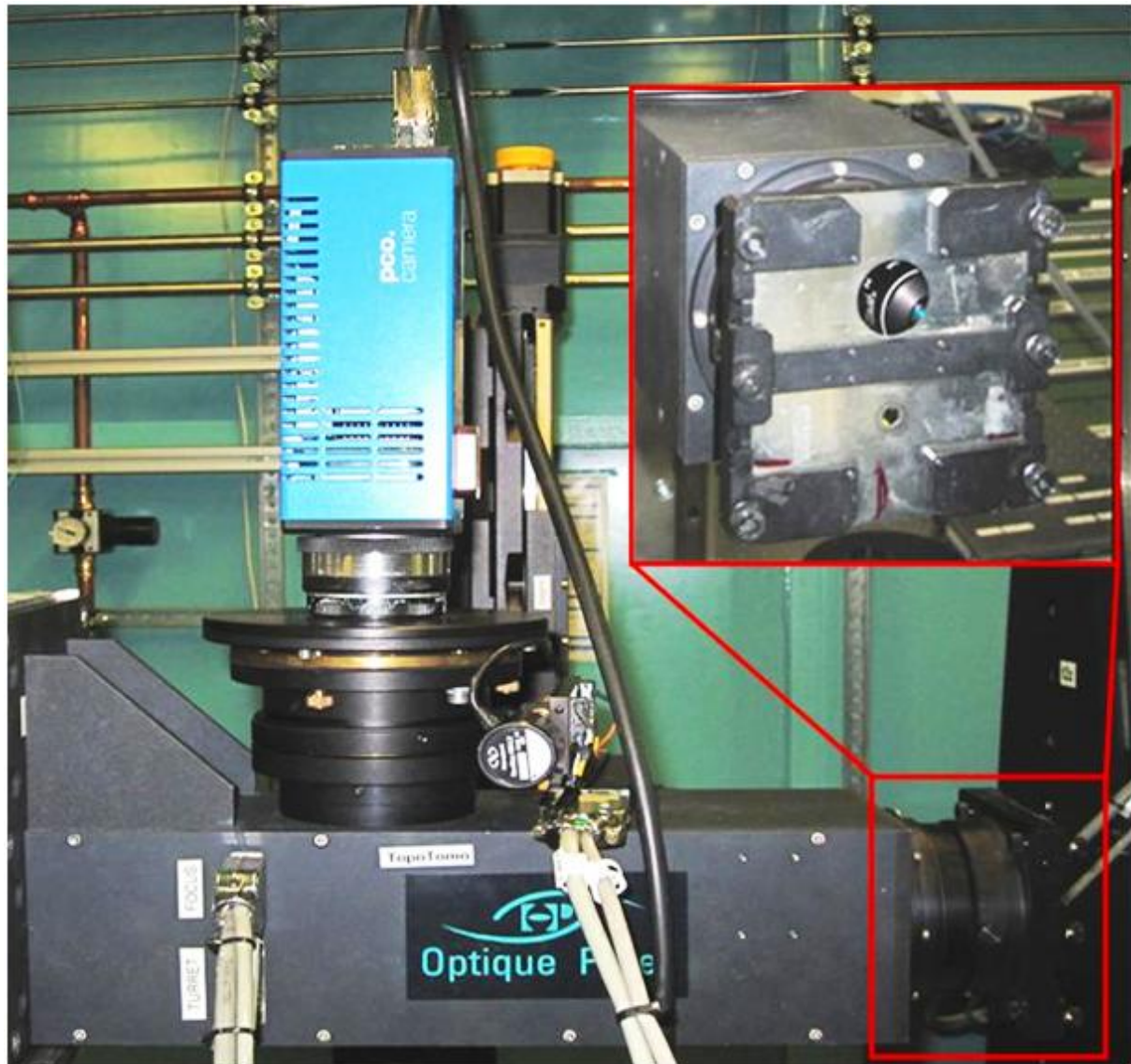


Figure 5.120: The ANKA detector setup used for the measurements here, inset shows the sample holder and the objectives.

This is an indirect X-ray imaging detector; the system configuration is shown in Figure 5.121. The X-rays and the CCD camera are positioned at right angles to prevent radiation damage to the CCD camera. The scintillator image is relayed by a mirror tilted at 45-degrees to the CCD camera.

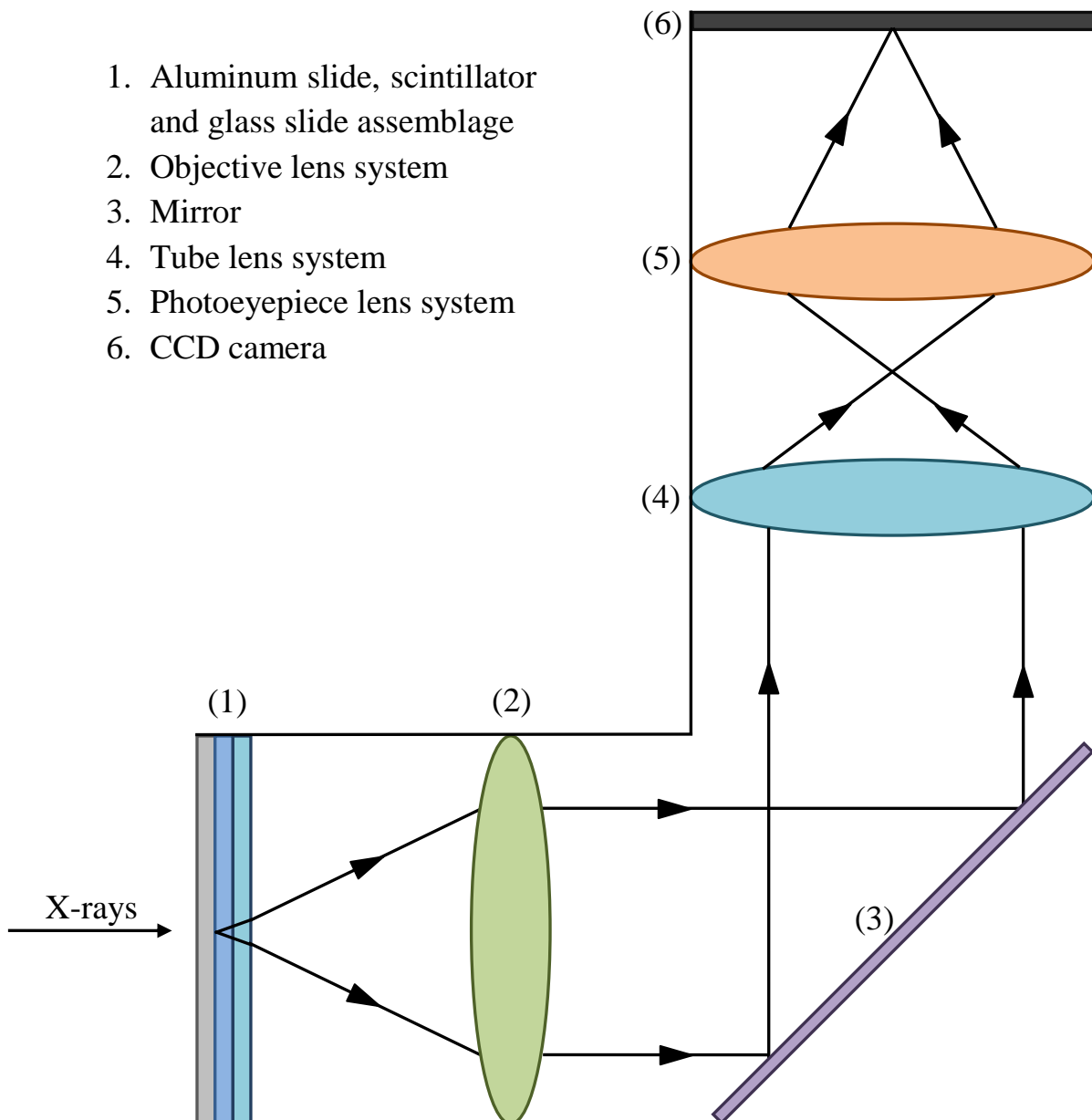


Figure 5.121: X-ray imaging based on transparent scintillator screens, diffraction limited microscope objectives and a CCD camera.

5.4.1 Flat Field Image Recording

Flat field images of all the SrI₂ – scintillator samples and the YAG – scintillator reference sample were measured. The purpose of the flat field image recording is to check for inhomogeneities in the emission of the samples. The flat field image of the YAG-scintillator in Figure 5.122 looks very homogenous; the few dark spots on it are as a result of handling of this sample.



Figure 5.122: The flat field image of the YAG – scintillator at 12 keV; 200 ms integration time and 400 μm thick.

Figure 5.123 shows the flat field image of the first ever SrI_2 -scintillator screen made. The quartz glass used to cover the detector was glued using Apiezone wax. The Apiozone wax remains soft allowing the glass to slide over the crystal screen. The image below shows some inhomogeneities, produced due to the staining of the glass slide by the Apiezon wax. Visible also are few white lines due to light scattering caused by the breakage of the scintillator thin screen during mounting operations. In order to record high quality X-ray radiography images in this work, the packaging of the scintillator thin screens had to be improved.

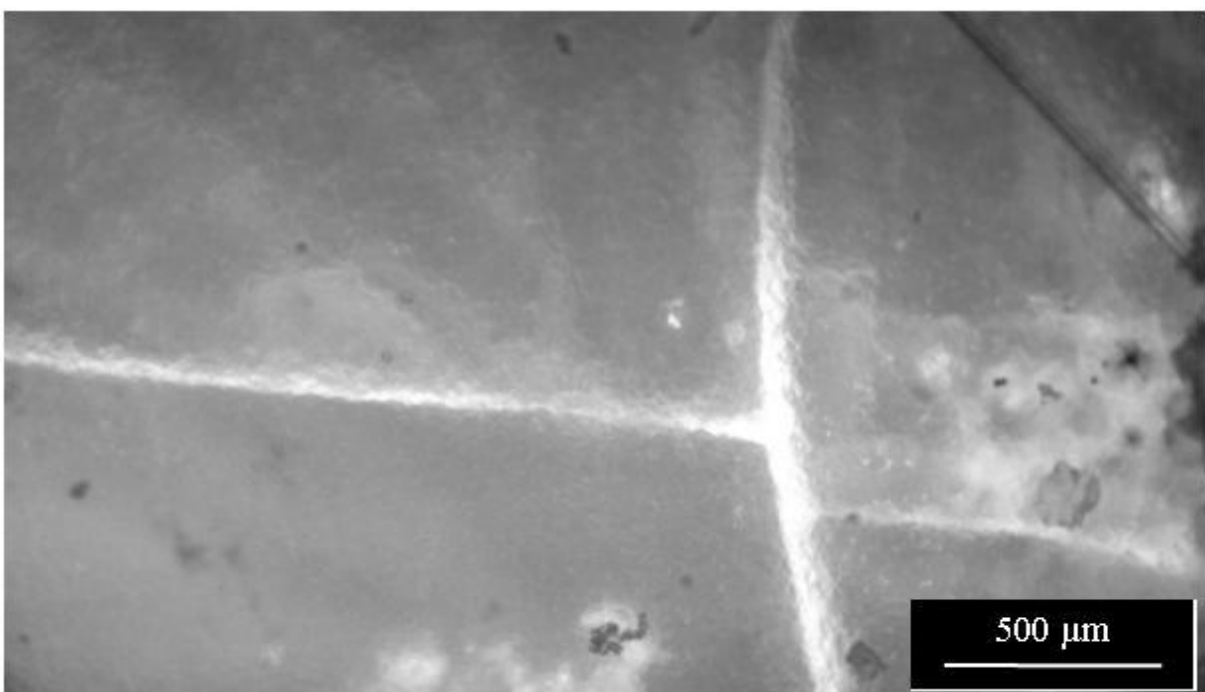


Figure 5.123: The flat field image recorded with the SrI_2 -3 at 25 keV and 360 μm thick. The first thin screen sample made showing some inhomogeneity problems.

Experiments and Results - 5

Here an attempt was made at improving the packaging technique. Two samples were made from the same crystal ingot SrI₂-5. For the first sample referred to here as SrI₂ – 5(a), optical coupler (Bicron BC-630) was applied between the scintillator screen and the quartz glass window to minimize back reflection, trapping and scattering of the light photons in the scintillator. The recorded flat field image in Figure 5.124 shows some inhomogeneities resulting probably from handling, and a fracture plane on the left side.



Figure 5.124: The flat field image recorded with the SrI₂ – 5(a) at 12 keV; 300 μm thick; Bicron BC-630 opt. Coupler and 50 ms integration time were used.

Figure 5.125 shows the flat field image recorded with the second sample, hereby referred to as SrI₂ – 5(b). No optical coupler was employed. This image shows higher emission intensity than the first sample and also less inhomogeneity. This is probably due to the scattering of the light photons.

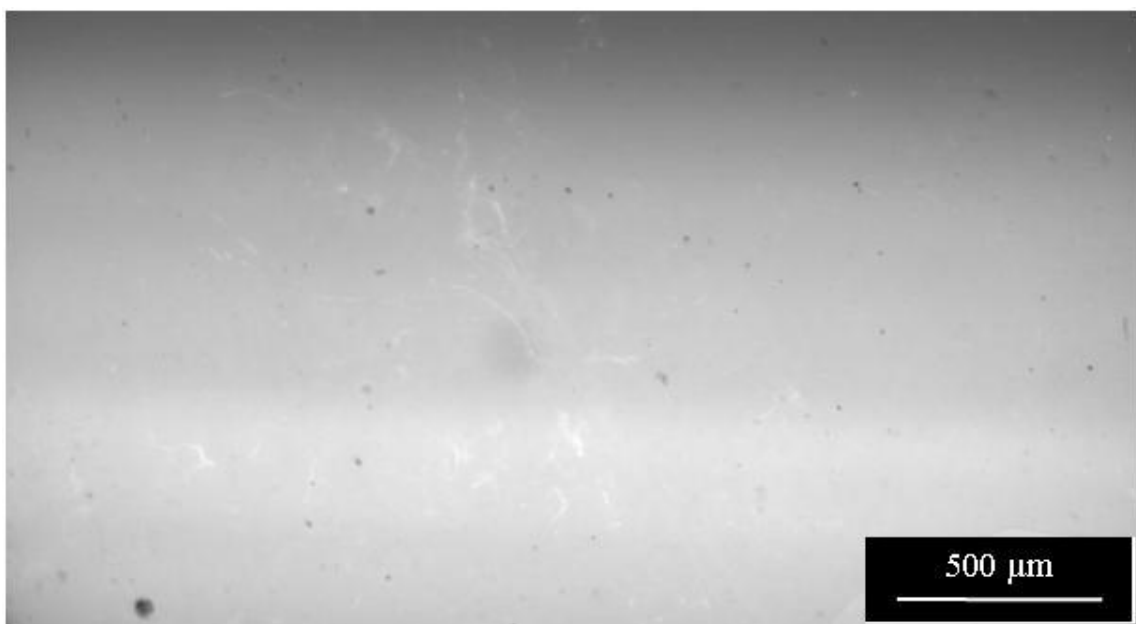


Figure 5.125: The flat field image recorded with the SrI₂ – 5(b) at 12 keV; 380 μm thick; No opt. Coupler; 50 ms integration time was used.

Experiments and Results - 5

The flat field image of the sample-6 in Figure 5.126 shows little or no inhomogeneities. This marked an improvement in the scintillator thin screen packaging. The optical coupler tested here was the EPO-TEK 305/B4 optical adhesive (epoxy).

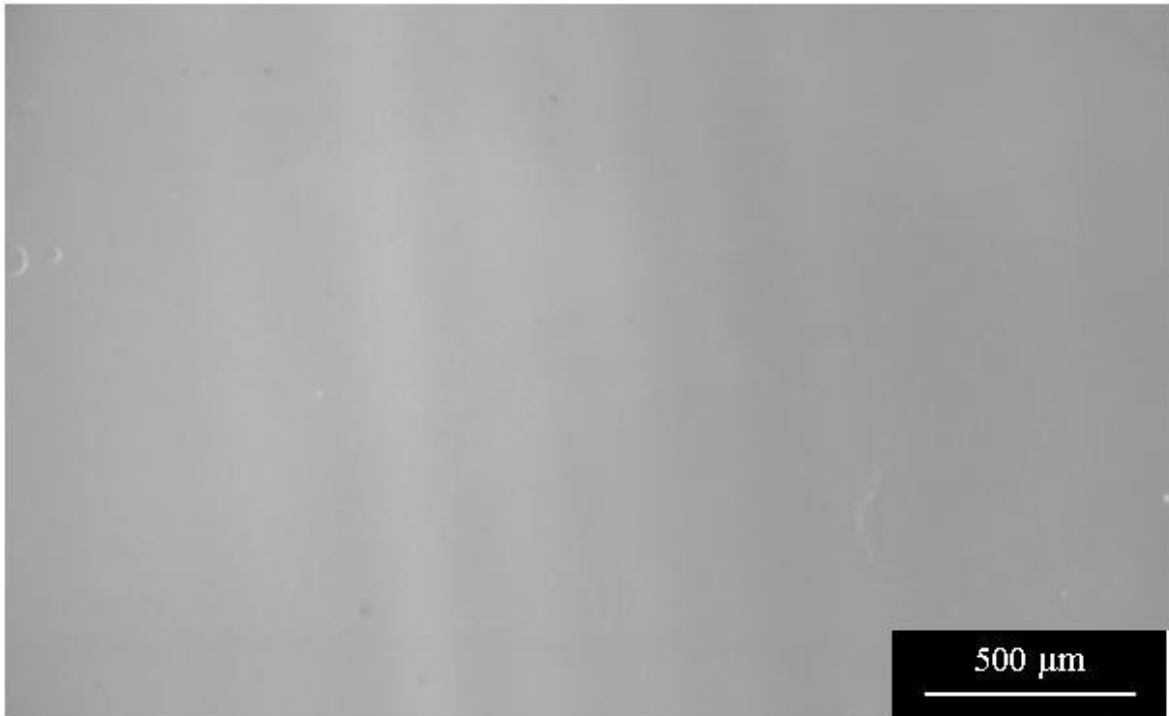


Figure 5.126: The flat field image recorded with the SrI_2 – 6 at 12 keV; 400 μm thick; EPO-TEK 305/B4 opt. Adhesive and 2 minutes integration time were used.

5.4.1.1 Estimate of the Light Yield from the Flat Field Images

The light yield of the thin SrI_2 – scintillating screens were estimated from the mean value of counts in the same region of the flat field images. The light yield of the sample – 1 was calculated. Flat field images of this sample were recorded at 12, 20, 25 keV. The transmitted X-ray flux was corrected for the thickness of the aluminium filter positioned before the scintillating screen as in Figure 5.127.

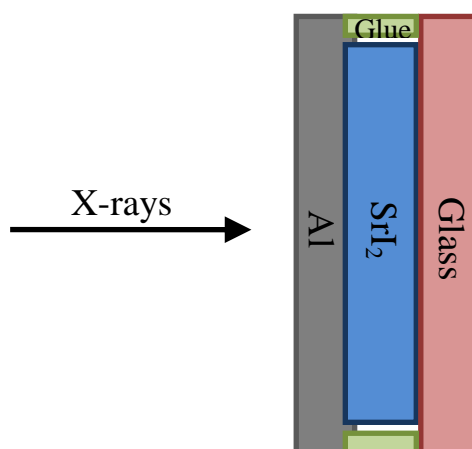


Figure 5.127: SrI_2 – thin screen packaging.

The thickness of the Aluminium slides varied for different samples, Figure 5.128 shows the calculated X-ray transmission of a 210 μm thick aluminium slide [henke.lbl.gov]. The transmitted X-rays at 12 keV is equal to 0.44, at 20 keV is 0.83 and at 25 keV is 0.91.

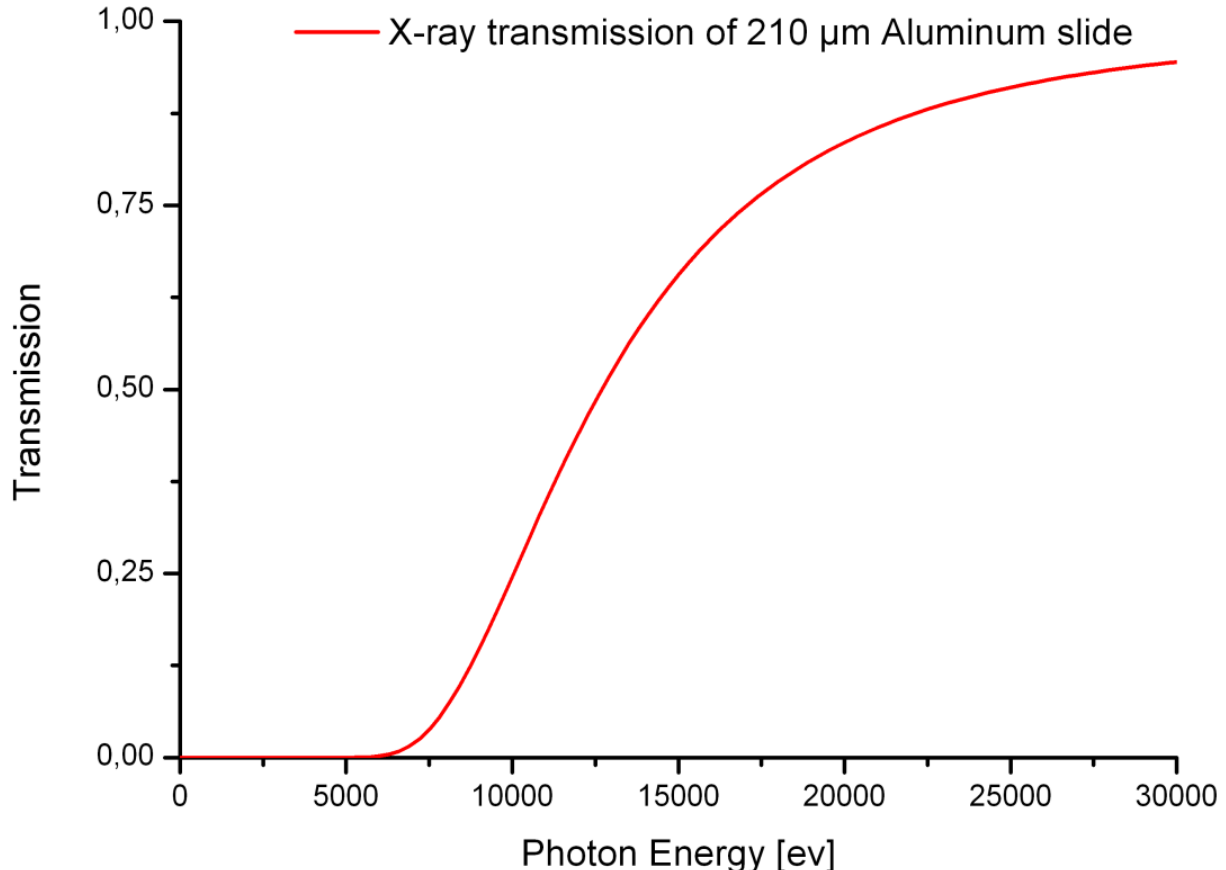


Figure 5.128: Calculated X-ray transmission of a 210 μm aluminium slide.

The mean values of the counts after correcting for X-ray absorption efficiencies of SrI_2 and YAG are listed in Table 5.5. The light yield of the SrI_2 – screen was higher than the YAG – screen by a factor between 4.28 and 4.98.

Energy (keV)	SrI ₂ counts	YAG counts
12	103256	22173
20	43533	8732
25	38104	8889

Table 5.5: Gray values (counts) from the recorded flat field images.

5.4.2 Mesh Image Recording (Image Spatial Resolution and Contrast)

The spatial resolution of the SrI_2 -screens was tested with a tee-mesh pattern. It is a metal mesh, and has wires of few micrometers in width. Figure 5.129 shows the resolution of the tee-mesh image recorded with YAG – scintillator. All the images recorded with SrI_2 – samples are compared to this image. The resolution and contrast of this image recorded with the YAG – scintillator screen is very high.

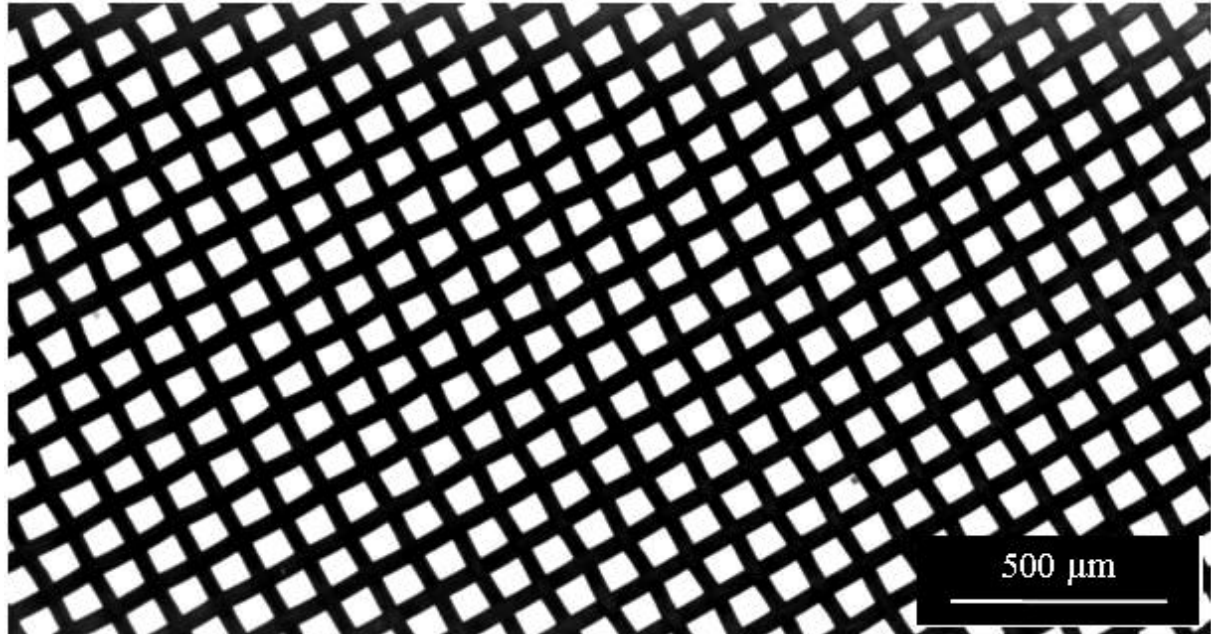


Figure 5.129: The tee mesh image recorded with the YAG – scintillator at 12 keV; 200 ms integration time was used; sample was 400 μm thick.

The tee-mesh image recorded with the first SrI_2 – screen is shown in Figure 5.130. The problems with the resolution of this image can be attributed to the packaging, which was still at its early stage. It was very difficult measuring this sample due to the sliding of the detector window over the sample, because of the soft Apiezone wax used. The image contrast is suspected to be reduced by light scattering.

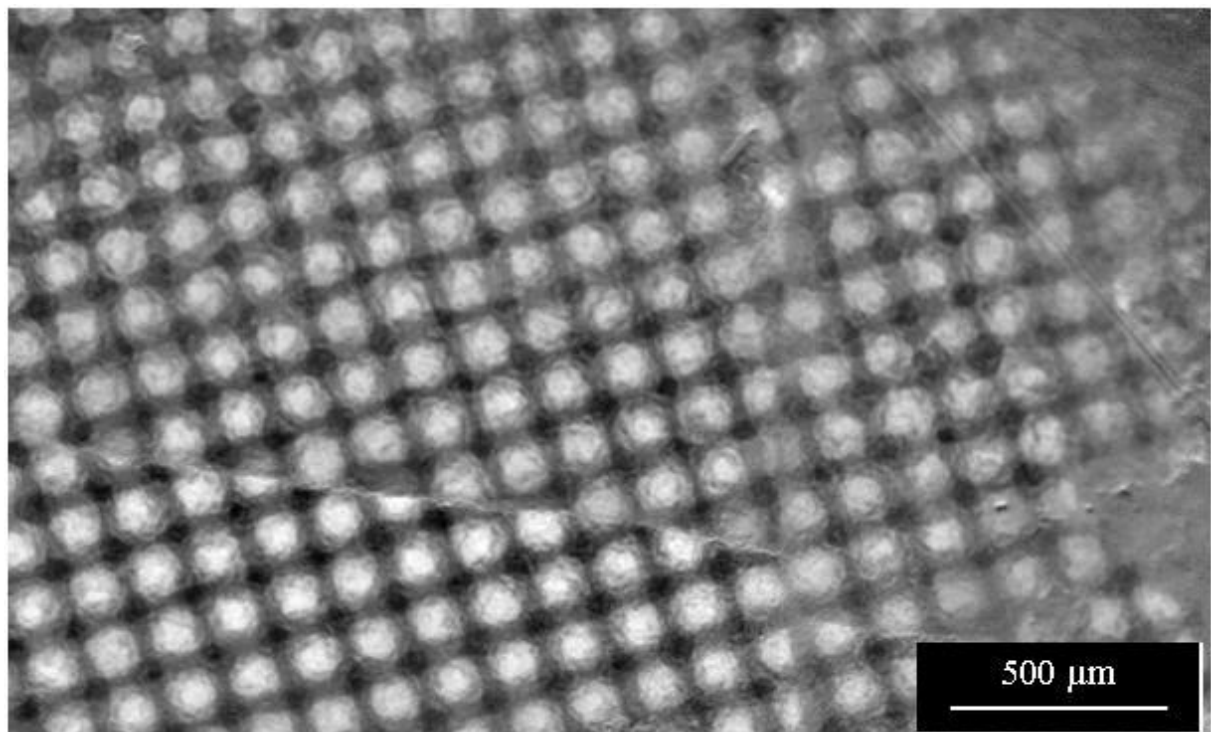


Figure 5.130: The tee mesh image recorded with the SrI_2 -3 at 25 keV; sample was 360 μm thick.

Experiments and Results - 5

The resolution of the image with the sample - 5(a) in Figure 5.131 is similar to that recorded with the YAG – screen. Visible on this image are also stains, which are well resolved. The good contrast of this image is attributed to the optical coupler applied between the scintillator screen and the detector window. From this moment, detector windows were also glued using an epoxy kit (KL-320K) from Lesker.

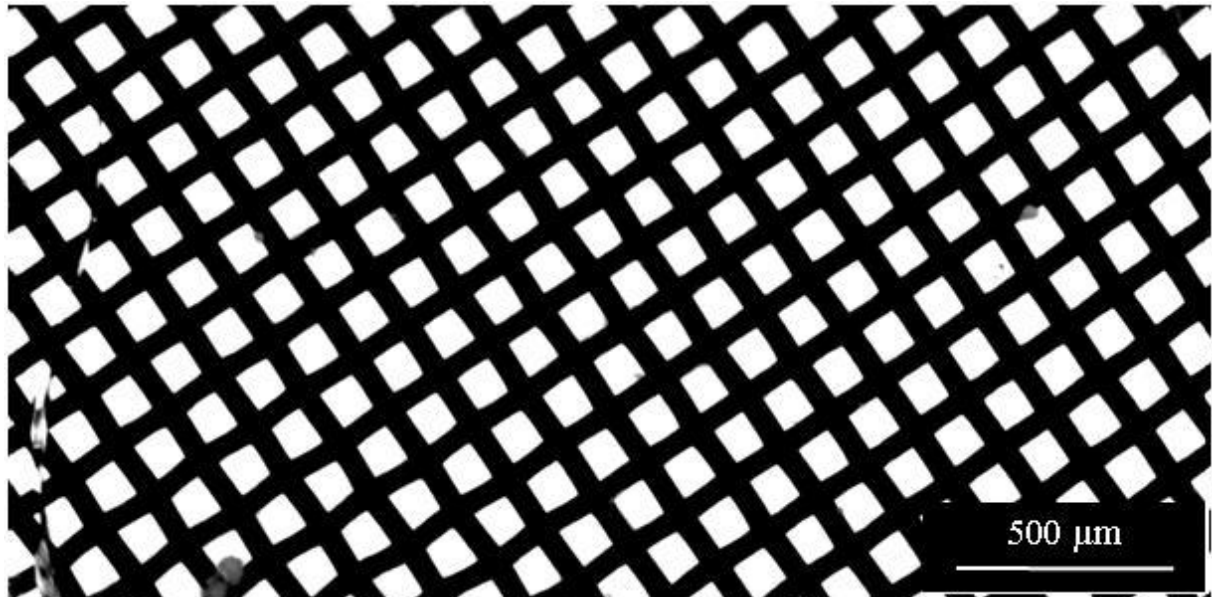


Figure 5.131: The tee mesh image recorded with the SrI_2 – 5(a) at 12 keV; 300 μm thick; Bicron BC-630 opt. Coupler and 50 ms integration time were used.

The packaging of the sample – 5(b) is similar to the sample – 5(a). In order to check the effect of the optical coupler employed in sample – 5(a), no optical coupler was used here. The sample – 5(b) was also 80 μm thicker than sample – 5(a). It is well known that the resolution of a scintillator based system also depends on the screen thickness. The resolution of the image of the sample – 5(b) in Figure 5.132 is good; all tee-mesh wires are visible. The contrast of this image is poorer than that recorded with the sample – 5(a). It looked like there were scratches on the surface of the scintillator screen visible on this image. These scratches tend to reflect the scintillation light in different directions, leading to the reduction of the image contrast.

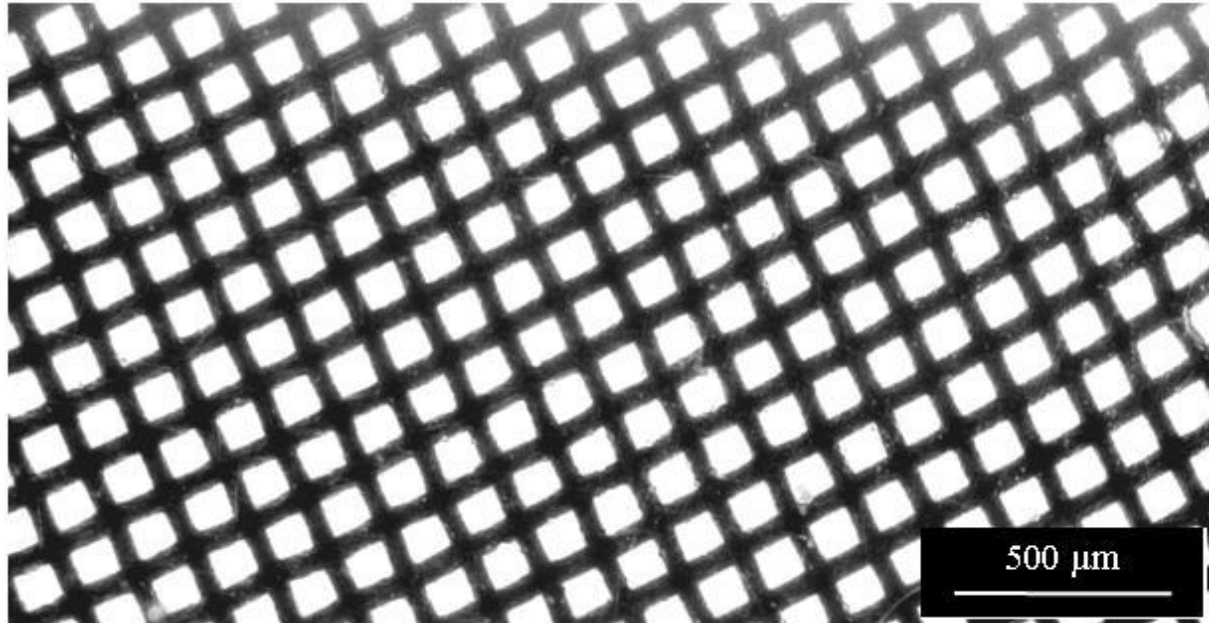


Figure 5.132: The tee mesh image recorded with the $\text{SrI}_2 - 5(\text{b})$ at 12 keV; 380 μm thick; No opt. Coupler used; 50 ms integration time was used.

The resolution of the tee mesh image recorded with sample – 6 is good and also comparable to that of the YAG - screen. The contrast of this image can also be described as high, as shown in Figure 5.133. Visible on this image are few bubbles on the right side which will be discussed later.

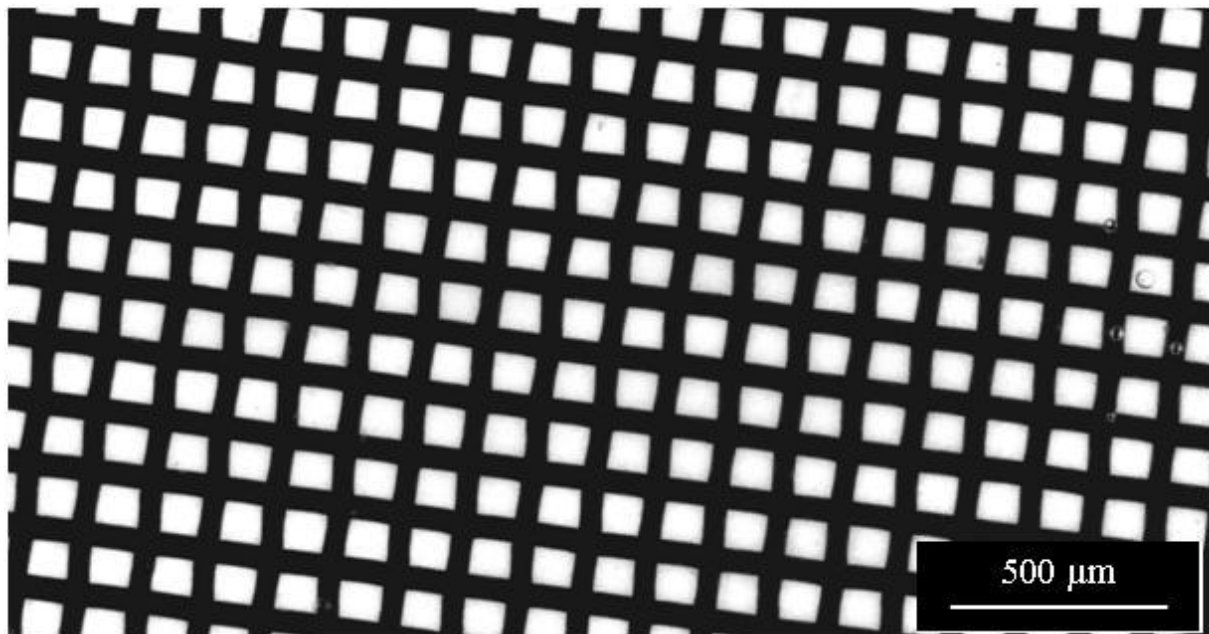


Figure 5.133: The tee mesh image recorded with the $\text{SrI}_2 - 6$ at 12 keV; 400 μm thick; EPO-TEK 305/B4 opt. Adhesive and 2 minutes integration time were used.

5.4.3 Radiographic Images

The samples – 5(a) and – 6 were used to record radiographic images of light-weighted objects. Again, the YAG – scintillator was used as the reference sample. Figure 5.134 shows the radiographic image of an ant obtained with the YAG – scintillator screen. This measurement was done at 12 keV X-ray energy using 200 ms integration time. Notice here the resolution and contrast of the image.

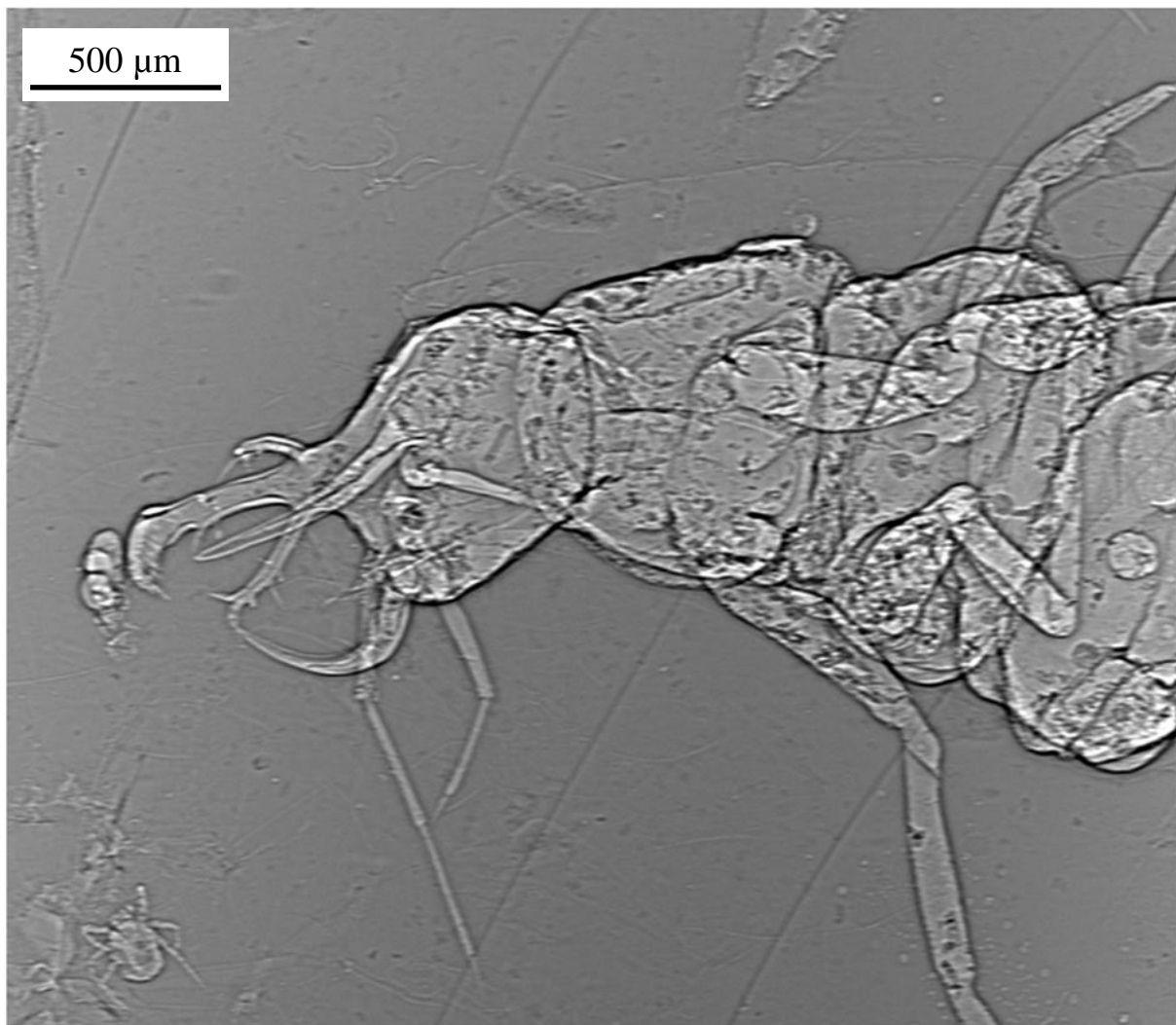


Figure 5.134: Radiography image of an ant recorded with the YAG – scintillator at 12 keV; 200 ms integration time; 400 μm thick. Object distance to scintillator screen was 6 cm.

The same ant was imaged using the SrI_2 sample – 5 (a) as shown in Figure 5.135. The same excitation energy 12 keV was used with a 50 ms integration time. The resolution of this image is comparable to that of the YAG, despite the inhomogeneities seen on the flat field image of this sample, which are attributed to difficulties in the packaging process. More work was done after this measurement to refine the whole packaging process leading to better results in sample – 6.

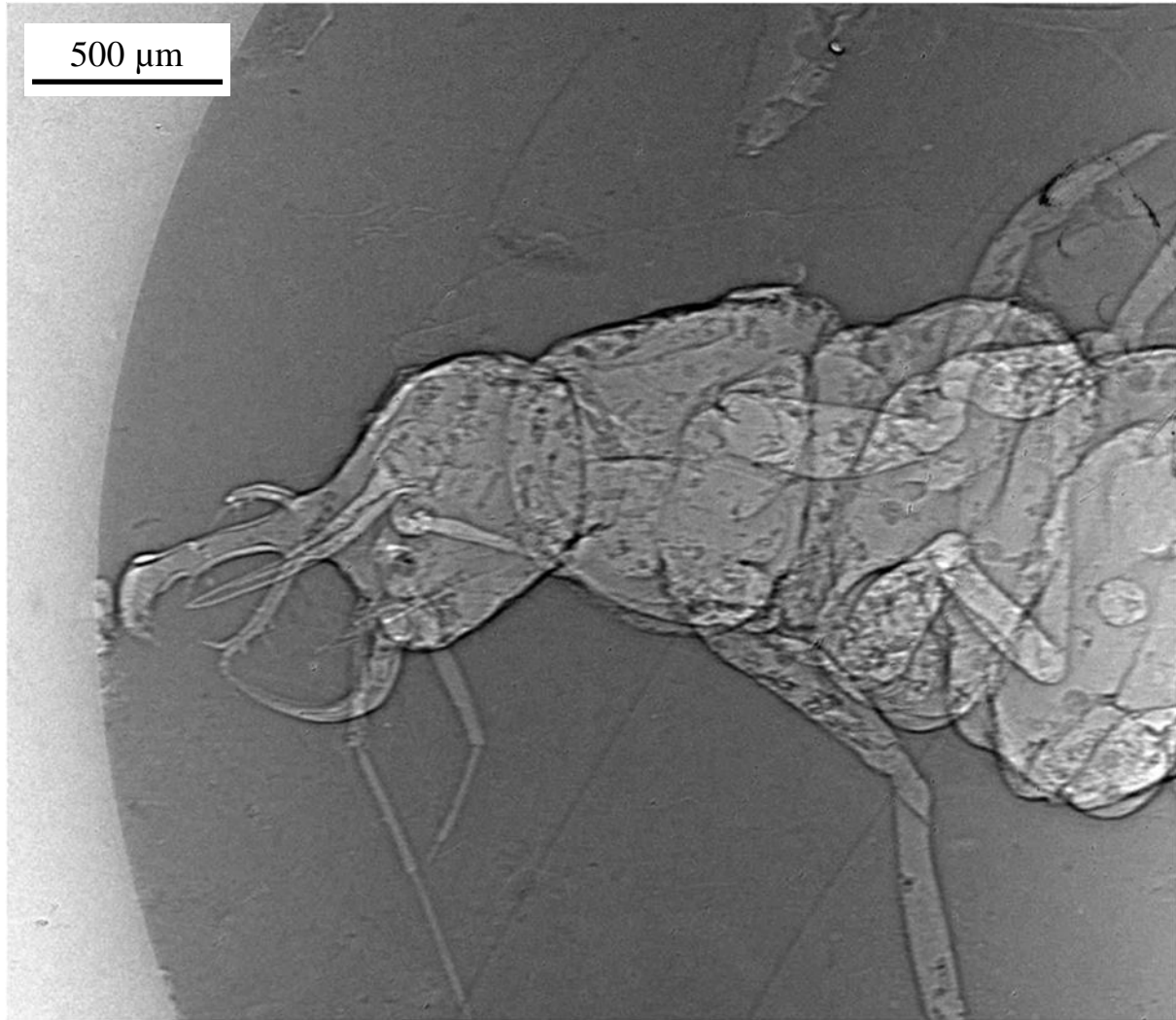


Figure 5.135: Radiography image of an ant recorded with the SrI₂ – 5(a) at 12 keV; 300 μm thick; Bicron BC-630 opt. Coupler; 50 ms integration time; Object distance to scintillator screen was 6 cm.

The sample – 6 was made 4 months after samples – 5 (a & b). Instead of the Bicron BC-630 optical grease, an optical adhesive (epoxy) was used. The spatial resolution of the samples was tested using lithography printed gold-patterns shown in Figure 5.136. This printed pattern can be rearranged into different structures for measurement. The tested regions are highlighted in red.

Experiments and Results - 5

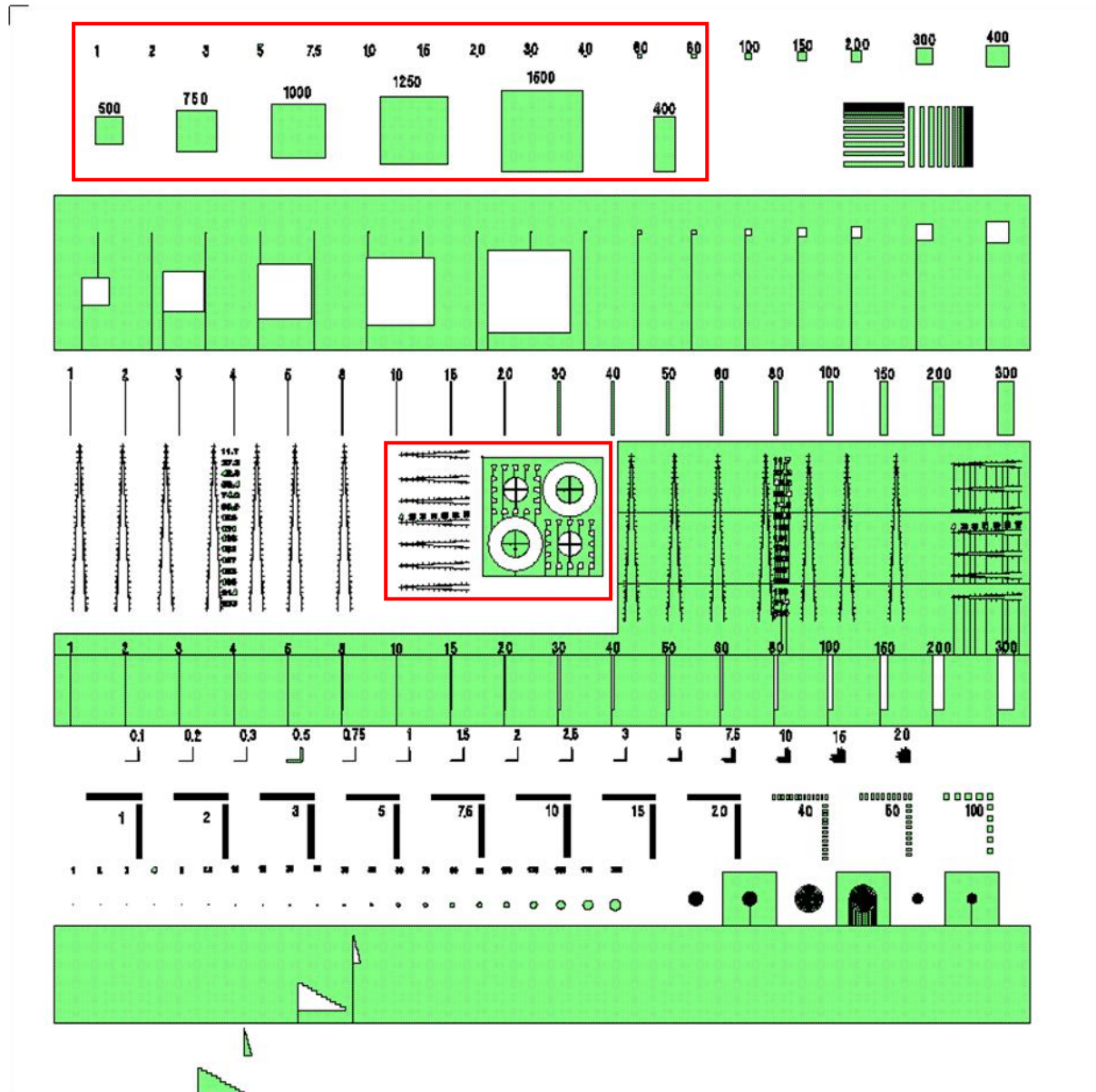


Figure 5.136: Lithography printed gold - pattern used for spatial resolution tests (Area 20 x 20 mm). The tested regions are highlighted in red.

At 15 keV X-ray energy, radiographic images of the region highlighted in red in the middle of Figure 5.136 were recorded using two different SrI_2 – screen samples. Figure 5.137 shows the test structure image recorded using the sample – 5(a). This measurement was done four months after the first measurements to check for any degradation of this sample. The resolution and contrast of this image are similar to other images recorded with this sample. There were also no signs of detector degradation.

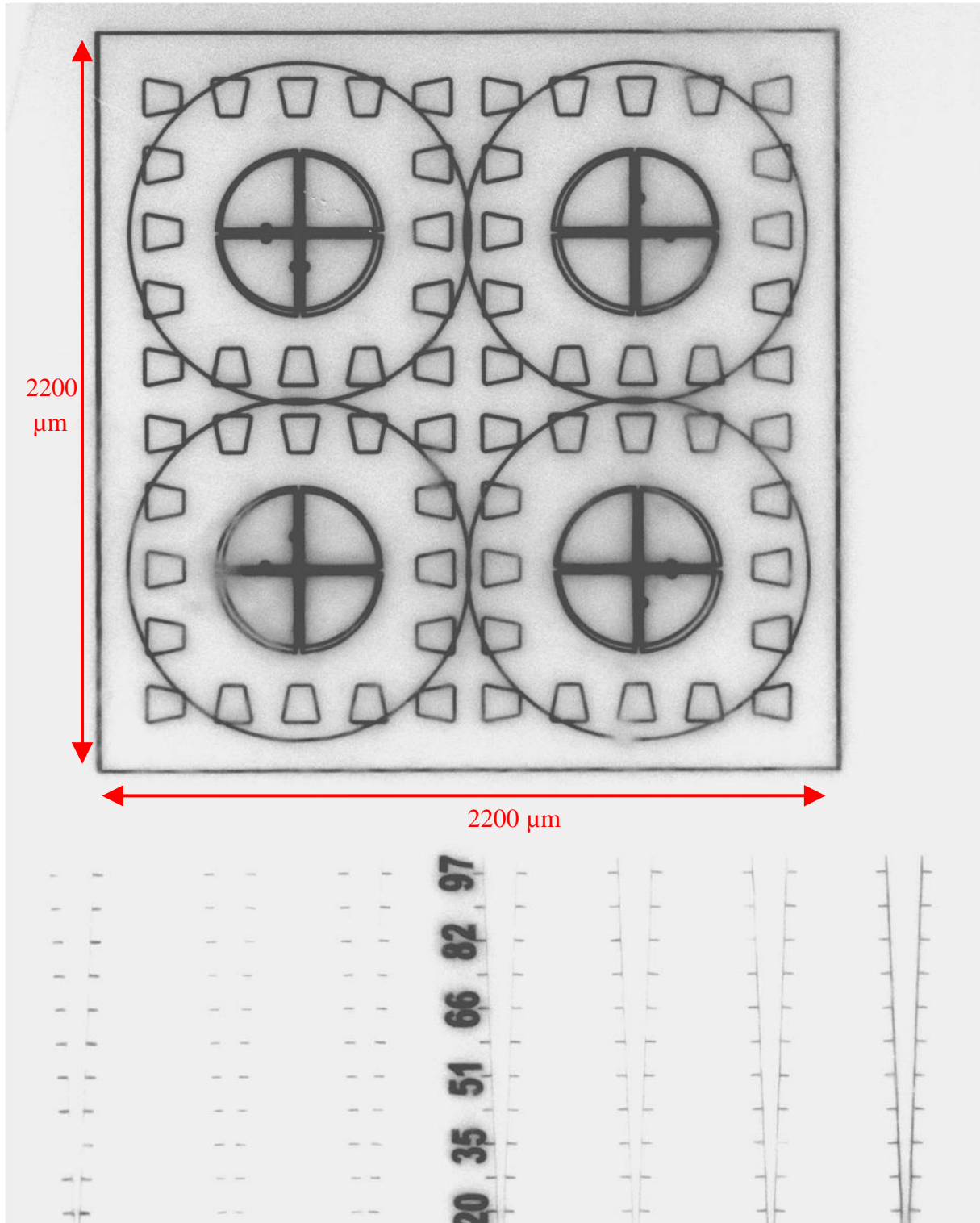


Figure 5.137: Test pattern image recorded with the SrI_2 – 5(a) at 15 keV; 300 μm thick; Bicron BC-630 opt. Coupler; 15 seconds integration time; Image recorded 4 months later and the object distance to the scintillator screen was 3 cm.

The same pattern image was also recorded using sample – 6 as shown in Figure 5.138. The experimental conditions were similar. The resolution and contrast of this image are good and also comparable to other images recorded with this sample.

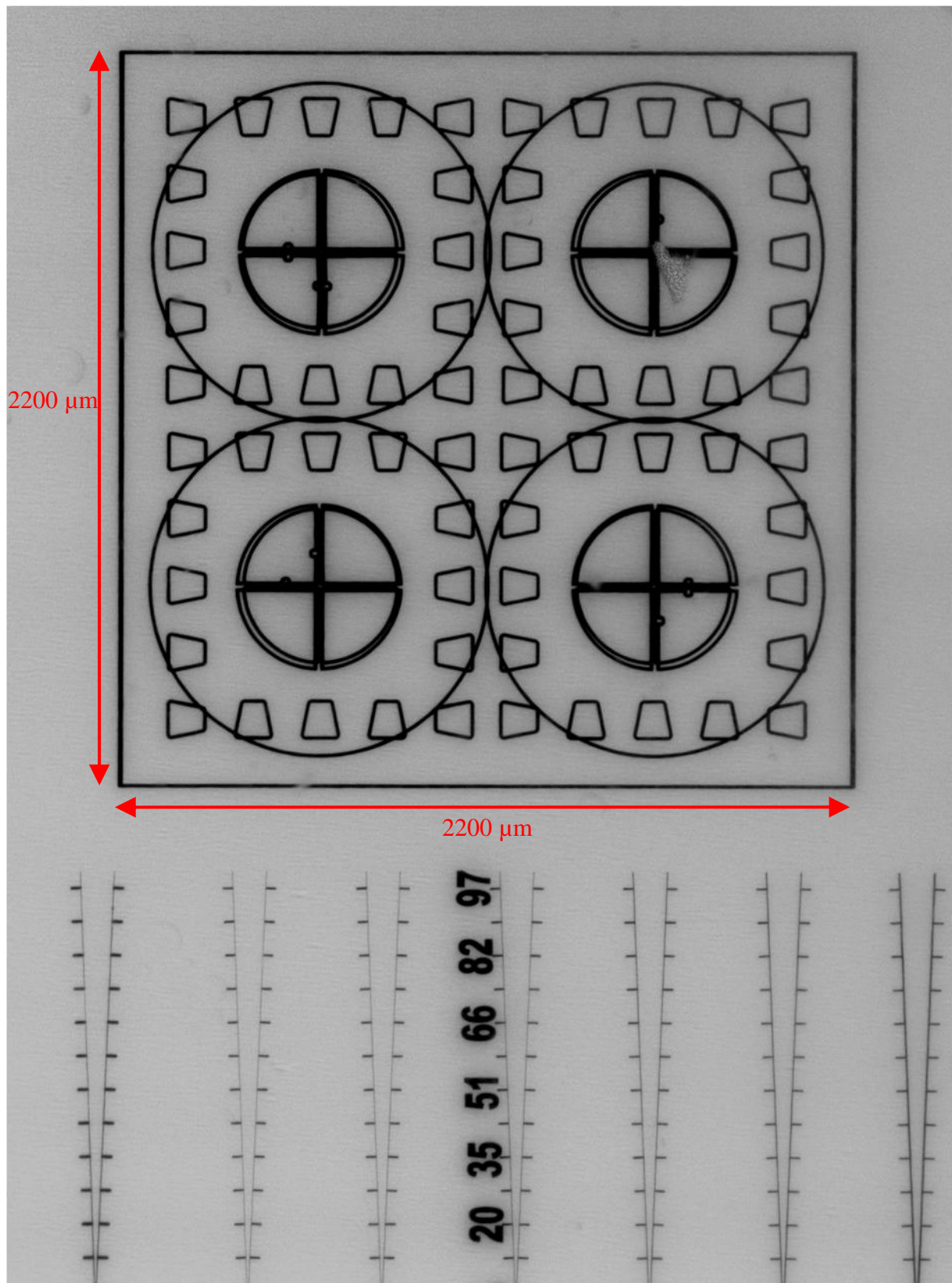


Figure 5.138: Test pattern image recorded with the $\text{SrI}_2 - 6$ at 15 keV; 400 μm thick; EPO-TEK 305/B4 opt. Adhesive and 15 seconds integration time were used. Object distance to scintillator screen was 3 cm.

Experiments and Results - 5

The upper region of Figure 5.136 highlighted in red was also rearranged and imaged using the sample – 6. The image is shown in Figure 5.139. The test pattern was not placed in the center of the active window although, the square corresponding to the 12 line pairs mm^{-1} shows a good resolution. The excitation energy was 15 keV using 2 minutes integration time.

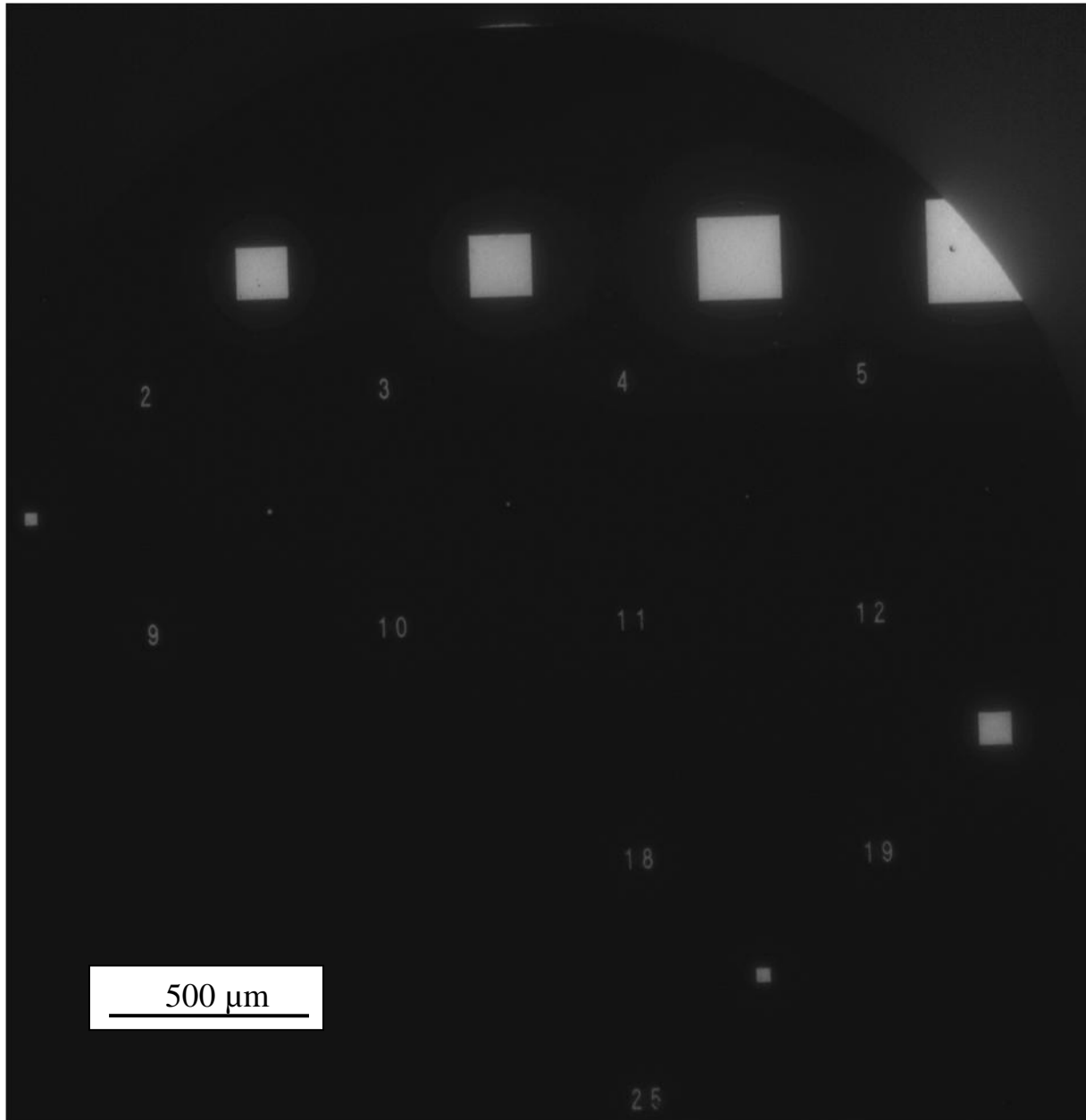


Figure 5.139: Test pattern image recorded with the SrI_2 – 6 at 15 keV; 400 μm thick. EPO-TEK 305/B4 opt. Adhesive and 2 minutes integration time were used.

We also recorded images of a chip as shown in Figure 5.140 with the sample - 6. The resolution and contrast of this image are good. The structuring on the micro chip and the wire bonding were all good resolved. The problem with this image is the bubbles. The bubbles emanate from the optical coupler used which is a two component optical adhesive. The bubbles are produced during the mixing of the components, and are only present at the corners of the scintillator screen. 50 ms integration time was used.

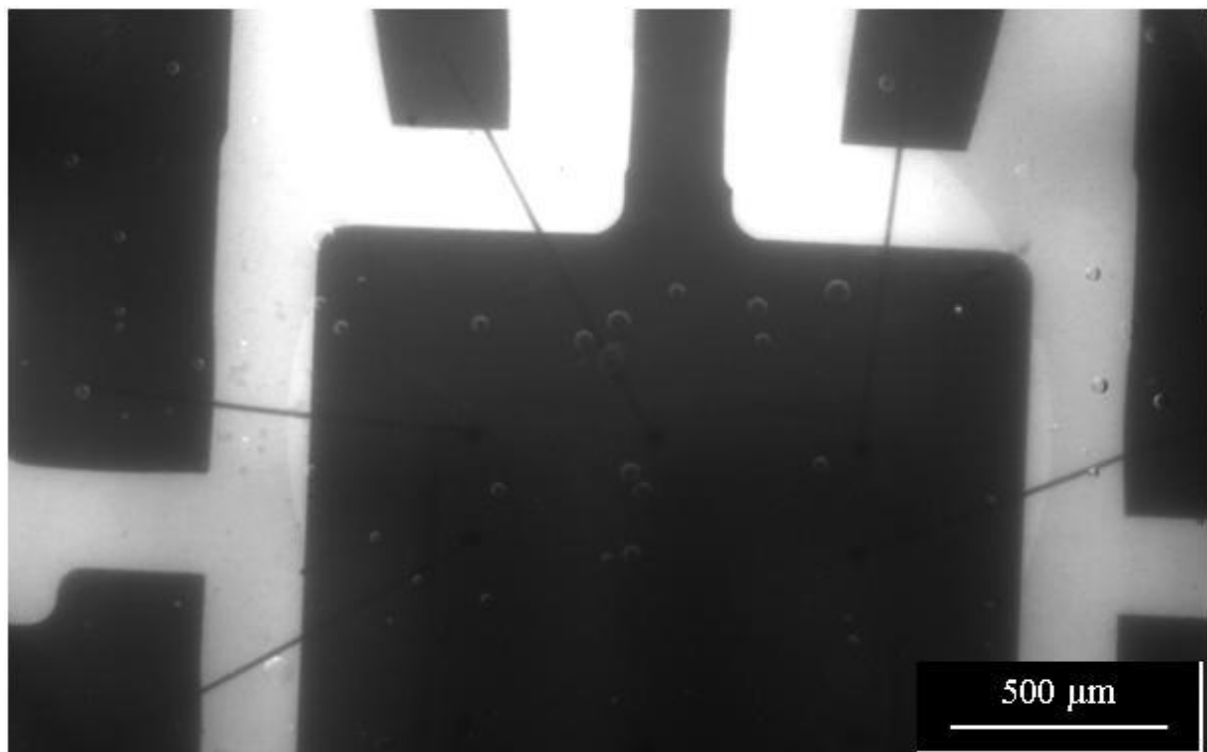


Figure 5.140: Image of a chip recorded with the $\text{SrI}_2 - 6$ at 12 keV; 400 μm thick. EPO-TEK 305/B4 opt. Adhesive and 50 ms integration time were used.

Figure 5.141 shows the same image as in Figure 5.140. A colour scheme was used here to indicate the emission intensity (optical density) distribution of the image, and the resolution was shown to have improved.

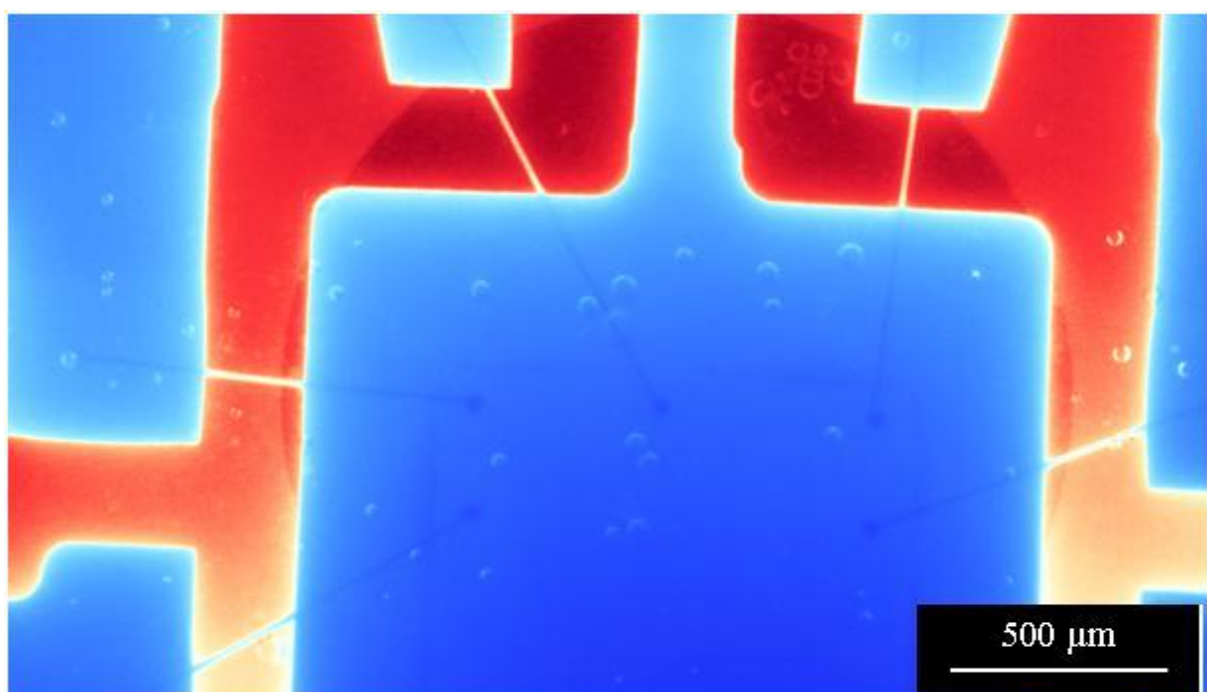


Figure 5.141: The same image of the chip using a colour scheme to depict the emission intensities.

Experiments and Results - 5

A second image of the chip was recorded using 120 ms integration time. The resolution also improved tremendously, probably because a better light image was produced in the 120 ms integration time.

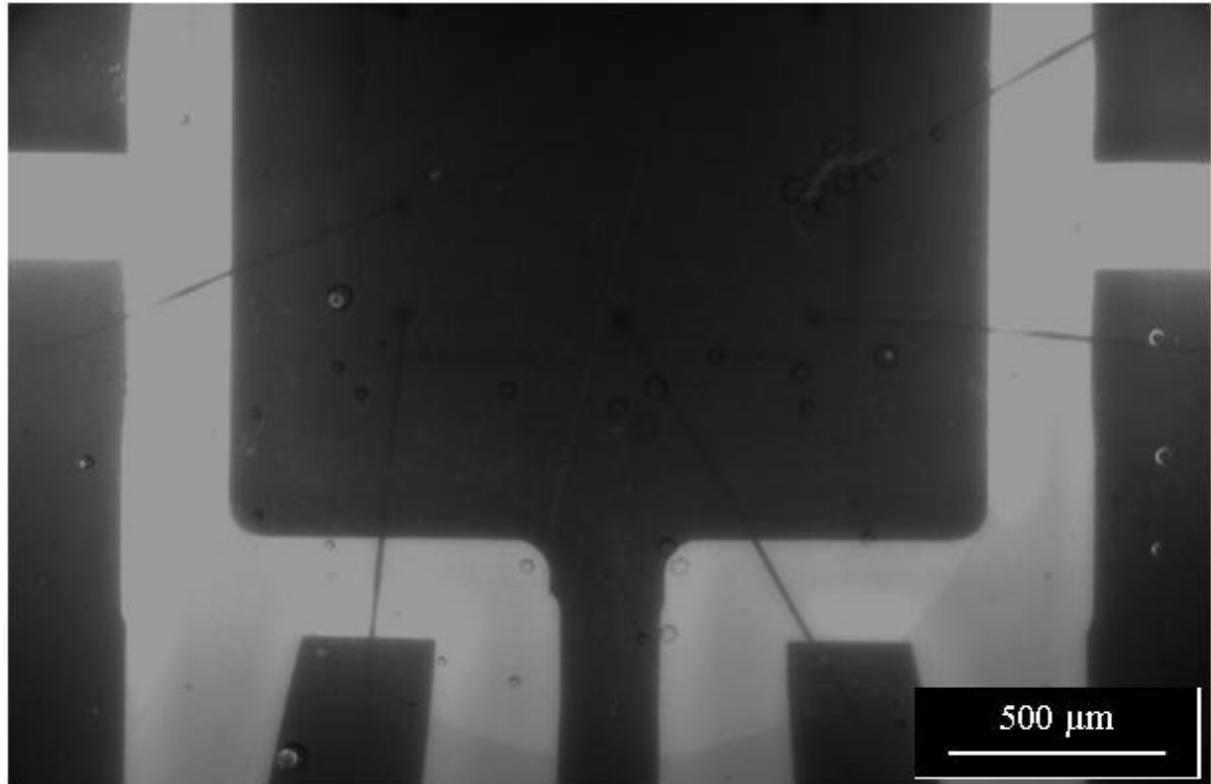


Figure 5.142: Another image of the same chip recorded with the SrI₂ – 6 at 12 keV; 400 μm thick. EPO-TEK 305/B4 opt. Adhesive and 120 ms integration time were used.

Darkening of the active detector area in the last measurement was noticed after a week. Investigations showed the darkening to be produced in the epoxy (EPO-TEK 305/B4 opt. Adhesive) that served as the optical coupler. Probably the optical coupler was not radiation hard. The darkening is shown in Figure 5.143.

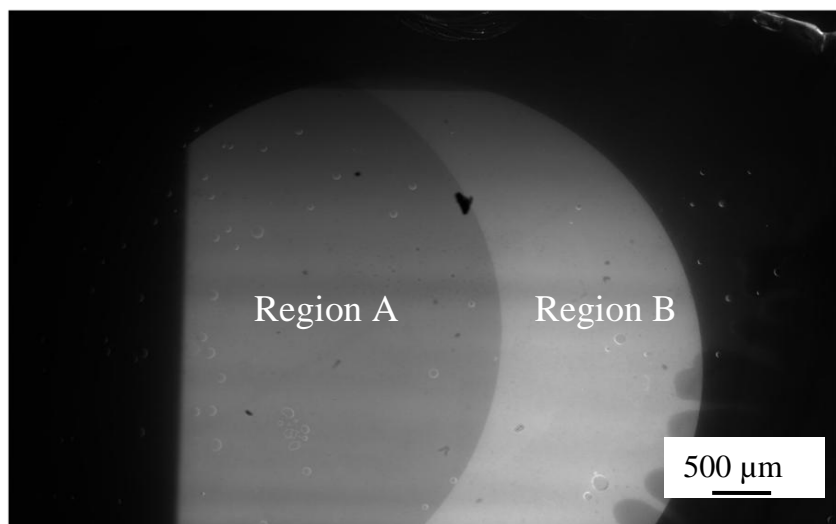


Figure 5.143: Darkening noticed on the SrI₂ – 6 detector after a week due to radiation damage on the EPO-TEK 305/B4 opt. Adhesive.

5.4.4 First X-Ray Tomography Images using SrI₂

For the experiments conducted here, a scintillator thin screen SrI₂ - 7 was made from slice 2 in Figure 5.111. The thickness of the SrI₂ - 7 was 400 µm. Using 16.5 keV X-ray excitation energy and 3.5 seconds integration time, a radiography image of a copper grid was recorded as shown in Figure 5.144. The diameter of the copper grid was 3 mm with wires of 8 µm. This image was recorded to check the resolution and the homogeneity of the emission of this sample.

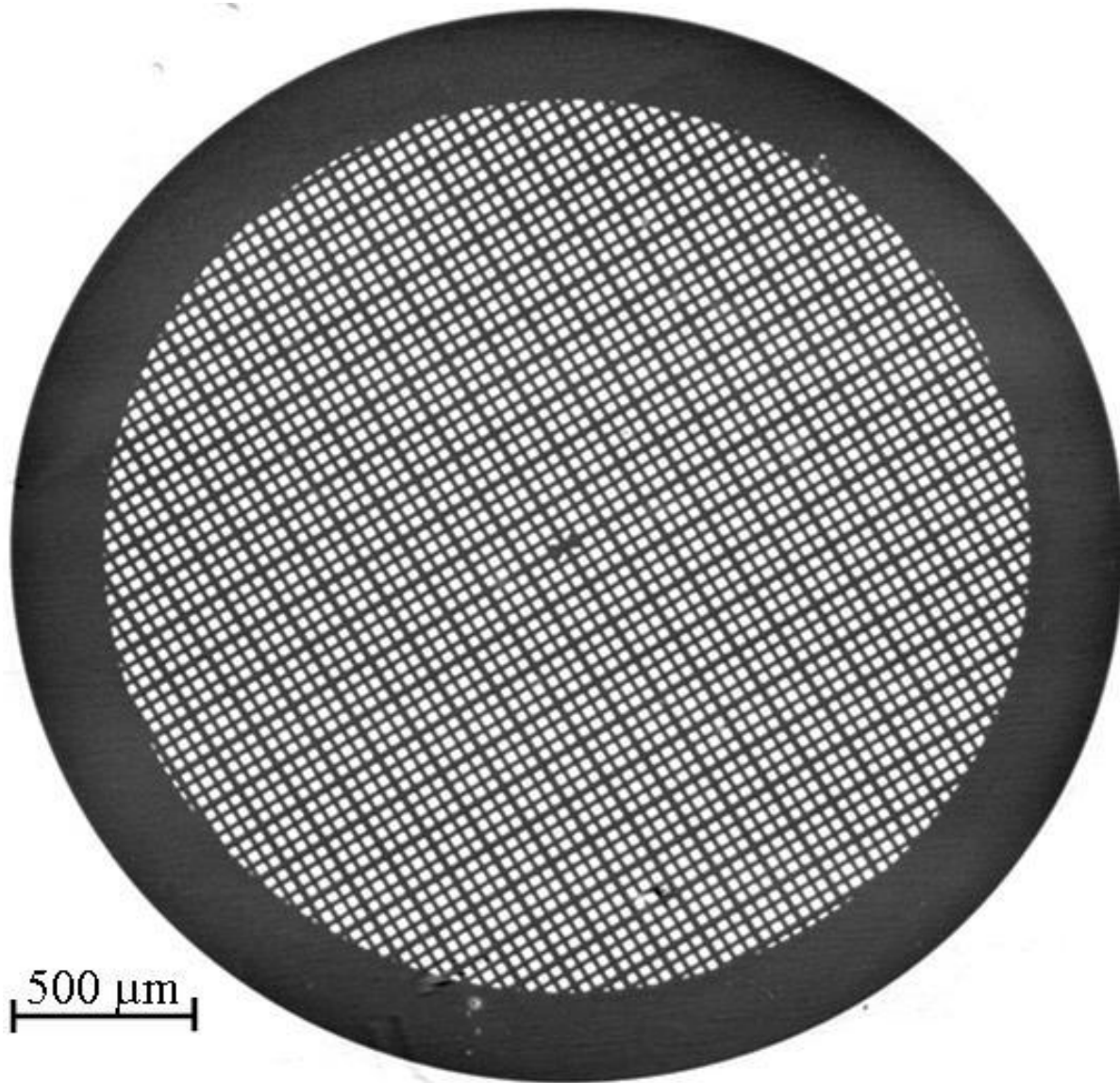


Figure 5.144: Radiography image of a 3mm diameter copper grid with 8 µm wires.

The theory and advantages of phase contrast over absorption contrast X-ray tomography has been discussed in chapter 2.5.3. Owing to the high quality of the radiographic images recorded in this work, the applicability in X-ray tomography was also investigated.

Experiments and Results - 5

The detector was beamed to $2 \times 2 \text{ mm}^2$ for the recording of the tomography images. The sample distance to the detector was 23.5 cm. The X-ray excitation energy used for the experiments was 16.5 keV. A total of 1200 image projections were recorded using 3.5 seconds integration time.

After the reconstruction, a software known as „ANKAphase“ was used to process the phase contrast radiographs. The ANKAphase reconstructs the projected thickness of the object(s) imaged using a single – distance non – iterative phase – retrieval algorithm described by David Paganin [Weitkamp 2011].

The sample imaged here was a bug known as „*Trigonopterus vandekampi*“. Figure 5.145 shows the same projection of the sample in absorption contrast and phase contrast mode. It is important to note the resolution and contrast of the phase contrast image. Distinguishing the different organs in the absorption contrast mode is almost impossible, while the organs and bubbles in the glue at the back of the bug are very visible in the phase contrast image.

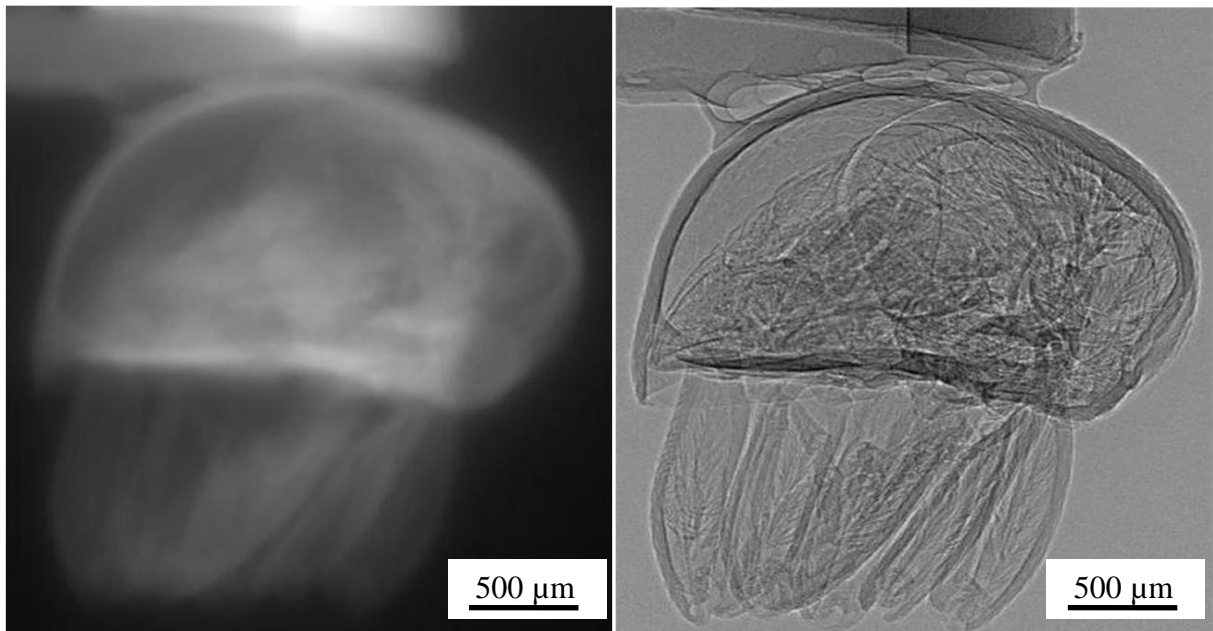


Figure 5.145: Single projection images of a bug „*Trigonopterus vandekampi*“ in absorption contrast and phase contrast mode.

Two different projections of the internal organs of the bug are shown in Figure 5.146. These images can be described as having high resolution and high contrast; nevertheless it is very difficult to distinguish the different internal organs.

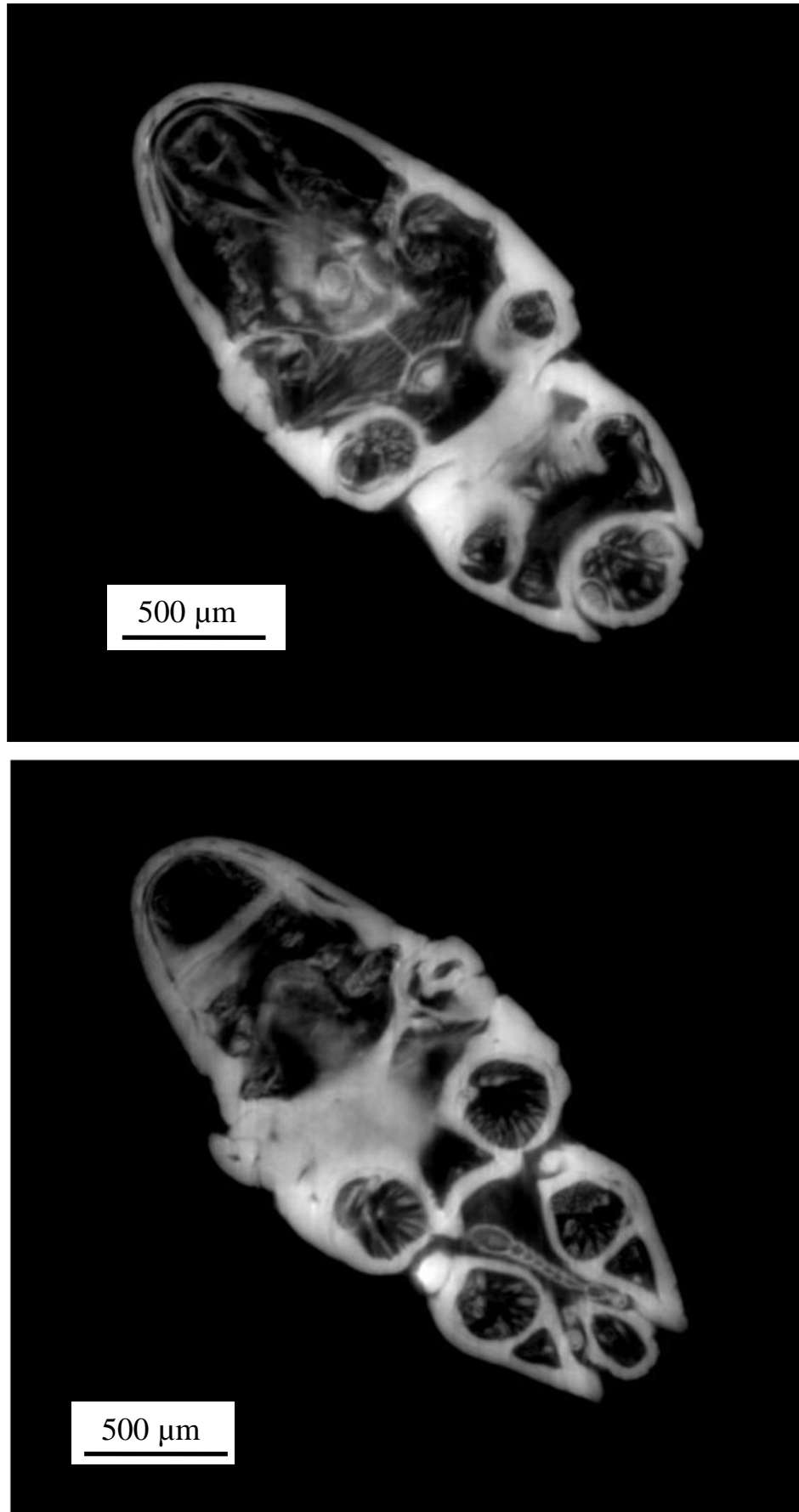


Figure 5.146: High resolution and high contrast (absorption contrast) images of the bug „*Trigonopterus vandekampi*“ showing the internal organs.

Experiments and Results - 5

Figure 5.147 shows the image (side view) of the bug „*Trigonopterus vandekampi*“ sample recorded. It is important to note here the quality of the image, especially the scales on the body of the bug.

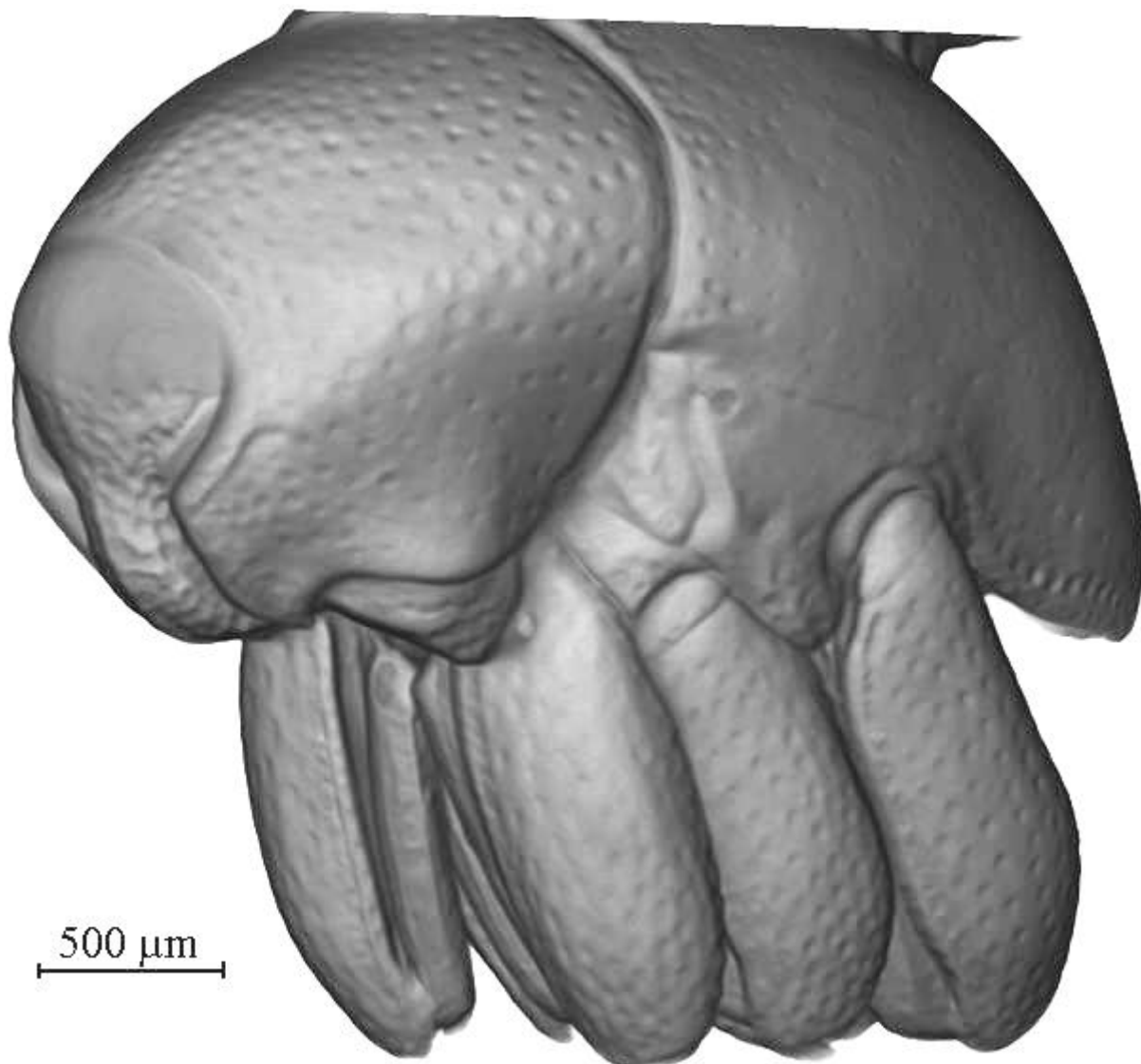


Figure 5.147: Tomography image (side view) of the bug „*Trigonopterus vandekampi*“ showing a good resolution of the scales on the body.

Experiments and Results - 5

An image of the internal organs is shown in Figure 5.148. This image reveals the shrinking of the internal organs with time. It is also possible in the image to distinguish the different internal organs from the image.



Figure 5.148: A view of the internal organs of the bug „*Trigonopterus vandekampi*“.

A view of the internal organs in the head region (Figure 5.149) reveals a network of muscles; these are thought to be responsible for the movement of the head. Other important features are the scales on the internal body; they seem to show a different pattern from the scales on the outside body in Figure 5.147.

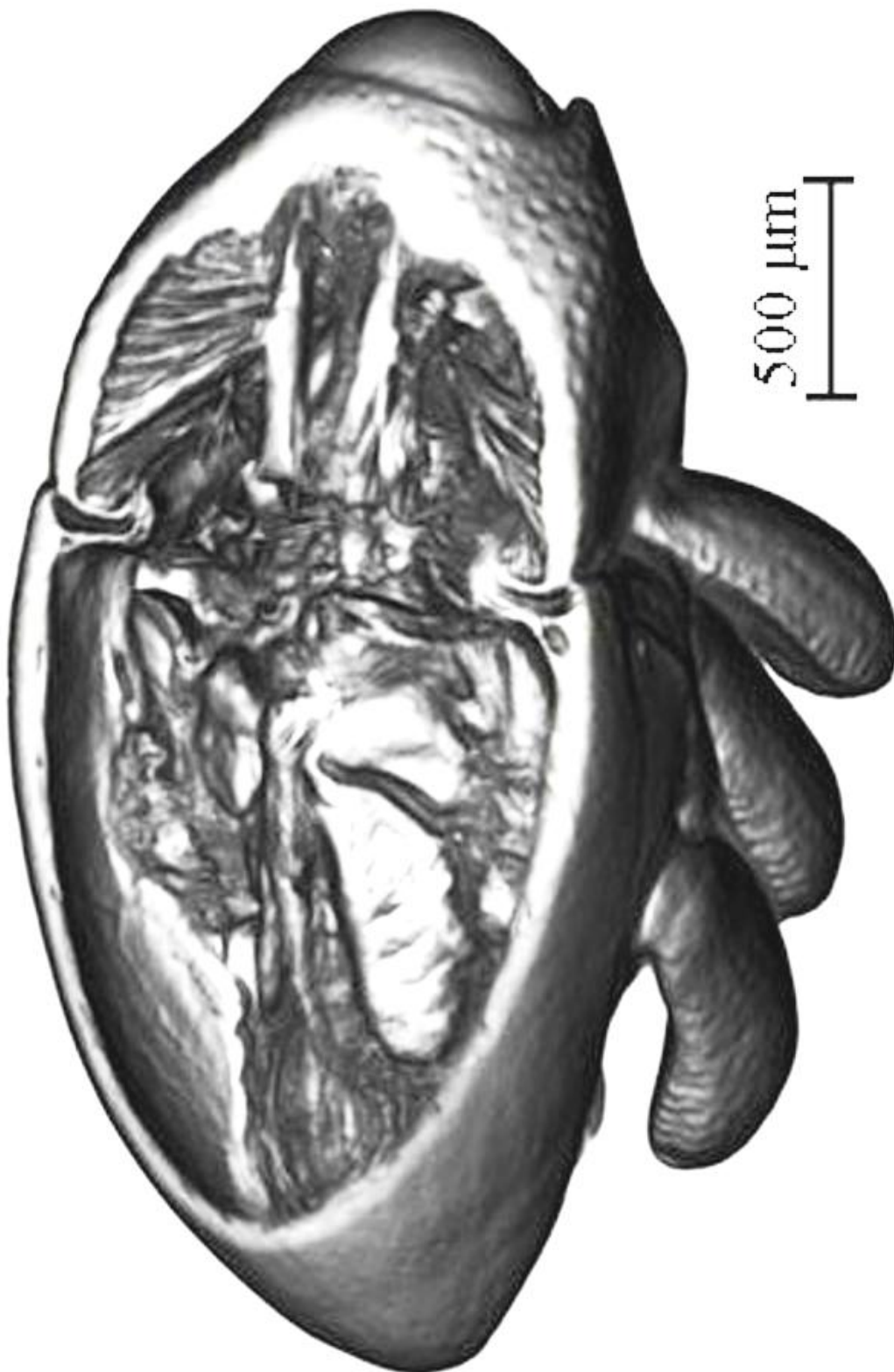


Figure 5.149: An image of the bug „*Trigonopterus vandekampi*“ revealing the muscles that control the movement of the head and also scales on the internal body.

Experiments and Results - 5

Images of the bottom view and the front view are shown in Figure 5.150 and Figure 5.151 respectively. The quality of these images is high and also revealing of every feature of the bug imaged.

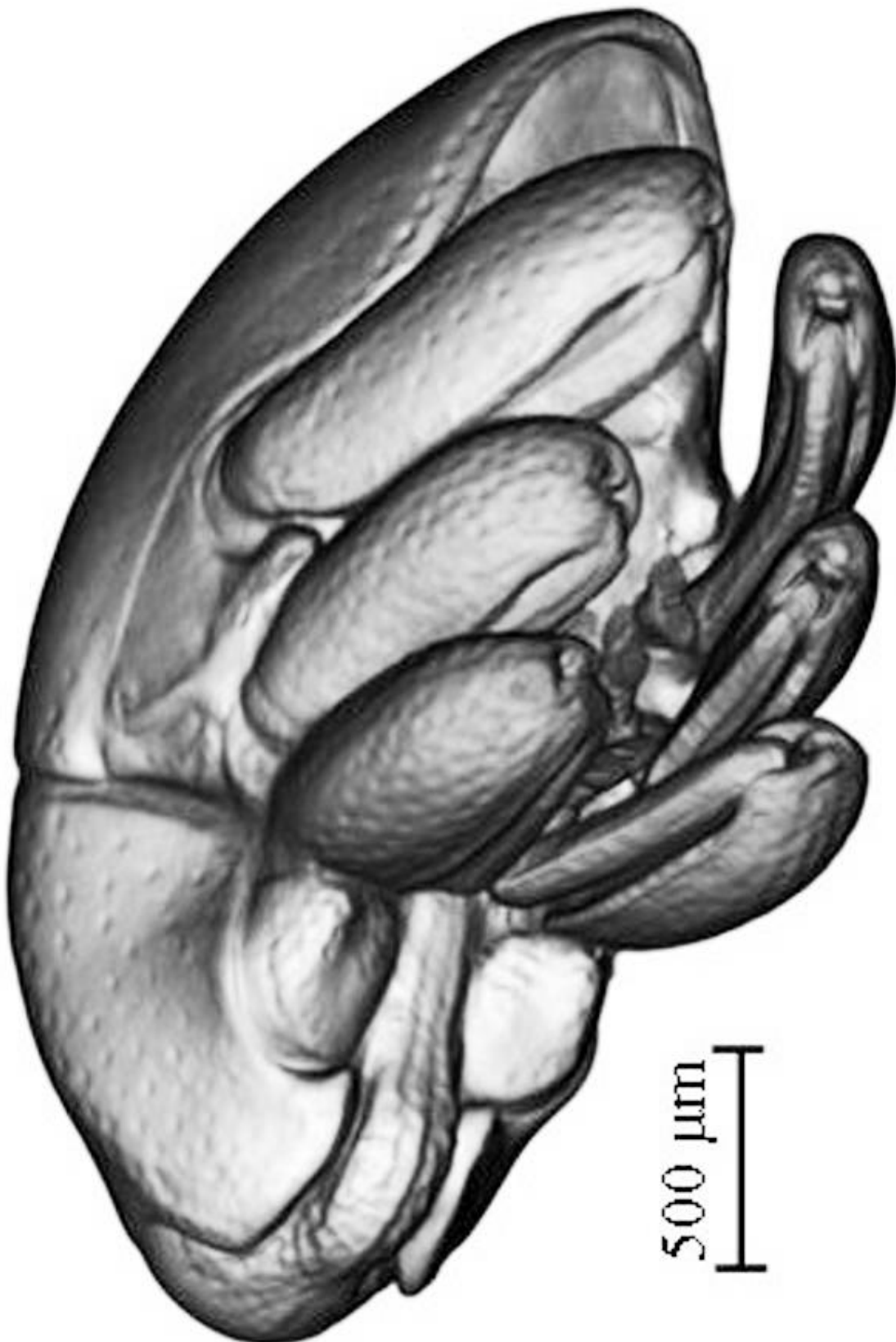


Figure 5.150: An image of the bug „*Trigonopterus vandekampi*“ showing the legs.



Figure 5.151: The front view of the bug „*Trigonopterus vandekampi*“.

The quality of the tomography images is high. Such image qualities are normally achieved using non – hygroscopic scintillators with no packaging effects on the image quality. Being able to attain such image qualities despite the embedding layers covering the SrI₂ – scintillator thin screens suggests that the packaging technique developed and used here is very good. Another factor that might have played a very important role is also the high quality of the scintillator crystal; this is confirmed by the good energy resolution (2.7% at 662 keV) of the bulk sample as shown in Figure 5.117.

In a scintillator based X-ray imaging detector system, the image resolution depends on three factors:

- I. The optical system; the fundamental maximum to the resolution of any optical system (microscope, telescope) is limited by the diffraction limit.
- II. The absorption process can also limit the spatial resolution of imaging detectors when secondary processes (i.e. characteristic X-rays and secondary electrons) deposit their energies far from the primary photon interaction site.
- III. The thickness of the scintillator (geometry) is also an important factor that influences the spatial resolution of a scintillator based detector system. There exists a maximum optimum thickness of a scintillator screen for given parameters of the optical collection system. A thicker screen will indeed absorb high energy photons more efficiently, but the image on the CCD camera becomes blurred [Koch 1998]. With a thinner scintillator screen, sharper images will be produced due to less lateral spreading of the scintillation light [Tous 2010].

The optimum highest screen thickness for the chosen parameters of the imaging system used here was 400 µm. Figure 5.152 shows the calculated X-ray attenuation efficiency in different thickness of SrI₂ - screens. If we assume only the photoelectric effect at the energies used here due to the absorption efficiency of the SrI₂, we can consider the absorption process not being an influencing factor. The resolution of the images presented here could have been influenced only by geometry (thickness and total packaging of the scintillator screens) and optical system problems.

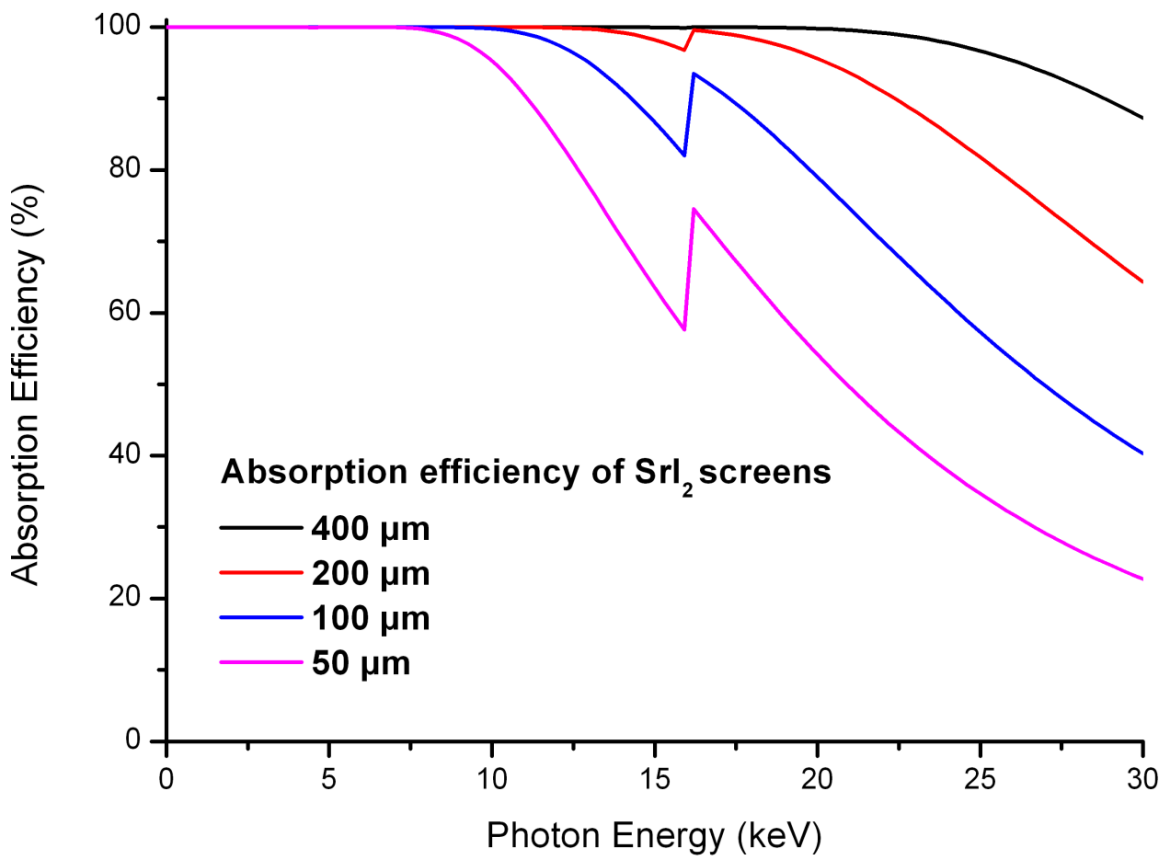


Figure 5.152: Calculated X-ray absorption efficiency of SrI_2 – scintillator thin screens.

Bibliography

[Chang 1974]

Chong E. Chang, William R. Wilcox: Control of Interface Shape in the vertical Bridgman-Stockbarger Technique. *Journal of Crystal Growth* 21 (1974) 135-140.

[Gero 2013]

<http://www.gero-gmbh.de/deutsch/industrieofen/rohrofen/standardrohrofen-f.html>.
Page accessed February 12, 2013.

[Birks 1964]

J. B. Birks: The Theory and Practice of Scintillation Counting. Pergamon Press LTD. 1964.

[Cecilia 2009]

A. Cecilia, A. Rack, D. Pelliccia, P. -A. Douissard, T. Martin, M. Couchaud, K. Dupré, T. Baumbach: Studies of LSO:Tb radio-luminescence properties using white beam hard X-ray synchrotron irradiation. *Radiation Effects and Defects in Solids* 164: 9, 517 -522 (2009).

[Sturm 2010]

Benjamin W. Sturm, Nerine J. Cherepy, Owen B. Drury, Peter A. Thelin, Scott E. Fisher, Stephen A. Payne, Arnold Burger, Lynn A. Boatner, Joanne O. Ramey, Kanai S. Shah, Rastgo Hawrami: Effects of packaging SrI₂(Eu) scintillator crystals. *Nucl. Instr. and Meth. A* (2010).

[Martin and Koch 2006]

Thierry Martin and Andreas Koch: Recent developments in X-ray imaging with micrometer spatial resolution. *J. Synchrotron Rad.* (2006). 13, 180-194.

[Baumbach 2007]

Prof. Dr. Tilo Baumbach: Novel Ceramic Thin Film Based Scintillator for High Resolution X-Ray Imaging. Report on Deliverable D 1.2. 21 May 2007.

[henke.lbl.gov]

http://henke.lbl.gov/optical_constants/filter2.html. Page accessed 25.02.2013.

[Koch 1998]

Andreas Koch, Carsten Raven, Per Spanne, Anatoly Snigirev: X-ray imaging with submicrometer resolution employing transparent luminescent screens. *J. Opt. Soc. Am. A/Vol. 15, No. 7/July 1998.*

Experiments and Results - 5

[Tous 2010]

J. Tous, P Horodysky, K. Blazek, M. Nikl: High Resolution Thin Scintillator Imaging Plates Used for X-Ray NDT Applications. 2nd International Symposium on NDT in Aerospace 2010-Poster 4.

[Weitkamp 2011]

T. Weitkamp, D. Haas, D. Wegrzynek, A. Rack: ANKAphase – software for single – distance phase retrieval from inline X-ray phase – contrast radiographs. J. Synchrotron Rad. (2011). 18, 617 – 629.

6 Discussion of Results and Comparison with Literature

Chapter Overview

Abstract

6.1 Discussion of Results	171
6.2 Comparison of Results with Literature	174
Bibliography	177

Abstract

$\text{SrI}_2:\text{Eu}^{2+}$ single crystals are the prerequisites for its application as scintillators, in order to avoid light trapping and scattering at the grain boundaries. This work was focused on discovering the problems associated with the growth of single crystals and addressing them. The crystal growth experiments (crystal quality and diameter) improved with time as demonstrated in chapter 5.1.3, so also the crystal packaging. These were confirmed by the scintillation measurement results presented in Table 6.1. The comparison of FMF crystals with a FISK SrI_2 - sample shows that more can be extracted from FMF samples through improved packaging using spectralon.

6.1 Discussion of Results

Table 6.1 summarizes the scintillation characteristics of the crystals produced in this work. These results are based on measurements carried out at the research centre, Jülich. During the measurements, a commercial $\text{NaI}:\text{Tl}$ – scintillator (36.5 cm^3) wrapped in Teflon tape was measured as the reference sample. The light yield of the SrI_2 – scintillator samples were determined by comparing their current pulse heights to the current pulse height of the NaI – scintillator. It is important to mention here that the light yield of the SrI_2 – scintillators wrapped in aluminium foil reflector is just a rough estimate; it is erroneous to compare them with a sample wrapped in Teflon tape due to the different reflectivity of the Teflon tape and aluminium foil. SrI_2 – scintillator samples wrapped in Teflon tape are indicated in the table below.

The results show that the light yields increased with improvement in the packaging technique, the energy resolution and scintillation decay time on the other hand also decreased with packaging. This is attributed to a better light collection efficiency of the samples. The light collection efficiency is the probability that a photon produced in the scintillator also leaves the scintillator and is known to depend on the crystal quality (impurity and defects) and also on the packaging of the scintillator, among other factors. Crystals from zone-refined starting

materials showed a higher light yield, better energy resolution and faster scintillation light decay.

The light yield and scintillation decay time of the sample – 5 crystals are uncharacteristic of SrI_2 . A possible explanation is an experimental error during the measurements. The samples will be measured again to investigate the cause of the abnormalities in the scintillation characteristics.

The sample – 1 was packaged without optical coupler resulting in the scintillation photon yield of 50 000 ph/MeV. Bicron BC-630 was used in the first sample – 3 packaging increasing the light yield with up to 5 000 ph/MeV, the Eu – concentration of the sample - 3 was 6 mol%. The second improved packaging also improved the light yield with ~ 5 000 ph/MeV.

Sample	Light yield (ph/MeV)	Energy resolution (% at 662 keV) FWHM	Decay time (μs)	Emission wavelength (nm)
SrI₂:5% Eu-1	50 000 (Teflon)	15.9	1.39	431
SrI₂:6% Eu-3a 1st packaging 2nd packaging	55 000 (Teflon)	15.4	1.38	432
	60 849	11.7	1.18	
SrI₂:6% Eu-3b	52 000 (Teflon)	20	1.38	432
SrI₂:6% Eu-5a	143 040	12	0.7	427
SrI₂:6% Eu-5b	154 393	14.6	0.69	427
SrI₂:5% Eu-6a	99 447	9.8	1.15	427
SrI₂:5% Eu-6b	89 820	10.6	1.17	427
SrI₂:5% Eu-6c	83 553	9.9	1.18	427
SrI₂:5% Eu-6d	74 472	13	1.18	427

Table 6.1: Scintillation characteristics of SrI_2 – scintillators produced in this work.

The ^{137}Cs pulse height spectra of the samples measured at the FISK University are summarized in Figure 6.1. The energy resolution of these samples lies between 4.1% and 6.6% at 662 keV (FWHM).

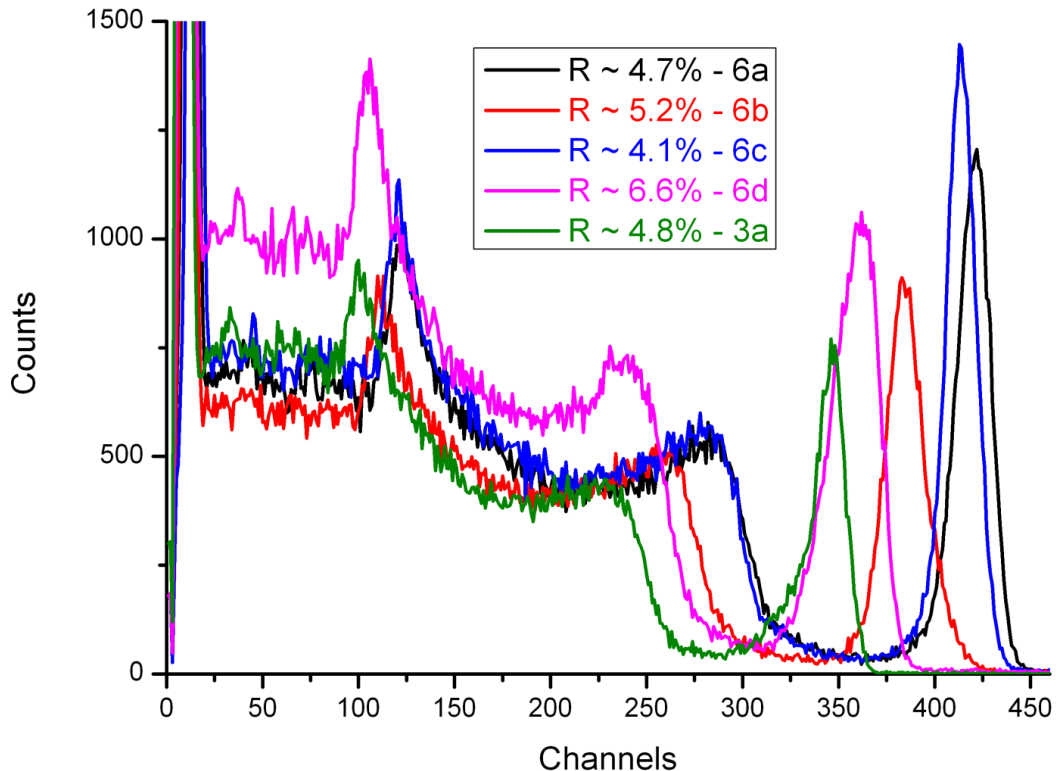


Figure 6.1: The ^{137}Cs - isotope pulse height spectra recorded at the FISK University with SrI_2 – scintillator detectors made in this work.

Figure 6.2 summarizes the scintillation timing of the few samples measured at the FISK University. The decay time constants lie between $1.3 \mu\text{s}$ and $1.6 \mu\text{s}$.

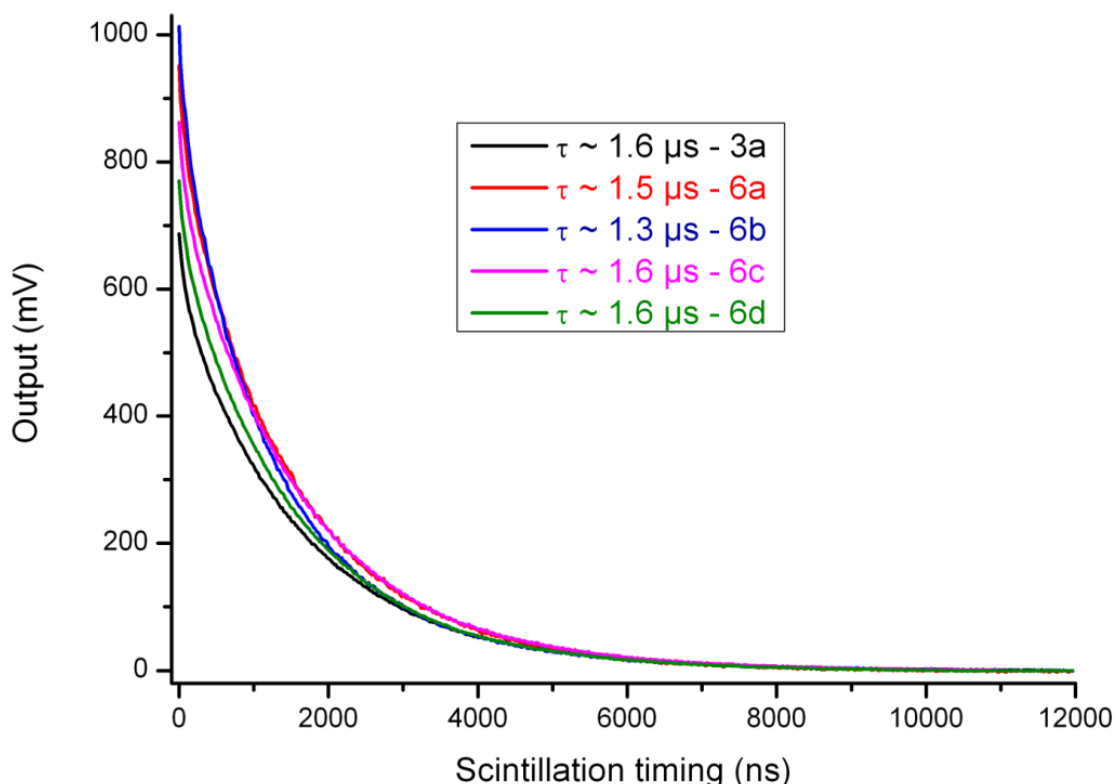


Figure 6.2: Scintillation timing of SrI_2 – scintillators produced in this work and measured at the FISK University.

The sample – 7 was polished and packaged at the Lawrence Livermore National Laboratories using custom made materials. The measurements were done at the FISK University, Tennessee. Utilizing these opportunities was very necessary for a good comparison of the quality of the crystals made in this work with commercial SrI₂ – scintillator crystals. The scintillation characteristics of the sample – 7 are summarized in Table 6.2.

Sample – 7 Geometry	Cylindrical	Tapered	Tapered and Canned
Light Yield (ph/MeV)	72 960	97 660	87 400
Energy Resolution (% at 662 keV)	3.99	2.76	2.73
Peak to Compton ratio	6.3	7.9	6.9

Table 6.2: Scintillation characteristics of sample – 7.

6.2 Comparison of Results with Literature

The energy resolution of a SrI₂ – crystal (grown and packaged in FMF) was compared to FISK SrI₂ – crystal in Figure 6.3. The group of Prof. Arnold Burger at the FISK- University is world renowned worldwide for high quality SrI₂ – scintillator crystals. The energy resolution of the FISK sample wrapped in aluminum foil was 3.8 % compared to the FMF sample with 4.1% (FWHM at 662 keV).

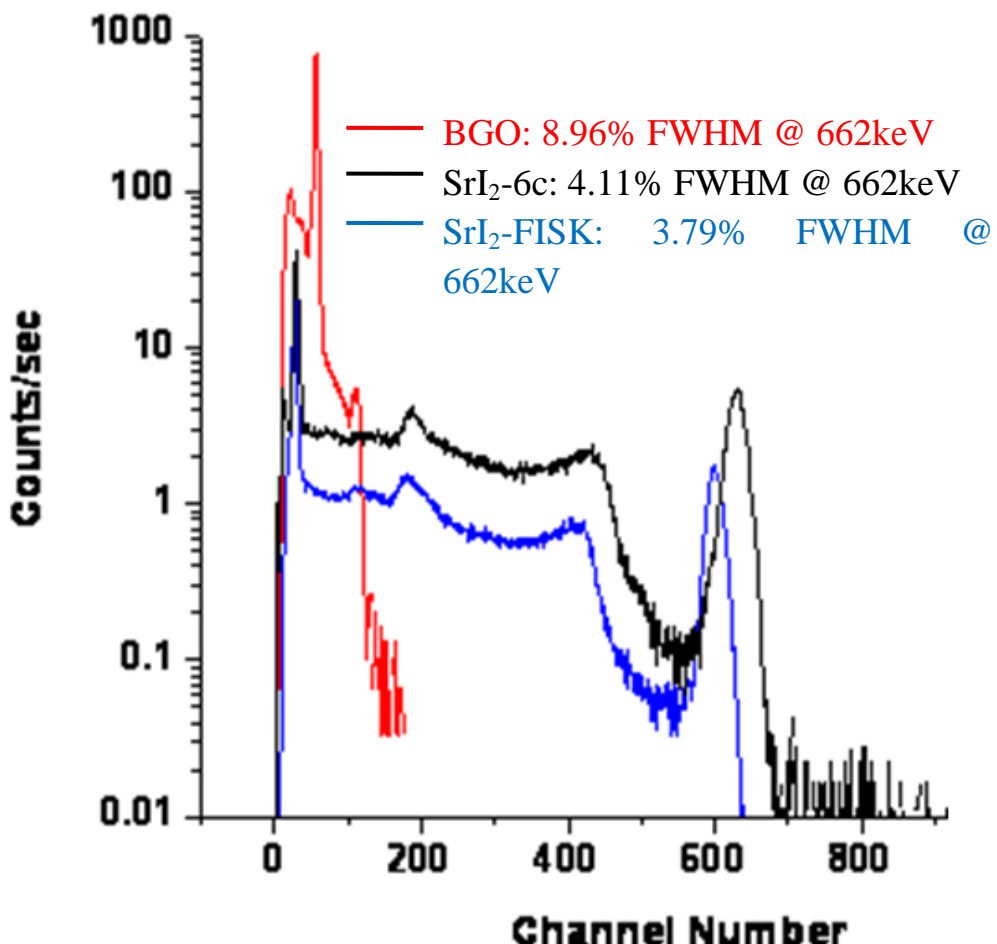


Figure 6.3: Observed ¹³⁷Cs spectra using a FISK SrI₂ – crystal, FMF SrI₂ – crystal and Saint-Gobain BGO – crystal.

The scintillation timing of the FISK sample is also compared to the FMF sample in Figure 6.4. The FISK sample has a shorter scintillation decay time constant of 0.98 μ s. The reason for the better energy resolution and shorter decay time constant of the FISK sample may be because of a better light collection efficiency due to improved packaging.

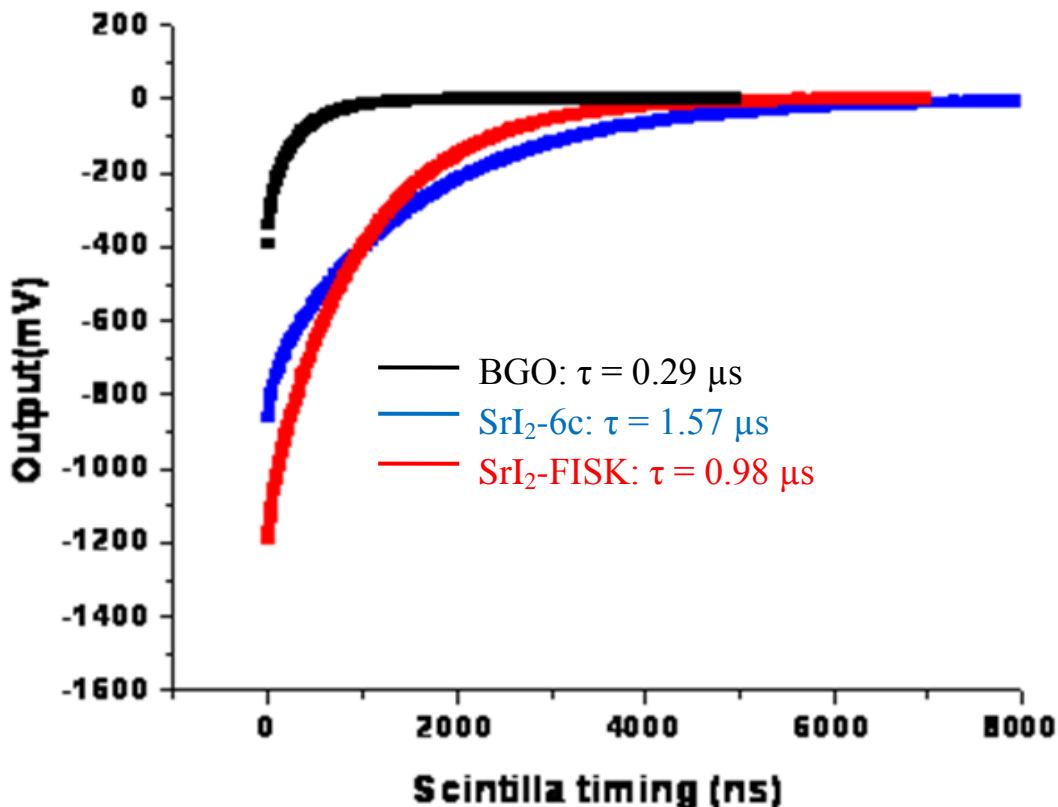


Figure 6.4: Scintillation timing of a FISK SrI_2 – crystal, FMF SrI_2 – crystal and Saint-Gobain BGO – crystal.

The scintillation characteristics of all FMF – samples wrapped in aluminium foil are compared to a FISK – sample also wrapped in aluminium foil in Table 6.3.

Scintillator	Eu conc. %	Decay time μ s	Light Yield ph/keV	Energy resolution FWHM at 662 keV %
Fisk SrI_2	2.5	0.98	85	3.8*
FMF SrI_2 - 3a	6	1.58	76	4.9
FMF SrI_2 - 6a	5	1.47	97	4.8
FMF SrI_2 - 6b	5	1.28	92	5.4
FMF SrI_2 - 6c	5	1.57	95	4.1
FMF SrI_2 - 6d	5	1.52	82	7.6

Table 6.3: Comparison of the FMF samples with a FISK university sample.

The scintillation characteristics of the SrI_2 – scintillator crystals grown in this work are presented. The light yield, energy resolution and scintillation decay time correspond to values reported by [Van Loef 2009], [Cherepy 2010] and few others. [Cherepy 2010] attributed the lengthening of the scintillation decay time to reabsorption and reemission of the scintillation light at subsequent emission centres as demonstrated in Figure 6.5.

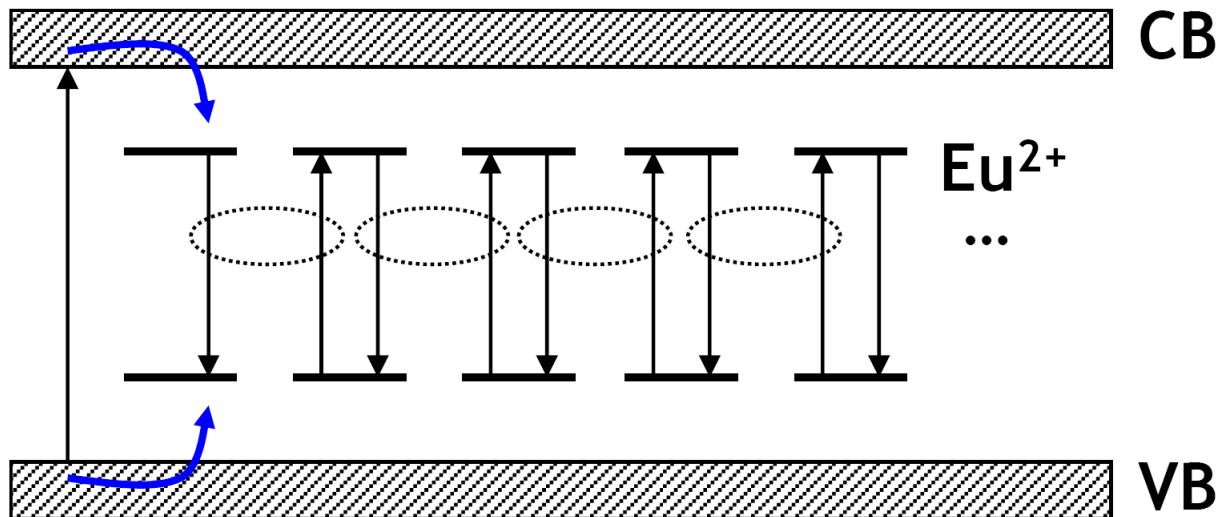


Figure 6.5: Lengthening of scintillation decay [Cherepy 2010].

The results portray FMF samples as high quality crystals of international standard. The energy resolution of the FISK - sample wrapped in spectralon was 2.9 % at 662 keV (FWHM) while the energy resolution decreased to 3.8% with the same sample wrapped in aluminium foil giving room to a prediction of 3.2% energy resolution for the FMF sample – 6c if wrapped in the same spectralon reflector and maybe 2.9% with the same geometry as the FISK sample.

Bibliography

[Van Loef 2009]

Edgar V. van Loef, Cody M. Wilson, Nerine J. Cherepy, Giulia Hull, Stephen A. Payne, Woon-Seng Choong, William W. Moses and Kanai S. Shah: Crystal growth and scintillation properties of strontium iodide scintillators. IEEE Trans. Nucl. Sci, Vol. 56, No.3, June 2009.

[Cherepy 2010]

Nerine Cherepy, L. Boatner, A. Burger, K. Shah, Steve Payne, Alan Janos, Austin Kuhn: Overview of Strontium Iodide Scintillator Materials. LLNL presentation April 1, 2010. (LLNL-PRES-426327).

7 Summary and Outlook

Chapter Overview

7.1 Summary	178
7.2 Outlook	179

7.1 Summary

Just as the title of this thesis implies; $\text{SrI}_2:\text{Eu}^{2+}$ - scintillators were developed in this work. The initial aim of this work was the growth of single crystals as large as 1 – inch (2.54 cm) diameter, the processing and packaging of the single crystals to a detector suitable for spectroscopic systems, as well as the determination of the detector characteristics. Later the scope of this work was extended to the development of the SrI_2 – scintillator for high resolution and high contrast X-ray imaging.

Some of the material problems of SrI_2 and EuI_2 that needed to be considered at any stage of this research work were: hygroscopicity, oxygen – and light sensitivity.

These materials decolourized under the light when stored in transparent laboratory bottles, so they were consequently stored in dark bottles and away from light sources (sun). Once the supply ampoules containing these materials were opened, it was noticed that they showed a kind of reaction, even when stored in air-tight bottles in the glovebox. We avoided buying them in large quantities, since they could not be stored.

A special arrangement was made for the crystal growth of the SrI_2 , in order to prevent melt hydration and oxidation. The crystal growth was carried out in sealed silica ampoules. This was made possible by the low melting point of the SrI_2 (~ 550 °C). Unfortunately, the direct thermal contact between the growing crystal and the ampoule tend to induce thermal stress in the crystal. To address this problem, we carried out liquid encapsulated Bridgman crystal growth, which proved itself to be unsuitable. The introduction of Argon gas in the growth ampoule also did not yield any fruitful results either. In this work, it was possible to find a solution to this problem. Iodine gas; one of the constituent elements was introduced into the growth ampoules. Upon crystallization, the SrI_2 crystal pulls from the ampoule wall, Iodine gas diffuses between the crystal and the ampoule, thereby maintaining good thermal conductivity and stoichiometry of the melt. This progress led to the growth of high quality crystals as large as 1-inch.

The next stage of this work is the crystal packaging. Needed here is a packaging technique, adequate to prevent crystal deterioration (hydration) during field use and at the same time allowing for maximal scintillator crystal performance. Conventional packaging techniques such as wrapping of crystals in Teflon tapes were tried out. But it was not possible to bring out the best scintillation properties of the crystals produced at the initial stage of this work, probably due to their small sizes. A new technique was developed and tried out in this work; embedding scintillator crystals in cone-shaped reflectors made of Aluminium foil. Good results were recorded with this new packaging. More work on the packaging technique is still underway, maybe employing spectralon to improve the light collection efficiency of assembled scintillator detectors.

Pulse height spectra of the ^{137}Cs – isotope (662 keV) were observed with SrI_2 scintillator crystals produced in this work, the calculated energy resolution was as low as 2.7% (FWHM). Till date the SrI_2 -scintillator is used in various gamma ray spectroscopy applications, but never for X-ray imaging purposes due to the difficulties associated with making few micrometer thick samples. Investigative studies, where very thin SrI_2 – scintillator screens were applied in X-ray imaging, produced high resolution and high contrast radiographic and tomography images. This preliminary study did open another area of field use for the SrI_2 - scintillator. With SrI_2 – scintillator screens the integration time needed to acquire X-ray images was reduced by a factor 4, this was attributed to its high light yield which was also approximately by a factor 4 higher than the YAG – scintillator reference sample. This development could lead to a reduction in the radiation dose administered to patients in practical application.

The results achieved in this work so far are very motivating, so more research work is underway.

7.2 Outlook

Future work will be aimed at:

- Growing crystals as large as 2 - inches to meet the application needs.
- Improving raw materials through more zone refining prior to crystal growth. The probability of growing a single crystal depends on the purity of the raw materials.
- Improving the packaging techniques. Spectralon would be used as a reflector since the obtainable energy resolution depends on the reflectivity of the packaging materials.
- Measuring the optical absorption spectra and UV-diffuse reflectivity of SrI_2 – crystals. Better understanding of these properties would help in improving the packaging and performance of the scintillators.

Summary and Outlook - 7

- Outdoor measurements at Schauinsland Mountains. A pilot project has been carried out by Dr. Markus Dambacher where a semiconductor radiation detector based on (Cd,Zn)Te was used in outdoor environmental radioactivity monitoring, repeating this successfully with a SrI₂ - scintillator based detector could further expand the possible application areas of the scintillator.

Attachments

List of Figures

Figure 2.1: The electromagnetic spectrum.....	5
Figure 2.2: X-ray production in an x-ray tube [NDT 2012].....	5
Figure 2.3: Production of Bremsstrahlung and characteristic x-rays.....	6
Figure 2.4: The mass attenuation coefficient of SrI ₂ as a function of photon energy showing a steep increase at photon energies equal the K-edges of iodine (33.17 keV) and strontium (16.10 keV) [XCOM].	7
Figure 2.5: Principles of radiative and non-radiative transitions in atoms.....	8
Figure 2.6: Compton scattering of a photon.....	9
Figure 2.7: Classification of radiation detectors.....	11
Figure 2.8: Types of luminescence [Kobayashi 2003].	11
Figure 2.9: Excitation, fluorescence and Phosphorescence.....	12
Figure 2.10: The energy resolution.....	14
Figure 2.11: Shifting of the emission wavelength as a function of temperature in X-ray excited emission of SrI ₂ :5% Eu ²⁺ [Mikhail 2011].	15
Figure 2.12: Temperature dependence of the SrI ₂ :5%Eu ²⁺ light output [Mikhail 2011].....	16
Figure 2.13: Spectral response characteristics of most photocathodes [HAMAMATSU].....	18
Figure 2.14: The excitonic luminescence model of scintillation in inorganic scintillators, from [Pédrini 2005] and modified for clarity.....	21
Figure 2.15: The cross luminescence model of scintillations, modified version from [Lecoq 2006] ..	22
Figure 2.16: The extrinsic luminescence model of scintillation involving rare earth ions [Pédrini 2005].....	23
Figure 2.17: Configuration co-ordinate diagram of a luminescence center [Birks 1964].	24
Figure 2.18: Compact (handheld) scintillator-based detector systems.....	26
Figure 2.19: Block diagram of a scintillator-based detector system.....	26
Figure 2.20: PMT scintillation counter. Reproduced after [Birks 1964] and modified for better understanding.....	28
Figure 2.21: Signal processing in a scintillator detector.....	29
Figure 2.22: Nuclear level diagram of ¹³⁷ Cs.....	29
Figure 2.23: Scintillator crystal and PMT shielded by lead-blocks.....	30
Figure 2.24: The components of a pulse height spectrum.....	31
Figure 2.25: Typical pulse shape of scintillator detectors.....	33
Figure 2.26: Basics of a scintillator based X-ray imaging detector system.....	35
Figure 2.27: Mass attenuation coefficient (μ/ρ) of several materials encountered in diagnostic X-ray imaging [Seibert 2005].	36
Figure 2.28: X-ray imaging with a scintillator and an optical system. An image in z_0 is focused on the CCD, an image in $z_0 + \delta z$ is out of focus at the CCD [Martin and Koch 2006].....	37
Figure 2.29: Degradation of spatial resolution caused by light spreading in the scintillator. d is the thickness of the scintillator screen.....	38
Figure 2.30: Formation of penumbra or geometric unsharpness at a finite value of the effective focal spot size. Decreasing the focal spot and the object-to-detector distance decreases the unsharpness	

Attachments

(SOD is the source-to-object distance; SID is the source-to-image distance and P the penumbra region)	39
Figure 2.31: Spatial resolution measurement. a) imaging of a point; b) recording the optical density across the sample line; c) PSF calculated by converting the optical density to relative exposure as a function of position [Hasegawa 1987]	40
Figure 2.32: Image contrast [Hasegawa 1987]	41
Figure 2.33: Principles of absorption contrast and phase contrast X-ray imaging	43
Figure 3.1: Phase diagram of SrI ₂ created using the software: Tapp V2.2 (E S Microware)	48
Figure 3.2: TG/DSC result of the SrI ₂ - first batch (Alfa Aesar, 99.99%-metal basis)	50
Figure 3.3: TG/DSC result of SrI ₂ – second batch (Sigma Aldrich, 99.99%-metal basis)	50
Figure 3.4: TG/DSC result of SrI ₂ – third batch (Sigma Aldrich, 99.99%-metal basis)	50
Figure 3.5: TG/DSC result of SrI ₂ – fourth batch (Sigma Aldrich, 99.99%-metal basis)	51
Figure 3.6: TG/DSC result of SrI ₂ – fifth batch (Sigma Aldrich, 99.99%-metal basis)	51
Figure 3.7: A 3D projection of the SrI ₂ crystal structure, green is the Strontium-ion and violet are the Iodine-ions [Wikipedia]	52
Figure 3.8: The coordination of the units making up the SrI ₂ crystal structure [Wikipedia]	52
Figure 3.9: A luminescence center in the bandgap of a scintillator	53
Figure 3.10: Energy-level positions of divalent lanthanides in a wide bandgap ionic crystal (ideal scenario). The first digit in bracket is the number of electrons in f-orbital, second digit the oxidation state and letter A is host material [Dorenbos 2004]	54
Figure 3.11: Schematic configuration coordinate diagram of Eu ²⁺ [Thomas 1992]	55
Figure 3.12: Result of the TG /DSC measurement on the EuI ₂	56
Figure 3.13: Dependence of light yield on Eu ²⁺ -concentration in SrI ₂ [Glodo 2010]	56
Figure 4.1: Different grain selector designs [Wilke 1973]	61
Figure 4.2: Ampoule designs (grain selectors) tested in this work: 1) Silica glass; 2) Iodine or Boron oxide; 3) SrI ₂	61
Figure 4.3: Some of the manufactured ampoules. a) 1.5 cm diameter; b) 2.54 cm (1‘‘) diameter; c) 1 cm diameter. Dark colour in the grain selector region is the iodine-gas growth atmosphere	62
Figure 4.4: Baking and evacuation of ampoules prior to the crystal growth: 1) Vacuum-pump system; 2) Furnace and heating elements; 3) The ampoule	63
Figure 4.5: Circulation of the argon gas for drying: P is the pressure gauge; F is the moisture meter; 1 – 12 are valves	64
Figure 4.6: The glovebox in the synthesis laboratory of the crystallography department, all preparation work on the SrI ₂ – material/crystal is done here. The moisture content is always maintained at < 1 ppm	64
Figure 4.7: Dependence of the free (Gibbs) energy on the seed-embryo radius	68
Figure 4.8: Dependence of the nucleation rate on temperature	69
Figure 4.9: The adsorption layer theory of crystal growth	70
Figure 4.10: The screw dislocation theory of crystal growth	71
Figure 4.11: Vertical Bridgman furnace configuration	72
Figure 4.12: Vertical Stockbarger furnace configuration	73
Figure 4.13: The single-zone Bridgman furnace	74
Figure 4.14: The designed Bridgman/Stockbarger setup before construction (not to scale)	75
Figure 5.1: Measured temperature profiles of the single zone vertical Bridgman furnace	79
Figure 5.2: Image of the simulated furnace and its components	80
Figure 5.3: Simulated temperature field in the furnace	81

Attachments

Figure 5.4: Comparison of the simulated and the measured temperature profiles.	82
Figure 5.5: Lowering of the growth ampoule through the furnace. Inset in (b) shows the deformation of the spatial temperature field by the ampoule.	83
Figure 5.6: Simulation showing the crystallization process. a) Self-seeding process, b) – h) notice the changes in the shape of the crystal growth front, i) is the end of crystallization.....	84
Figure 5.7: The constructed Bridgman/Stockbarger furnace. a) the pulling gears, b) the pulling motor, c) switch for the pulling unit, d) the pulling finger, e) water cooling supply, f) inset: the growth chamber, g) inset: Fiberfrax, h) upper zone, i) Almemo for automatic temperature recording, j) laptop for monitoring the growth temperature, k) furnace control unit, l) the lower zone.....	86
Figure 5.8: Measured temperature profiles of the vertical Bridgman/Stockbarger furnace.	87
Figure 5.9: Differential scanning calorimetry curves of SrI ₂ . An endothermic process in red showing the melting and the exothermic process in blue showing the crystallization.	88
Figure 5.10: The SrI ₂ : 5% Eu – ampoule as grown. 1 cm diameter.	89
Figure 5.11: SrI ₂ : 5% Eu – ampoule showing different regions marked in red.....	89
Figure 5.12: Harvested crystals.	89
Figure 5.13: A polished sample.	90
Figure 5.14: Liquid encapsulated Bridgman-ampoule.	91
Figure 5.15: The ampoule before the crystal growth. Notice the two regions; (a) is SrI ₂ and (b) B ₂ O ₃ .91	91
Figure 5.16: The ampoule after growth. 1 cm diameter.	91
Figure 5.17: Cracks seen on the ampoule wall. Red coloration due to escaping iodine gas.	91
Figure 5.18: The ampoule no. 3 after growth. 1 cm diameter.	92
Figure 5.19: Dark coloration visible in the ampoule.	92
Figure 5.20: Single crystal blocks visible due to cracking of the crystal during the cooling process.	92
Figure 5.21: First to freeze region showing a good nucleation work.	93
Figure 5.22: Some of the harvested crystals.	93
Figure 5.23: Polished samples from ampoule no.3.	93
Figure 5.24: Ampoule no. 4 before the crystal growth. Notice the yellowish coloration in the ampoule.	94
Figure 5.25: The first to freeze region showing some colorations.	94
Figure 5.26: Yellowish to dark colorations in the ampoule.	94
Figure 5.27: The ampoule no.4. 1 cm diameter.	94
Figure 5.28: The ampoule no.5. Notice the design of the grain selector.	95
Figure 5.29: Ampoule no.5 under a white light.	95
Figure 5.30: Harvested crystals.	95
Figure 5.31: Polished samples.	96
Figure 5.32: Ampoule no. 6. Notice here the glass rod at first to freeze region.	96
Figure 5.33: Ampoule under light. 1.5 cm diameter.	96
Figure 5.34: Some harvested and polished crystals.	97
Figure 5.35: Polished samples optically coupled to the quartz glass window using epotek opt. adhesive.	97
Figure 5.36: 1“ (1-inch) diameter ampoule after dehydration. Notice the yellowish coloration.	98
Figure 5.37: a) A 15 cm long furnace used for zone-refining and the pulling mechanism. b) SrI ₂ melt during the zone-refining.	99
Figure 5.38: The ampoule after zone-refining.	99
Figure 5.39: 1-inch ampoule after the crystal growth.	99
Figure 5.40: The ampoule under white light. Notice the dark coloration at the first to freeze region. .	99

Attachments

Figure 5.41: The first to freeze region showing the excess iodine growth gas.	99
Figure 5.42: The harvested crystal.	100
Figure 5.43: Homogenous crystal emission under UV-light. No defects visible.	100
Figure 5.44: The ampoule after growth. 1 cm diameter.	101
Figure 5.45: The ampoule under white light. Marked in red are defects.	101
Figure 5.46: Notice the design of the grain selector, this was done to subdue multiple grain growth.	101
Figure 5.47: Inside of the Bridgman/Stockbarger furnace after the crystal growth.	101
Figure 5.48: The oxidized copper-metal growth chamber.	102
Figure 5.49: Materials for the crystal encapsulation.	102
Figure 5.50: The basics of the first packaging used in this work with (a) the quartz glass detector window; (b) the aluminum container; (c) the reflector and (d) the crystal. This was modified in the second packaging by applying an optical coupler between the crystal and detector window.	103
Figure 5.51: The first encapsulation with the crystal wrapped in a Teflon tape reflector.	103
Figure 5.52: The second technique with the thickness of the Al-container reduced and the crystal optically coupled to the quartz glass using Bicron BC-630. Notice the bleeding between the crystal and the quartz glass.	104
Figure 5.53: The basics of the third packaging technique developed and tested in this work. Notice the form of the aluminum reflector. (a) is the quartz-glass detector window, (b) is the aluminum container, (c) is the reflector and (d) the crystal.	105
Figure 5.54: Paths taken by light photons leaving the crystal from the side.	105
Figure 5.55: The third packaging technique. (a) polished crystal, (b) crystal glued to the quartz glass using (EPO-TEK 305/B4 Opt. Adhesive). (c) Aluminum foil used as a reflector.	105
Figure 5.56: Packaging of the SrI ₂ -scintillator thin screens for X-ray imaging. (a) is 150 – 170 µm quartz glass slide; (b) is the scintillator screen 400 µm max. thickness; (c) is the aluminum back slide ~ 210 µm thick.	106
Figure 5.57: A 360 µm SrI ₂ -scintillator thin screen for X-ray imaging.	107
Figure 5.58: The measured crystal slightly < 1 cm ³ .	108
Figure 5.59: Pulse height spectrum of ¹³⁷ Cs-isotope recorded with the sample - 1.	108
Figure 5.60: The recorded scintillation light decay curve with a decay constant of 1.39 µs.	109
Figure 5.61: The radioluminescence spectrum showing a 431 nm emission wavelength.	109
Figure 5.62: The first packaging and the first measurement of sample 3a (< 1 cm ³). Bicron BC-630 optical coupler applied between crystal and detector window and Teflon tape served as a reflector.	110
Figure 5.63: Pulse height spectrum of ¹³⁷ Cs recorded with this sample.	111
Figure 5.64: Scintillation light decay curve with a decay constant of 1.38 µs.	111
Figure 5.65: The second packaging using EPO-TEK 305/B4 Opt. Adhesive and aluminum foil as reflector.	112
Figure 5.66: The sample emission under UV-light.	112
Figure 5.67: Pulse height spectrum of the ¹³⁷ Cs-isotope recorded after the second packaging showing improvement in the energy resolution.	113
Figure 5.68: Scintillation light decay curve showing a reduced decay constant of 1.18 µs.	113
Figure 5.69: Pulse height spectrum of the ¹³⁷ Cs-isotope recorded at the FISK University with a 4.8% energy resolution (FWHM).	114
Figure 5.70: The decay curve recorded at the FISK University (1.58 µs decay constant).	114
Figure 5.71: The radioluminescence spectrum showing a 432 nm emission wavelength.	115
Figure 5.72: Sample 3b packaged with Bicron BC-630 opt. Coupler.	115
Figure 5.73: Pulse height spectrum of the ¹³⁷ Cs-isotope observed with this sample.	116

Attachments

Figure 5.74: The scintillation decay time curve.....	116
Figure 5.75: The emission spectrum peaking at 432 nm.....	117
Figure 5.76: Sample 5a ($\sim 1 \text{ cm}^3$) optically coupled using EPO-TEK 305/B4 Opt. Adhesive and aluminum foil served as a reflector.....	118
Figure 5.77: Pulse height spectrum of the ^{137}Cs -isotope observed with this sample.....	118
Figure 5.78: The scintillation decay time spectrum.....	119
Figure 5.79: The emission spectrum showing a 427 nm emission peak.....	119
Figure 5.80: Sample 5b ($> 1 \text{ cm}^3$) optically coupled using EPO-TEK 305/B4 Opt. Adhesive and aluminum foil served as a reflector.....	120
Figure 5.81: Pulse height spectrum of ^{137}Cs observed with this sample.....	120
Figure 5.82: The scintillation decay time spectrum.....	121
Figure 5.83: 427 nm emission of the sample-5b.....	121
Figure 5.84: Sample 6a ($\sim 1 \text{ cm}^3$) packaging. Optical coupler: EPO-TEK 305/B4 Opt. Adhesive and aluminum foil served as the reflector.....	122
Figure 5.85: Emission of sample 6a under UV-light.....	122
Figure 5.86: Pulse height spectrum of the ^{137}Cs -isotope recorded with 9.8% energy resolution (FWHM).....	123
Figure 5.87: The scintillation decay time spectrum.....	123
Figure 5.88: Pulse height spectrum of the ^{137}Cs -isotope observed with this sample at the FISK University.....	124
Figure 5.89: Decay time spectrum recorded at the FISK University.....	124
Figure 5.90: The 427 nm emission wavelength.....	125
Figure 5.91: Sample 6b ($< 1 \text{ cm}^3$) packaging. Optical coupler: EPO-TEK 305/B4 Opt. Adhesive. Reflector: aluminum.....	125
Figure 5.92: Pulse height spectrum of the ^{137}Cs -isotope observed with this sample.....	126
Figure 5.93: The decay time spectrum recorded.....	126
Figure 5.94: Pulse height spectrum of the ^{137}Cs -isotope observed with this sample at the FISK University.....	127
Figure 5.95: The decay time spectrum.....	128
Figure 5.96: Sample-6b emission spectrum with peak at 427 nm.....	128
Figure 5.97: Sample 6c ($> 1 \text{ cm}^3$) packaging. Optical coupler: EPO-TEK 305/B4 Opt. Adhesive. Reflector: aluminum.....	129
Figure 5.98: Emission of sample 6c under UV-light.....	129
Figure 5.99: The pulse height spectrum of the ^{137}Cs -isotope.....	130
Figure 5.100: The scintillation decay time profile.....	130
Figure 5.101: Pulse height spectrum of the ^{137}Cs -isotope observed with this sample at the FISK University.....	131
Figure 5.102: The scintillation decay time profile.....	131
Figure 5.103: Radioluminescence spectrum of sample-6c with emission peak at 427 nm.....	132
Figure 5.104: Sample 6d ($> 1 \text{ cm}^3$) packaging. Optical coupler: EPO-TEK 305/B4 Opt. Adhesive. Reflector: aluminum.....	132
Figure 5.105: Emission of sample 6d under UV-light.....	133
Figure 5.106: The pulse height spectrum of the ^{137}Cs -isotope.....	133
Figure 5.107: The scintillation decay time profile.....	134
Figure 5.108: The pulse height spectrum of the ^{137}Cs -isotope (FISK University).....	134
Figure 5.109: The scintillation decay time spectrum.....	135

Attachments

Figure 5.110: Radioluminescence spectrum of the sample-6d showing a 427 nm emission.....	135
Figure 5.111: Different slices of this crystal were made for γ – ray spectroscopy, X-ray imaging and structural analysis, only the spectroscopic results recorded using region – A regarded here as sample – 7 will be reported.....	136
Figure 5.112: The sample – 7 after polishing and cylindrical in geometry.....	136
Figure 5.113: Pulse height spectrum observed with the cylindrical sample – 7.....	137
Figure 5.114: The sample – 7 having a tapered geometry for the second measurement.....	137
Figure 5.115: The pulse height spectrum observed with the tapered sample – 7.....	138
Figure 5.116: The sample – 7 canned for longer field use	138
Figure 5.117: The pulse height spectrum observed with the tapered and canned sample – 7.....	139
Figure 5.118: Calculated absorption efficiencies of 5 μm SrI_2 and YAG – scintillators.	140
Figure 5.119: PCO 4000 quantum efficiency [Baumbach 2007].	141
Figure 5.120: The ANKA detector setup used for the measurements here, inset shows the sample holder and the objectives.....	142
Figure 5.121: X-ray imaging based on transparent scintillator screens, diffraction limited microscope objectives and a CCD camera.....	143
Figure 5.122: The flat field image of the YAG – scintillator at 12 keV. 200 ms integration time. 400 μm thick.....	144
Figure 5.123: The flat field image recorded with the SrI_2 -3 at 25 keV. 360 μm thick. The first thin screen sample made showing some inhomogeneity problems.	144
Figure 5.124: The flat field image recorded with the SrI_2 – 5(a) at 12 keV. 300 μm thick. Bicron BC-630 opt. Coupler. 50 ms integration time	145
Figure 5.125: The flat field image recorded with the SrI_2 – 5(b) at 12 keV. 380 μm thick. No opt. Coupler. 50 ms integration time	145
Figure 5.126: The flat field image recorded with the SrI_2 – 6 at 12 keV. 400 μm thick. EPO-TEK 305/B4 opt. Adhesive. 2 minutes integration time.....	146
Figure 5.127: SrI_2 – thin screen packaging. Orange is the vacuum epoxy glue.....	146
Figure 5.128: Calculated X-ray transmission of a 210 μm aluminum slide.....	147
Figure 5.129: The tee mesh image recorded with the YAG – scintillator at 12 keV. 200 ms integration time. 400 μm thick.	148
Figure 5.130: The tee mesh image recorded with the SrI_2 -3 at 25 keV. 360 μm thick.	148
Figure 5.131: The tee mesh image recorded with the SrI_2 – 5(a) at 12 keV. 300 μm thick. Bicron BC-630 opt. Coupler. 50 ms integration time	149
Figure 5.132: The tee mesh image recorded with the SrI_2 – 5(b) at 12 keV. 380 μm thick. No opt. Coupler. 50 ms integration time	150
Figure 5.133: The tee mesh image recorded with the SrI_2 – 6 at 12 keV. 400 μm thick. EPO-TEK 305/B4 opt. Adhesive. 2 minutes integration time.....	150
Figure 5.134: Radiography image of an ant recorded with the YAG – scintillator at 12 keV. 200 ms integration time. 400 μm thick. Object distance to scintillator screen 6 cm.	151
Figure 5.135: Radiography image of an ant recorded with the SrI_2 – 5(a) at 12 keV. 300 μm thick. Bicron BC-630 opt. Coupler. 50 ms integration time. Object distance to scintillator screen 6 cm....	152
Figure 5.136: Lithography printed gold - pattern used for spatial resolution tests. The tested regions are highlighted in red.....	153
Figure 5.137: Test pattern image recorded with the SrI_2 – 5(a) at 15 keV. 300 μm thick. Bicron BC-630 opt. Coupler. 15 seconds integration time. Image recorded 4 months later. Object distance to scintillator screen 3 cm.....	154

Attachments

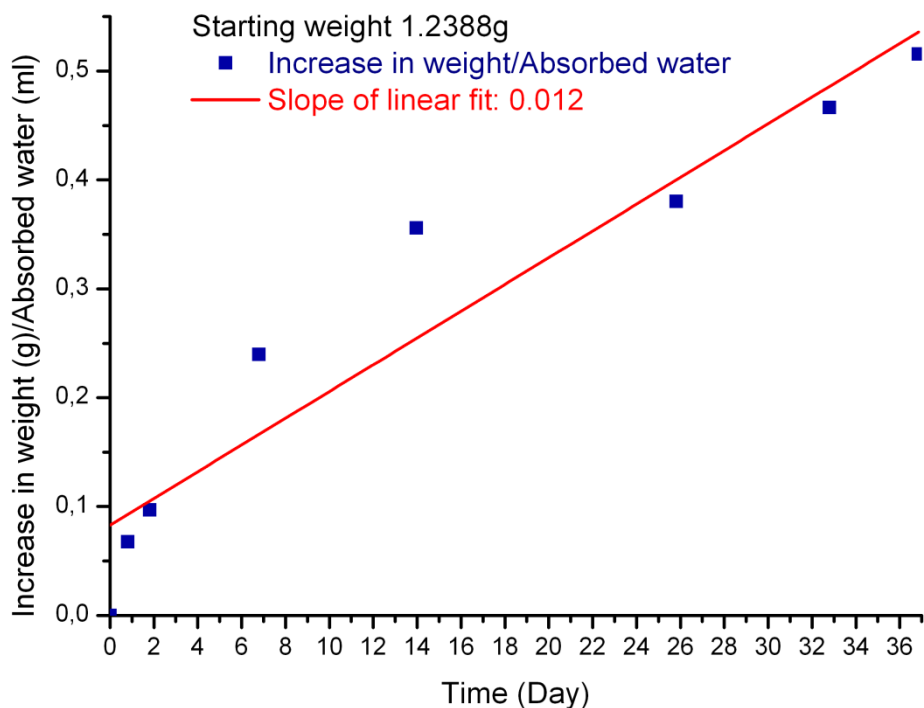
Figure 5.138: Test pattern image recorded with the SrI ₂ – 6 at 15 keV. 400 µm thick. EPO-TEK 305/B4 opt. Adhesive. 15 seconds integration time. Object distance to scintillator screen 3 cm.	155
Figure 5.139: Test pattern image recorded with the SrI ₂ – 6 at 15 keV. 400 µm thick. EPO-TEK 305/B4 opt. Adhesive. 2 minutes integration time.....	156
Figure 5.140: Image of a chip recorded with the SrI ₂ – 6 at 12 keV. 400 µm thick. EPO-TEK 305/B4 opt. Adhesive. 50 ms integration time.....	157
Figure 5.141: The same image of the chip using a colour scheme to depict the emission intensities.	157
Figure 5.142: Another image of the same chip recorded with the SrI ₂ – 6 at 12 keV. 400 µm thick. EPO-TEK 305/B4 opt. Adhesive. 120 ms integration time.	158
Figure 5.143: Darkening noticed on the SrI ₂ – 6 detector after a week due to radiation damage on the EPO-TEK 305/B4 opt. Adhesive.	158
Figure 5.144: Radiography image of a 3mm diameter copper grid with 8 µm wires, the line at the top of this image is a breakage plane from sample handling.....	159
Figure 5.145: Single projection images of a bug „Trigonopterus vandekampi“ in absorption contrast and phase contrast mode.....	160
Figure 5.146: High resolution and high contrast (absorption contrast) images of the bug „Trigonopterus vandekampi“ showing the internal organs.	161
Figure 5.147: Tomography image (side view) of the bug „Trigonopterus vandekampi“ showing a good resolution of the scales on the body.	162
Figure 5.148: A view of the internal organs of the bug „Trigonopterus vandekampi“	163
Figure 5.149: An image of the bug „Trigonopterus vandekampi“ revealing the muscles that control the movement of the head and also scales on the internal body.....	164
Figure 5.150: An image of the bug „Trigonopterus vandekampi“ showing the legs.	165
Figure 5.151: The front view of the bug „Trigonopterus vandekampi“	166
Figure 5.152: Calculated X-ray absorption efficiency of SrI ₂ – scintillator thin screens.	168
Figure 6.1: The ¹³⁷ Cs - isotope pulse height spectra recorded at the FISK University with SrI ₂ – scintillator detectors made in this work.....	173
Figure 6.2: Scintillation timing of SrI ₂ – scintillators produced in this work and measured at the FISK University.	173
Figure 6.3: Observed ¹³⁷ Cs spectra using a FISK SrI ₂ – crystal, FMF SrI ₂ – crystal and Saint-Gobain BGO – crystal.....	174
Figure 6.4: Scintillation timing of a FISK SrI ₂ – crystal, FMF SrI ₂ – crystal and Saint-Gobain BGO – crystal.	175
Figure 6.5: Lengthening of scintillation decay [Cherepy 2010].....	176

List of Tables

Table 1.1: Characteristics of SrI ₂ and LaBr ₃ scintillators [Cherepy 2010].....	1
Table 3.1: Summary of the I-Sr binary system phase diagram [Massalski 1990] [Okamoto 2000].	49
Table 3.2: Structural properties of SrI ₂ and EuI ₂	57
Table 5.1: Temperature gradient of the single-zone Bridgman furnace.....	79
Table 5.2: Data on the two Gero furnace segments used.	85
Table 5.3: Scintillator characteristics of YAG- and SrI ₂ – scintillators.....	140
Table 5.4: PCO 4000 technical data [Baumbach 2007].	141
Table 5.5: Gray values (counts) from the recorded flat field images.	147
Table 6.1: Scintillation characteristics of SrI ₂ – scintillators produced in this work.....	172
Table 6.2: Scintillation characteristics of sample – 7.....	174
Table 6.3: Comparison of the FMF samples with a FISK university sample.....	175

Hygroscopic Test

In order to understand how hygroscopic or how fast the SrI₂ absorbs moisture from the atmosphere, 1.2388g of the SrI₂ was exposed to the ambient atmosphere. The weight increase of the SrI₂ is plotted below against the time. The amount of moisture absorbed each day is given by the slope of the graph. Images of the sample melting in the absorbed moisture are also shown. Room moisture concentration could not be measured due to lack of hygrometer.



Day 0: 1.2388g



Day 1: 1.3064g



Day 7: 1.4785g



Day 14: 1.5947g



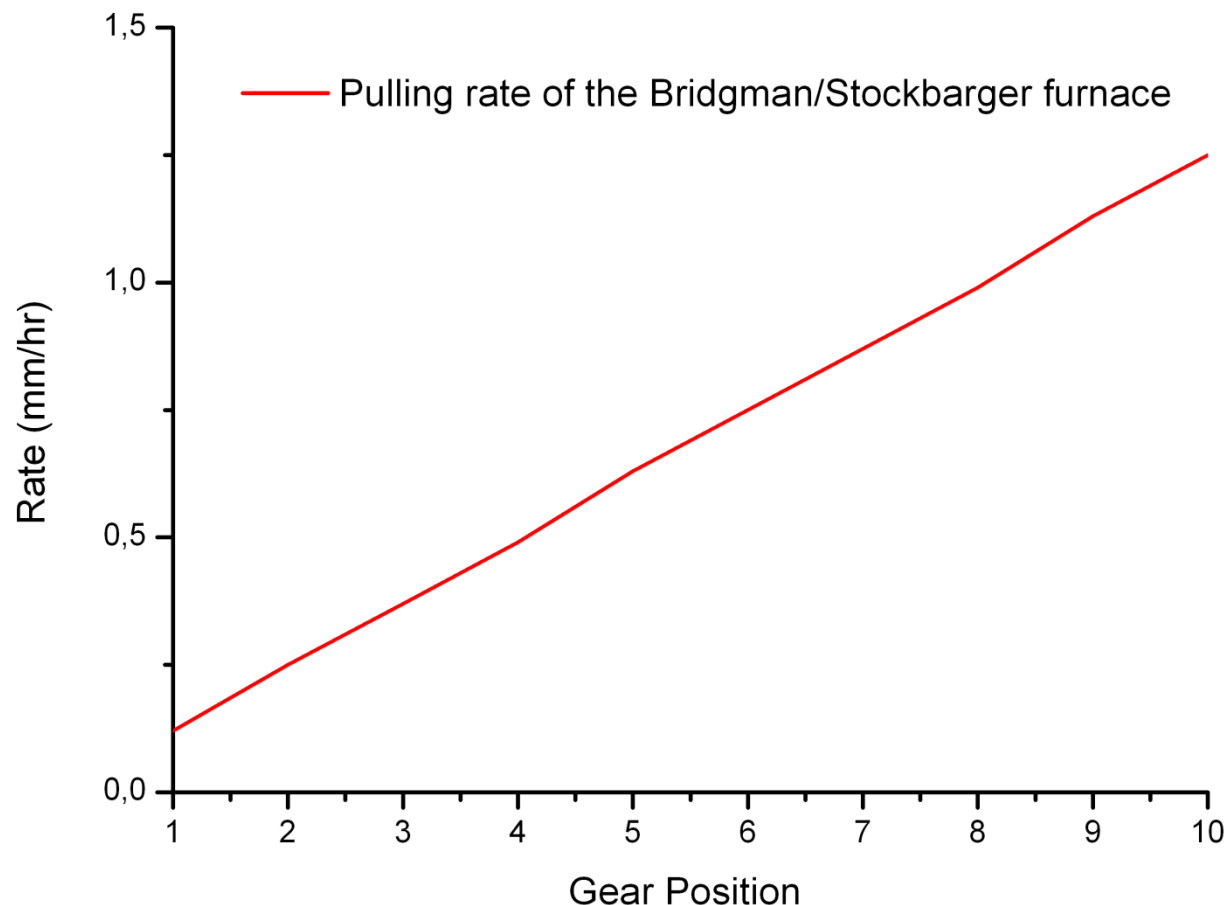
Day 33: 1.7054g



Day 37: 1.7545g

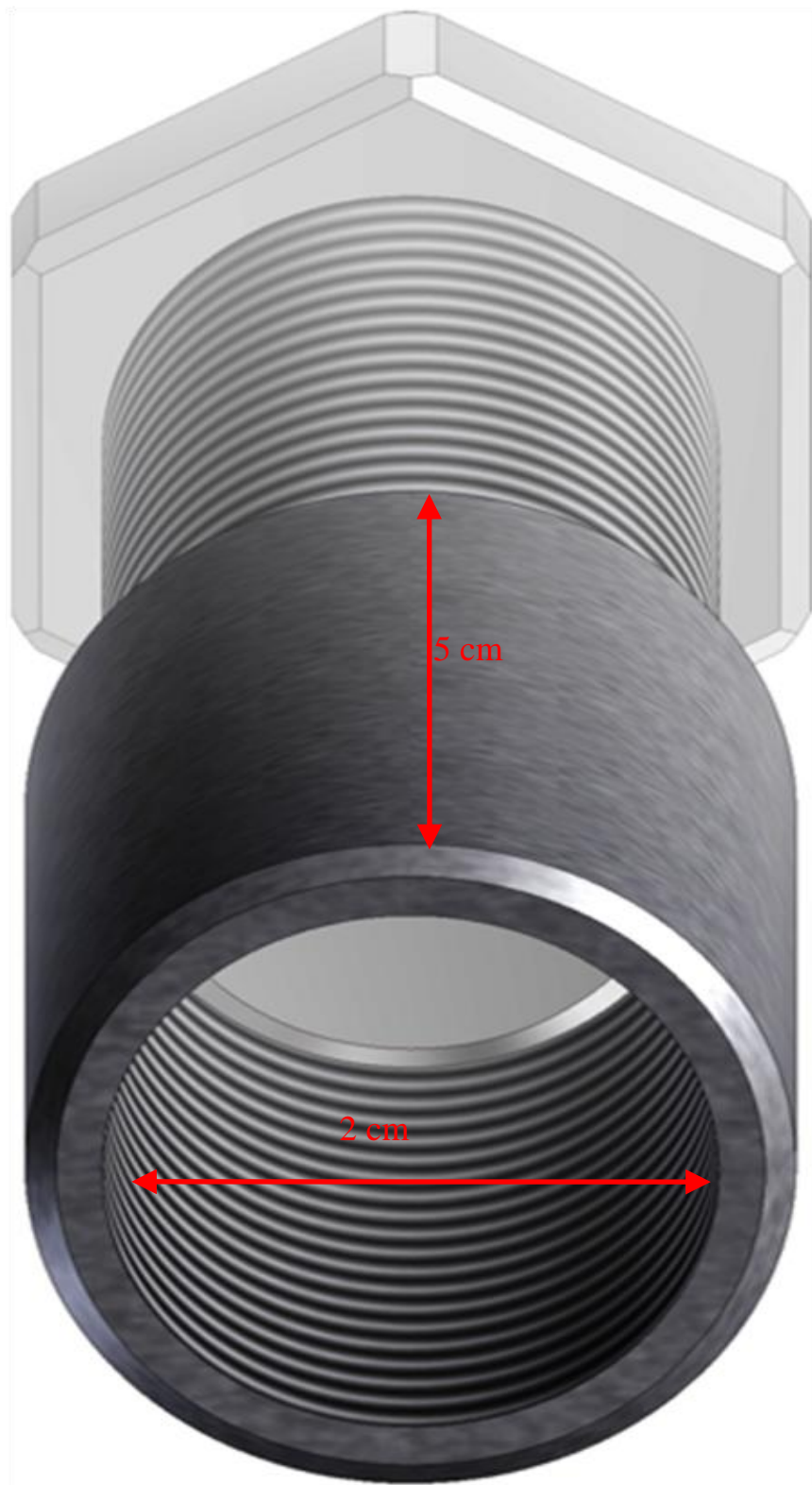
Pulling Rate of the Bridgman/Stockbarger Crystal Growth Equipment

The pulling rate profile was plotted based on data recorded during crystal growth experiments.



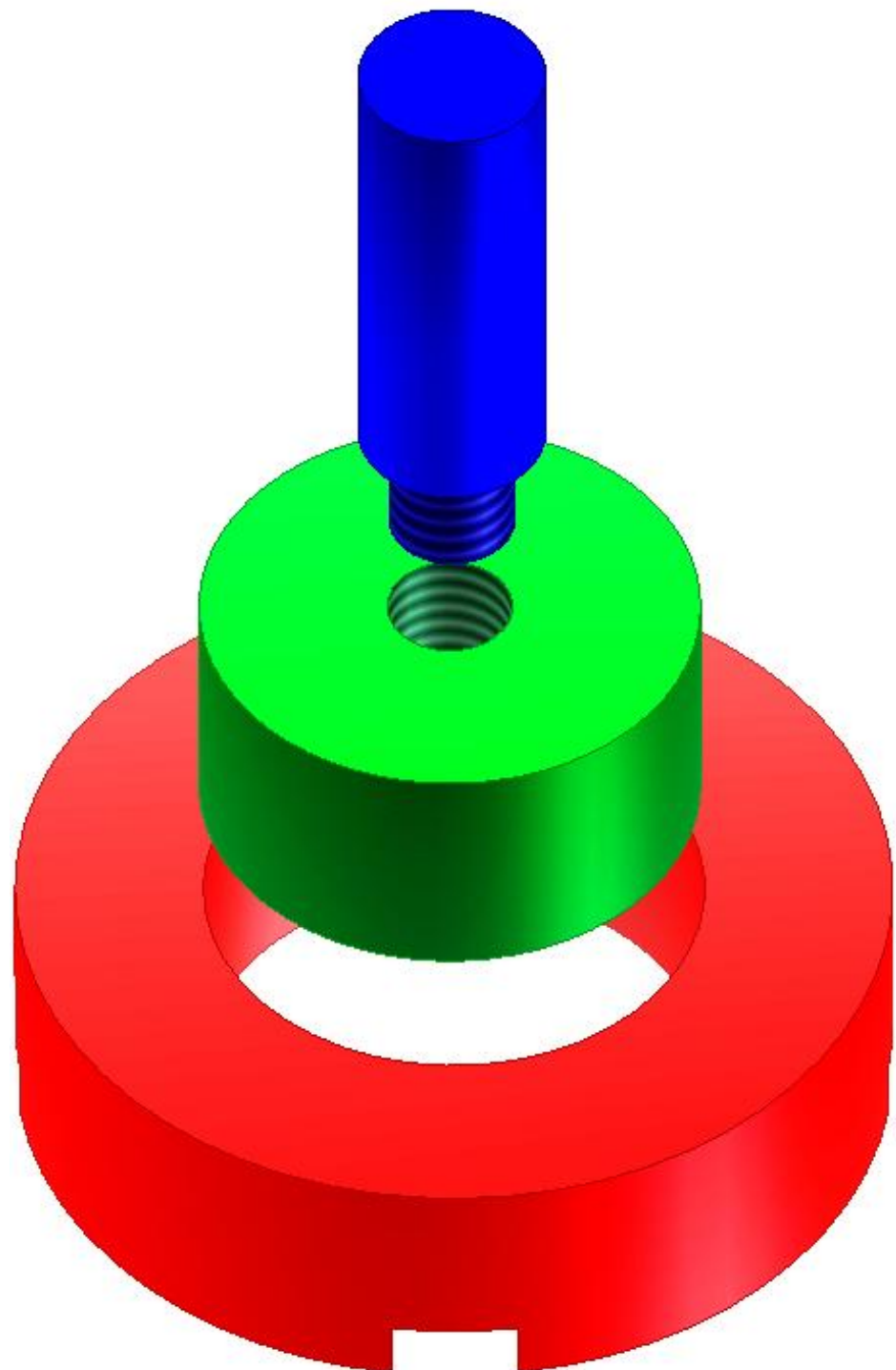
Polishing Stamps

Constructed polishing stamps, that made possible the polishing of the micrometer samples. The advantage of the first polishing stamp was its adjustable depth. This allowed gradually grinding crystals down to 1mm and polishing of one side. Crystals of up to 1.5 cm diameter can be prepared using this stamp.

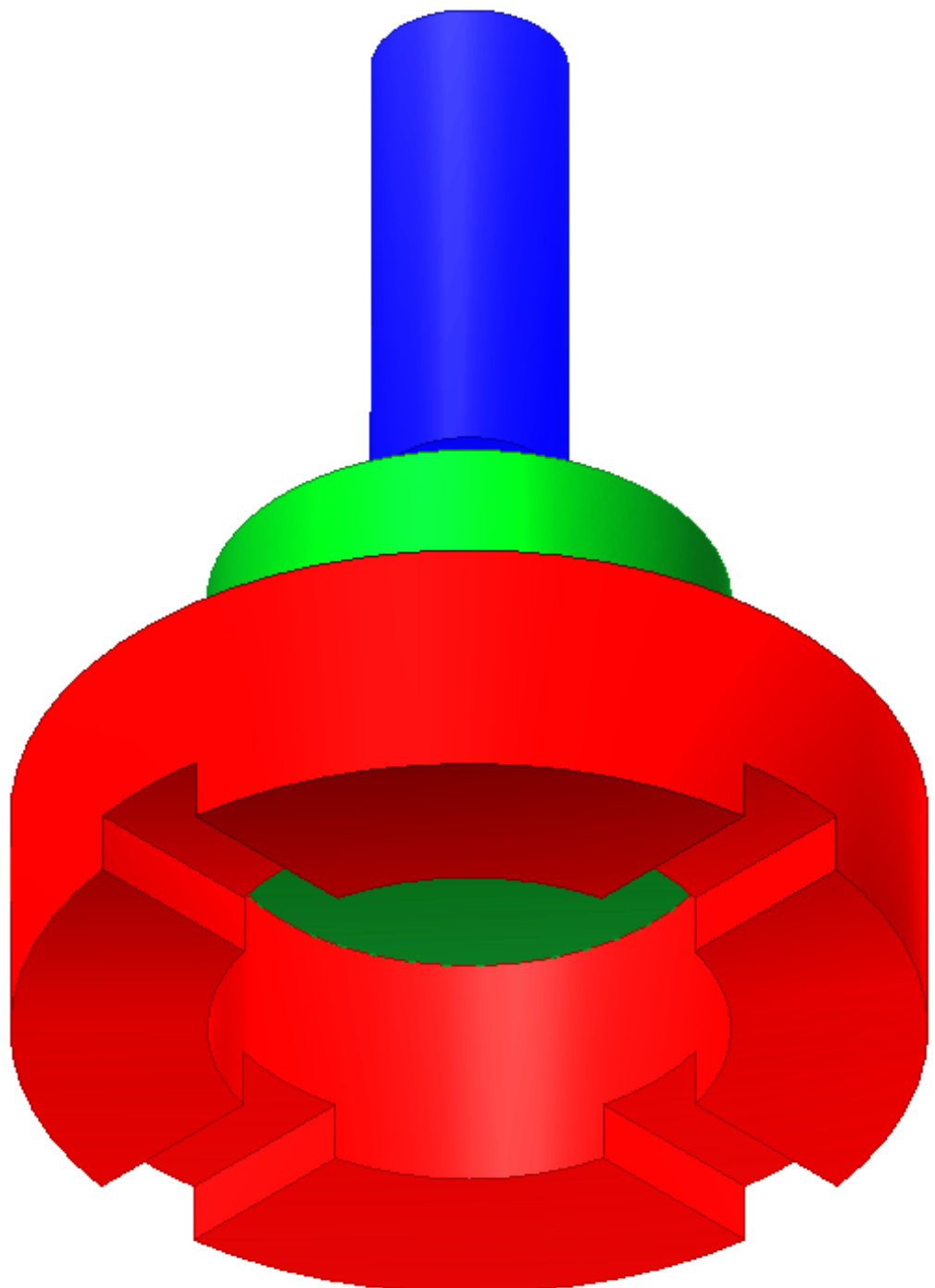


Attachments

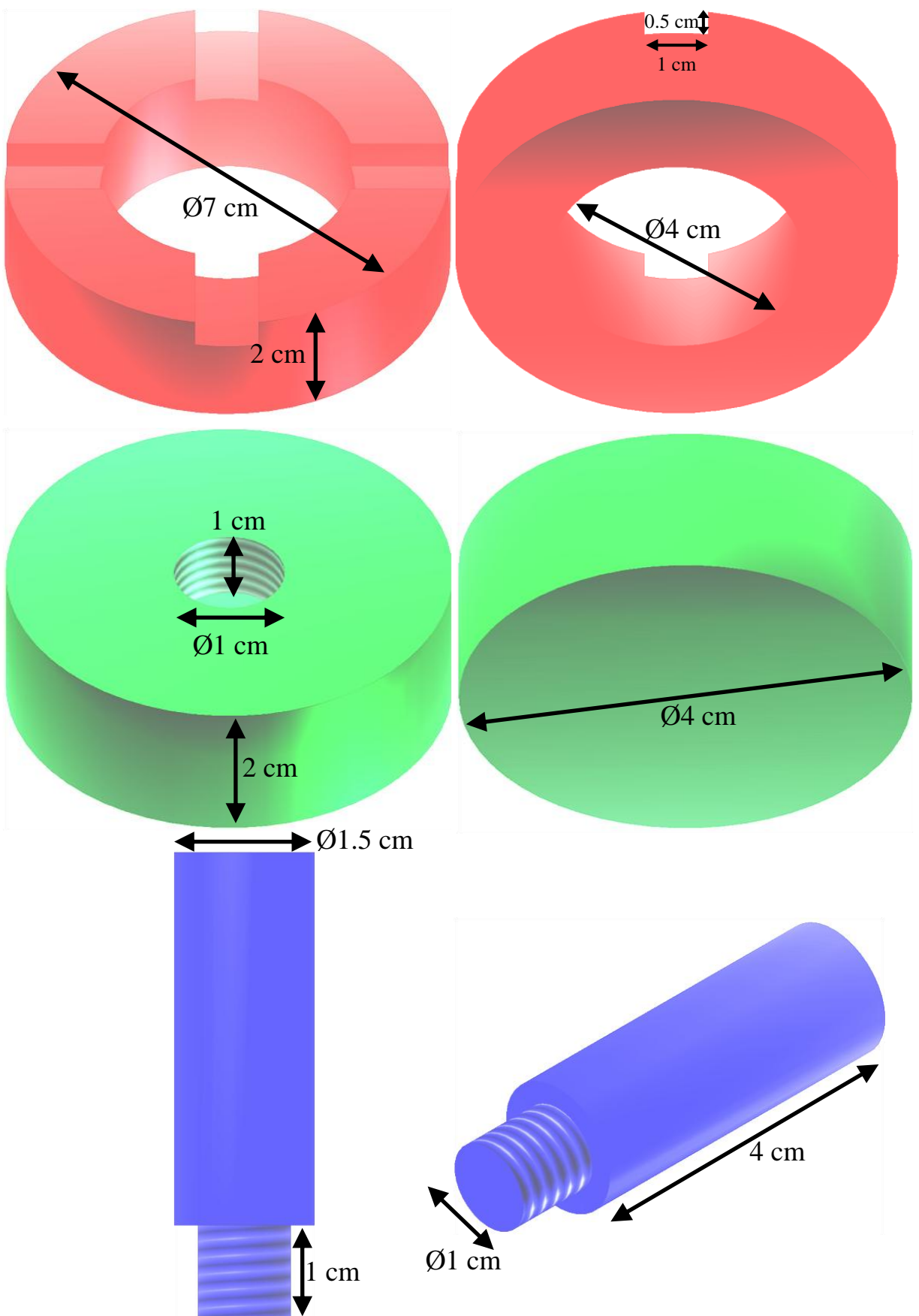
This stamp can handle crystals up to 3 cm diameter. It is used after one side of crystal thin screens has been polished and permanently glued to an Aluminum disc. The advantage of this stamp is that, it prevents tilting of samples, the end products are flat samples of equal thickness.



Attachments

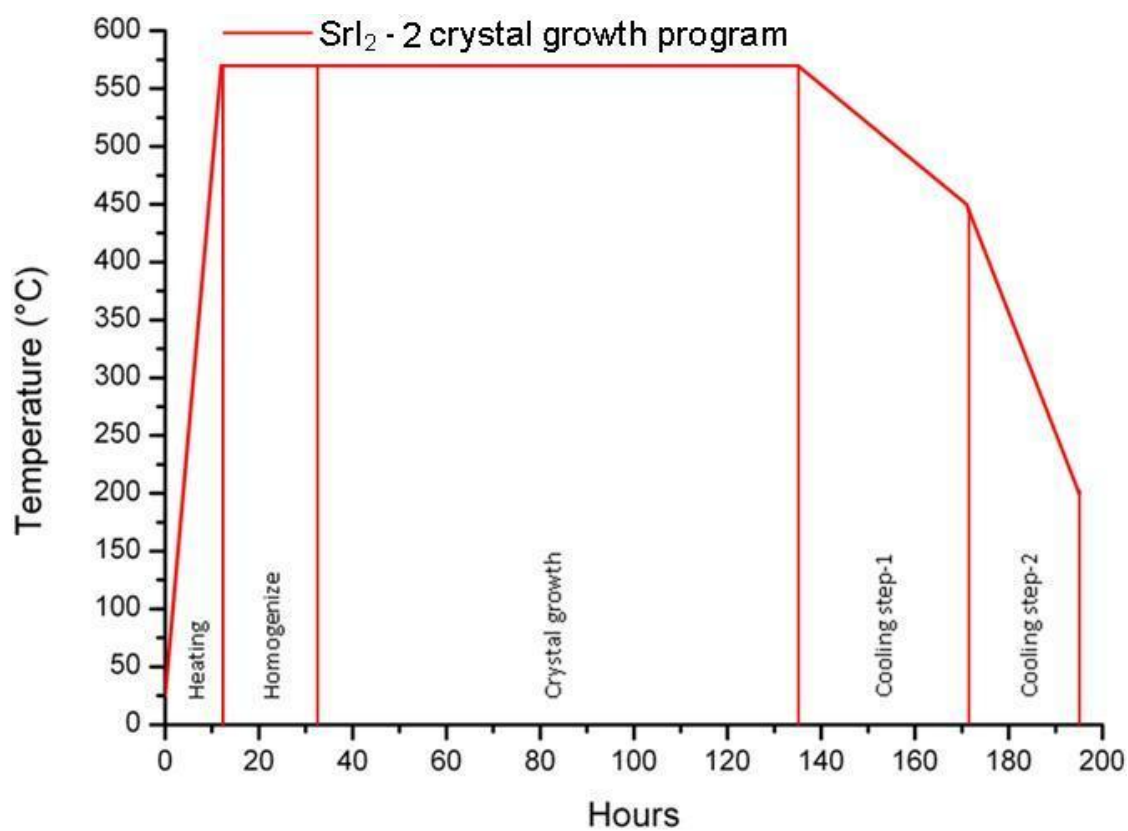
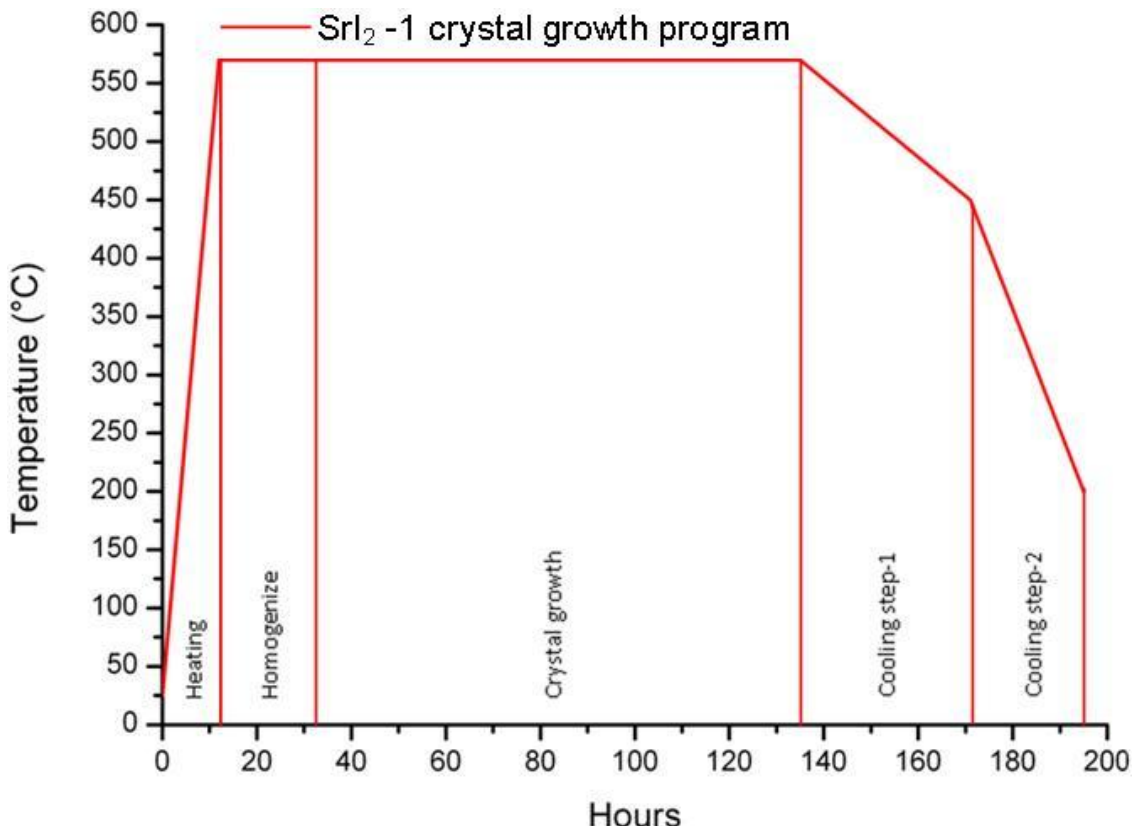


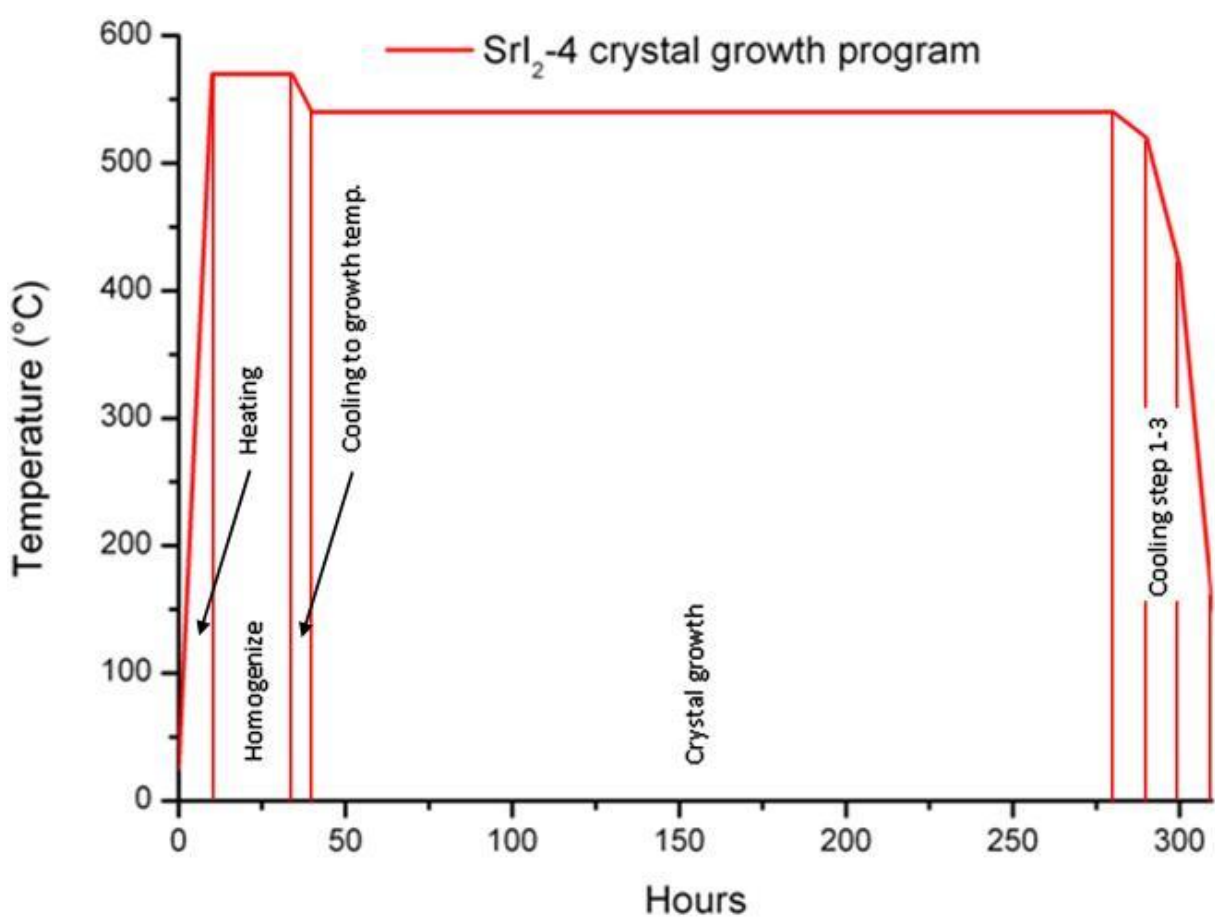
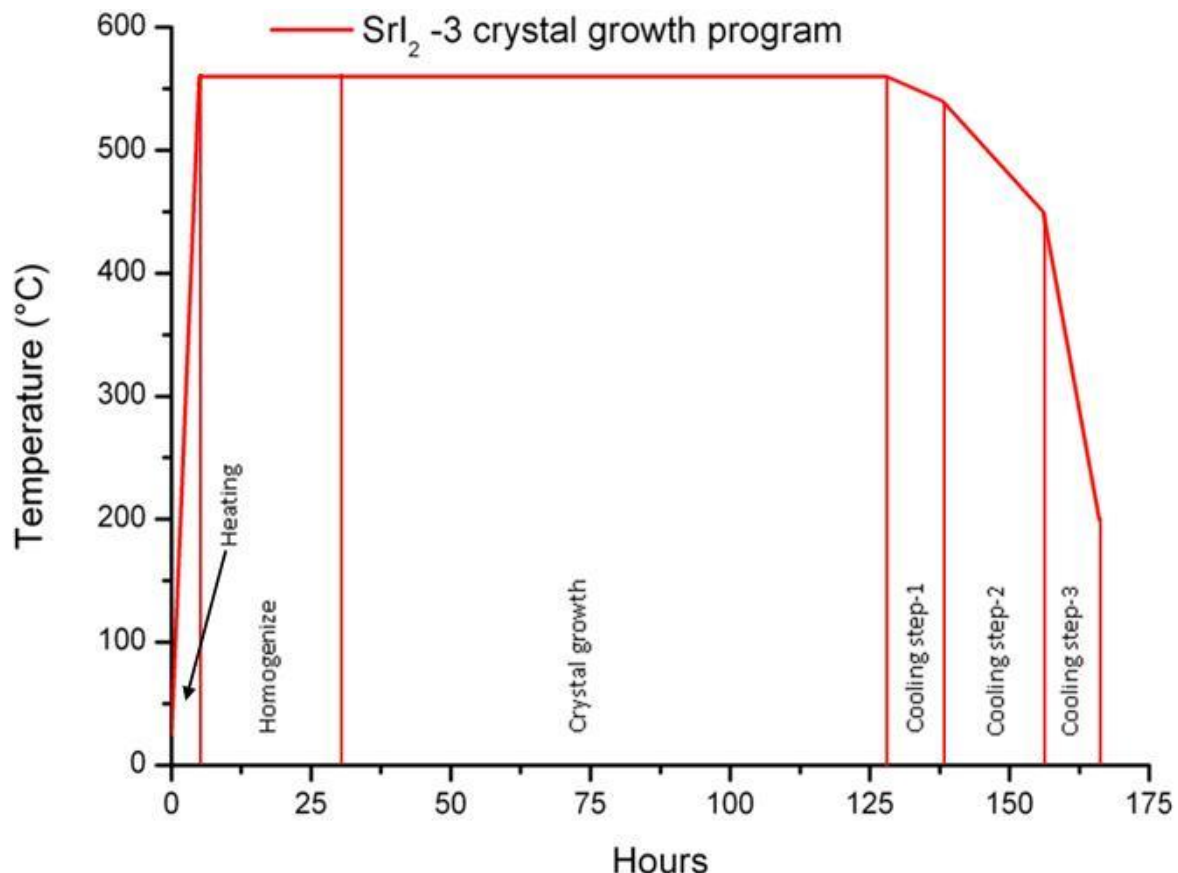
Attachments

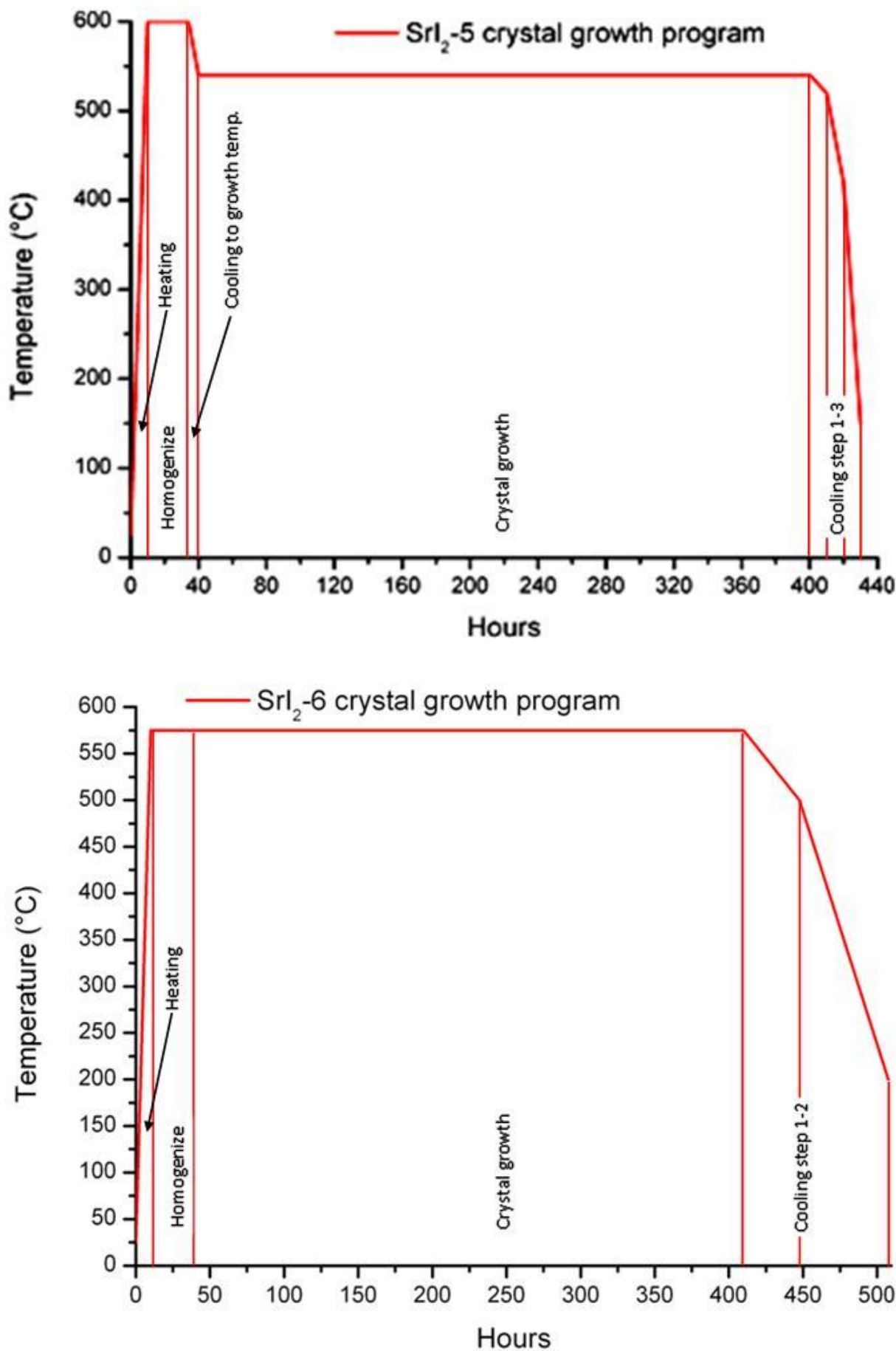


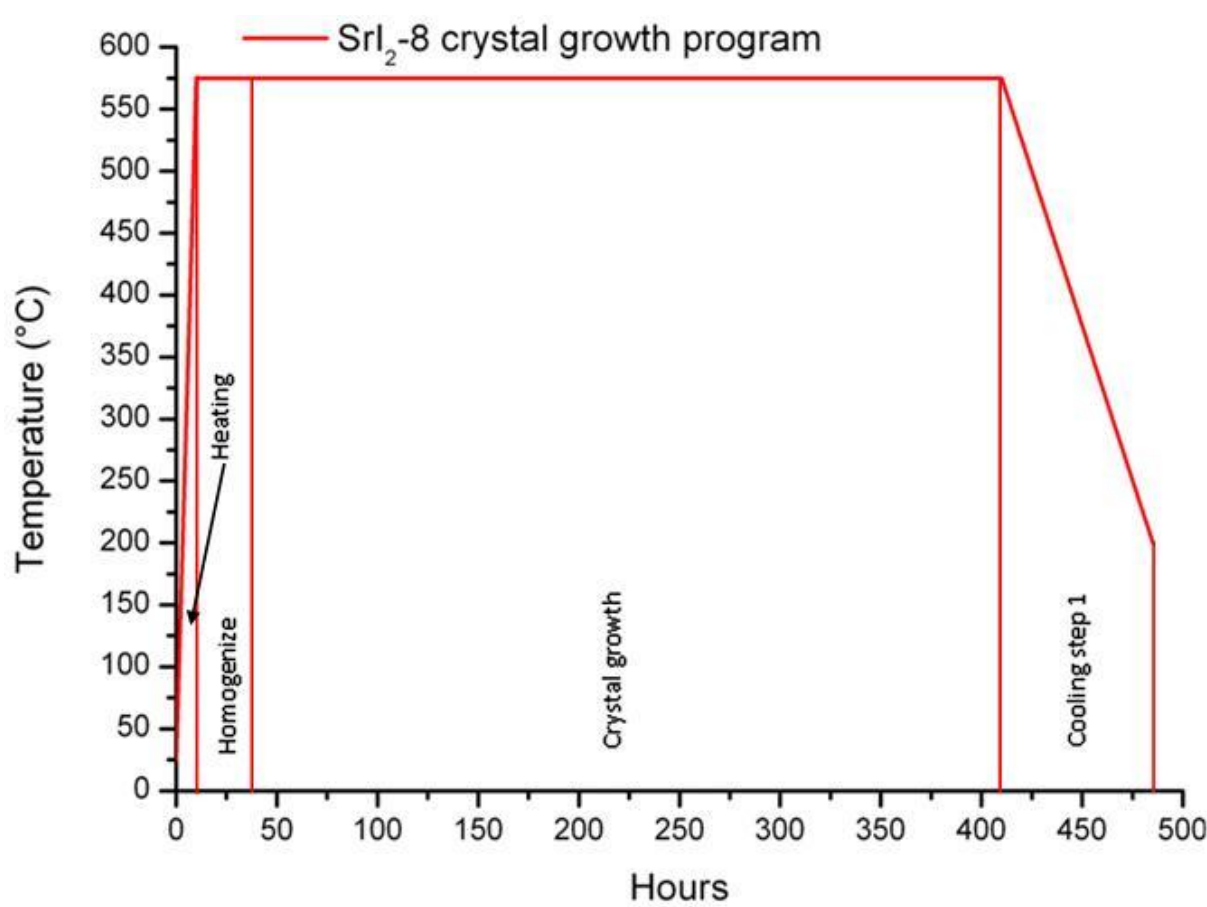
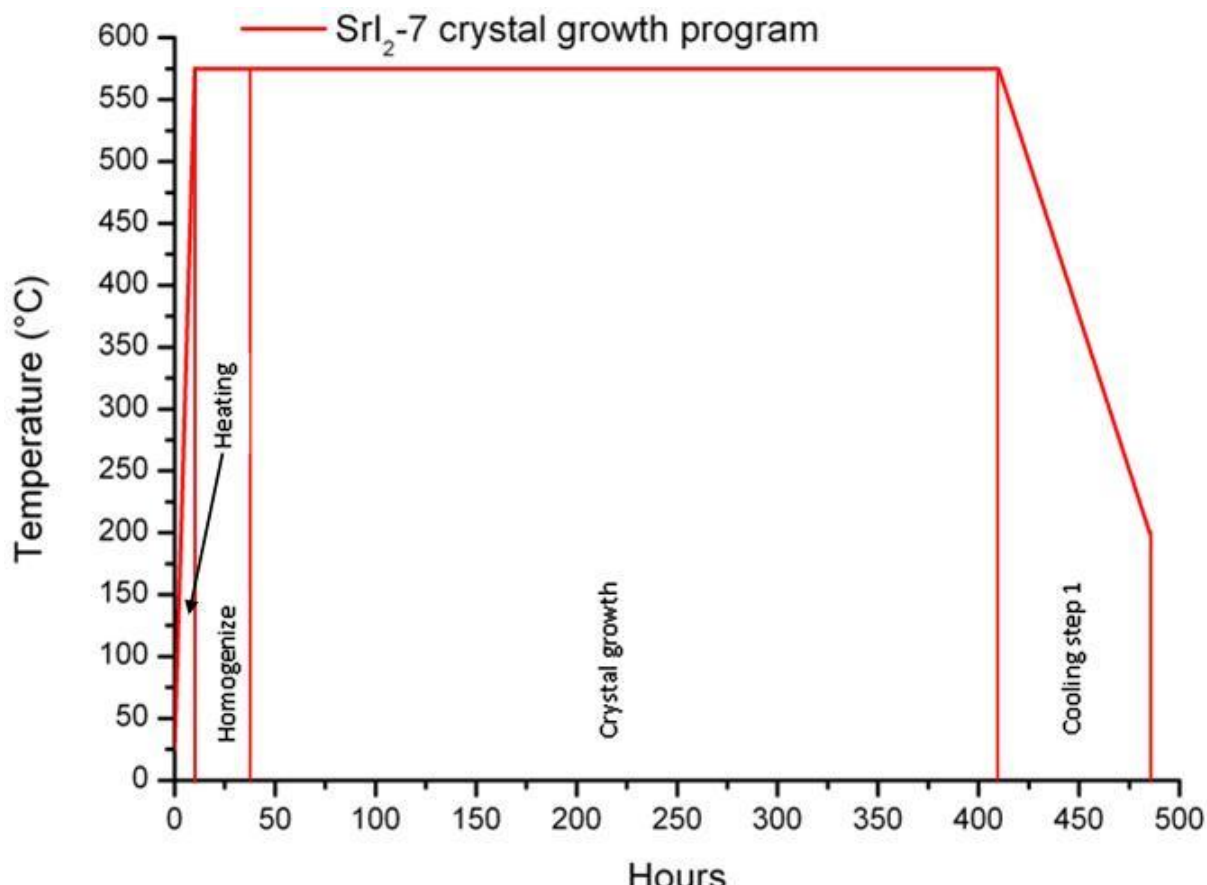
Crystal Growth Programs

Different crystal growth programs used in the course of this work.









Attachments

Glovebox Dewpoint/Moisture Concentration Table (Mecaplex AG)

Taupunkt [°C]	Feuchtigkeit [ppm]	Taupunkt [°C]	Feuchtigkeit [ppm]	Taupunkt [°C]	Feuchtigkeit [ppm]
0	6000	-30	380	-60	10,6
-1	5500	-31	342	-61	9,2
-2	5100	-32	309	-62	8
-3	4700	-33	276	-63	6,98
-4	4350	-34	249	-64	6,08
-5	3980	-35	222	-65	5,28
-6	3650	-36	200	-66	4,58
-7	3380	-37	179	-67	3,96
-8	3080	-38	162	-68	3,40
-9	2840	-39	144	-69	2,94
-10	2590	-40	128	-70	2,53
-11	2360	-41	114	-71	2,17
-12	2160	-42	102	-72	1,87
-13	1980	-43	90	-73	1,61
-14	1800	-44	80	-74	1,37
-15	1650	-45	71,9	-75	1,17
-16	1500	-46	63,5	-76	1,01
-17	1360	-47	56,2	-77	0,86
-18	1250	-48	49,9	-78	0,73
-19	1140	-49	44	-79	0,618
-20	1030	-50	39	-80	0,522
-21	940	-51	34,2	-81	0,498
-22	860	-52	30,4	-82	0,378
-23	765	-53	26,7	-83	0,315
-24	697	-54	23,4	-84	0,262
-25	625	-55	20,6	-85	0,221
-26	553	-56	18,2	-86	0,186
-27	517	-57	15,9	-87	0,156
-28	467	-58	13,9	-88	0,130
-29	426	-59	12,1	-89	0,110

Attachments

Structural Data on Space Group – Pbca

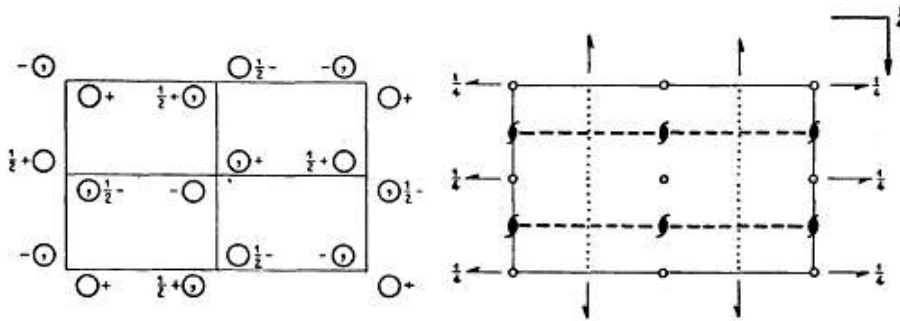
Structural data as published in the international tables for X-ray crystallography. Vol. 1. Symmetry Groups. By THE KYNOCH PRESS. BIRMINGHAM, ENGLAND. 1969.

Pbca
D_{2h}¹⁵

No. 61

P 2₁/*b* 2₁/*c* 2₁/*a*

m m m Orthorhombic



Origin at I

Number of positions,
Wyckoff notation,
and point symmetry

Co-ordinates of equivalent positions

Conditions limiting
possible reflections

8 *c* 1 $x, y, z; \frac{1}{2}+x, \frac{1}{2}-y, z; \bar{x}, \frac{1}{2}+y, \frac{1}{2}-z; \frac{1}{2}-x, \bar{y}, \frac{1}{2}+z;$
 $\bar{x}, \bar{y}, \bar{z}; \frac{1}{2}-x, \frac{1}{2}+y, z; x, \frac{1}{2}-y, \frac{1}{2}+z; \frac{1}{2}+x, y, \frac{1}{2}-z.$

General:

hkl: No conditions
0kl: $k=2n$
h0l: $l=2n$
hk0: $h=2n$
h00: ($h=2n$)
0k0: ($k=2n$)
00l: ($l=2n$)

4 *b* I 0,0,½; ½,½,½; 0,½,0; ½,0,0.
 4 *a* I 0,0,0; ½,½,0; 0,½,½; ½,0,½.

Special: as above, plus
 } *hkl*: $h+k, k+l, (l+h)=2n$

Symmetry of special projections

(001) *pgm*; $a'=a/2, b'=b$

(100) *pgm*; $b'=b/2, c'=c$

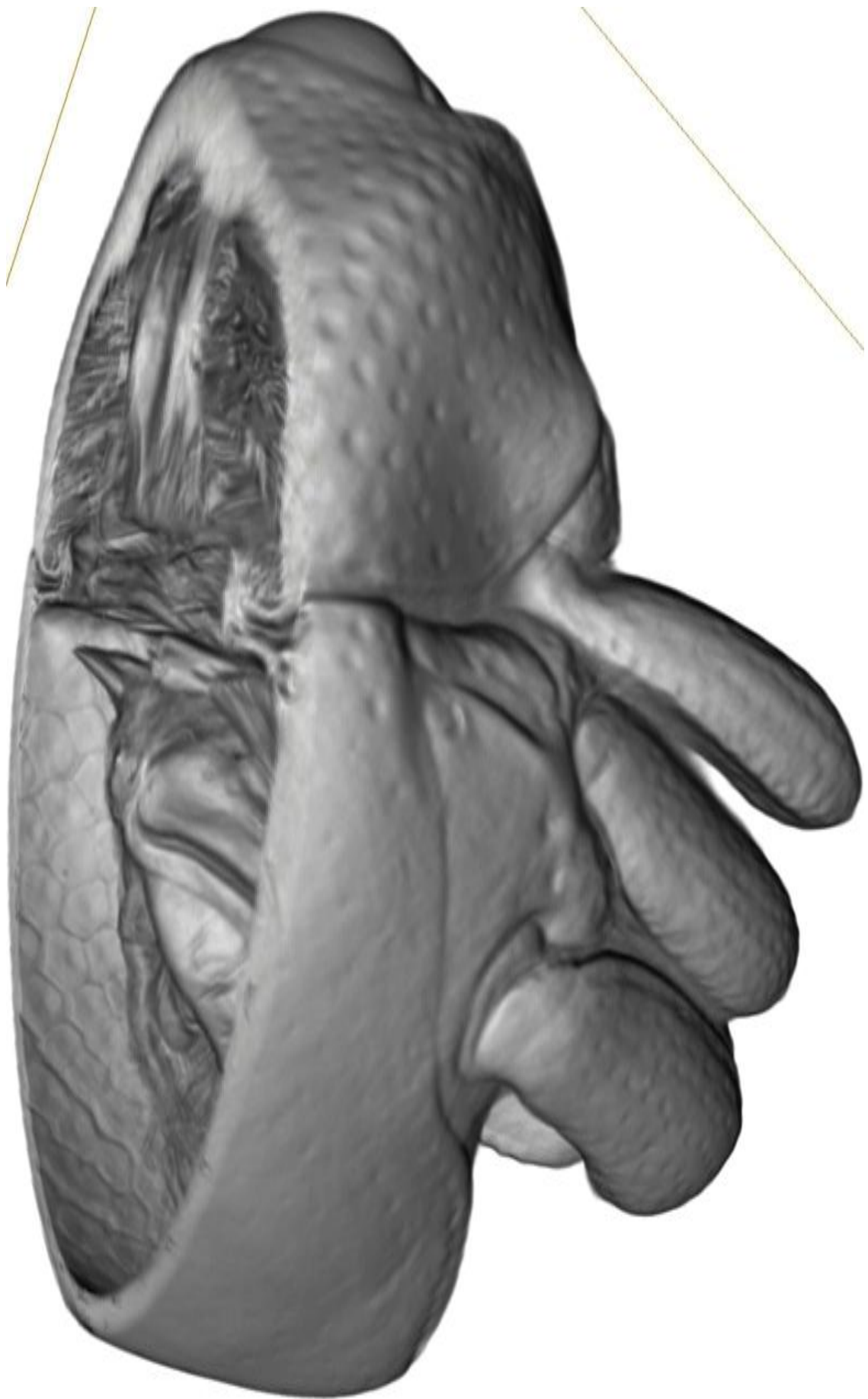
(010) *pgm*; $c'=c/2, a'=a$

Attachments

More 3D - images of the Bug „*Trigonopterus vandekampi*“ (not to scale).



Attachments

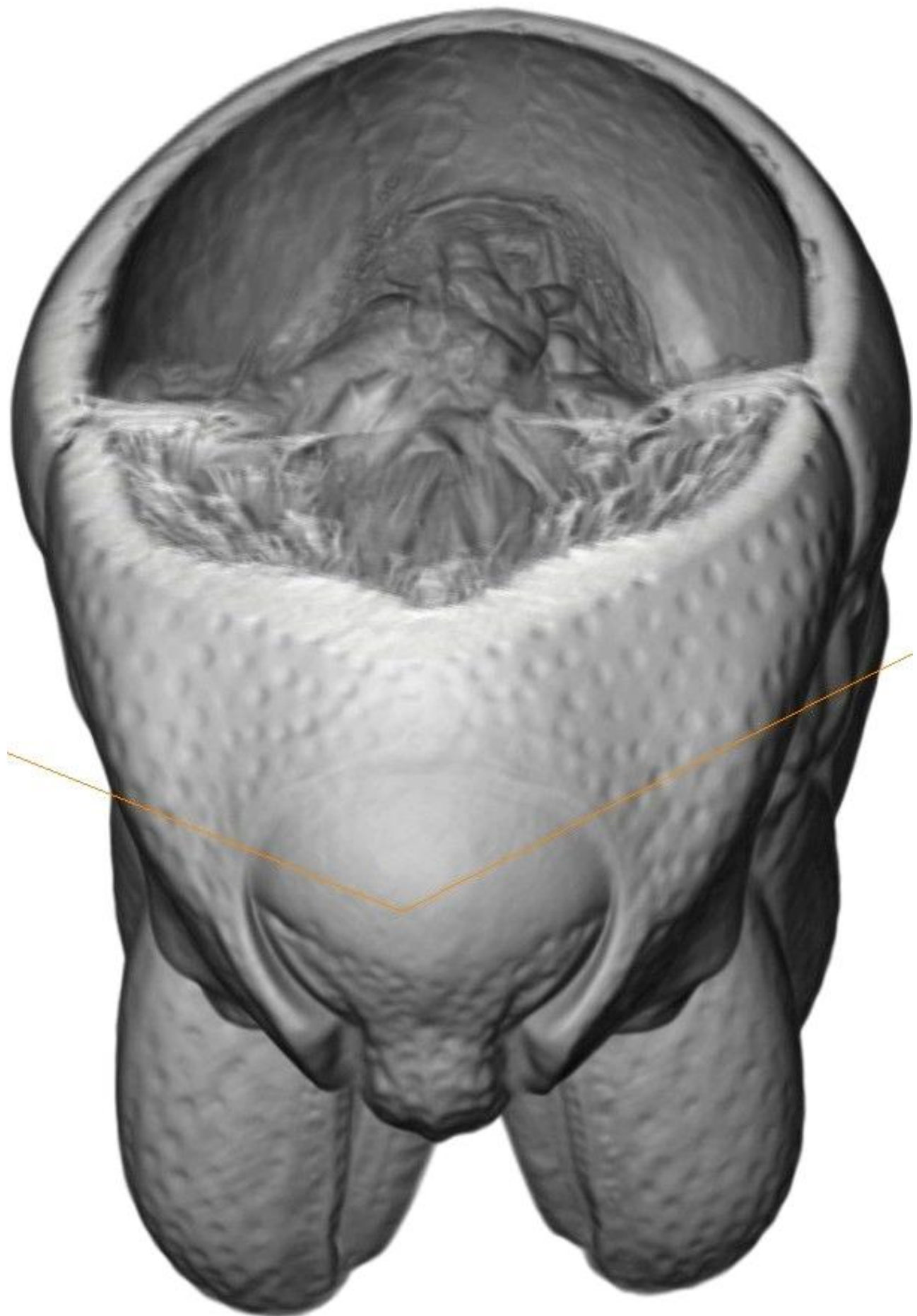




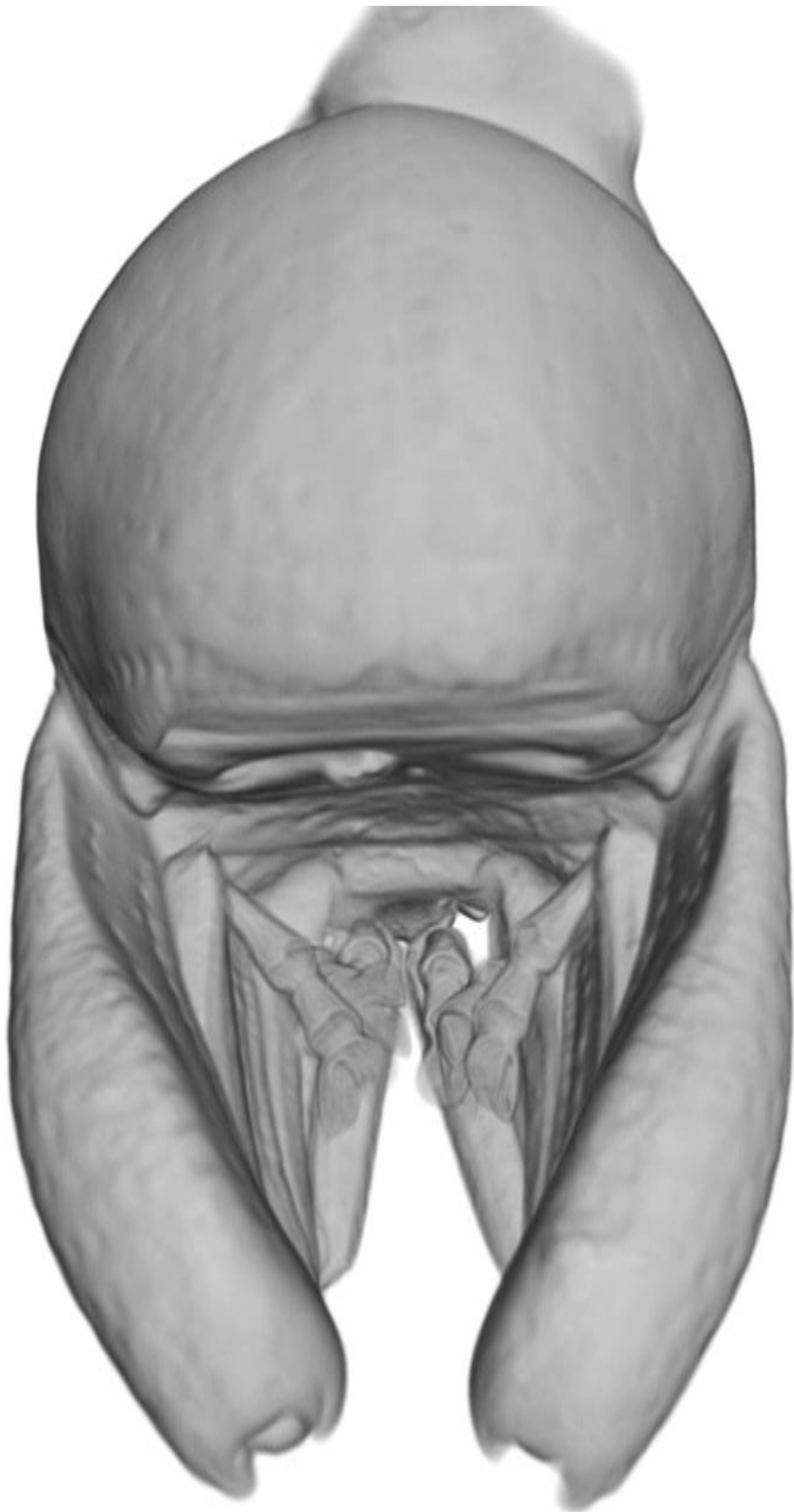
Attachments



Attachments



Attachments



Equipments and Software

1. Tapp V2.2 from E S Microware
2. Autodesk Inventor Professional 2010